

Alma Mater Studiorum – Università di Bologna
in cotutela con Università Claude-Bernard di Lione

DOTTORATO DI RICERCA IN

CHIMICA

Ciclo XXXII

Settore Concorsuale: 03/C2 - CHIMICA INDUSTRIALE

Settore Scientifico Disciplinare: CHIM/04 – CHIMICA INDUSTRIALE

**PHOTOCATALYTIC PRODUCTION OF CHEMICALS AND HYDROGEN
FROM BIOMASS**

Presentata da: Valeriia Maslova

Coordinatore Dottorato

Prof.ssa Domenica Tonelli

Supervisor

**Prof.ssa Stefania Albonetti
Dr.ssa Elsje Alessandra Quadrelli**

Co-supervisore

Prof. Francesco Basile

Esame finale anno 2020

N°d'ordre NNT : xxx



THESE de DOCTORAT DE L'UNIVERSITE DE LYON

opérée au sein de
l'Université Claude Bernard Lyon 1

Ecole Doctorale N° ED206
Chimie de Lyon

Spécialité de doctorat : Chimie
Discipline : Chimie Industrielle Durable

Soutenue publiquement le 03/02/2020, par :
Valeriia Maslova

Production photocatalytique de produits chimiques et d'hydrogène à partir de biomasse

Devant le jury composé de :

Prof. Francesco Di Renzo	Ecole Nationale Supérieure de Chimie de Montpellier	Rapporteur
Prof. Siglinda Perathoner	Università di Messina	Rapporteuse
Prof. Paolo Fornasiero	Università di Trieste	Examinateur
Prof. Shashank Mishra	Université Claude Bernard Lyon1	Examinateur
Dr. Carlo Lucarelli	Università di Bologna	Examinateur
Prof. Stefania Albonetti	Università di Bologna	Directrice de thèse
Prof. Francesco Basile	Università di Bologna	Co-directeur de thèse
Dr. Elsje Alessandra Quadrelli	Université Claude Bernard Lyon1	Directrice de thèse

Université Claude Bernard – LYON 1

Président de l'Université	M. Frédéric FLEURY
Président du Conseil Académique	M. Hamda BEN HADID
Vice-Président du Conseil d'Administration	M. Didier REVEL
Vice-Président du Conseil des Etudes et de la Vie Universitaire	M. Philippe CHEVALLIER
Vice-Président de la Commission de Recherche	
Directeur Général des Services	M. Damien VERHAEGHE

COMPOSANTES SANTE

Faculté de Médecine Lyon-Est – Claude Bernard	Doyen : M. Gilles RODE
Faculté de Médecine et Maïeutique Lyon Sud Charles. Mérieux	Doyenne : Mme Carole BURILLON
UFR d'Odontologie	Doyenne : Mme Dominique SEUX
Institut des Sciences Pharmaceutiques et Biologiques	Directrice : Mme Christine VINCIGUERRA
Institut des Sciences et Techniques de la Réadaptation	Directeur : M. Xavier PERROT
Département de Formation et Centre de Recherche en Biologie Humaine	Directrice : Mme Anne-Marie SCHOTT

COMPOSANTES & DEPARTEMENTS DE SCIENCES & TECHNOLOGIE

UFR Biosciences	Directrice : Mme Kathrin GIESELER
Département Génie Electrique et des Procédés (GEP)	Directrice : Mme Rosaria FERRIGNO
Département Informatique	Directeur : M. Behzad SHARIAT
Département Mécanique	Directeur M. Marc BUFFAT
UFR - Faculté des Sciences	Administrateur provisoire : M. Bruno ANDRIOLETTI
UFR (STAPS)	Directeur : M. Yannick VANPOULLE
Observatoire de Lyon	Directrice : Mme Isabelle DANIEL
Ecole Polytechnique Universitaire Lyon 1	Directeur : Emmanuel PERRIN
Ecole Supérieure de Chimie, Physique, Electronique (CPE Lyon)	Directeur : Gérard PIGNAULT
Institut Universitaire de Technologie de Lyon 1	Directeur : M. Christophe VITON
Institut de Science Financière et d'Assurances	Directeur : M. Nicolas LEBOISNE
ESPE	Administrateur Provisoire : M. Pierre CHAREYRON

Acknowledgments

This work was funded by SINCEM grant. SINCEM is a Joint Doctorate Program selected under the ERASMUS MUNDUS Action 1 Programme (FPA 2013-0037).



First of all, I would like to express my gratitude to my supervisors, **Prof. Stefania Albonetti**, **Prof. Francesco Luca Basile**, **Dr. Elsje Alessandra Quadrelli** and **Dr. Alessandra Sanson** for the support in this PhD journey at University of Bologna (UNIBO), University of Claude Bernard Lyon 1 (UCBL) and Institute of Science and Technology of Ceramics (ISTEC-CNR) for their patience and kindness, knowledge and experience, and for the given opportunity to open new horizons in my professional development.

I would like to acknowledge other SINCEM consortium members who made this program possible and for the opportunity to discuss on my research work during the SINCEM School meetings: **Prof. Francesco Di Renzo**, **Prof. Gabriele Centi**, **Prof. Siglinda Perathoner**, **Prof. Regina Palkovitz**, **Prof. Steve Howdle**, **Prof. Raffaele Pirone**, **Prof. Fabrizio Cavani**, **Prof. Walter Leitner**.

I also would like to thank secretary office at UNIBO and UCBL and in particularly, SINCEM manager, **Dr. Marina Grandini**, for continuous support and help in administrative questions.

I would like to acknowledge **Dr. Francesca Ospitali** for performing TEM and SEM measurements and their interpretation, for assistance in different spectroscopical analyses, **Dr. Alessandra Petroli** and **Dr. Rita Mazzoni** for assistance in NMR analyses, **Salvatore Spatola** for XRF measurements and intranet technical assistance at UNIBO. Advices, introduction to different new characterization tools and discussions provided by **Dr. Kai Szeto**, **Laurent Veyre**, **Christine Lucas**, **Dr. Frédéric Lefebvre**, **Nesrine Cherni**, **Dr. Mostafa Taoufik**, **Ruben Vera** have been a great help in the accomplishing research activities at UCBL.

Special acknowledgement to my colleagues and dear friends at UNIBO, **Dr. Nicola Schiaroli**, **Dr. Alice Lolli**, **Dr. Erica Lombardi**, **Dr. Francesco Puzzo**, **Dr. Tomaso Tabanelli**, **Dr. Lorenzo Grazia**, **Dr. Mattia Meloni**, **Dr. Juliana Velásquez**, **Dr. Sara Andreoli**, **Dr. Stefania Solmi**, **Dr. Andrea Vasso**, **Dr. Chiara Molinari**, **Dr. Andrea Cingolani**, **Giancosimo Sanghez De Luna**, **Andrea Fasolini**, **Jacopo De Maron**, **Eleonora Monti**, **Laura Setti**, **Annalisa Sacchetti**, **Giulia Balestra**, **Luca Ganzerla**, **Federico Bugli**, **Amer Inayat**, **Tito Della Rosa**, at UCBL, **Dr. Marc Renom Carrasco**, **Dr. Iurii Suleimanov**, **Dr. Martin Jakoobi**, **Vittoria Chiari**, **Clement Demarcy**, **Sebastien Lassalle**, **Isis N'Dala-Louika** and at ISTEC-CNR, **Dr. Nicola Sangiorgi**, **Dr. Alex Sangiorgi**, **Dr. Angela Gondolini**, **Dr. Elisa Mercadelli**, **Linda Bergamini** and all the researchers, PhDs, PostDoc colleagues and trainees, for the help, the support, the opportunity to discuss on different scientific subjects and not only, for lots of funny moments.

My sincere gratitude to all my dear SINCHEM friends who always encouraged me throughout my PhD life by their enthusiasm, willpower and striving for excellence: **Dr. Andres Sierra Salazar**, **Dr. Tapish Saboo**, **Dr. Olena Vozniuk**, **Dr. Pooja Gaval**, **Dr. Aisha Matayeva**, **Paola Blair Vasquez**, **Medet Zhukush**, **Dr. Sonia Aguilera**, **Dr. Danilo Bonincontro**, **Dr. Phuoc Ho Hoang**, **Dr. Maria Gyngazova**, **Ulisse Montanari**, **Ferenc Martinovic**, **Marcelo Alves Favaro**, **Ravi Srivastava**, **Akash Kaithal**, **Dr. Nguyen Tran**, **Samantha Molina Gutierrez**, **Ana Patricia Costa Pacheco**, **Hua Wei**, **Dr. Daniel Aguilera**, **Dr. Matilde Solmi**, **Dr. Payal Baheti**, **Dr. Iqra Zubair**, **Dr. Kristin Tolod**, **Dr. Shiming Chen**, **Dr. Chalachew Mebrahtu**, **Dr. Alba Rodriguez**, **Dr. Tahrizi Andana**.

I would like to thank various people, represented by the European Commission, to all the professors and managers of SERP-Chem Erasmus Mundus Joint Master Program, the director, **Prof. Sandrine Lacombe**, and the committee, **Prof. Nicolas Rabasso** (University of Paris-Sud), **Prof. Mario Rocca** (University of Genova), **Prof. Eduardo Marques** (University of Porto) and **Prof. Bohdan Skalski** (Adam Mitskevich University) for the given opportunity to gain invaluable experience and skills during my studies in European Union following the Master program at University of Paris Saclay and University of Porto. I also want to thank **Dr. Thomas Pino** and **Dr. Minh-Huong Ha-Thi** for the knowledge transmitted during my internship at Institut des Sciences Moléculaires d'Orsay (ISMO). I want to thank also my supervisor from the home country university (Donetsk National University), **Dr. Olena Khyzhan**, for the advices and support.

Finally, I want to express my endless gratitude to my beloved family for their support and love throughout my life.

Abstract

Sustainable industrial conversion of biomass as renewable and abundant feedstock is becoming increasingly attractive as to synthesize high-value-added products, which can be utilized in energy sector, food, polymer, cosmetics and pharmacological industries, as well as in production of fine chemicals.

In this work, with the aim to tackle several approaches towards sustainable chemistry, we used biomass derived 5-hydroxymethyl-2-furfural (HMF) in aerobic photo-oxidation. Partial oxidation products of this reaction, for instance 2,5-diformylfuran (DFF) and 2,5-furane dicarboxylic acid (FDCA), are of particular interest for the polymer industry. Glycerol as a multi-ton by-product of biodiesel production was also subjected to anaerobic photo-reforming in order to obtain hydrogen gas and liquid-phase products.

Solar-assisted reactions were performed by means of heterogeneous photocatalysis, in mild conditions such as atmospheric pressure, room temperature and water as a benign solvent. Titanium dioxide was used as a photo-active catalyst. Despite of the fact that TiO_2 is the most active, non-toxic and low-cost material, its wide bandgap allows employing only UV irradiation that covers just 5% of the solar spectrum. Thus, the introduction of noble metal nanoparticles makes it possible to embrace the problem of visible light absorption as well as to reduce electron-hole pair recombination in the semiconductor.

Titanium dioxide was synthesized in the form of nano-powder using a microemulsion-mediated system. Au, Ag, Pt noble metal nanoparticles, Au-Ag, Au-Cu alloys and core-shell nanoparticles, and NiO metal oxide nanoparticles were deposited on TiO_2 support. This was done either by deposition-precipitation or incipient wetness impregnation method. Metal precursor salts or pre-formed nanoparticles were employed in the latter method. The prepared catalysts were characterized by XRD, DRS, N_2 physisorption, TEM, SEM and RAMAN analysis. Their catalytic activity was compared to that of commercially available titanium dioxide powders such as P25 and DT-51. The influence of the support, the size and type of the deposited metal and metal oxide nanoparticles on the photo-catalytic transformation of HMF and glycerol was evaluated. In the case of HMF, the influence of the base addition and the oxygen content on the reaction selectivity was also studied. The effect of the crystalline phase composition and morphology of TiO_2 in the glycerol photo-reforming reaction was assessed as well.

The surface of the synthesized TiO_2 nano-powders was investigated by means of Surface Organometallic Chemistry (SOMC) approach. In particular, the surface was characterized by

chemical titration and DRIFT techniques. Furthermore, the SOMC concept allowed preparing of well-dispersed Pt nanoparticles on the TiO₂ surface. The photo-catalytic activity of this sample in the glycerol photo-reforming process was tested and compared to that of other Pt-containing catalysts prepared by conventional techniques.

In view of avoiding the agglomeration and sedimentation of suspended titania powders in water media, thick films of synthesized and commercial TiO₂ were deposited on a conductive substrate using screen-printing technique. The prepared electrodes were characterized by profilometry, SEM, XRD, optical, electrical and photo-electrochemical methods.

Riassunto

La conversione sostenibile della biomassa su scala industriale, considerata una fonte rinnovabile e abbondante, sta diventando sempre più attraente per sintetizzare prodotti dall'alto valore aggiunto che possono essere utilizzati nel settore energetico, alimentare, dei polimeri, della cosmesi e delle industrie farmaceutiche.

Con l'obiettivo di affrontare diversi approcci per una chimica più sostenibile, in questo lavoro abbiamo utilizzato un derivato della biomassa, il 5-idrossimetil-2-furfurale (HMF), nella reazione di foto-ossidazione aerobica. I prodotti di ossidazione parziale di questa reazione come il 2,5-diformylfurane (DFF), il 2,5-furane dicarboxylic acid (FDCA), sono di particolare interesse per l'industria dei polimeri. Anche il glicerolo, che è sottoprodotto in grandi quantità durante la produzione di biodiesel, è stato studiato nel foto-reforming anaerobico per ottenere idrogeno gassoso e prodotti in fase liquida.

Le reazioni sono state condotte mediante fotocatalisi eterogenea, usando condizioni blande e non impattanti a livello ambientale, lavorando a pressione atmosferica, temperatura ambiente e utilizzando acqua come solvente. Il biossido di titanio è stato usato come catalizzatore foto-attivo. Nonostante il fatto che il TiO_2 sia il catalizzatore più attivo, non tossico e meno costoso, il suo ampio bandgap consente di utilizzare solo la radiazione UV che copre soltanto il 5% dello spettro solare. In questo contesto, la presenza di nanoparticelle di metallo nobile permette di sfruttare anche lo spettro visibile e di ridurre la ricombinazione delle coppie elettrone-vacanza nel semiconduttore.

Il biossido di titanio è stato sintetizzato sottoforma di nano-polvere usando un sistema mediato da microemulsione. Le nanoparticelle di Au, Ag, Pt, NiO e quelle che formano leghe o nanoparticelle di tipo core-shell di Au-Ag e Au-Cu sono state depositate sul supporto di TiO_2 utilizzando il metodo di deposizione-precipitazione o quello di incipient wetness impregnation. Per quest'ultimo sono stati utilizzati o i sali dei precursori metallici o le nanoparticelle metalliche pre-sintetizzate. I catalizzatori sono stati caratterizzati tramite analisi XRD, DRS, TEM, SEM, RAMAN e di fisisorbimento di N_2 .

L'attività catalitica è stata confrontata con quella ottenuta utilizzando delle polveri di TiO_2 commerciali come il P25 e il DT-51. È stata studiata l'influenza del supporto, della dimensione e del tipo di nanoparticelle sulla trasformazione foto-catalizzata sia del HMF che del glicerolo. Nel caso del HMF, è stato studiato anche l'effetto dell'aggiunta di una base e del contenuto di ossigeno sulla selettività della reazione, mentre per la reazione di foto-reforming del glicerolo è stata studiata come le diverse fasi cristalline del TiO_2 e la morfologia influenzino le performance catalitiche.

La superficie della nano-polvere di TiO_2 sintetizzata è stata studiata utilizzando l'approccio della Surface Organometallic Chemistry (SOMC). In particolare, la superficie è stata caratterizzata tramite titolazione chimica e analisi DRIFT. Inoltre, grazie a questo approccio è stato possibile preparare un campione con delle nanoparticelle di Pt altamente disperse sulla superficie di TiO_2 . L'attività fotocatalitica di questo campione è stata studiata nel processo di foto-reforming del glicerolo e i risultati sono stati confrontati con quelli ottenuti con un catalizzatore contenente Pt preparato usando i metodi di sintesi più tradizionali.

Al fine di evitare l'agglomerazione e la sedimentazione delle polveri di TiO_2 sospese in mezzi acquosi, sono stati depositati film sottili di TiO_2 sintetizzato e commerciale su substrati conduttivi usando la tecnica della serigrafia. Gli elettrodi ottenuti sono stati poi caratterizzati tramite analisi di profilometria, SEM, XRD, metodi ottici, elettrici e foto-elettrochimici.

Résumé

La conversion industrielle durable de la biomasse en tant que matière première renouvelable et abondante devient de plus en plus attrayante pour la synthèse de produits à haute valeur ajoutée pouvant être utilisés dans les secteurs de l'énergie, de l'alimentation, des polymères, de la cosmétique et de la pharmacologie, ainsi que dans la production de produits chimiques fins.

Dans le but de traiter plusieurs approches de la chimie durable, nous avons utilisé le 5-hydroxyméthyl-2-furfural (HMF) issu de la biomasse dans un processus de photo-oxydation aérobie. Les produits d'oxydation partielle de cette réaction, en particulier le 2,5-diformylfurane (DFF) et l'acide 2,5-furane-dicarboxylique (AFDC), présentent un grand intérêt pour l'industrie des polymères. Le glycérol en tant que sous-produit majeur de la production de biodiesel a également été soumis à un photo-reformage anaérobie afin d'obtenir de l'hydrogène gazeux et d'autres produits liquides.

Ces réactions photo-catalytiques hétérogènes ont été réalisées sous irradiation du soleil dans des conditions douces telles que la pression atmosphérique, la température ambiante et l'eau en tant que solvant bénin. Le dioxyde de titane a été utilisé comme catalyseur photo-actif. Bien que le TiO_2 soit le matériau le plus actif, non toxique et peu coûteux, sa large bande interdite ne permet d'utiliser que des irradiations UV qui ne représentent que 5% du spectre solaire. Ainsi, l'introduction de nanoparticules de métaux nobles permet de résoudre le problème de l'absorption de la lumière visible ainsi que de réduire la recombinaison électron-trou dans le semi-conducteur.

Le dioxyde de titane a été synthétisé sous forme de nanopoudres en utilisant un système de microémulsion. Des nanoparticules de métaux nobles tels que Au, Ag, Pt, des alliages comme Au-Cu, Au-Ag, et des nanoparticules d'oxyde métallique NiO ont été déposées sur TiO_2 , qui a été utilisé en tant que support. Ceci a été réalisé soit par un procédé de dépôt-précipitation soit par l'imprégnation à humidité naissante. Des sels de précurseurs métalliques ou des nanoparticules préformées ont été utilisés dans le dernier cas. Les catalyseurs ainsi obtenus ont été caractérisés par DRX, DRS, physisorption de N_2 , analyse TEM, SEM et RAMAN.

Leur activité catalytique a été comparée à celle de poudres de dioxyde de titane disponibles dans le commerce telles que P25 et DT-51. L'influence du support, de la taille et du type de nanoparticules métalliques et d'oxydes a été évalué pour la transformation photo-catalytique de l'HMF et du glycérol. Dans le cas de HMF, l'influence de l'addition de bases et la teneur en oxygène a également été étudiée sur la sélectivité de la réaction. L'effet de la composition de la phase cristalline et de la morphologie de TiO_2 a également été abordé pour la réaction de photo-reformage du glycérol.

La surface des nanopoudres de TiO_2 synthétisées a été étudiée au moyen d'une approche de chimie organométallique de surface (COMS). En particulier, la surface a été caractérisée par les

techniques de titrage chimique et DRIFT. En outre, le concept SOMC a permis de préparer des nanoparticules de Pt bien dispersées sur la surface de TiO₂. L'activité photo-catalytique de cet échantillon dans le processus de photo-formage du glycérol a été testée et comparée à celle des autres catalyseurs contenant des nanoparticules de Pt préparées par des techniques classiques.

Afin d'éviter l'agglomération et la sédimentation de poudres d'oxyde de titane en suspension dans le milieu aqueux, des couches épaisses de TiO₂ synthétisé et commercial ont été déposées sur un substrat conducteur en utilisant une technique de sérigraphie. Les électrodes ainsi obtenues ont été caractérisées par profilométrie, SEM, DRX, méthodes optiques, électriques et photoélectrochimiques.

Chapter 1. Aim and structure of the work

The overall aim of this research work consists of two parts:

1. Design of the novel photo-active catalytic systems.
2. Sustainable conversion of HMF and glycerol molecules.

In particularly, the first part will be mainly described in **Chapter 3**, where the synthetic procedure of TiO₂ *via* water-in-oil microemulsion is discussed, as shown on the flowchart below. Modifications of this system as to improve the photo-catalytic activity will be described throughout the thesis depending on the reaction studied. Thus, the preparation of Au, Au-Cu, Ag and Au-Ag nanoparticles (NPs) by different synthetic methods will be discussed in **Chapter 4** together with the study of their activity on selective photo-oxidation of HMF. Au and Au-Cu systems will be also tested in the reaction of glycerol photo-reforming (**Chapter 5**). The synthetic procedure of Pt and NiO NPs and their effect on glycerol photo-reforming will be described in **Chapter 5**. The study of surface chemistry of prepared TiO₂ will be shown in **Chapter 6**, where preparation of Pt NPs by surface organometallic chemistry approach and their activity in the glycerol photo-reforming will be discussed. And finally, **Chapter 7** will be dedicated to TiO₂ thick film preparation and characterization.

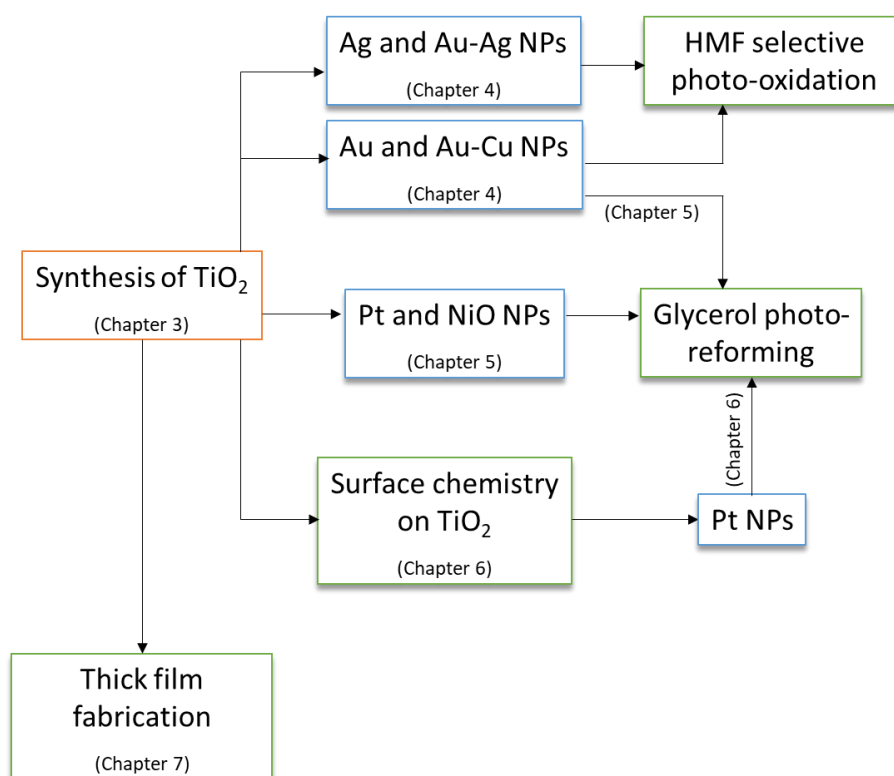


Table of content

<i>Abstract</i>	10
<i>Riassunto</i>	12
<i>Résumé</i>	14
<i>Chapter 1. Aim and structure of the work</i>	16
<i>Chapter 2. Introduction</i>	22
<i>Chapter 3. Synthesis of titanium dioxide powders by microemulsion method</i>	47
3.1. Experimental section	47
3.1.1. Material preparation	47
3.1.1.1. Chemicals.	47
3.1.1.2. Synthesis of titanium dioxide by microemulsion method.	47
3.1.2. Material characterization	49
3.1.2.1. X-ray Diffraction (XRD)	49
3.1.2.2. Diffuse reflectance spectroscopy (DRS).	49
3.1.2.3. N ₂ physisorption.	49
3.1.2.4. RAMAN spectroscopy.	49
3.2. Results and Discussions	50
3.2.1. Characterization of materials	50
<i>Chapter 4. Heterogeneous photo-oxidation of HMF</i>	57
4.1. Experimental section	57
4.1.1. Material preparation	57
4.1.1.1. Chemicals.	57
4.1.1.2. Incipient wetness impregnation of pre-formed Au, Au-Cu, Ag and Au-Ag nanoparticles by glucose reduction method	57
4.1.1.3. Deposition-precipitation method of Au nanoparticles.	58
4.1.2. Material characterization	58
4.1.2.1. Transmission Electron Microscopy (TEM).	59
4.1.2.2. X-ray Diffraction (XRD)	59
4.1.2.3. Photocatalytic test	59
4.2. Results and Discussions	61
4.2.1. Preliminary tests	61

4.2.1.1. Effect of support and Au NPs deposition	61
4.2.1.2. The effect of base on the photocatalytic reaction	65
4.2.1.3. The effect of oxygen.	68
4.2.1.4. Effect of radical scavenger.	69
4.2.2. Effect of different noble metal co-catalysts	71
Chapter 5. Glycerol photo-reforming	78
5.1. Experimental section	78
5.1.1. Synthesis and deposition of nanoparticles	78
5.1.1.1. Chemicals.	78
5.1.1.2. Synthesis of Pt/TiO ₂ by deposition-precipitation method.	78
5.1.1.3. Preparation of Pt/TiO ₂ by incipient wetness impregnation.	79
5.1.1.4. Preparation of NiO _x /TiO ₂ by incipient wetness impregnation.	79
5.1.2. Material characterization	79
5.1.2.1. Thermogravimetric analysis (TGA).....	79
5.1.2.2. Temperature programmed desorption (TPD).....	79
5.1.2.3. Scanning Electron Microscopy (SEM).	80
5.1.3. Test and product identification	80
5.1.3.1. Photocatalytic test.....	80
5.1.3.2. Identification and quantification methods.	80
5.2. Results and discussions	86
5.2.1. Summary on material characterization	86
5.2.2. Comparative study of different metal and metal oxide nanoparticles over TiO ₂ supports	91
5.2.3. Photo-reforming of glycerol over Pt-based catalysts.....	96
5.2.3.1. Glycerol conversion as a function of time.....	96
5.2.3.2. Effect of phase composition.	99
5.2.3.3. Reaction with glyceraldehyde and dihydroxyacetone as intermediate products of glycerol photo-reforming.	100
5.2.4. Effect of catalyst morphology	104
Chapter 6. Surface chemistry on lab-synthesized titanium dioxide	109
6.1. Experimental section	109
6.1.1. Material preparation.....	109
6.1.1.1. Chemicals.	109
6.1.1.2. Dehydroxylation of TiO ₂ -m_A surface.	109

6.1.1.3. Chemical titration.	109
6.1.1.4. Grafting of Pt(COD)Me ₂ over dehydroxylated TiO ₂ -m_A-T surface.	110
6.1.1.5. Reduction of Pt(COD)Me ₂ to form Pt nanoparticles (NPs).....	110
6.1.2. Material characterization	110
6.1.2.1. XRD analysis.	110
6.1.2.2. Diffuse reflectance infrared fourier transform spectroscopy (DRIFTS).	110
6.1.2.3. Nitrogen physisorption analysis.	111
6.1.2.4. Elemental analysis.	111
6.1.2.5. Nuclear magnetic resonance (NMR).....	111
6.1.2.6. Transmission Electron Microscopy (TEM).	111
6.1.3. Photocatalytic test on glycerol.....	112
6.2. Results and Discussions	113
6.2.1. Characterization of materials	113
6.2.1.1. Dehydroxylation of TiO ₂ -m_A surface.	113
6.2.1.2. Chemical titration of dehydroxylated TiO ₂ -m_A.	117
6.2.1.3. Grafting of Pt(COD)Me ₂ over dehydroxylated titania and reduction to form Pt nanoparticles (NPs).	118
6.2.2. Effect of deposition method on glycerol photo-reforming	123
Chapter 7. Titanium dioxide thick film preparation and characterization	126
7.1. Experimental section	126
7.1.1. Material preparation.....	126
7.1.1.1. Chemicals.	126
7.1.1.2. TiO ₂ ink fabrication.	126
7.1.1.3. TiO ₂ ink deposition by screen-printing technique.	127
7.1.2. Material characterization	128
7.1.2.1. XRD.	128
7.1.2.2. Profilometry.	128
7.1.2.3. SEM	128
7.1.2.4. Optical characterization.....	128
7.1.2.5. Electrochemical characterization.....	129
7.1.2.6. Photo-electrochemical characterization.	129
7.2. Results and Discussions	130
7.2.1. Formulation and deposition of TiO ₂ ink.....	130
7.2.2. Characterization of TiO ₂ films.....	131

7.2.2.1. Profilometry.....	131
7.2.2.2. XRD.....	131
7.2.2.3. SEM.....	133
7.2.2.4. Optical characterization.....	134
7.2.2.5. Electrochemical characterization.....	137
7.2.2.6. Photoelectrochemical characterization.....	147
<i>Conclusions</i>	149
<i>Bibliography</i>	153

Chapter 2. Introduction

2.1. Biomass valorisation	23
2.1.1. Lignocellulose	23
2.1.1.1. HMF as a platform chemical	25
2.1.1.2. Heterogeneous photo-oxidation of HMF.....	28
2.1.2. Triglycerides	29
2.1.2.1. Glycerol as a platform chemical	29
2.1.2.2. Hydrogen as fuel	31
2.1.2.3. Photo-reforming of glycerol.....	32
2.2. Titanium dioxide: synthesis and characterization towards applications in photocatalysis	36
2.2.1. Methods of synthesis	36
2.2.2. Characterization of TiO ₂	37
2.3. Heterogeneous photocatalysis.....	40
2.4. Film preparation techniques.....	43
2.5. Introduction to Surface Organometallic Chemistry (SOMC)	45

Chapter 2. Introduction

2.1. Biomass valorisation

Recently, the attention to carbon-based industry for energy and commodity chemicals has been augmented because of a detrimental effect of its intensive use and consumption, resulted in depletion of petroleum resources, environmental and political concerns. One of the promising approaches to overcome these issues is the use of plant-based raw materials (biomass) as renewable and abundant feedstock, and its eco-friendly conversion into high-value-added products.^[1] The concept of biorefinary has been introduced by the International Energy Agency (IEA). The term biorefinary is defined as “the sustainable processing of biomass into a spectrum of marketable products and energy”.^[2] Nonetheless, this concept has already been used in oil and fats industries, transforming by-products into chemicals and fuels. Particular attention is devoted to biofuels that is a general term for fuels derived from biomass feedstock, for example, biodiesel, bio-ethanol, bio-hydrogen, bio-oil, and bio-gas. Currently biofuel is divided into 1st and 2nd generations. While the 1st one is in the competition with food and feed industries that causes ethical, political and environmental issues, the use of the 2nd generation biomass, based on raw materials from waste, residues or non-food crop, give a rise to a more reasonable and greener pathway in modern chemical industry.^[3]

The primary components of biomass feedstock are i) terpenes, ii) carbohydrates (lignocellulose), iii) proteins, iv) triglycerides.^[4] And it is worth noting that they can be interconvertible.

2.1.1. Lignocellulose

Nowadays lignocellulosic biomass represents a major target for industries and science, because it is non-edible, and produced in large quantities every year in form of forestry, agricultural and agroindustrial lignocellulosic wastes. Nonetheless, the conversion of lignocellulose is a complex process. The **Figure 2.1** represents the simplified scheme of lignocellulose conversion. Primarily, the direct gasification in steam and/or oxygen at 750-1000°C gives syn gas (H₂ and CO) among the mixture of CO₂, CH₄, char and other by-products.^{[5][6]} Syn gas can be then transformed via Fisher-Tropsch process as to produce hydrocarbons for chemicals and fuels. However, other reactions can be applied such as methanol synthesis towards low olefins and production of benzene, toluene and xylene isomers (BTX), and water-gas-shift (WGS) towards hydrogen production. Instead, pyrolysis is the process of simultaneous and successive reactions when biomass is heated in inert atmosphere in the range of temperatures from 300 to 800°C. The primary product of biomass pyrolysis is bio-oils

represented by the mixture of water, char, gases and numerous carboxylic acids, saccharides, ketones, aldehydes, alcohols, and aromatic derivatives.^[5] While the pre-treatment process is mainly based on the hydrolytic step, which divides lignocellulose into its constituent biopolymers: a phenolic-based polymer (lignin, 20%) and two polysaccharides (cellulose and hemicellulose, 65%).^{[4] [7]}

Currently, lignin is considered as the largest renewable source of aromatic building blocks. Fundamental studies on lignin conversion reported various methods of depolymerization by means of homogeneous, heterogeneous, electro-, photo-, and enzymatic catalysis.^[8]

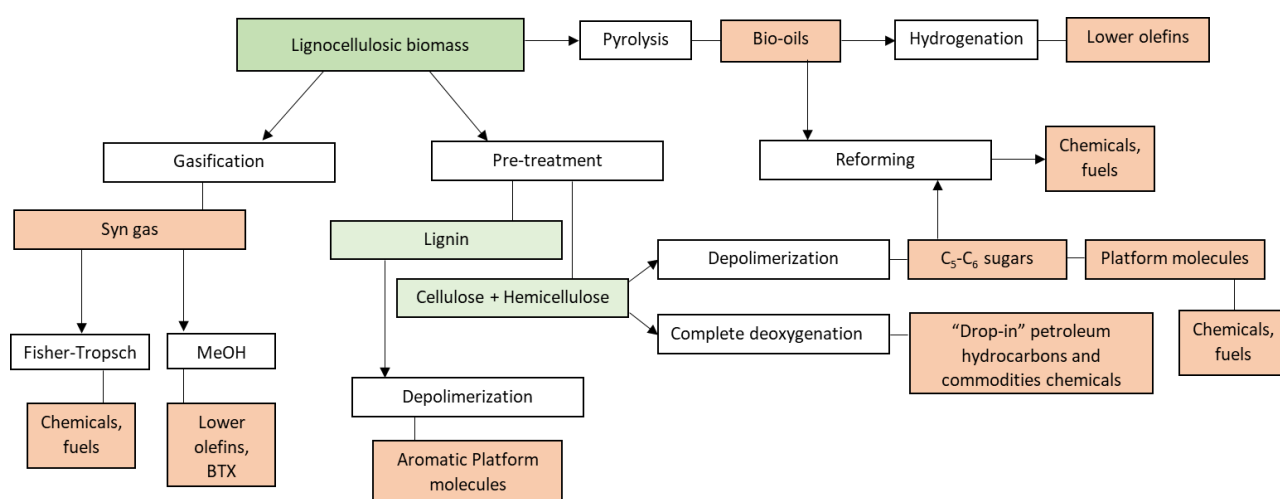


Figure 2.1. Simplified scheme of lignocellulose conversion, adapted and modified from^{[4][8][7][5]}.

On the other hand, the cellulosic biomass is converted via complete deoxygenation to “drop-in” petroleum, and can be further processed to commodity chemicals using established petrochemical technologies in already available reactors. Another way to valorize cellulosic biomass is in its direct conversion to oxygenates (and nitrogenates)^[4] via hydrolysis of the polysaccharides to C₅-C₆ sugars, and its further upgrade to platform chemicals. In addition, **Figure 2.1** demonstrates that C₅-C₆ sugars and bio-oils can be further upgraded to bio-fuels and chemicals by means of reforming process. Reforming is usually realized with metal-supported catalysts under the steam at high temperatures (~850°C), or in liquid water at lower temperatures (250-300°C), which is called aqueous phase reforming (APR). Because of milder conditions and the use of water as reaction medium, the process of APR has recently become of a great interest as to produce bio-derived fuels and chemicals.

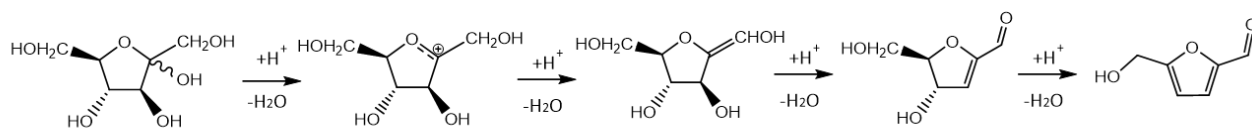
The molecule of 5-hydroxymethylfurfural (HMF) is one of the sugar-derived building blocks chemicals^[9] that stands out among the others due to several reasons that will be discussed in next paragraph.

2.1.1.1. HMF as a platform chemical

The interest to furanic derivatives from biomass sources has been grown significantly in last decades.^[10] First of all, these five-membered ring compounds attract by their multifunctionality, possessing furanic ring, alcohol, aldehyde and carboxylic groups. Secondly, it comes from renewable sources, which are abundant, diverse and cheap. Nevertheless, HMF is the main candidate in replacing the oil-derived platform molecules in production of polymers, chemicals and fuels. HMF is a natural molecule found in food upon heating or cooking (Maillard reaction). The global market of HMF is fast-growing, and its price in 2022 is estimated to be 123k million USD.^[11] Recently, many catalytic pathways for production of HMF via acid-catalyzed dehydration of different carbohydrates as fructose and glucose have been described.^{[12],[13],[14]} The use of glucose reported to give lower yield of HMF due to the higher stability of glucopyranoside ring structure compared to fructose.^{[15][16]} Secondly, low activity of glucose is due to enolization of the aldehyde group, which is the limiting step, leading to low conversion and selectivity.

Depending on the configuration of fructose (cyclic or linear), the mechanism of HMF synthesis is represented in two ways shown in **Figure 2.2**.

(A)



(B)

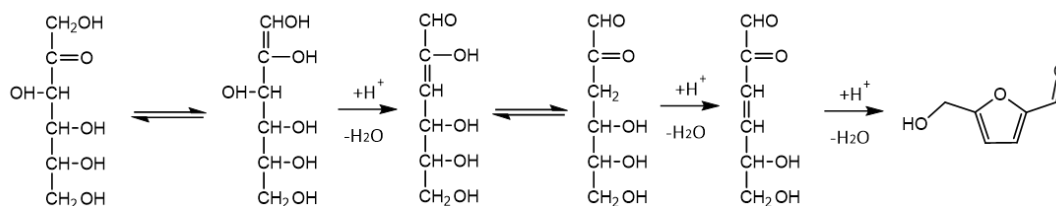


Figure 2.2. Mechanism of cyclic D-fructofuranose (A), and linear D-fructose (B) dehydration to HMF.^{[17][18]}

In the cyclic configuration, D-fructofuranose is dehydrated to form a carbenium ion, which undergoes three subsequent dehydration steps to yield HMF. While, linear D-fructose is isomerized into a 1,2-enediolglucose, which undergoes three dehydration steps through 3-deoxy-hexosulose and 5,6-dihydroxy-2-oxohex-3-enal formation, resulting in HMF.

Broad application of HMF is evident. **Figure 2.3** illustrates the transformation of HMF to some value-added intermediates, although not limited to. Thus, by means of *selective oxidation*, HMF can be converted to 2,5-furandicarboxylic acid (FDCA). Together with HMF, FDCA is known as

“Sleeping Giants” because of its enormous market potential.^{[19],[20]} For instance, FDCA can be used as an oil-free alternative to terephthalic acid in polymer manufacturing.^[21] Moreover, HMF can be also selectively oxidized to 2,5-diformylfuran (DFF), a precursor for pharmaceutical and antifungal agents, furanic biopolymers and furan-urea resins.^[22] The molecule of 2,5-dimethylfuran (DMF) can be obtained from HMF *hydrogenation* reaction. DMF is considered as potential biofuel.^[14] While *reduction* of HMF gives 2,5-bis(hydroxymethyl) furan (BHMF) known as intermediate in the pharmaceutical industry, synthesis of crown ethers and polymers.^[20] In specific conditions, HMF can undergo *ring-opening reaction*, where the main products are levulinic and formic acids.^[23] Levulinic acid is a building block in polymer industry and production of bio-solvents. While hexanediol is extensively used in polymer production, coatings, and adhesives.^[24]

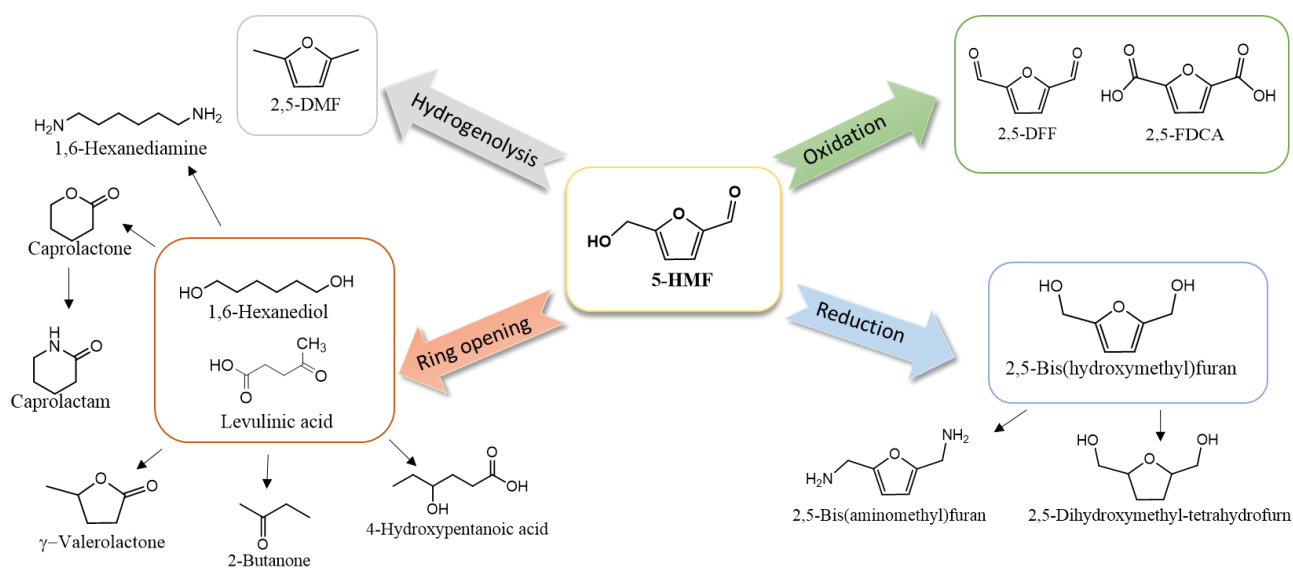


Figure 2.3. Scheme of some chemicals obtained from HMF as a platform molecule. Adapted and modified from reference^[7].

In particular, poly(ethylene furanoate), PEF, can be successfully produced by polycondensation of FDCA with ethylene glycol. Recent studies have demonstrated that PEF is a 100% renewable polymer with an enhanced oxygen and carbon dioxide permeability compared to poly(ethylene terephthalate), PET, despite a greater CO₂ solubility observed for PEF.^[24]

Considering the industrial application, some pilot scale plants have been already developed by Dupont. Instead, Avantium is currently setting the flagship plant for PEF production from FDCA to be launched by 2023. Recently, Motagamwala and co-workers^[25] have reported that Avantium has developed FDCA production process, in which methoxymethylfurfural is used as the substrate, while Co(OAc)₂, Mn(OAc)₂, and HBr as homogeneous catalytic systems in acetic acid medium. Such

approach leads to 96% of FDCA, avoiding the problems associated with low stability of HMF in acidic/basic conditions, low solubility of FDCA in common solvents and incomplete oxidation of HMF to FDCA. However, the remained insoluble fractions of intermediates of oxidation require their further purification. Moreover, the use of corrosive media and dangerous compounds triggers some questions on sustainability of the process.

Therefore, the preparation of active and stable metal-supported catalysts systems able to perform HMF oxidation in aqueous media are currently under a great interest.^[26] The accepted pathway of HMF oxidation to FDCA is depicted on **Figure 2.4**, showing the intermediates products.

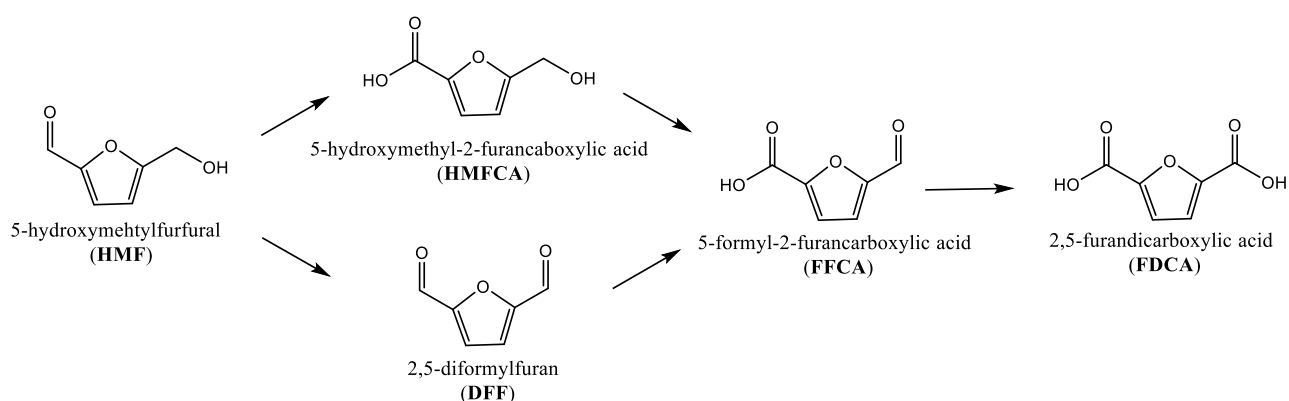


Figure 2.4. Reaction scheme of HMF partial oxidation.

Numerous studies have been done up to date on heterogeneous selective oxidation of HMF to FDCA. Mainly Au, Pd, Pt and also these metals in form of alloy supported on metal oxides (TiO_2 ^{[27],[13],[23],[21]}, CeO_2 ^{[28],[21]}, NiO ^[29] etc.) have shown an improved activity towards FDCA, operating at mild temperatures (50-90°C), in the presence and absence of base as co-catalyst. S. Davis and co-workers^[30] emphasized the pivotal role of inorganic base in fast transformation of HMF to HMFA. However, the base also leads to a formation of insoluble oligomers (humins), which lower the overall atom efficiency of the process. On the other hand, higher temperatures have to be applied to make HMF to FDCA oxidation process feasible in the base-free conditions.^[31]

In the last decade, selective conversion of HMF using photo-active material has a growing interest, since it implies the use of solar light as energy source, ambient temperature and pressure, and water as a green solvent. Among the semiconductors tested in photocatalytic conversion of HMF up to date, the materials based on TiO_2 ,^{[32],[33],[34]} Nb_2O_5 ,^[35] CdS ^[36] and $g\text{-C}_3\text{N}_4$ ^{[37],[38],[39],[40],[41],[42]} were reported.

2.1.1.2. Heterogeneous photo-oxidation of HMF.

The first work on photocatalytic selective oxidation of HMF in water was published by V. Augugliaro et al.,^[32] which reported the use of TiO₂ nanoparticles in different morphologies. Authors noted the tendency of complete mineralization of HMF to CO₂ and H₂O through the formation of DFF and some aliphatic intermediates. Furthermore, the results showed that high specific surface area, low crystallinity and reduced hydroxylation degree of synthesized TiO₂ seem to be the influencing parameters, showing a less significant effect of over-oxidation of DFF. In attempt to improve the selectivity, in the work of I. Krivtsov et al.,^[33] the oxygen vacancies were introduced to TiO₂ by N-doping. The results showed the selective conversion of HMF to DFF, followed by mineralization of molecules to CO₂ and H₂O. This behavior is expected since under UV light aqueous suspension of TiO₂ is known to generate radicals such as superoxide ($\cdot\text{O}_2^-$), hydroperoxyl ($\text{HO}\cdot_2$) and hydroxyl ($\cdot\text{OH}$), leading to a complete oxidation of aliphatic and aromatic compounds.^{[43],[44]} Zhou and co-workers^[34] discovered the enhancement of absorbing capability of TiO₂ in visible spectrum by Surface Plasmon Resonance (SPR) phenomena by deposited Au nanoparticles, giving almost complete conversion of HMF to HMFCFA in basic conditions, where the role of Na₂CO₃ was suggested as $\cdot\text{OH}$ scavenger. Alternatively, Nb₂O₅ was applied in photo oxidation of HMF under visible light.^[35] Ascribing to a better oxygen dissolution in benzotrifluoride, yield of DFF was reached as high as 90.6% in this solvent. Several recent studies on photocatalytic selective HMF oxidation have been done by using graphitic carbon nitride (g-C₃N₄) semiconductor.^{[37],[38],[39],[40],[41],[42],[45]} The bandgap of this material is 2.7 eV, which enable g-C₃N₄ to absorb in visible range of solar spectrum, where the light is generated with the highest irradiance. Additionally, the energy of valence band of g-C₃N₄ is 1.4 eV that makes it difficult the formation of $\cdot\text{OH}$. Therefore, the key role in photo-oxidation of HMF by g-C₃N₄-based catalysts was played by $\cdot\text{O}_2^-$ radical. Indeed, I. Krivtsov and co-workers^[37] reported remarkably improved selectivity of DFF using this material compared to TiO₂. Moreover, the group of M. Ilkaeva^[39] successfully tested g-C₃N₄-based materials in a pilot plant in Plataforma Solar de Almería (Spain). Recently, the group of H. Zhang^[42] have demonstrated selective oxidation of HMF with WO₃/g-C₃N₄ composite under visible light, and ascribed the high DFF selectivity (87.2%) to a better electron-hole pair separation in the composite. Secondly, authors suggested both $\cdot\text{O}_2^-$ and h⁺ are responsible for HMF photo-oxidation based on tests with scavengers. Nonetheless, the group of V. Battula^[41] managed to reach >99% selectivity of DFF and obtain a hydrogen gas after 6 h of anaerobic HMF conversion with Pt over mesoporous g-C₃N₄ catalyst under natural sunlight.

2.1.2. Triglycerides

Triglycerides is another wide category of biomass feedstock in the production of bio-fuels. These molecules composed by glycerin, which is coupled in ester form to long alkyl-chain fatty acids. Triglycerides are usually found in vegetable and animal oil and fat. Currently, rapeseed, soybean, sunflower and palm oil are the most widely used as a triglycerides source for bio-fuel production. However, other sources of triglycerides can be found in waste streams of food industries, animal waste and algae, which are in fact a more sustainable supplies that do not compete with food and the extensive use of soil.^[46]

The main application of triglycerides is the production of bio-diesel or FAME (fatty acid methyl esters) by reaction of transesterification with methanol (**Figure 2.5**) However, under the catalytic hydrodeoxygenation, hydrodecarboxylation or decarbonylation reactions the triglycerides can be converted into straight chain hydrocarbons (green diesel) as well (**Figure 2.5**).^[47]

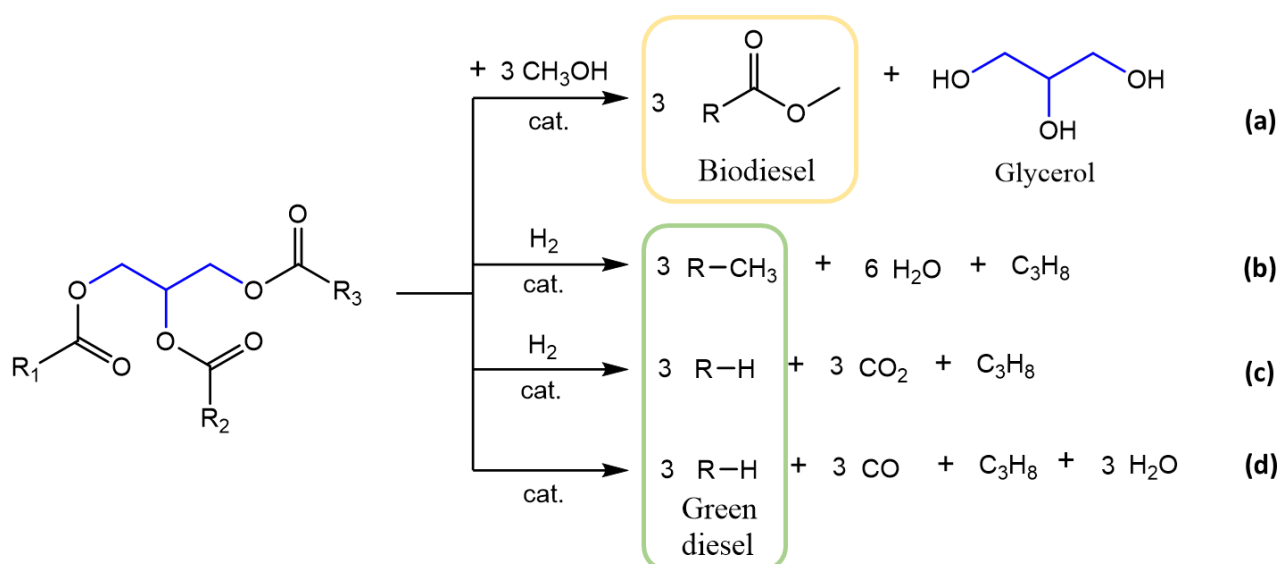


Figure 2.5. Triglyceride transformation into bio-fuels via catalytic process of: (a) transesterification, (b) hydrodeoxygenation, (c) hydrodecarboxylation, (d) decarbonylation. Adapted and modified from^[47].

However, the main drawback of biodiesel is its low thermal and oxidation stability in comparison with petroleum-derived diesel. Therefore, biodiesel is used in concentration as high as 7 vol.% in a mixture with ordinary diesel.^[47]

2.1.2.1. Glycerol as a platform chemical

Figure 2.5 demonstrates that molecule of glycerol is the co-product of triglyceride transesterification, which amounts *ca.* 10 kg (with purity of 50-55%) per 100 kg of biodiesel

produced.^[48] Additionally, glycerol is also found in polyol-containing wastewaters.^[49] With the increase of biodiesel production from 15,000 to 430,000 barrels in the period of 2000-2012, the price of crude glycerol decreased dramatically in US and European Union.^[48] Currently, glycerol is considered as a suitable chemical platform for synthesis of valuable chemicals (in food, cosmetics, pharmaceutical industries, etc.) and energy carrier such as hydrogen. Owing three hydroxyl groups, glycerol participates as substrate in thermo-, electro-, and photo-reforming, hydrogenolysis, dehydration, esterification, etherification, oligomerization, polymerization, carbonylation, and oxidation,^[50] producing variety of value-added chemicals (**Figure 2.6**) for the agrochemical and polymer industry, but also can be used as solvents, surfactants, adhesives, coatings and building blocks for other compounds.

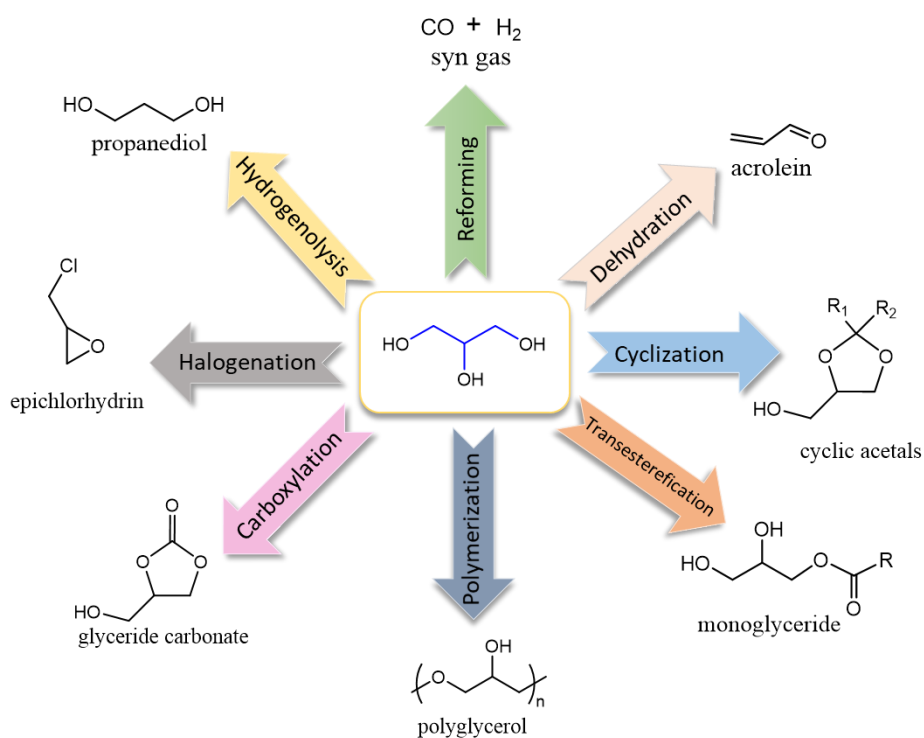
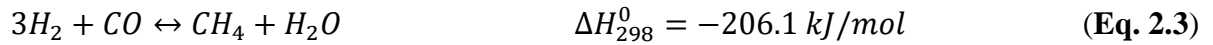
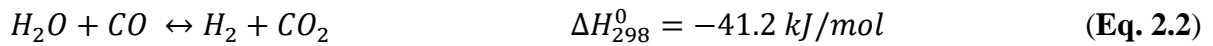


Figure 2.6. The scheme of glycerol conversion to valuable chemicals. Adapted and modified from^[50].

Furthermore, in the last decades the production of hydrogen from glycerol is believed to be not only the most promising sustainable alternative to the use of fossils as energy source, but also the way to increase the profit of biodiesel production.

Developed by the group of Dumesic et al. the APR process, found its application in glycerol valorization.^[51] Compared to the steam reforming, this process avoids thermal degradation of feedstock and cost-related issues with vaporization step. The moderate temperatures and pressures allow to couple APR process with water-gas-shift (WGS) reaction, improving the hydrogen yield by

reaction of CO with water. Typically, APR is carried out in a batch or fixed bed continuous flow reactors, depending whether the target product is in the gas phase (H_2) or liquid phase (alcohols, aldehydes and ketones, acids, glycols, and etc.). Reactions below show the APR process (**Eq. 2.1**) for oxygenates with the ratio of C to O atoms equal to 1, coupled with WGS (**Eq. 2.2**).



J. Gao and co-workers^[52] demonstrated that at temperatures of APR process, the methanation of CO (**Eq. 2.3**) can be feasible at high pressures and high H_2/CO ratio. In contrast to CO, the hydrogenation of CO_2 (**Eq. 2.4**) is more difficult at the same conditions used. In addition, the formation of alkanes via methanation (**Eq. 2.5**) and even the Fischer-Tropsch reaction (**Eq. 2.6**) energetically more favorable than reforming. This implies that the C-O bond breaking, followed by hydrogenation, is more advantageous than the C-C cleavage and WGS.^[6] To circumvent the side reactions, a suitable catalyst must be designed, which is i) active in C-C bond cleavage, such as Group VIII metals, and ii) capable of CO conversion from the metal surface, avoiding coke formation, iii) inactive in C-O bond breaking, suppressing parallel reactions in water.^[51] Typically, the metals such as Ru, Ni, Ir, Rh, Fe, Co, Pt, Pd and Cu meet the requirements mentioned above.^[6] Nonetheless, the support play an important role as well. It was reported that the basic supports such as MgO, ZrO_2 , Al_2O_3 and also TiO_2 show promising results towards hydrogen production and low amount of alkanes.^[6]

2.1.2.2. Hydrogen as fuel

Hydrogen is considered as cheap and clean energy carrier, because the result of reaction between hydrogen and oxygen is the water and chemical energy stored in H-H bonds.^[53] Moreover, gravimetric energy density of hydrogen is 120 MJ/kg that is three times higher than that of any other liquid fuel. However, the disadvantage of hydrogen as an energy source is its low energy output with respect to the occupied volume. For instance, under ambient conditions 1 liter of gaseous hydrogen contains only 10.8 kJ of energy, while that of petroleum is six orders of magnitude higher.^[54] Therefore, the use of hydrogen as future fuel alternative is restricted by the problems associated with

its storage and convey. So far, there are several industrial ways to circumvent this problem, including physical methods as compression up to 100 MPa, transformation into liquefied form at 20 K or cryo-compressed form at 20 K and at least 30 MPa; but also adsorption on activated carbon or zeolites, or chemical sorption forming metal hydrides.^[55] Recently, another promising way to store hydrogen such as catalytic hydrogenation (e.g. of N₂ and CO₂), was improved by introducing the concept of Liquid Organic Hydrogen Carrier (LOHC). This technology implies reversible hydrogenation and dehydrogenation of liquid organic compounds (methylcyclohexane, decalin, dibenzyltoluene, or dodecahydrocarbazole) in the presence of suitable heterogeneous catalysts (Pt-based catalysts in combination with Sn, In, K, Na; but also Ir- and Ag-based catalysts for dehydrogenation).^{[54],[56],[57]}

In general, production of hydrogen from biomass can be achieved by its direct gasification (750-1100°C) or indirect transformation that implies hydrolysis (100-200°C) or pyrolysis (450-650°C) of biomass with subsequent reforming of platform molecule.^[5]

Regarding the use of glycerol as a feedstock, hydrogen can be obtained by steam reforming, autothermal reforming, supercritical water reforming, partial oxidation reforming, and APR as was mentioned earlier.^[58] Global reaction follows the equation:

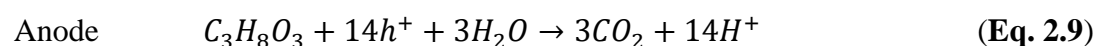
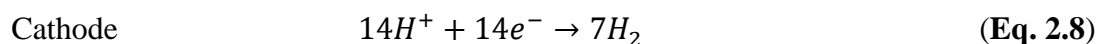


Overall reaction is endothermic process. This infers that the high energy consumption leads to high operating costs.

2.1.2.3. Photo-reforming of glycerol

In contrast to the abovementioned methods that require harsh conditions, the photo-reforming of glycerol has gained a great interest in the field of hydrogen energy as well as selective transformation of glycerol into valuable chemicals.

Among the catalysts studied for glycerol photo-reforming, TiO₂-based materials have drawn the greatest attention. Most of them consist of a noble metal co-catalyst which serves as cathode (**Eq. 2.8**) or electron trap, thus, responsible for H₂ evolution. While the surface of semiconductor is considered as anodic site (**Eq. 2.9**), where the photo-generated hole participates in oxidation of substrate.^{[5],[59],[49]}



Interestingly, in the last ten years^[60] the authors focused mainly on the anaerobic hydrogen production from glycerol using Pt,^{[61],[59],[62],[63],[64],[65]} Au,^{[61],[65],[64]} Pd,^{[61],[66],[67],[65]} Cu₂O^{[68],[69],[70],[71]} and NiO^[72] nanoparticles introduced on commercial TiO₂ (Degussa P25; 80% anatase, 20% rutile) by different methods of preparation such as conventional impregnation, deposition-precipitation, photodeposition, and equilibrium deposition filtration using different sources of irradiation. Thus, **Table 2.1** demonstrate some works on the hydrogen production from glycerol photo-reforming, considering the use of solar simulator as a source of light.

Table 2.1. State-of-the-art on photo-reforming and selective photo-oxidation of glycerol towards hydrogen and chemicals production under simulated solar irradiation, if not indicated otherwise.

H₂ production rates from glycerol photo-reforming			
Catalyst [synthesis]	Rate ($\mu\text{mol}\cdot\text{g}_{\text{cat}}^{-1}\cdot\text{h}^{-1}$)	conditions	Ref.
ZnS/ZnO (nanotubes)	384	H ₂ O/glycerol (9:1)	[73]
Bi ₂ WO ₆	7400	H ₂ O/glycerol (1:1)	[74]
ϵ -Fe ₂ O ₃ /Si(100) [CVD]	25463	H ₂ O/glycerol (9:1)	[75]
Au(1.5%)/P25	27500	H ₂ O/glycerol (9:1)	[76]
Pt(1%) / P25	4280	H ₂ O/glycerol (30:1)	[62]
CuO(1.5%)/P25(nanotubes)	99823	H ₂ O/glycerol (19:1)	[77]
RGO(3%)-Cu ₂ O(1%)/TiO ₂	110968	H ₂ O/glycerol (19:1)	[78]
Selective glycerol photo-oxidation			
Catalyst [synthesis]	Product	conditions	Ref.
P25-fluorinated	Glyceraldehyde (GAD), Dihydroxyacetone (DHA)	Aerobic, pH 5.5	[79]
P25, home-made TiO ₂ [hydrothermal]	GAD, DHA, formic acid	Aerobic, pH 7, UV	[80]

P25 and Pt/P25	GAD, acetol, acetaldehyde, methanol, ethanol	Anaerobic, 40 h	[81]
Rh/P25	GAD, DHA, formaldehyde and glycolaldehyde	Anaerobic	[49]
Au/ P25	Formic acid	Aerobic, pH 9	[82]
Au _x Cu / TNA	DHA, glyceric acid, glycolic acid	Aerobic	[83]
Au/P25	DHA, glyceric acid, glycolic acid, GAD	Aerobic, 90°C, visible	[84]

On the other hand, the literature on selective photo-oxidation of glycerol under aerated and unaerated conditions is quite scarce. **Table 2.1** collects the current state-of-the-art on the selective photo-oxidation of glycerol under simulated solar light, if not indicated otherwise.

Glyceraldehyde (GAD) and 1,3-dihydroxyacetone (DHA) were the main photo-oxidation products observed by Maurino et al.^[79] The authors used commercially available catalysts (Degussa P25 and Merck) and its fluorinated forms under aerobic conditions. Later, Augugliaro et al.^[85] reported the selective aerobic photo-oxidation of glycerol, yielding GAD, DHA, and formic acid over commercial P25 and homemade anatase and rutile TiO₂. Under anaerobic conditions Kondarides et al.^[81] described the formation of acetol, acetaldehyde, methanol, and ethanol using P25 and Pt/P25 catalysts after 40 h of reaction. However, the authors suggested that the detected products may originate from GAD, which is formed along with acetol at the first step of oxidation. Sanwald et al.^[49] performed anaerobic glycerol photo-reforming applying catalyst based on Rh nanoparticles over P25. It has been proposed that glycerol oxidation occurs via direct hole transfer with C-C scission or indirect hole transfer followed by the abstraction of α -hydrogen with respect to OH-groups, forming corresponding ketons or aldehydes. Within the liquid products GAD, DHA, formaldehyde and glycolaldehyde were observed as main products. Besides, the challenge associated with the use UV light, which refers only to 5% of the solar spectrum, directed the research towards the development of catalysts capable of absorbing the visible light. The surface plasmon resonance phenomenon, the collective oscillations of free electrons on the metal surface,^[86] inherent to the noble-metal nanoparticles. This concept results in visible light absorption and energy transfer to the semiconductor. Pan et al.^[87] reported the use of Au nanoparticles over P25 for glycerol photo-oxidation towards formic acid in basic conditions. It has been demonstrated that the combination of glycerol as an efficient hole scavenger and plasmonic nanoparticles enhanced the yield of formate

from 0.9 to 7 mmole/(g_{cat}*h) with respect to TiO₂ alone. The effect of bimetallic Au_xCu core-shell nanoparticles immobilized into anodized TiO₂ nanoarrays has been studied by the group of Guo and Sun,^[83] using oxygen as oxidant. DHA, glyceric acid and glycolic acid were the predominant liquid phase products, although GAD and tartronic acid were also formed. It has been reported that the presence of Au_xCu nanoparticles enhance glycerol photo-oxidation due to the visible light induced SPR. Furthermore, with the increase of gold content, the conversion increased: Au₃Cu > AuCu > AuCu₃. In the work of Tüysüz et al.^[88] glycerol was converted into DHA, along with glyceric acid, glycolic acid, and GAD as side products under base-free conditions, using Au nanoparticles deposited on P25 as catalyst and oxygen as oxidizing agent. The authors emphasized the benefit of SPR, showing the higher conversion of glycerol and selectivities of DHA compared to the reaction in the dark, although all the reactions were performed at 90°C.

These results suggest that even though the yield of GAD, DHA and other products is still low, it is possible, indeed, to oxidize selectively glycerol by means of solar energy over TiO₂-based catalysts.

2.2. Titanium dioxide: synthesis and characterization towards applications in photocatalysis

2.2.1. Methods of synthesis

Among the preparation methods of metal oxides, gas phase and liquid phase techniques are the main ones. In case of solution route, it is possible to govern on the stoichiometry, to prepare various morphologies and composite materials, and to coat the complex shapes. The used methodologies for TiO₂ preparation from solution are mostly based on the sol-gel, hydrothermal and electrochemical procedures.

In material science and ceramic engineering, a wet-chemical technique, the sol-gel process, is widely used, because it is relatively cheap and easy in manufacturing method. This process undergo in four steps: i) hydrolysis, ii) polycondensation, iii) drying and iv) thermal decomposition.^[89]

Hydrothermal treatment is one of the most widely used methods for increasing the crystallinity of TiO₂. In principle, implementing high temperatures and pressures in an aqueous solution one can facilitate the conversion of amorphous TiO₂ into crystalline one. It has been reported that using the hydrothermal treatment it is possible to change the morphology, microstructure, and phase composition of materials by varying the reaction parameters.^[90] Nevertheless, one of the drawbacks of this method is relatively low specific surface area at high crystallinity.

In contrast to abovementioned synthetic routes, where the difficulty arises in avoiding the range of high temperatures, the electrochemical method provides a film's preparation diversity and low temperatures approach. In a typical process, the conducting plate positioned in an electrolyte represents the anode. The cathode is usually platinum rod. Power supply generates electrons that move to positive anode, forming hydroxylated oxide. However, the number of parameters has to be controlled such as applied potential, time of anodization, electrolyte concentration etc.^[91]

In recent years, the synthesis of inorganic nanoparticles using the reverse microemulsion method (or water-in-oil, w/o, RM) has received considerable interests.^[92] In microemulsion technique, micelles play role of a nano-reactors, where the reaction occurs between materials to overcome solubility problems, incompatibility within phases and to allow a compartmentalization and concentration of the reagents. There are a number of advantages of this technique compared to traditional methods: it improves the size distribution and allows controlling the size of nanoparticles^{[93],[94],[95],[96],[97]} and morphology,^{[98],[95],[99]} changing the size of micelles by altering the surfactant-to-water ratio. Additionally, microemulsion method gives access to controlling the crystalline phase composition of TiO₂. Besides, it provides an improved control over bimetallic system composition, where the initial ratio of the metal precursor concentrations in the water droplets

will in principle correspond to the final composition of the particles obtained after reduction or post-treatment.^{[100],[101]} This type of synthesis is usually done at room or moderate temperatures and at relatively short reaction time compared to other methods.^{[96],[102]} Furthermore, microemulsion-mediated TiO₂ seemed to be more stable to heat treatment, keeping anatase as major phase in the range from 400-600°C and value of surface area one order of magnitude higher than of sol-gel catalysts.^[97]

In spite of advantageous properties and performance of nanoparticles obtained by w/o microemulsions, this method did not find widely its application at the industrial level, mainly due to the use of organic solvents in large excess as continuous phase. Nevertheless, in the field of catalysis, excellent catalytic performances of catalysts prepared by microemulsion method compared to other procedures have been reported.^{[100],[101]}

2.2.2. Characterization of TiO₂

Regarding the acidity/basicity of TiO₂, there are two kinds of acid sites on surfaces of metal oxide such as: Brønsted-acid sites (surface-bound hydroxyl group, Ti-OH) and Lewis-acid sites (exposed Tiⁿ⁺ cation). While O₂⁻ represents the Lewis basic site.^[103] The reported value of acid sites of TiO₂ from RM method was characterized by its high density^[97] what was also in agreement with ammonia TPD analysis of TiO₂ synthesized at University of Bologna (TiO₂-m) (**Table 2.2**). As it can be seen from the **Table 2.2**, within the list of differently synthesized materials, microemulsion-made TiO₂ is characterized by a higher acid site density than the values of commercially available DT-51 and TiO₂ found in literature.^{[97],[104],[105],[106]} Such behavior can be explained by the relatively high surface area.^[97] However, pre-treatment temperature of the surface is important step prior TPD analysis and also considerable parameter in comparative study.

Table 2.2. Value of acid site density and corresponding temperatures of calcination and heat treatment prior TPD measurement.

Method; [supplier]	Acid site density (mmol/g)	Calcination Temperature (°C)	Temperature of heat treatment (°C)	Ref.
Microemulsion, TiO ₂ -m	0.59	400	700	[107]
[DT-51 CristalActiv]	0.40	as received	700	[107]
[ST-01; Ishihara Ltd.]	0.13	as received	150	[104]
Sol-gel	0.26	80	150	[104]
Sol-gel; [Kanto Chemical]	0.32	as received	300	[105]
Sol-gel	0.47	500	200	[106]

Microemulsion	0.11	600	340	[97]
Sol-gel	0.04	600	340	[97]
Sol-gel	0.03	600	340	[97]

The effect of TiO₂ crystalline size on its photo-activity has been evidenced by numerous studies. Researchers have reported that the photo-reactivity of TiO₂ can be enhanced as the particle size decreases. This was attributed to the increased densities of the active sites of the photocatalysts due to the higher surface-to-bulk ratio of smaller particles in comparison with larger particles.^[108] The advantageous feature of microemulsion synthesis to control the particles size distribution allows better understanding the effect of crystalline size of titania (and other semiconductors) on photocatalytic results. Moreover, synthesis of TiO₂ in liquid phase by microemulsion is not well studied in heterogeneous photocatalysis and is not so widely implemented nowadays as compared to sol-gel, hydrothermal route and electrochemical procedures.^[89]

Control of phase composition in TiO₂ crystals is another promising strategy towards optimization of photo-redox reactions.^[99] It is an overall known fact that anatase is more reactive than rutile. Several explanations were given, including higher surface adsorption capacity toward hydroxyl groups by anatase and a lower charge carrier recombination rate than rutile. In addition, lifetime of photogenerated electrons and holes in anatase is about an order of magnitude larger than those ones in rutile, thus greatly enhancing the chance of generated electrons and holes in anatase participating in surface chemical reactions.^{[109],[110]} The studies of organic pollutants and dye degradation support the reactivity of anatase compared to rutile due to its high crystallinity and ability to trap electrons in oxygen vacancies, preventing from electron-hole recombination.^{[99],[97],[111]} Nevertheless, it was also demonstrated that the catalysts composed by the mixture of rutile and anatase phases were more active than single phase at the same calcination temperature in reactions of CO₂ photo-reduction as well as phenol and p-coumaric acid photo-degradation, which was explained by the enhanced charge separation at the heterojunction interface of the two crystal phases.^{[112],[113]} It is interesting to add that electrons, holes and reaction oxygen species generated upon the UV irradiation can be preferentially accumulated on one facet or another. On anatase, the photogenerated electrons usually migrate to the {101} planes while photo-generated holes direct to the {001} planes. Thus, the {001} facets can be considered as predominantly oxidative surfaces.^[99]

It is worth mentioning that stability of crystalline phase is size-dependent. In the range below 14 nm anatase is the most stable form. Meanwhile, rutile is the thermodynamically stable form above 35 nm at all temperatures and atmospheric pressure, and brookite is a metastable at intermediate particle size.^[114] One way to change phase composition is to vary the calcination temperatures of

solids. Thus, phase transformation of amorphous structure to anatase form occurs in temperature range from 350 to 450°C. Anatase to rutile transition starts from 500°C, but the transition temperature can differ depending on the preparation conditions of anatase.^{[113], [115]} Along with phase transformation, crystallinity of TiO₂ increases with increase of calcination temperature.

Crystallinity is believed to be one of important parameters affecting the photocatalytic activity, however the effect of the crystallinity has not found its acceptance widely. On one side, improving crystallinity in TiO₂ through calcination at high temperature can reduce the density of structural defect sites, which by itself serve as recombination centers for electron-hole pairs or compromise charge carrier separations in the material what is beneficial for pollutants decomposition and water splitting reactions and photo-reduction of CO₂.^{[111],[115],[113]} On the other hand, above certain value of temperatures, activity of TiO₂ can decrease due to the growth of grains and decrease of specific surface area, which is another previously mentioned parameter affecting photo-catalytic reaction.

In addition, amorphous solids in the catalyst are isolates and represent the defect in the lattice. As a result, it inhibits the generation of hydroxyl-radicals on the surface of semiconductor and complicates the interaction between the surface sites and the reaction intermediate, reducing its decomposition. Thus, on one side this results in poor activity of TiO₂, but on another side it improves the selectivity of biomass photo-oxidation into desirable product instead of its over-oxidation.^{[32],[113],[33]} The idea that amorphous materials may be utilized in selective photocatalytic reactions providing milder oxidation may find its application in flow chemistry. In recent years, the selective photocatalysis has become a new and fast-developing field that extends to several novel applications. In addition to selective photocatalysis, among approaches to enhance selectivity by altering either hole formation in valence band or •OH production is to tailor the band gap, phase, or crystal facets. Combination of molecular selective adsorption with photocatalysis, known as surface modification, can be another promising strategy.^[99]

An interesting correlation was found between calcination temperature, crystalline size and degree of crystallinity for the titanium nano-oxides, showing that there is a critical crystallite size at a range of 450-500°C, below which a higher number of crystal defects are present and not compensated by higher surface area.^[97]

2.3. Heterogeneous photocatalysis

According to IUPAC the term “photocatalysis” refers to the change in rate of a chemical reaction or its initiation under UV, vis, IR radiation in presence of the photocatalyst that absorbs light and is involved in the chemical transformation of the reactant partner.^[116] Thus, heterogeneous photocatalysis can be defined as a reaction initiated by interaction of electromagnetic radiation with appropriate energy and a semiconductor. As a result of this interaction, upon the absorption of incident photon energy by the semiconductor, photogenerated charges, electron-hole ($e^- - h^+$) pairs, are created.

On **Figure 2.7** the basic phenomena occurred at a semiconductor upon impingement of a photon are illustrated. When the electromagnetic irradiation ($h\nu$) with the energy equal or greater than the band gap (E_g) interacts with the semiconductor (SC), meaning that SC absorbs this energy, the electron-hole ($e^- - h^+$) pairs are separated (a): electron is transferred to conduction band (CB), while the positive hole remains in valence band (VB). These charge carriers may subsequently be trapped by molecules or radicals (b), undergoing redox reactions (c).^{[117][44]} Otherwise, charge carriers can recombine (d), if, for instance, the redox half-reactions are thermodynamically unfavorable.

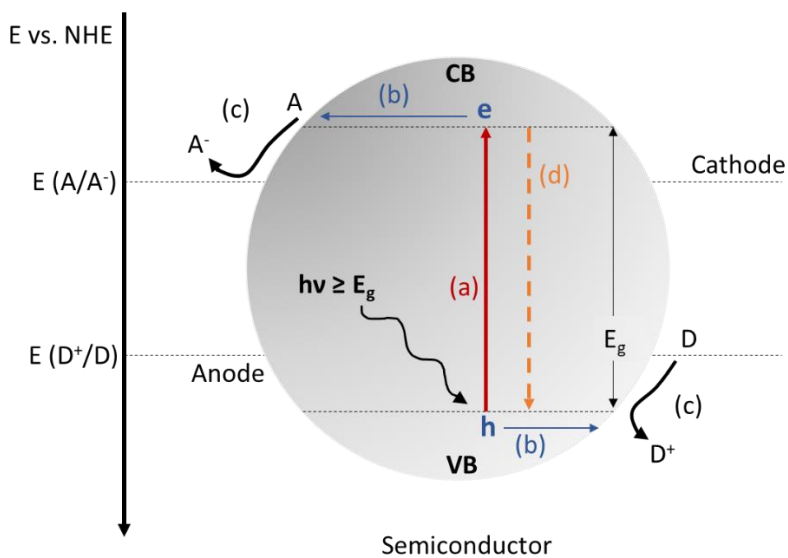


Figure 2.7. The schematic representation of the processes taken place upon SC excitation: (a) electron-hole pairs separation, (b) surface migration, (c) redox reactions with adsorbed chemicals (acceptor, A, and donor, D), (d) recombination.

This implies that electrochemical potential of electron and hole has to be more negative or positive than the redox potential of the corresponding chemical species (acceptor, A, and donor, D) to be reduced or oxidized, respectively.

One of the most studied semiconductor is TiO₂. In water, upon band gap excitation, the series of reactions can take place:^[117]



The most reactive oxygen species is hydroxyl radical ($\cdot\text{OH}$), which is formed by oxidation of hydroxyl group on the surface of SC by photo-generated hole. While superoxide radical ($\cdot\text{O}_2^-$) is formed due to the reaction of the electron with oxygen.

First publications on the heterogeneous photocatalysis were devoted mainly to water splitting and environmental remediation by means of pollutants degradation. In the last decades though, the heterogeneous photocatalysis also became a “green” alternative to organic synthesis through photo-oxidation or photo-reduction,^[118] avoiding the use of toxic chemicals, oxidants and harsh conditions.

However, heterogeneous photocatalysis can suffer from low selectivity in partial oxidation of organic substrates (especially in aqueous media) due to the aggressive reactivity of the generated radicals. Another limitation is the absorption of UV light (which is just 5% of solar spectrum) by the majority of the SC. Two ways were established to circumvent these drawbacks: efficient modifications of the semiconductor catalyst and/or operating conditions.^[118] Regarding the first way, the parameters influencing the efficiency of material were already mentioned in paragraph 2.4, such as crystallinity, type of polymorph, acid-base properties, specific surface area, exposure of certain facet, but also a presence of doping or photosensitizers, deposition of the metal on the SC surface or implantation inside the lattice, position of CB and VB.^{[117][119]} On the other hand, operating parameters such as geometry of the reactor, solvent, pH, concentration of substrate and catalyst, type of impinging light must be taken into consideration.^[118]

Recently, F. Parrino and co-workers^[120] in their review on heterogeneous photocatalysis aspects highlighted the importance of the reactor geometry, since it significantly influences the radiant field distribution and the mass transfer dynamics. The use of microreactors demonstrated a promising approach as to increase the rate of reaction compared to the conventional reactors, reduce the plant space and cost of installation, improve the light penetration and so on. Nonetheless,

microreactors found its application mainly in environmental processes, and their use in synthesis of organics is still under investigation.^[120]

2.4. Film preparation techniques

As was mentioned in the previous paragraph 2.3, the type of reactor strongly affects the photocatalytic results. Considering the photoreactors with immobilized photocatalyst, the type of film deposition has to be taken into consideration, since the active layer has to be mechanically resistant and sufficiently porous.^[120]

The films fabrication could be classified to two groups by the way of preparation such as *top-down*, starting from the larger piece of material and subsequent process of chemical milling, etching to get a nanoscale material (lithography), and *bottom-up*. The latter includes atomic layer deposition (ALD), molecular self-assembly, for instance, evaporation-induced self-assembly (EISA) such as dip- and spin-coating, chemical vapor-phase deposition (CVD).^[121]

Among the variety of coating techniques, the dip-coating, spin-coating, spray-coating or inkjet printing are commonly used for precursor solutions of single and mixed oxides.^[122] Spin-coating and dip-coating are well appropriated for large-scale production, highly convenient and fast techniques with the highest degree of control, making it the most applied processes for R&D. The synthetic steps for these techniques are usually following the same order: i) initial chemical solution formulation, ii) solution spreading on the surface of the substrate, iii) evaporation of the liquid solution layer, iv) layer post-processing, and v) final treatment of the layer for stabilization. Among the solvents, ethanol and propanol are the most implemented in these techniques, because they are volatile to be easily removed in evaporation step, good dispersers of precursor's oxides, possess low surface tension. Sometimes, water can be used as well as hydrolysis agent in couple with organic solvents to insure desired viscosity, polarity and surface tension. Organometallic compounds ($M(OR)_n$ where $M=Si, Ti, Al$ or $M(Ac)_n$ where $M=Zn, Mg$ etc.) or suspended nanoparticles or salts are used as precursors. The advantage in the use of the suspended particles is its high crystallinity that allows lowering the temperature reduction during annealing, which is the most common way of assembling particles into films. In the case of mesoporous films, the crystallinity of the nanoparticles helps to preserve the porous structure during the thermal removal of the template molecules.^[123] The porosity of nanoparticle-based films can be further improved by the addition of block copolymers in the evaporation-induced self-assembly process.^[124] For applications requiring high electrical conductivity (solar cells, displays, optoelectronic devices) though, it would be better to have the films as dense as possible.

Lithographic techniques are the major ones for top-down methods of nano-film fabrication. It is based on selective exposure through a mask (UV photolithography or X-ray lithography) and it is directly applied to the sol-gel coatings for the development of functional micropatterns with tunable

composition and morphology.^[125] Up to date there are known various branches of lithography such as microcontact printing (or soft lithography), nanoimprint lithography (NIL) with improved ultrahigh resolution of patterns, scanning-probe-based techniques such as atomic force microscope lithography, and dip-pen lithography.^{[126][127]}

One of the simplest and employed techniques of preparing thin films using pre-formed nanoparticles is tape casting (or doctor blade). In principle, the films (usually dense ceramics) are achieved by spreading a concentrated slurry of nanoparticles dispersed in a solvent (water or organic), containing binders and deflocculating agents on a sliding tape, following by the drying and firing steps. Phosphate esters, Menhaden fish oil, glyceryl trioleate are used as dispersants to avoid sedimentation and aggregation.^[128] Thickness of the film can be controlled by solvent content in the suspension or by several layer deposition. It is also possible to do 3D structures by superimposing deposited layers.^[129]

Compared to these techniques, the screen-printing, is low-cost method with an advantage of easier scale-up for producing high quality thick ($>10\ \mu\text{m}$) porous films of metal oxides.^[130] In principle, the paste is placed on the screen, followed by the squeezing of the paste along the support through the screen (**Figure 2.8**). The composition of the precursor paste, pressure and speed of the squeegee among the other parameters affect the homogeneity of the film, its adherence and roughness.^{[129][131]}

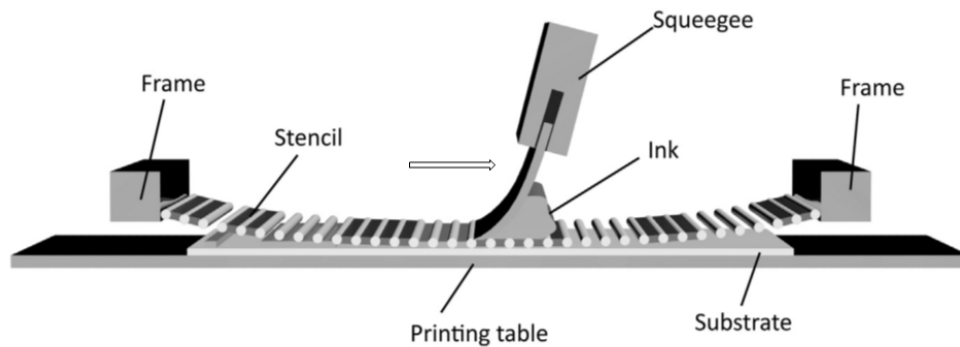


Figure 2.8. Screen-printing set-up and process. Adapted from^[131].

2.5. Introduction to Surface Organometallic Chemistry (SOMC)

By definition, the concept of organometallic chemistry suggests the formation of metal-carbon bond. The real boom of the studies and outstanding discoveries in this field started in US and Europe around 1960's. However, it was born far more earlier, in Parisian military pharmacy back to 1760.^[132] The introduction of the organometallic chemistry in heterogeneous catalysis (as to combine the benefits of homogeneous and heterogeneous catalysts) created a new concept called Surface Organometallic Chemistry (SOMC).^[133] This relatively new discipline aims at designing an heterogeneous catalyst with well-defined active sites by reacting in a controlled fashion the organometallic and coordination complexes with the surface of the solid oxide support, assessing a structure-activity relationship as in homogeneous catalysis in order to develop a better catalyst.^{[133],[134],[135],[136]} The control of a grafting process on an inorganic oxides can be realized by means of controlling the nature and concentration of reactive (typically hydroxyl) groups exposed on the surface of the support, since the amount of reacted complex will be proportional to the amount of the hydroxyls consumed as schematically illustrated on **Figure 2.9**.

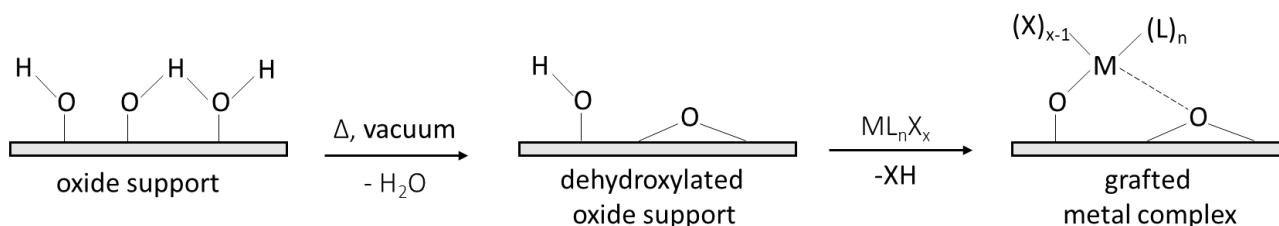


Figure 2.9. Scheme of catalyst preparation with a well-defined site using SOMC. ML_nX_x is the organometallic complex, where M is the metal, L is the functional ligand, X is the ancillary ligand. Adapted and modified from PhD thesis of T. Saboo.^[137]

Selection of appropriate oxide support, pretreatment process and organometallic complex control the reactivity between the surface and the incoming reactive metal-containing molecule and are thus crucial parameters to obtain grafting. Thus, the support, the metal (M), the functional ligand (L) and the ancillary ligand (X) have to be taken into consideration upon the grafting process.

Different supports can be used in SOMC such as silica, alumina,^[138] silica-alumina,^[134] zeolites,^[139] etc. However, the most widely used and studied support is silicon oxide whose surface consists of siloxane ($\equiv\text{Si-O-Si}\equiv$) and silanols ($\equiv\text{Si-OH}$) groups. Depending on the dehydroxylation temperature isolated, vicinal and germinal silanols are present on the surface of silica (**Figure 2.10**). Upon the increase of dihydroxylation temperature, vicinal silanols disappear, giving rise to isolated hydroxyl groups, which is followed by the decrease of OH concentration per nm^2 .^[134]

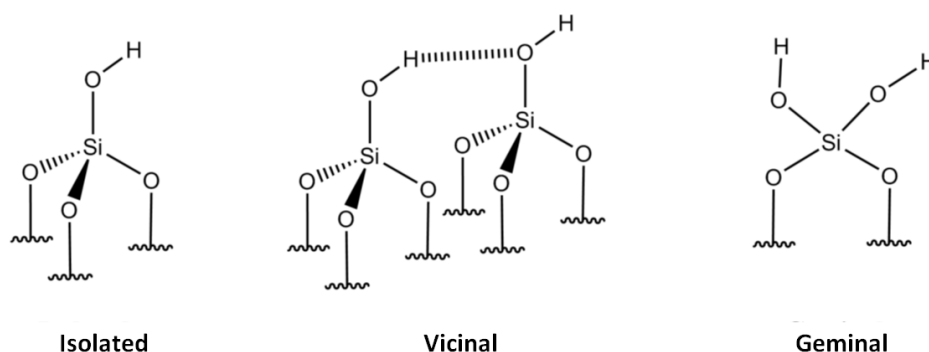


Figure 2.10. Different types of silanol groups on the surface of silica.

It is thus evident the importance of manipulating under the inert atmosphere, since water moisture in air can re-hydroxylate the surface, and, furthermore, decompose some types of organometallic complexes.

The materials prepared by SOMC approach as single-site catalysts found applications in various catalytic processes. Among them, reactions of metathesis, Ziegler-Natta polymerization, cyclotrimerization of alkynes demonstrated in **Figure 2.11**, etc.^[136] Nonetheless, the prepared materials can be further pre-treated as to obtain supported-metal nanoparticles and extended structures (e.g. MoS₂).^{[134],[140],[141]}

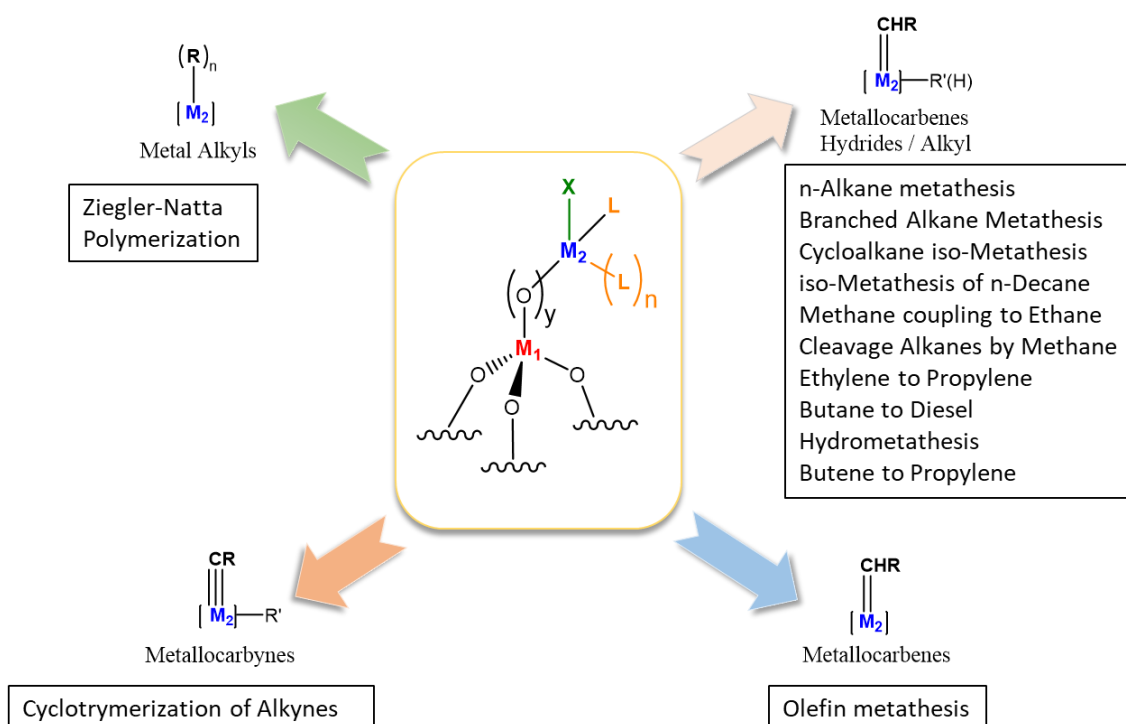


Figure 2.11. Surface organometallic complexes and corresponding catalytic reactions. Adapted and modified from reference ^[136].

Chapter 3. Synthesis of titanium dioxide powders by microemulsion method

3.1. Experimental section

This paragraph will be about the method of titanium dioxide synthesis via microemulsion mediated route developed by the group of Prof. F.L. Basile at University of Bologna, department of Industrial Chemistry “Toso Montanari”. The chemicals and essential steps for the synthesis and optimization as well as characterization method such as XRD, BET, DRS and RAMAN will be discussed.

3.1.1. Material preparation

3.1.1.1. Chemicals.

Powders for comparison: P25 (TiO₂ P25 Degussa), DT-51 (TiO₂ DT-51 Millennium CrystalACTIV).

Metal precursor: TBT (Titanium(IV) butoxide, 97%, Sigma Aldrich).

Surfactant and co-surfactant: Triton X-100 (Alfa Aesar), 1-hexanol (99%, Alfa Aesar).

Solvents: Cyclohexane (99%, Alfa Aesar), Ethanol (99.8%, Sigma Aldrich).

Hydrolyzing agent: HNO₃ (Nitric acid, 65%, Sigma Aldrich).

3.1.1.2. Synthesis of titanium dioxide by microemulsion method.

3.1.1.2.1. According to the preparation reported by M. Andersson et al.^[114] titanium dioxide was prepared by using a reverse microemulsion system, except that the temperature of the reaction mixture was kept between 72-74°C. In particular, a certain amount of cyclohexane, Triton X-100 and hexanol were mixed to form solution A (oil phase). After being stirred until become transparent, Titania butoxide was added to solution A. Solution B is a water phase, that is composed by MilliQ water and HNO₃. Solution C has the same composition as A. After addition B into C, forming solution BC, solution A having already Titanium butoxide is introduced to solution BC under stirring, forming ABC. Then, the resulted solution was transferred into three-neck round-bottom flask, equipped with thermometer, stirring system and refrigerator, and placed in a heating compartment. After 1 h of stirring, the solution was heated up to 74°C and kept for 5 h under vigorous stirring. Then, catalyst was separated by centrifugation and washed with ethanol 5 times, repeating

each time the centrifugation. Then, the catalyst was dried overnight at 100°C and calcined at 400°C for 3 h with the ramp of 2°C/min. Resulted powder is named as *TiO₂-m_A*.

- 3.1.1.2.2. Relatively pure rutile phase was obtained, following the same procedure, except the stirring was kept for 4 days at room temperature, without further heat-treatment. The obtained precipitate was then separated, washed, dried and calcined as mentioned above. The resulted powder is denominated as *TiO₂-m_R*.
- 3.1.1.2.3. Another titania powder was prepared by the method described in section 3.1.1.2.1, except that before the drying step at 120°C, the resulted paste was aged for 4 days and then calcined at 400°C for 3 h with the ramp of 2°C/min. The synthesis yielded the material with mixed phase 75% anatase and 25% rutile, which will be discussed more in detail below. The sample was denominated as *TiO₂-m_A-75%*.
- 3.1.1.2.4. This sample (*TiO₂-m_A-75%*) was post-treated by Spray-Freeze Drying (SFD) process. This is a peculiar process developed by the group of M. Blosi^[142] and consists in spraying an aqueous suspension into liquid nitrogen, followed by lyophilisation step. For this work, suspensions were prepared at an optimized concentration of 6% TiO₂ in distilled water. The suspension was then subjected to 24h of ball milling using zirconia grinding bodies. Through a peristaltic pump, the suspension was nebulized through the nozzle by nitrogen flow of 0.4 bar. The obtained spray was sent directly into a liquid nitrogen bath. Once the suspension is completely atomized, liquid nitrogen and water are sublimated during 4 days in lyophilizer. The obtained powder was calcined at 400°C for 3 h with the ramp of 2°C/min. The resulted powder is called *TiO₂-m_A-75%_SFD*.
- 3.1.1.2.5. In Chapter 7, TiO₂ with the mixed phase of anatase and rutile (50:50) was studied. The sample was prepared by physical mixing of different batches of powders prepared by the method described in 3.1.1.2.2 Nevertheless, probably some of the batches resulted in mixture of anatase and rutile. Therefore, the optimization of procedure described in 3.1.1.2 has to be optimized for scale-up process. The resulted powder is designated as *TiO₂-m-A-R*.
- 3.1.1.2.6. The size of titania nanoparticle can be tuned by the water-to-surfactant molar ratio (R_w). Thus, *TiO₂-m_A* was prepared with R_w 21. Another titania powder was prepared with larger amount of surfactant resulting in R_w 10. This powder was named as *TiO₂-m_Rw10*, respectively.

3.1.2. Material characterization

3.1.2.1. X-ray Diffraction (XRD).

XRD measurements were carried out at room temperature with a Bragg/Brentano diffractometer (X'pertPro PANalytical) equipped with a fast X'Celerator detector, using a Cu anode as the X-ray source ($K\alpha$, $\lambda=1.5418 \text{ \AA}$). Diffractograms were recorded in the range of $10-80^\circ 2\theta$ counting for 20 s every $0.05^\circ 2\theta$ step. Particle size determination was done by Scherrer equation as follows over the 100% peak:

$$d = k \times \lambda / \beta \times \cos \theta \quad (\text{Eq. 3.1})$$

where: d = mean size of crystallites, k = particle shape factor considered as spherical, λ = X-Ray wavelength, β = line broadening difference (FWHM) between the sample and Si standard, θ = Bragg angle.

3.1.2.2. Diffuse reflectance spectroscopy (DRS).

DRS analyses were done in a Perkin Elmer Lambda 19 instrument equipped with integrating sphere in the range 280-800nm.

3.1.2.3. N₂ physisorption.

Catalyst surface areas were measured by a N₂ physisorption apparatus (Sorpty 1750 CE instruments) and single-point BET analysis methods, in which samples were pre-treated under a vacuum at 125°C.

3.1.2.4. RAMAN spectroscopy.

Raman spectra were recorded at ambient temperature with 514 nm Ar⁺ laser excitation by Renshaw RM1000 spectrometer equipped with Leica DMLM microscope and CCD camera. Power output was 6.25 mW and grating 1200 lines/mm.

3.2. Results and Discussions

Paragraph 3.2 describes comparison between commercial P25, DT-51 titania and different synthesized materials such as TiO₂-m_A, TiO₂-m_R, TiO₂-m_A-75%, TiO₂-m_A-75%_SFD, TiO₂-m_A-Rw10, TiO₂-m_A-R in terms of phase composition, crystalline size, specific surface area and the optical characterization.

3.2.1. Characterization of materials

Figure 3.1 demonstrates the diffractograms of all the used powders. The content of different crystal structures has been estimated semi-quantitatively for all the materials using the program for deconvolution of spectra. Thus, commercial TiO₂ P25 consists of 80% anatase and 20% rutile, which is consistent with other works.^[143] From XRD data provided in **Figure 3.1** the average size of the P25 crystals was found 23 nm. Another commercial TiO₂ DT-51 nanocrystals consist of 100% anatase with the particles diameter of 20 nm. XRD analysis of synthesized TiO₂-m_A demonstrate that the main phase is represented by anatase (93%) with the small inclusion of rutile (7%) determined by the semi-quantitative method. This value is sensitive to the synthesis and may vary from 95 to 92% for anatase. From XRD patterns, the size of TiO₂-m_A calcined at 400°C was determined to be 8 nm, which confirms that the microemulsion technique permitted to obtain small crystallites, indeed. With the calcination temperature above 550°C, the phase transition starts to be observed to rutile crystal structure due to the sintering and formation of bigger particles. Indeed, as was reported previously,^[114] rutile is the thermodynamically stable form above 35 nm at all temperatures and atmospheric pressure, while anatase is more stable below 14 nm. Nevertheless, as one can see from the **Figure 3.1** and **Table 3.1**, microemulsion method allows synthesizing rutile with 11 nm crystallites.

The phase composition was also confirmed by RAMAN spectroscopy. On **Figure 3.2** one can see a clear presence of anatase phase in P25, DT-51 and TiO₂-m_A, demonstrating the bands with the corresponding assignments at 143 cm⁻¹ (E_g), 197 cm⁻¹ (E_g), 397 cm⁻¹ (B_{1g}), 516 cm⁻¹ (B_{1g}), and 638 cm⁻¹ (E_g). While, the bands of rutile phase in TiO₂-m_R could be observed at 143, 445 and 610 cm⁻¹ with B_{1g}, E_g and A_{1g} symmetry species, respectively. The band at 210 cm⁻¹ and a weak broad shoulder at approximately 707 cm⁻¹ have been attributed to second-order or two-phonon RAMAN scattering.^{[144][145][146]}

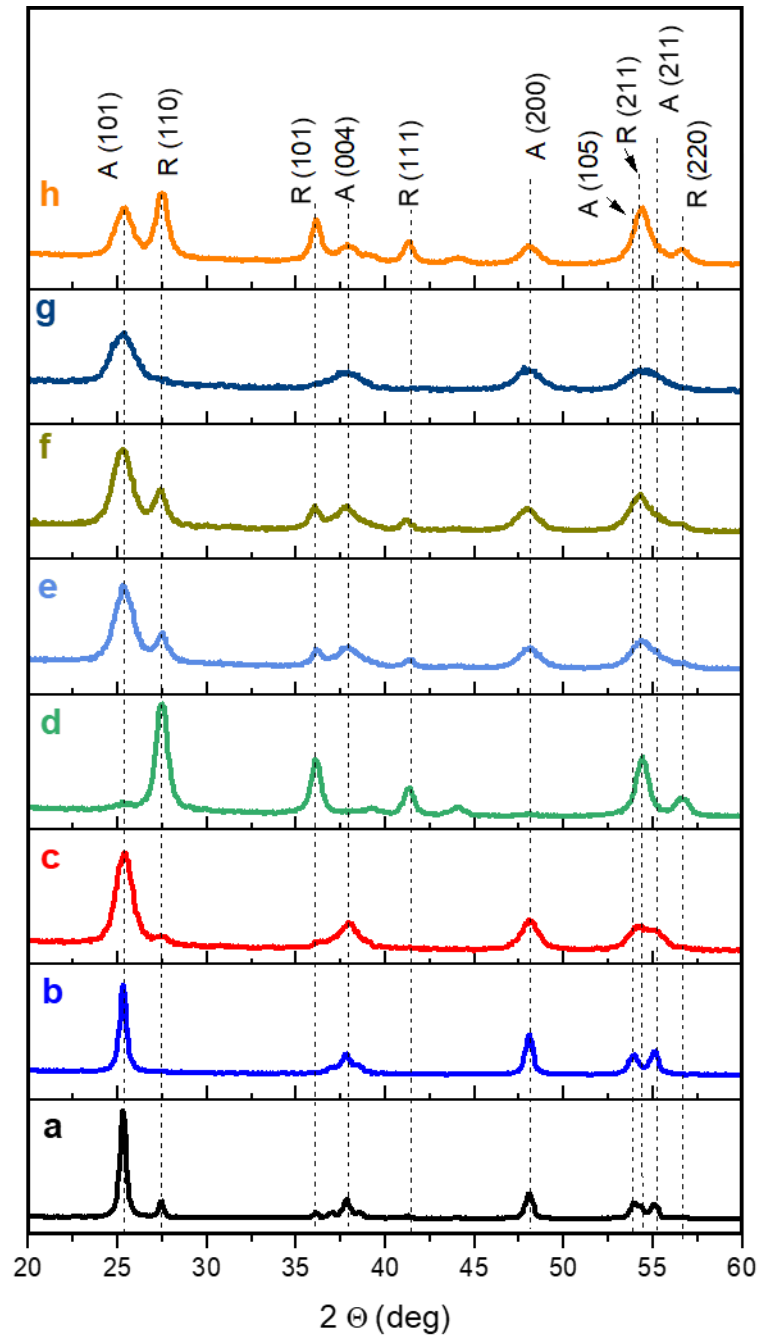


Figure 3.1. XRD of TiO₂ powders: a). P25, b). DT-51, c). TiO₂-m_A, d). TiO₂-m_R, e). TiO₂-m_A-75%, f). TiO₂-m_A-75%_SFD, g). TiO₂-m_A-Rw10, h). TiO₂-m_A-R.

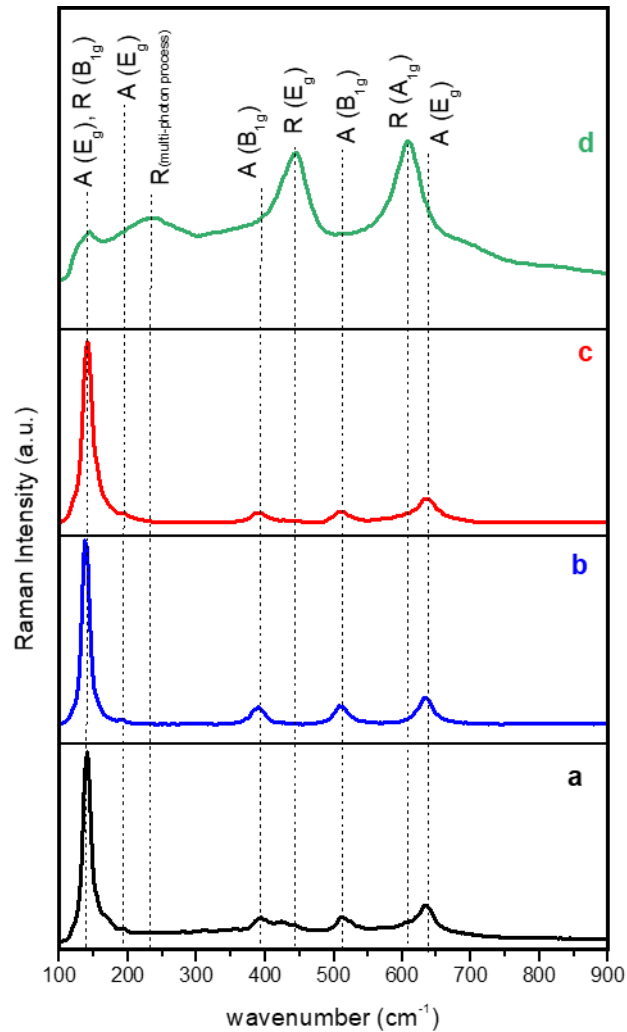


Figure 3.2. RAMAN spectra of TiO₂ powders: a). P25, b). DT-51, c). TiO₂-m_A, d). TiO₂-m_R.

The sample TiO₂-m_A-75%. resulted in mixed phase of 75% anatase and 25% rutile as shown in XRD presented in **Figure 3.1**. The same composition was kept for the post-treated material by Spray-Freeze Drying technique, TiO₂-m_A-75%_SFD, even after calcination step at 400°C. The crystalline sizes of materials were determined with respect to anatase (101) reflection, which is 7 nm for both the samples. Thus, SFD method does not alter the size of titania nanoparticles. The results are shown in **Table 3.1**.

XRD of TiO₂-m_A-Rw10 show broad patterns of anatase due to a formation of small 6 nm crystallites.

The mixed phase TiO₂-m_A-R resulted in 50 % Anatase and 50% Rutile with crystalline size found from anatase (101) and rutile (110) reflections, and equal to 7 and 11 nm, respectively.

Specific surface area was determined, and the results are shown in **Table 3.1**. BET measurements demonstrated that TiO₂-m_A has a big surface area. The obtained results indicated that

the procedure used for lab-synthesized titania preparation permitted to obtain a photocatalyst with a higher surface area and smaller crystallite size with respect to the commercial powders.

Table 3.1. The main results obtained from XRD and BET measurements, and the reference to a section of the corresponding preparation method.

Catalyst	S_{BET} (m^2/g)	d_{XRD} (nm)	synthesis
P25	49	23	commercial
DT-51	80	20	commercial
TiO ₂ -m_A	130	8	3.1.1.2.1
TiO ₂ -m_R	60	11 ^a	3.1.1.2.2
TiO ₂ -m_A-75%	140	7	3.1.1.2.3
TiO ₂ -m_A-75%_SFD	124	7	3.1.1.2.4
TiO ₂ -m_A-Rw10	130	6	3.1.1.2.6
TiO ₂ -m_A-R	99	7	3.1.1.2.5

^a Particle size determined for rutile (110) reflection by the Scherrer formula.

In addition, the microemulsion process allows tuning the particle size by changing the size of micelles. This is possible using different the water-to-surfactant molar ratio. Thus, with higher content of surfactant ($R_w=10$), the microemulsion process resulted in smaller titania particles compared to the ones with $R_w=21$, but no substantial difference in specific surface area was observed.

Nitrogen physisorption analysis revealed the differences in the volume and size of the pores of the two powders (**Figure 3.3**).

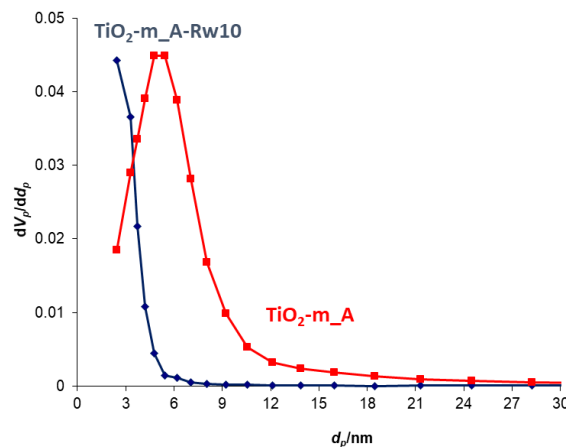


Figure 3.3. BJH plot of TiO₂-m_A (red) and TiO₂-m_A-Rw10 (dark blue).

TiO₂-m_A-Rw10 has smaller pores with the volume of 0.09 cm³/g and size of 2.43 nm as compared to TiO₂-m_A, having volume and size of pores of 0.29 cm³/g and 5.41 nm, accordingly.

The absorbing capability of photo-catalysts in the UV-visible region has been measured by Diffuse Reflectance Spectroscopy. Reflectance spectra on **Figure 3.4** indicate that absorption of TiO₂-m-based powders and P25 is slightly enhanced in the visible region with respect to the commercial DT-51. This behavior could be mainly due to the presence of a small amount of rutile in the lab-synthesized titania and P25, as highlighted from the XRD patterns reported in **Figure 3.1**. Indeed, it is known that energy bandgap of rutile is around 3.0 eV, while anatase is characterized by an energy bandgap of 3.3 eV. [89] To note, however, the band gap can be red shifted by 0.25 eV for oxygen deficient TiO₂ as was reported by T. Das and co-workers. [147]

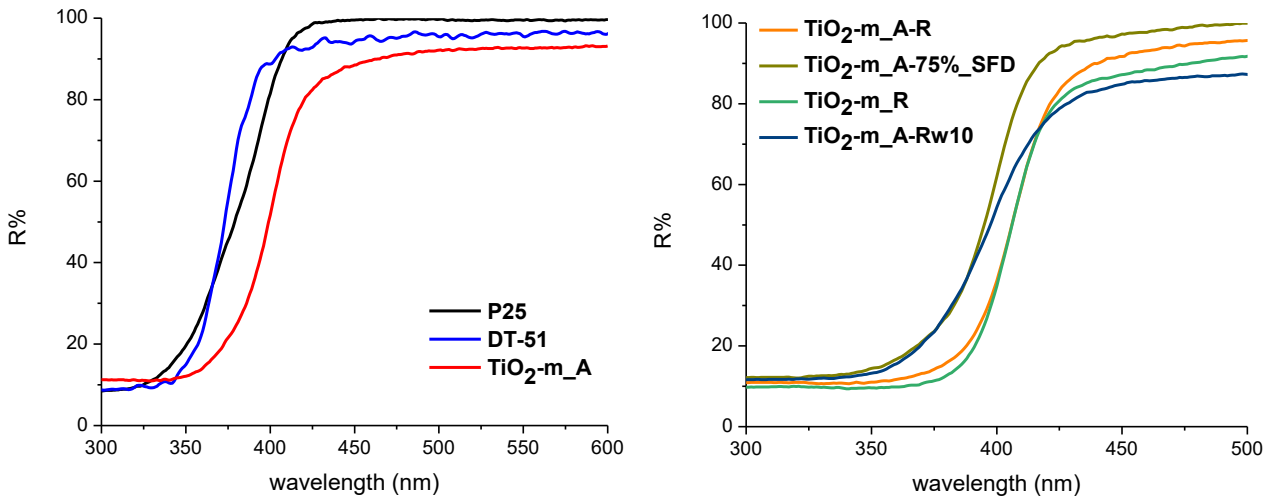


Figure 3.4. Reflectance spectra of different titanium dioxide powders.

From Reflectance spectra one can determine the value of energy bandgap (E_g):

$$E_g \text{ (eV)} = \frac{1240}{\lambda \text{ (nm)}} \quad \text{(Eq. 3.2)}$$

where $\lambda \text{ (nm)}$ is the wavelength found as intersection of two linear regions of the spectrum, projected on X axis. The results are shown in **Table 3.2**.

By converting Reflectance using **Eq. 3.3**, Kubelka-Munk (KM) spectra can be built as shown in **Figure 3.5**.

$$KM = \frac{(1-R)^2}{2R} \quad \text{(Eq. 3.3)}$$

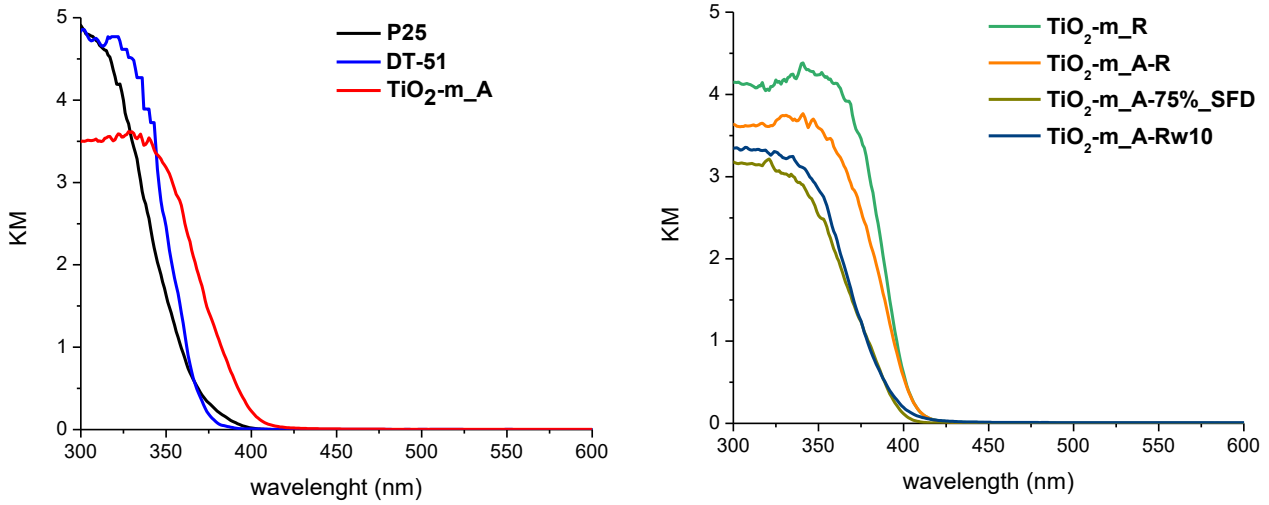


Figure 3.5. Kubelka-Munk (KM) spectra of TiO₂ powders.

The E_g of TiO₂ were found in the same way as for Reflectance. The results are shown in **Table 3.2**.

The bandgap of semiconductors could be calculated also using Tauc equation:

$$\alpha h\nu = A(h\nu - E_g)^n \quad (\text{Eq. 3.4})$$

where α is absorption coefficient, h is Planck's constant (J·s), A is the absorption constant, ν is the frequency of light (s^{-1}), and n is a corresponding coefficient that is 0.5 when associated with a direct allowed band gap transition and is 2 when associated with an indirect allowed band gap transition (related to TiO₂). The coefficient α is proportional to Kubelka-Munk function,^[148] which is usually denoted as $F(R)$ or KM . Therefore, the energy bandgap can be then estimated from Tauc plot (**Figure 3.6**), extrapolating the straight line part of $[F(R) h\nu]^{1/n}$ curves to energy axis, when $[F(R) h\nu]^{1/n}$ is equal to 0. The value of E_g of different TiO₂ powders were found from Tauc plot, and the results were presented in **Table 3.2**.

The results in **Table 3.2** show that the values of energy bandgap of the different types of titanium dioxide are slightly differ depending the method used.^[148] Nevertheless, all the samples absorb in the UV range of solar spectrum, and the bandgap calculated using Reflectance, KM or Tauc plot are generally following the same trend, and it decreases in the order: DT-51 > P25 > TiO₂-m_A-75%_SFD > TiO₂-m_A ~ TiO₂-m_A-Rw10 > TiO₂-m_R ~ TiO₂-m_A-R. Therefore, it is possible to

conclude that all the three methods could be valid for determination and comparison of band gap of powdered materials.

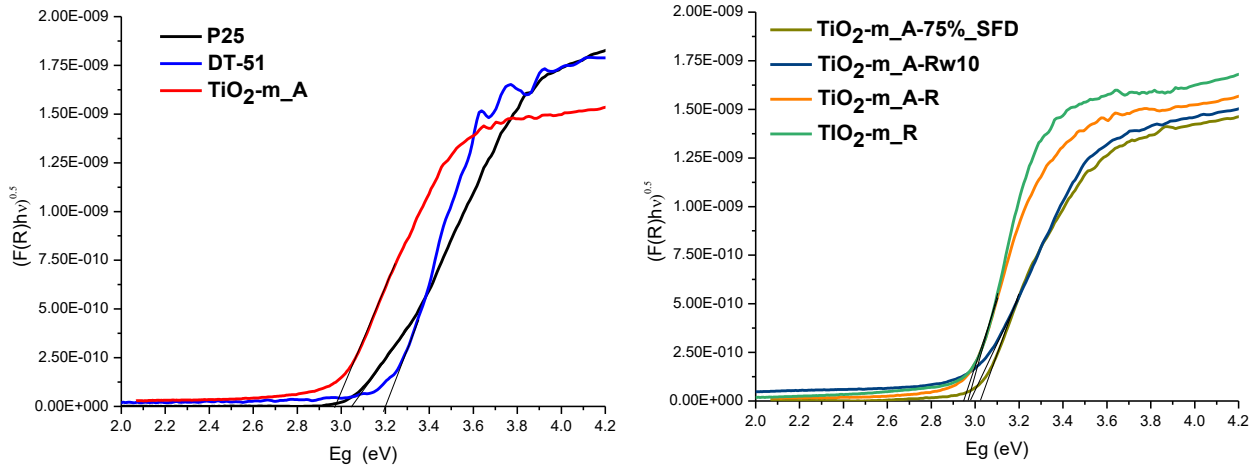


Figure 3.6. Tauc plot of prepared titania powders.

Table 3.2. Comparison of energy bandgap (E_g , eV) for TiO_2 powders by different methods of estimation.

sample	Reflectance	KM	Tauc plot
<i>DT-51</i>	3.19	3.26	3.20
<i>P25</i>	3.02	3.10	3.05
<i>TiO₂-m_A-75%_SFD</i>	3.00	3.08	3.02
<i>TiO₂-m_A</i>	2.98	3.08	2.98
<i>TiO₂-m_A-Rw10</i>	2.98	3.00	2.98
<i>TiO₂-m_R</i>	2.96	3.02	2.97
<i>TiO₂-m_A-R</i>	2.96	3.02	2.96

Chapter 4. Heterogeneous photo-oxidation of HMF

The part of this Chapter is based on the following article:

Lolli, V. Maslova, D. Bonincontro, F. Basile, S. Ortelli, and S. Albonetti, "Selective oxidation of HMF via catalytic and photocatalytic processes using metal-supported catalysts," *Molecules*, vol. 23, no. 11, 2018.

4.1. Experimental section

Paragraph 4.1 deals with the methods and chemicals utilized in preparation and deposition of metal nanoparticles such as Au, Cu and Ag on TiO₂-m_A support. The detailed procedure of preparation of lab-synthesized TiO₂ via microemulsion method (TiO₂-m_A) is described in Chapter 3. The prepared materials were characterized by XRD, TEM, N₂ physisorption analysis and DRS.

4.1.1. Material preparation

4.1.1.1. Chemicals.

Powders: P25 (TiO₂ P25 Degussa), DT-51 (TiO₂ DT-51 Millennium CrystalACTIV).

Metal precursors: HAuCl₄·3H₂O (Gold(III) chloride trihydrate, 99.99%, Sigma Aldrich), CuSO₄·5H₂O (Copper(II) sulphate pentahydrate, 99.5%, Sigma Aldrich), AgNO₃ (Silver nitrate, 99%, Alfa Aesar).

Chemicals for metal nanoparticles synthesis: NaOH (Sodium hydroxide, 99%, Sigma Aldrich), glucose (99.9%, Fluka), PVP (Polyvinylpyrrolidone, Sigma Aldrich).

Standards for HPLC calibration: HMF (5-hydroxymethyl furfural, 99%, AVA Biochem), DFF (2,5-diformylfuran, 99.99%, Toronto Reserch Chemicals), HMFCA (5-hydroxyfuran-2-carboxylic acid, 99.99%, Toronto Reserch Chemicals), FFCA (5-formyl-2-furancarboxylic acid, 99.99%, Toronto Reserch Chemicals), FDCA (2,5-furandicarboxylic acid, 99.99%, Toronto Reserch Chemicals).

4.1.1.2. Incipient wetness impregnation of pre-formed Au, Au-Cu, Ag and Au-Ag nanoparticles by glucose reduction method.

Lab-synthesized TiO₂-m_A was used as support for Au nanoparticles (NPs), which were prepared following the method developed by the group of Prof. S. Albonetti et al.^[28] In brief, to a

solution of glucose in water was added the necessary quantity of stabilizing agent, PVP. Once the solution reached the temperature up to 95°C, NaOH and an aqueous solution of 5 mM $\text{HAuCl}_4 \cdot 3\text{H}_2\text{O}$ were added and stirred for 2.5 min.

Bimetallic Au-Cu alloy and core-shell NPs were prepared in the molar ratio of Au:Cu = 3:1, 1:1 and 1:3 by the similar technique, adding $\text{CuSO}_4 \cdot 5\text{H}_2\text{O}$ as a precursor of copper NPs and keeping total concentration of metal precursor of 5 mM. The catalysts based on Ag and Au-Ag core-shell NPs were prepared using AgNO_3 precursor in molar ratio Au:Ag=1:1, with total metal concentration of 5 mM. The ratios of NaOH-, PVP- and glucose-to-metal were optimized with respect to the type of synthesis. The core-shell NPs were prepared by two sequential additions of solution of metal precursor, followed by 2.5 min of reaction for each.

Then, the sol of NPs was introduced onto $\text{TiO}_2\text{-m_A}$ support by incipient wetness impregnation technique for 5 times with 1.5 wt.% metal loading, following the drying step at 120°C. The catalysts were denoted as: Au/ $\text{TiO}_2\text{-m_A}$; $\text{Au}_3\text{Cu}_1/\text{TiO}_2\text{-m_A}$; $(\text{Au}_3)\text{Cu}_1/\text{TiO}_2\text{-m_A}$; $\text{Au}_1\text{Cu}_1/\text{TiO}_2\text{-m_A}$; $\text{Au}_1\text{Cu}_3/\text{TiO}_2\text{-m_A}$; Ag/ $\text{TiO}_2\text{-m_A}$; $(\text{Au}_1)\text{Ag}_1/\text{TiO}_2\text{-m_A}$.

4.1.1.3. Deposition-precipitation method of Au nanoparticles.

During the synthesis, a 0.001M solution of $\text{HAuCl}_4 \cdot 3\text{H}_2\text{O}$ was used at pH 9, adjusted by adding dropwise a 0.1 M NaOH solution. Similarly, the pH of an aqueous suspension (300 mL) of 2 g of support (DT-51 or $\text{TiO}_2\text{-m_A}$) was adjusted to 9. Then solution of $\text{HAuCl}_4 \cdot 3\text{H}_2\text{O}$ was added dropwise to the TiO_2 suspension under vigorous stirring at room temperature, maintaining pH 9. Once the entire gold solution was transferred to TiO_2 suspension, temperature was increased to 65°C. Once the temperature reached the desired value, the stirring was kept for 2 h. As was reported,^[149] this synthesis is supposed to result in the selective deposition of $\text{Au}(\text{OH})_3$ on the support. The solid was then separated from the solution by centrifugation, washed several times with water to remove chloride, dried at 110°C overnight and calcined at 300°C for 2 h with a rate of 2°C/min, resulted in metallic gold. The following procedure resulted in 1.5 wt.% of metal loading.

According to the type of support used, the resulted catalysts were denoted as Au/ $\text{TiO}_2\text{-m_A_DP}$ and Au/DT-51_DP.

4.1.2. Material characterization

The Diffuse Reflectance Spectroscopy (DRS) and BET analyses have been already described in Chapter 3, Section 3.1.2.2 and 3.1.2.3.

4.1.2.1. Transmission Electron Microscopy (TEM).

Morphological observations were done using TEM/STEM FEI TECNAI F20, which uses a high-angle annular dark field (HAADF) imaging mode at 200 kV. The sample was suspended in ethanol and treated in ultrasonic bath for 15 minutes. The suspension was deposited on a “quantifoil carbon film” Cu grid for TEM analysis, then dried at 100°C.

4.1.2.2. X-ray Diffraction (XRD).

XRD measurements were carried out at room temperature with a Bragg/Brentano diffractometer (X'pertPro PANalytical) equipped with a fast X'Celerator detector, using a Cu anode as the X-ray source ($K\alpha$, $\lambda=1.5418 \text{ \AA}$). Diffractograms were recorded in the range $10-80^\circ 2\theta$ counting for 20 s every $0.05^\circ 2\theta$ step. Diffractograms of Au NPs were recorded in the range $40-46^\circ 2\theta$ for 1500 s every $0.08^\circ 2\theta$ step, using nanoparticles colloids deposited on the glass and dried at 120°C.

4.1.2.3. Photocatalytic test.

The essential part of the experimental set-up is illustrated in **Figure 4.1**. It consists of the solar simulator LS0306 by LOT Quantum Design equipped with 300 W Xe-lamp, which generates light in range of 250-2500 nm with output of 1 sun at a distance of 18 cm. The light is delivered as 40 mm diameter collimated beam. The reactive mixture was placed in a top-irradiated glass photo-reactor that in turn comprises the circulating glycol bath for temperature control, inlet and outlet for gaseous compounds, stirring system and quartz disk for maintenance of light transmission, once the reactor is sealed. Tests were done in different conditions.

Primarily tests were done under the following conditions: 0.08 M aqueous solution of HMF with an HMF/Au molar ratio of 100, reaction time of 8 h, the temperature of 30°C and ambient pressure.

The set of other experiments were carried out with 20 mL 0.5 mM of HMF, 1 g/L of catalyst. The reaction was performed at 30°C and 1 atm of oxygen. Prior the reaction, the reactor with reaction medium was purged with oxygen for 20 min, and then sealed.

Initial time of reaction was considered, when the light was on. Some set of the reactions has been performed under visible light by fixing a 420 nm cut-off filter between the solar simulator and photo-reactor.

After reaction, samples were separated from the photocatalyst by centrifugation or filtration, diluted by 5 times in deionized water and analyzed by HPLC using Agilent Infinity 1200 liquid chromatograph equipped with a Aminex HPX 87-H 300 mm 7.8 mm column using a 0.005 M H_2SO_4 solution as the mobile phase. The identification of compounds was achieved by calibration using

reference commercial samples. Gaseous products were analyzed in an off-line Thermo Focus GC with a carbon molecular sieve column (CARBOSPHERE 80/100 6*1/8) and TCD detector or by Autosystem XL GC with CARBOXENE 1000 60-80 mesh column and flame ionization detector.

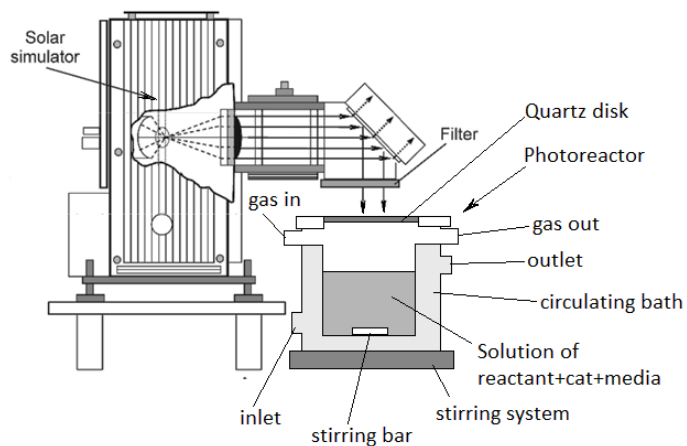


Figure 4.1. Schematic representation of experimental set-up. Adapted from^[75]

4.2. Results and Discussions

Paragraph 4.2 is about the comparison between commercial and home-made TiO₂ in terms of characterization and activity in the reaction of HMF photo-oxidation. The influence of metal nanoparticles, base addition, and oxygen content on product distribution in the photocatalytic process was evaluated.

4.2.1. Preliminary tests

4.2.1.1. Effect of support and Au NPs deposition

In order to carry out the photocatalytic oxidation of HMF, some preliminary tests using commercial DT-51 and home-made TiO₂ were performed. Then, Au nanoparticles were added to investigate the possibility to favour the selective conversion of HMF. Studied samples are reported in **Table 4.1**.

Table 4.1. Prepared samples and main characterization data obtained from XRD, DRS and BET measurements.

Sample	d (nm)	Eg ^b (eV)	S _{BET} (m ² /g)
DT-51	20 ^a	3.26	80
TiO ₂ -m_A	8 ^a	3.08	130
Au/DT-51_DP	<3*	3.22	80
Au/TiO ₂ -m_A_DP	-**	3.11	130

^a TiO₂ crystallites

^b determined from KM spectra

* Au nanoparticles

** Au XRD patterns could not be seen by XRD due to the presence of rutile

The absorbing capability of supports in the UV-visible region, their XRD patterns and estimated specific surface area have been already discussed in Chapter 3, Section 3.2.1. For convenience, these results are also collected in **Table 4.1**.

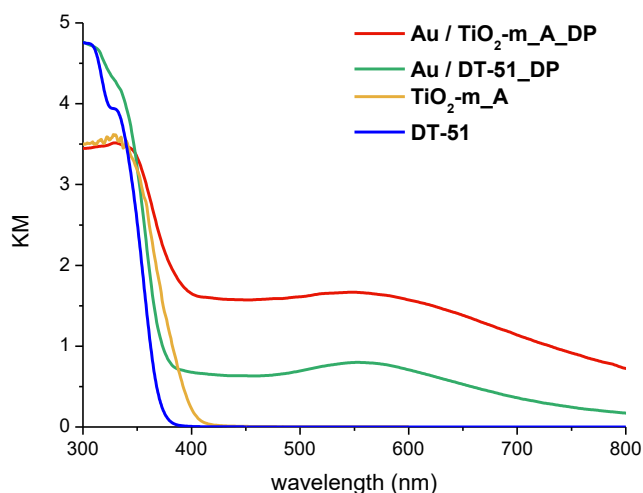


Figure 4.2. Kubelka-Munk (KM) spectra of commercial DT-51 and microemulsion-synthesized $\text{TiO}_2\text{-m}_A$ with Au deposited nanoparticles by deposition-precipitation method.

Comparison of Au-containing samples on **Figure 4.2** showed that all the materials demonstrated absorption in UV range of solar spectrum below 420 nm, due to band gap excitation in TiO_2 . The bandgap of Au-containing samples was found from Kubelka-Munk (KM) spectra (**Figure 4.2**) using **Eq. 3.2**. All the gold-containing powders exhibited a distinctive purple color. This is due to the Localized Surface Plasmon Resonance (LSPR) effect, which correspond to a band located at 550 nm, what is consistent with previously reported studies.^[150]

TEM images of the Au-containing photocatalysts (**Figure 4.3**) show that metallic particles are well-dispersed on both TiO_2 with a size of 2 nm. The higher surface area and smaller titania particles which characterized $\text{TiO}_2\text{-m}_A$ sample, did not significantly influence the particle size and distribution of gold which resulted to be very similar on what obtained over commercial TiO_2 . Indeed, in both cases, the deposition precipitation method allowed the preparation of 2 nm Au nanoparticles, homogeneously distributed on the support.

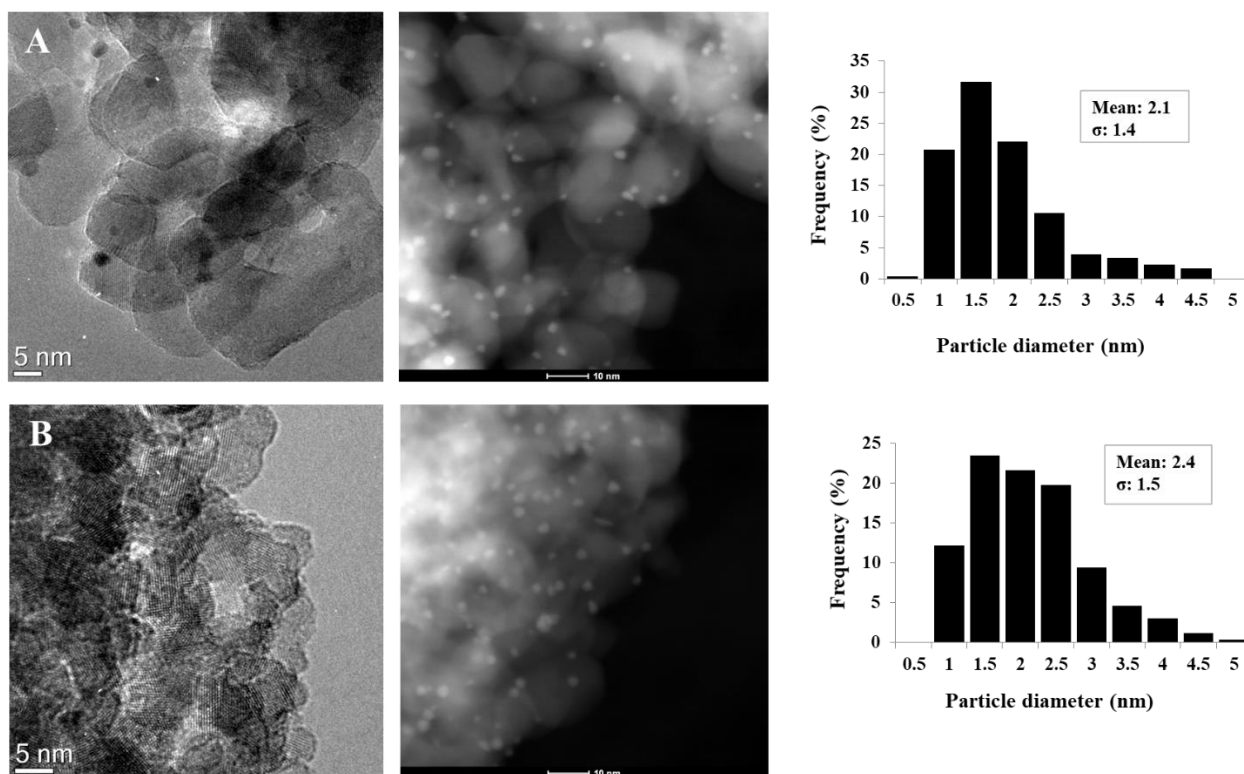


Figure 4.3. TEM images and gold nanoparticles size distribution for: A) Au/DT-51_DP and B) Au/TiO₂-m_A_DP.

The prepared materials were tested in the photocatalytic oxidation of HMF in water using simulated solar radiation. At first, home-made and commercial titania were used. The conversion of the two different titania are very similar (**Figure 4.4**), despite the different UV-vis diffuse reflectance absorption spectra.

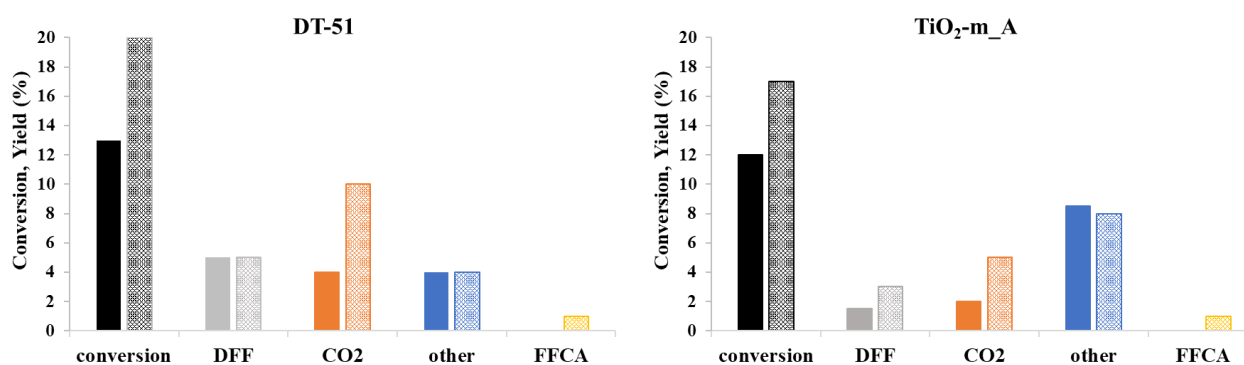


Figure 4.4. Photo-catalytic activity of the commercial (DT-51 and Au/DT-51_DP) and lab-synthesized samples (TiO₂-m_A and Au/TiO₂-m_A_DP). Reaction conditions: 8h, 30°C, HMF 0.08M. Legend: HMF conversion (■), DFF yield (■), FFCA yield (■), CO₂ yield (■), others (■). Bare supports are represented by full bars, gold supported catalysts have patterned bars.

The reaction did not take place in the dark and no oxidation of HMF was observed in the absence of catalyst and oxygen or air.

The main identified products in the reaction were 2,5-diformylfuran (DFF) and CO₂. The hypothesized mechanism for the formation of DFF and CO₂ can be summarized as reported in **Figure 4.5**, similarly to what have been suggested by Palmisano and co-workers.^[32] The reaction starts from the abstraction of a hydrogen with respect to OH-group in HMF molecule by either h⁺ or ·OH, with subsequent formation of the aldehyde. Then, DFF may be further oxidized and completely mineralized to CO₂ and H₂O through aliphatic intermediates, which is actually explaining the presence of carbon dioxide and other ring opened by-products as observed at low retention time from HPLC analysis (**Figure 4.6**).

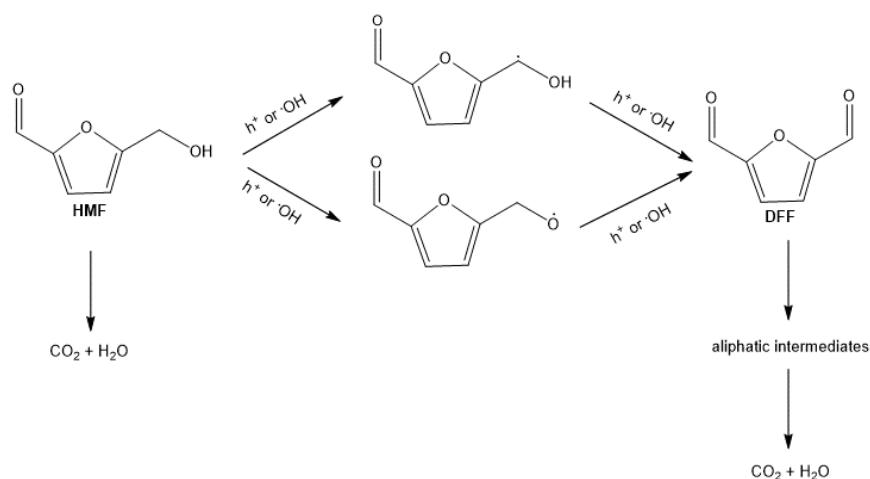


Figure 4.5. Proposed reaction pathway towards DFF formation over TiO₂ based samples.^[32]

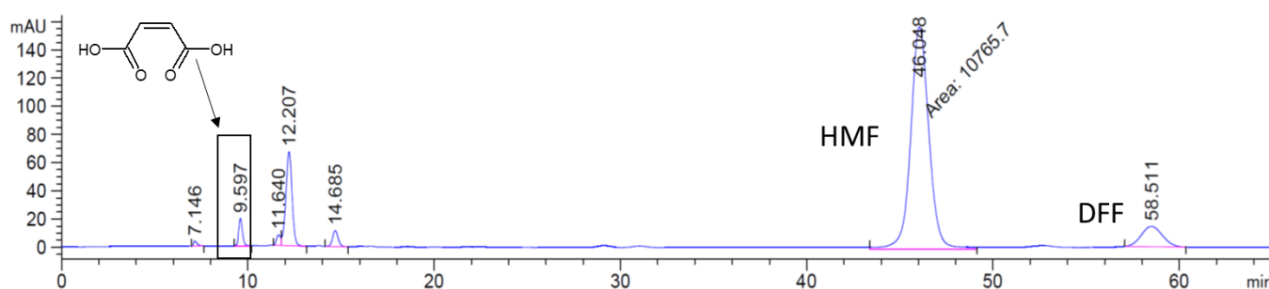


Figure 4.6. HPLC analysis of the reaction mixture using TiO₂-m_A or DT-51 catalysts.

As a matter of fact, both HPLC and ESI-mass analysis showed the presence of other compounds, within which we verified the presence of maleic acid. This compound has already been found in literature as a derivative of HMF oxidation^[151] using H₂O₂^[152]; so, it is possible that the

hydrogen peroxide formed by radical reaction using TiO_2 as photocatalysts in water^[43] promoted the formation of this compound. Other by-products may be formed in reaction with reactive oxygen species produced by the photocatalytic reaction over TiO_2 (such h^+ , $\cdot\text{O}_2^-$, $\cdot\text{OH}$ and H_2O_2); in fact, it is well known that aliphatic intermediates can be obtained from molecules that are able to form peroxy-bridge, as also observed in the photo-oxidation of phenol and other organic alcohols.^[43].199]

Comparing the commercial to the lab-synthesized titania, DFF and CO_2 yield was lower for $\text{TiO}_2\text{-m_A}$, but higher carbon loss was observed using this material. This suggests that $\text{TiO}_2\text{-m_A}$ has a higher reactivity in the formation of by-products. Indeed, HMF conversion value was very similar to that obtained with the commercial titania.

Effective improvement of the photocatalytic activities was observed with the introduction of gold onto the catalyst. Nevertheless, with the increase of HMF conversion a significant enhancement of CO_2 yield was observed suggesting the presence of metal mainly promotes the mineralization reactions.^[153] Indeed, DFF selectivity was higher using bare TiO_2 , suggesting the high activity observed of metal containing systems to be mainly associated to unselective reactions both on the commercial and on the homemade supports. Worth of notice is the FFCA formation when Au nanoparticles were deposited on TiO_2 (**Figure 4.4**).

4.2.1.2. The effect of base on the photocatalytic reaction

With the aim of improving the selectivity, Na_2CO_3 was added in the molar ratio of $\text{HMF}:\text{Na}_2\text{CO}_3 = 2$, to avoid unselective oxidation since this base was reported to act as a $\cdot\text{OH}$ radical scavenger.^[34]

The results shown in **Figure 4.7** demonstrated that with an addition of base, conversion of HMF increases and the production of higher amount of oxidation products such as FFCA and other by-products; HMFCFA appeared with all the catalytic systems but its formation was deeply enhanced with gold supported catalysts. The presence of HMFCFA is mainly attributed to the presence of a base. Therefore, an interesting consideration can be done evaluating the results obtained for the two different titanium oxides: HMF oxidation, which passes mainly through DFF formation with the consecutive formation of FFCA, can go through the other pathway in basic conditions, which includes HMFCFA formation. The change in the reaction mechanism can be observed even in the case of metal supported catalysts; in the presence of gold this effect is even more emphasized where more than 25% yield of HMFCFA is achieved with Au/DT-51_DP. Meanwhile, no DFF formation was observed in both cases, indicating that gold in the presence of a base is very active in HMF oxidation and the reaction pathway passes through HMFCFA formation since alcohol oxidation is the rate limiting step of the reaction.

Moreover, despite the low temperature utilized in these test (30°C), the basic pH enhances HMF degradation, leading to the formation of high molecular weight molecules such as humins,^[154] defined as “other”. As a matter of fact, in contrast to the reaction in base-free conditions, the other products such as maleic acid and CO₂ were not observed.

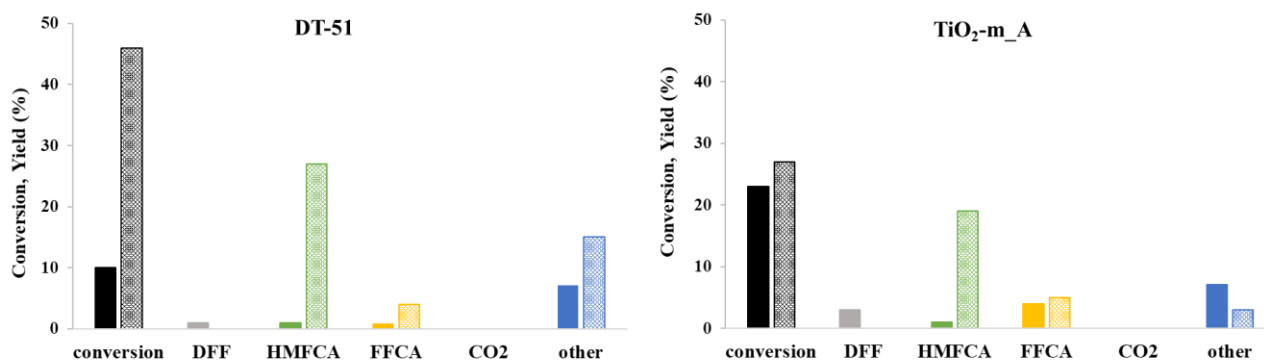


Figure 4.7. Photo-catalytic activity of the commercial (DT-51 and Au/DT-51_DP) and home-made samples (TiO₂-m_A and Au/TiO₂-m_A_DP) in presence of base with HMF:Na₂CO₃ = 2 molar ratio. Reaction conditions: 8h, 30°C, HMF 0.08M. Legend: HMF conversion (■), DFF yield (■), HMFCFA yield (■), FFCA yield (■), C-loss (■). Bare supports are represented by full bars, supported catalysts have patterned bars.

In order to evaluate the actual role of base in the system, experiments in the absence of light were performed. As it is shown in **Figure 4.8** both supports show the same trend of HMFCFA and FFCA selectivity in the dark, meaning that a *catalytic* reaction takes place for these catalysts in the similar manner. As a matter of fact, the role of NaOH as a homogeneous catalyst in oxidation of organic alcohols was rigorously studied and reported by Z. Yuan and co-workers.^[155] The effect of base is more substantial in the first step of HMF oxidation to yield HMFCFA and less significant in the formation of FFCA.

Au/DT-51_DP demonstrate comparable results in presence of light and in the dark. Whereas, Au/TiO₂-m_A_DP exhibited different activity. Higher FFCA selectivity was observed under illumination, suggesting that FFCA is mainly produced through a *photo-catalytic* reaction.

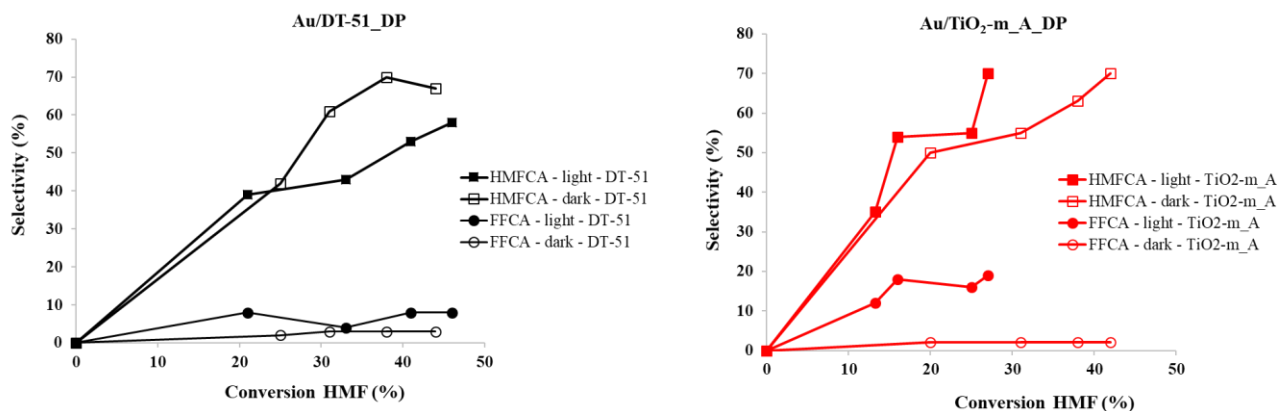


Figure 4.8. Overall selectivity of HMFCFA (squares) and FFCA (circles) as a function of HMF conversion for Au/DT-51_DP (black) and Au/TiO₂-m_A_DP (red) catalysts under the dark (empty markers) and illumination (filled markers) in presence of base with HMF: Na₂CO₃ = 2 molar ratio.

Figure 4.9 summarizes the two different pathways of HMF oxidation that are observed for Au-containing catalysts and pristine supports. In the presence of base, reaction pathway is mainly towards HMFCFA and FFCA formation. Results of HMF photo-oxidation for bare TiO₂ showed also DFF formation, that can bring us to the clue that FFCA can be also formed through fast oxidation of DFF using gold containing system. The presence of coloured, high molecular weight products in the reaction mixture confirm the formation of humins-like compounds at basic pH. On the contrary, in the absence of base, HMF is mainly converted to DFF, which can be transformed in FFCA using gold supported catalysts or can go through some ring opening reaction leading to the formation of aliphatic products and CO₂. Some mineralisation products can also be derived from HMF as reported from Yurdakal et al.^[32]

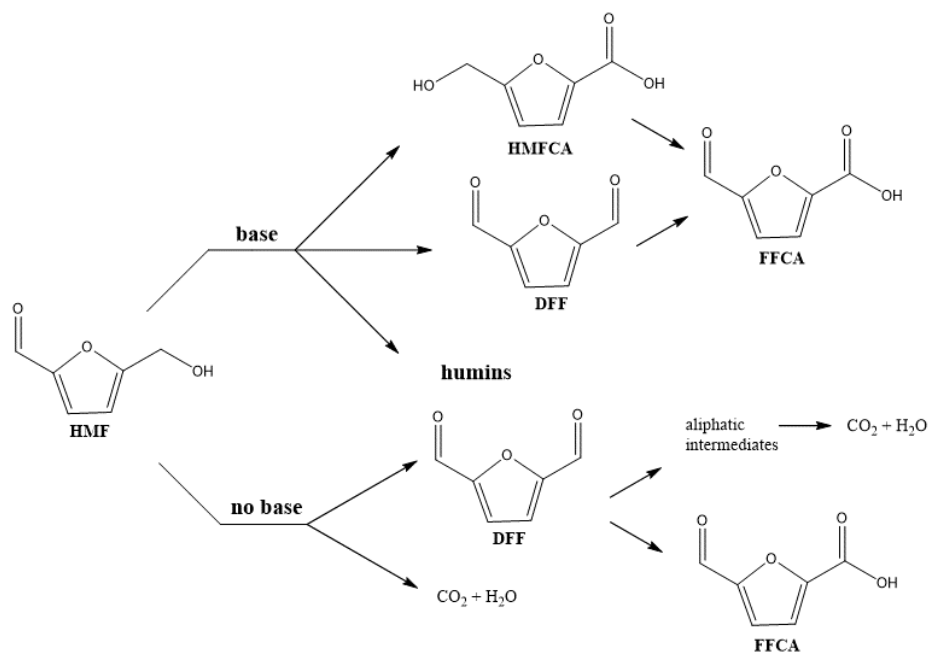


Figure 4.9. Reaction pathway of HMF photo-oxidation in the presence and absence of base.

4.2.1.3. The effect of oxygen.

In attempt to elucidate the oxygen effect on photo-catalytic reaction, experiments using different quantity of oxygen were performed (**Table 4.2**) for microemulsion-based support. In the case of titania alone, with an increase of oxygen fraction in the reactor, the conversion of HMF increased from 10% to 22%, leading to a higher formation of DFF, CO₂ and aliphatic by-products. Considering Au-containing material, HMF conversion results were comparable, regardless the oxygen content. No activity was observed for both systems in anaerobic conditions, when N₂ gas was used. Therefore, one can suggest that molecular oxygen plays a pivotal role when bare titania was used as catalyst. The role of oxygen is twofold: it can be activated by the photogenerated electrons, leading to a formation of various reactive oxygen species, and consequently, it acts as an electron trap, lowering the recombination process.^[156] On the other hand, the effect of oxygen content is not substantial on the photo-catalytic reaction in the presence of Au NPs, probably because of the rate limiting step, which is the charge transfer between TiO₂ and Au in this case. The hot electrons from Au NPs have sufficient energy to overcome the Schottky barrier and to be injected into the CB of TiO₂.^{[157],[158]} The electrons on the surface of TiO₂ or Au can be then scavenged by molecular oxygen molecules, yielding active superoxide radical species.^[156]

Table 4.2. HMF conversion (X) and products yields (Y) for TiO₂-m_A and Au/TiO₂-m_A_DP with different oxygen content (volume fraction). Reaction condition: 8h, 30°C, HMF 0.08M.

Catalyst	O ₂ (%)	X _{HMF} (%)	Y _{DFF} (%)	Y _{FFCA} (%)	Y _{CO₂} (%)	Y _{Other} (%)
TiO ₂ -m_A	11	10	2	-	3	5
	21	12	2	-	2	8
	100	22	5	-	8	9
Au/TiO ₂ -m_A_DP	11	12	2	-	2	8
	21	17	3	1	5	8
	100	15	3	1	8	3

The effect of oxygen content on aliphatic products formations was studied. Thus, the results of area under the peak at 12 min of retention time (**Figure 4.6**) was monitored by HPLC. The correlation of the resulted peak area obtained in reaction with microemulsion-based titania and different amount of O₂ is reported in **Figure 4.10**. It could be seen that oxygen content promotes the formation of the aliphatic product. This effect is more remarkable when the bare support is used.

These preliminary results open an overview of the reaction mechanism for HMF photooxidation. It has been demonstrated that the base content, oxygen amount and the presence of the metal are the parameters influencing HMF photo-oxidation mechanism.

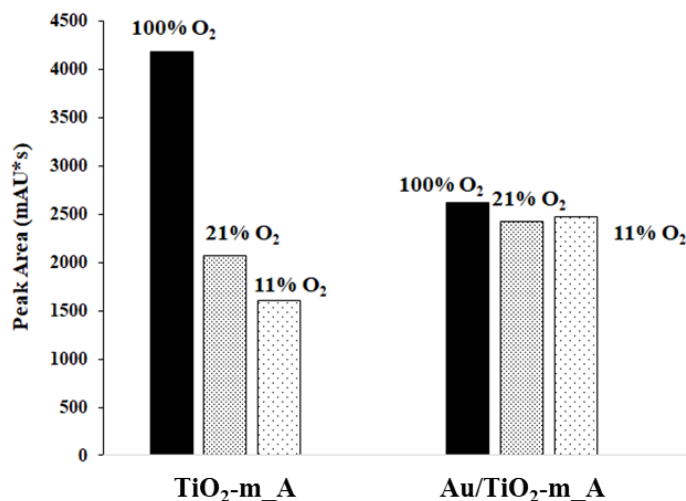


Figure 4.10. Effect of oxygen content on the formation of aliphatic products of HMF photo-oxidation.

4.2.1.4. Effect of radical scavenger.

A deeper insight to mechanism understanding is currently ongoing, similarly to what has been recently reported in literature.^{[159],[42],[45],[160]} Preliminary tests were carried out using the radical scavengers such as p-benzoquinone for superoxide radical $\cdot\text{O}_2^-$, CuCl_2 for electrons e^- , sodium acetate for holes h^+ ,^[161] tert-Butyl alcohol for hydroxyl radicals $\cdot\text{OH}$ scavenging. The tests were carried out using DT-51, since this catalyst demonstrated greater activity than $\text{TiO}_2\text{-m}_A$.

The results are illustrated on **Figure 4.11**. The conversion of HMF increases in time, regardless the introduction of additives. However, a degree of oxidation depends on the type of scavenger added. A similar behavior could be noticed between reactions with no additives and when a hole's scavenger was used. With the addition of scavengers for hydroxyl radical and electron, HMF conversion is decreasing, and it is more significantly lowered when superoxide's scavenger was used.

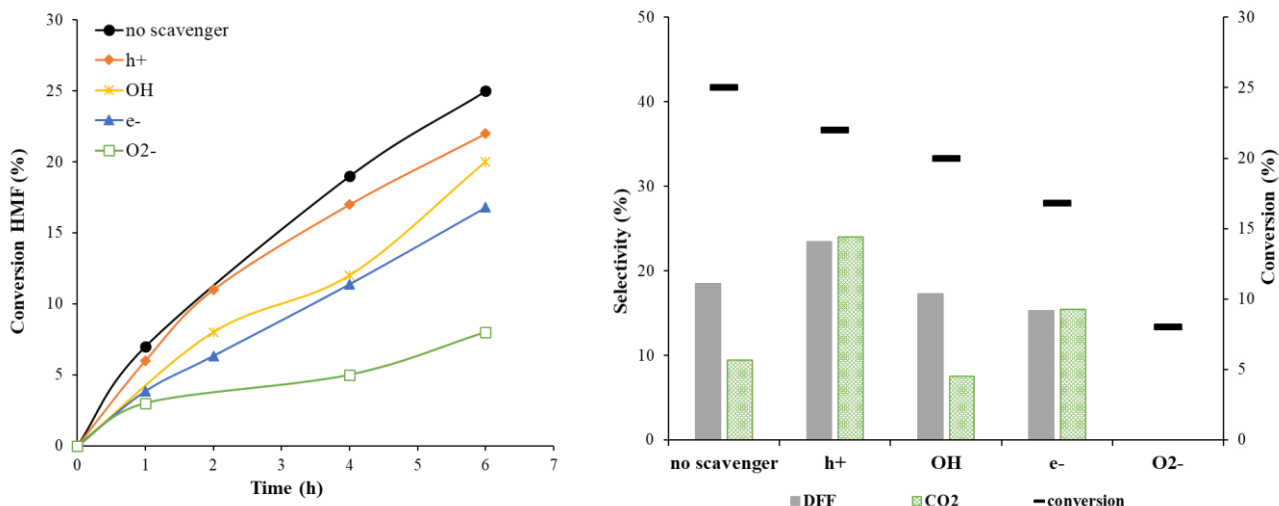


Figure 4.11. Effect of scavengers (of charges and radicals) on the HMF conversion with time, and the corresponding selectivity to DFF and CO₂ after 6 h of irradiation in the presence of DT-51. Reaction conditions: 30°C, HMF 0.08M, O₂ 12 ml/min, HMF:scavenger=2 molar ratio.

A comparison of product distribution indicates that h⁺, [•]OH and e⁻ do not influence a DFF formation, suggesting that these species have a minor effect of partial oxidation of HMF to DFF. An increase of DFF selectivity in the reaction with CH₃COONa was also observed by I. Krivtsov and co-workers,^[160] when sodium formate was used as a h⁺ scavenger and g-C₃N₄ as a catalyst. On the other hand, high CO₂ selectivity in the reaction with CH₃COONa can be explained by “photo-Kolbe” reaction,^[161] where CH₃COONa generates CO₂ reacting with hole. A decrease in selectivity of CO₂, when tert-Butyl alcohol was added, suggest that hydroxyl radicals are the main species responsible for over-oxidation process. Finally, when superoxide radical was scavenged, the conversion of HMF dramatically decreased with any products of interest detected, supporting the idea that this species is a major participant in partial oxidation of HMF.

4.2.2. Effect of different noble metal co-catalysts

The following part of work was carried out with a more diluted HMF concentration and lower catalyst loading to insure that all the particles interact effectively with light. Within bare supports (**Figure 4.12**), P25 converts 100% HMF to CO₂ and other by-products. DT-51 shows moderate reactivity, converting about 50% of HMF mainly to CO₂ and other by-products. However, DFF and some traces of HMFCFA and FFCA were observed. While TiO₂-m_A demonstrates milder oxidation with higher selectivity to desired DFF, also favoring formation of HMFCFA and FFCA intermediates. Thus, TiO₂-m_A could be utilized as a support for metal nanoparticles to study their effect on HMF photo-oxidation since this type of titania demonstrates results of a more selective HMF conversion, the reason of which could be the presence of some defective sites (oxygen vacancies, uncoordinated Ti ions, grain boundaries etc.),^{[162][163]} which suppress the generation of reactive oxygen species.

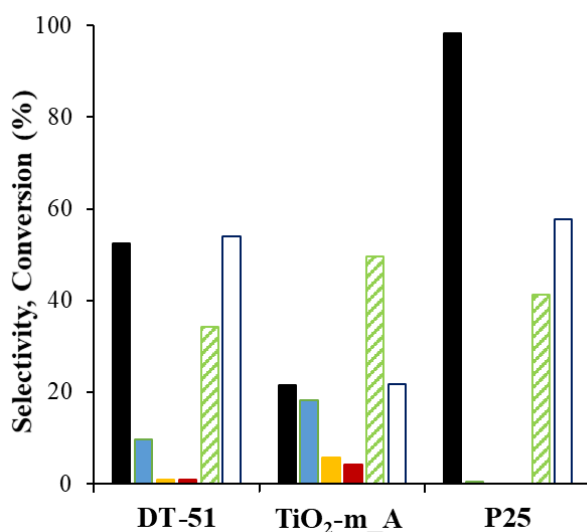


Figure 4.12. Photo-catalytic HMF oxidation with different TiO₂. Reaction conditions: 30°C; 0.5 mM aq. HMF; 1g/L catalyst; O₂ 1 atm; 1h. Legend: HMF conversion (■), DFF yield (■), HMFCFA yield (■), FFCA yield (■), CO₂ yield (■), other (□).

Reaction time was studied using the Au/TiO₂-m_A catalyst and the results are shown in **Figure 4.13**. As a general observation, the over-oxidation occurs as the HMF conversion increases with reaction time. To note, even though the conversion of HMF is quite low within 15 min in these conditions, the partial photo-oxidation is still feasible with high selectivity of HMFCFA and DFF. Therefore, the process of HMF photo-oxidation can be potentially developed for industrial application, using pervaporation technique that is in principle based on “permeation” through selective membrane and “evaporation” processes,^{[164][165][166]} which could avoid further degradation of liquid phase products. This method was successfully developed and implemented by the group of

G.Camera-Roda for the synthesis of vanillin by photo-oxidation of ferulic acid on TiO₂ catalysts.^{[167][168][169]}

For the further studies, 1 h of reaction has been selected as a good compromise between HMF conversion and product selectivity.

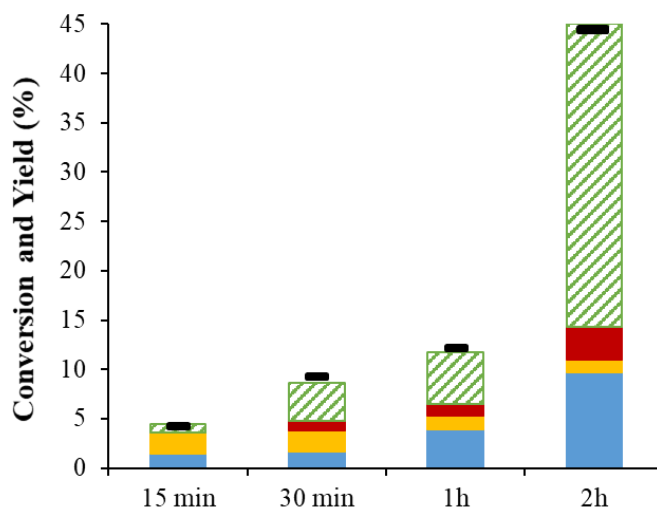


Figure 4.13. Photo-catalytic HMF oxidation and product distribution with Au/TiO₂-m_A. Reaction conditions: 30°C; 0.5 mM aq. HMF; 1g/L catalyst; 1.5% wt. Au NPs; O₂ 1 atm. Legend: HMF conversion (■), DFF yield (■), HMFCFA yield (■), FFCA yield (■), CO₂ yield (■).

With the aim to elucidate the role Au NPs on photo-oxidation of HMF and to lower the cost of prepared catalyst, gold-copper alloy and core-shell nanoparticles were deposited on TiO₂-m_A support in different molar ratio. Secondly, Au-Cu nanoparticles deposited on TiO₂ showed improved the results of catalytic partial oxidation of HMF towards the furan dicarboxylic acid (FDCA) production compared to monometallic gold due to a better sample stability and resistance to poisoning.^{[23][21]}

The colloidal pre-formed nanoparticles were deposited on the glass for XRD analysis. From the diffractograms shown in **Figure 4.14**, the particle size was determined by Scherrer formula. The results presented in **Table 4.3** demonstrate that with alloying process and synthesis of core-shell, the size of nanoparticles increases. In contrast to monometallic Au NPs, the XRD of monometallic Ag NPs revealed the presence of big 10 nm cluster. This suggests that the synthesis of Ag NPs formation still requires optimization of reducing and/or stabilizing agents content.

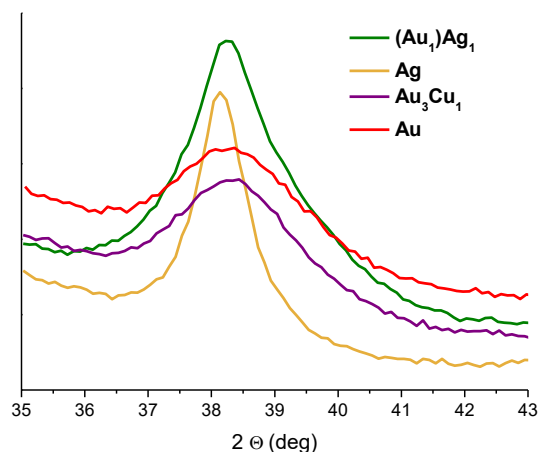


Figure 4.14. XRD patterns of Au, Au-Cu, Ag and Au-Ag NPs colloids deposited on glass.

The optical characterizations of synthesized catalysts were assessed by DRS. The Kubelka-Munk spectra are shown in **Figure 4.15**. As in previous paragraph, all the samples have the absorption edge in UV range of light. The introduction of Au NPs on TiO₂-m_A changes the band gap towards visible spectrum, however it is not the case for other types of nanoparticles.

The peak of plasmon resonance of Au₃Cu₁ alloy and (Au₃)Cu₁ core-shell are very similar, while the peak of Au₁Cu₁ and Au₁Cu₃ switches to longer wavelengths with the increase of the amount of copper, presumably due to the formation of bigger particles compared to the bimetallic ones with high content of Au.

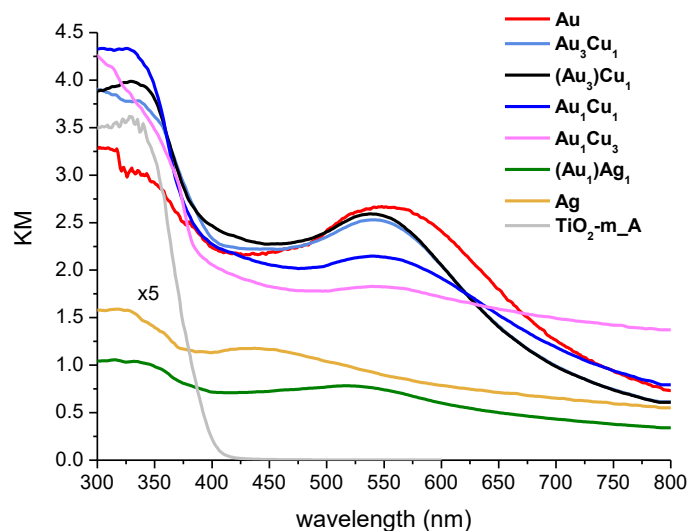


Figure 4.15. Kubelka-Munk (KM) spectra of Au, Au-Cu, Ag and Au-Ag NPs supported on TiO₂-m_A.

Table 4.3 shows that the size of bimetallic nanoparticles slightly increased compared to monometallic gold. The specific surface area of catalyst was investigated by BET measurement. The method utilized for deposition of NPs did not cause a significant change of the specific surface area

of support, indicating that the incipient wetness impregnation is fast, cheap and reliable method. On the contrary, higher content of copper in Au₁Cu₃/TiO₂-m_A catalyst lowered the specific surface area that could be explained by the presence of big copper or copper oxide nanoparticles that could block the surface of small 8 nm TiO₂-m_A particle.

Table 4.3. Characterization data obtained from XRD, DRS and BET measurements for TiO₂-m_A support and different metal nanoparticles supported on TiO₂-m_A.

Catalyst	TiO ₂ -m_A	Au	Au ₃ Cu ₁	(Au ₃)Cu ₁	Au ₁ Cu ₁	Au ₁ Cu ₃	Ag	(Au ₁)Ag ₁
S _{BET} (m ² /g)	130	130	108	109	103	28	108	109
d _{XRD} (nm)	8 ^a	4	6	7	-	-	10	6
E _g ^b (eV)	3.08	3.03	3.10	3.10	3.16	3.22	3.27	3.09

^a TiO₂ crystallites

^b determined from KM spectra

The results on activity of the prepared materials are shown in **Figure 4.16**. Au NPs lead to a lower conversion of HMF than support alone and supported gold-copper NPs, however the selectivity to desired products (DFF, HMFCFA, FFCA) is greater compared to other catalysts. Additionally, no unknown products from the degradation of HMF were observed for monometallic Au/TiO₂-m_A. Whereas, bimetallic Au₃Cu₁ alloy and core-shell as well as Au₁Cu₁ showed a high quantity of CO₂ and other unknown by-products, indicating that the reaction is quite unselective using copper as co-catalyst. Comparing the HMF conversion with bimetallic Au-Cu catalysts, it decreases with the increase of copper content and when this metal was used as a shell of nanoparticle. Besides, Au₁Cu₃ catalyst dramatically lowered HMF conversion, suggesting that the presence of copper inhibits overall HMF selective photo-oxidation process. This can be due to the damping of SPR property of Au NPs by copper or its surface oxides. Therefore, the role of SPR of Au is essential to drive the selective HMF photo-oxidation.

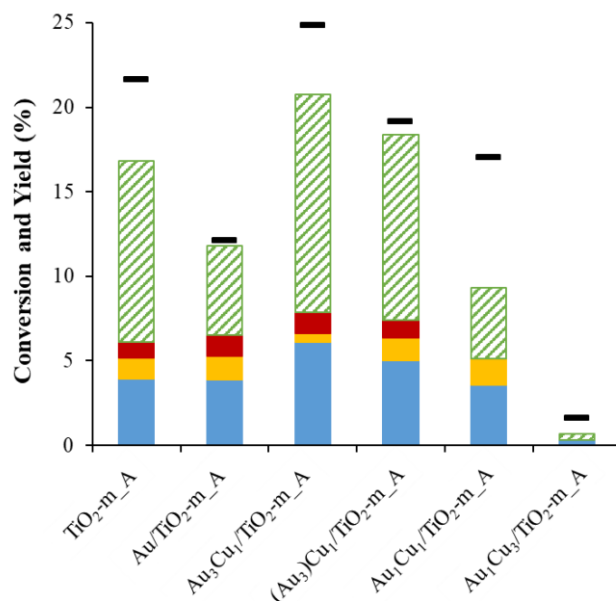


Figure 4.16. Photo-catalytic HMF oxidation and product distribution with metal-decorated TiO₂-m_A. Reaction conditions: 30°C; 0.5 mM aq. HMF; 1g/L catalyst; 1.5% wt. total metal NPs loading; O₂ 1 atm. Legend: HMF conversion (■), DFF yield (■), HMFCFA yield (■), FFCA yield (■), CO₂ yield (■).

In order to exploit the effect of other noble metals, which are able to generate a significant SPR response,^[170] and their combinational effect, monometallic Ag and (Au₁)Ag₁ core-shell nanoparticles were deposited on TiO₂-m_A.

Figure 4.15. compares KM of Ag-containing powders with the other samples. Silver nanoparticles have a peak of absorption around 420 nm granting them a yellowish color. This band is attributed to LSPR of Ag NPs.^[170] Relatively low intensity of Ag/TiO₂-m_A catalyst is explained by the dilution of this material with KBr (used as reference) due to the low amount of powder. Core-shell (Au)₁Ag₁ NPs have a wider LSPR response ranging from 450 to 650 nm due to the combined absorption of gold and silver nanoparticles.^[171]

The results on HMF photo-oxidation using these materials are shown in **Figure 4.17**. In contrast to monometallic Au/TiO₂-m_A, Ag and (Au₁)Ag₁ supported on TiO₂-m_A did not lead to FFCA after 1h. This is in agreement with the work of R. Schald and co-workers,^[172] who demonstrated that catalytic partial oxidation of HMF in basic aqueous media with Ag/TiO₂ catalyst results mainly in HMFCFA production and only some traces of FDCA were observed, while FFCA intermediate was not detected. While the group of J. An^[173] reported that Ag/ZrO₂ in basic aqueous media was not able to catalyze the further oxidation of HMFCFA to FFCA or FDCA. In addition, higher CO₂ selectivity was found for Ag-containing materials compared to monometallic Au/TiO₂-m_A.

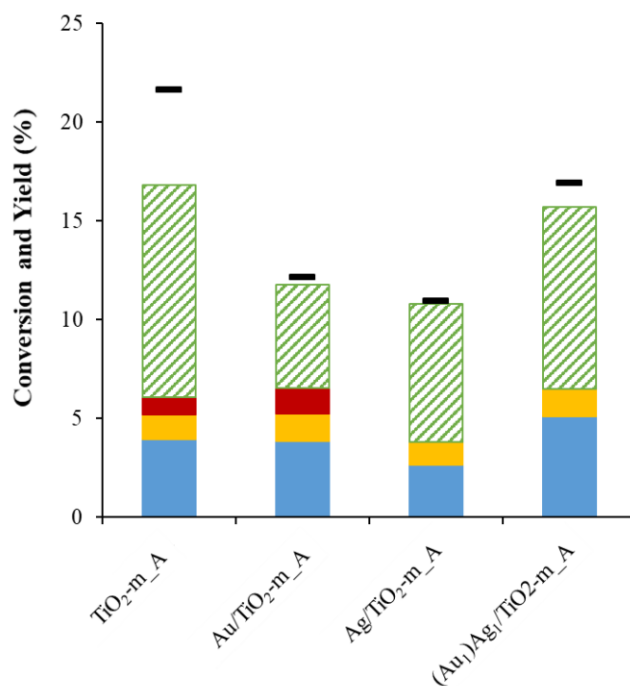


Figure 4.17. Photo-catalytic HMF oxidation and product distribution with metal-decorated TiO₂-m_A. Reaction conditions: 30°C; 0.5 mM aq. HMF; 1g/L catalyst; 1.5% wt. total metal NPs loading; O₂ 1 atm. Legend: HMF conversion (■), DFF yield (■), HMFCFA yield (■), FFCA yield (■), CO₂ yield (■).

The effect of type of irradiation (UV-visible and visible) was studied using Au/TiO₂-m_A catalyst. The reaction under visible light was performed applying long-pass wavelength filter, which blocks the light below 420 nm. Comparing the results illustrated in **Figure 4.18**, the reaction under visible light led to a lower HMF conversion, but higher selectivity of HMFCFA compared to reaction with the presence of UV part of light. Moreover, DFF was only produced under UV light. On the basis of observed results, it is possible to suggest that TiO₂ support activated by UV light favours DFF formation and the over-oxidation process.

Therefore, selective photo-oxidation of HMF over TiO₂-based catalyst is a combination of oxidizing capability of support and metal nanoparticle, pH, reaction time, the source of oxidation and irradiation.

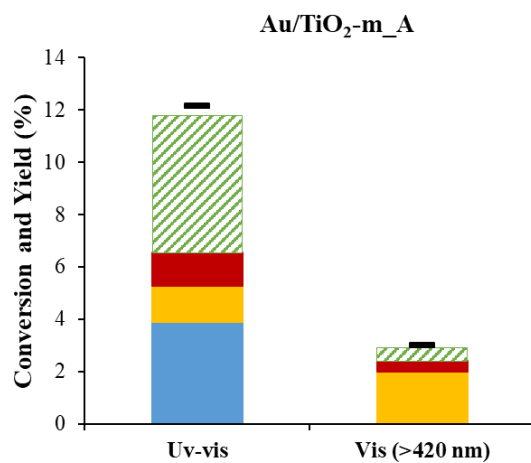


Figure 4.18. Effect of UV-visible and visible irradiation on photo-catalytic HMF oxidation and product distribution with Au/TiO₂-m_A. Reaction conditions: 30°C; 0.5 mM aq. HMF; 1g/L catalyst; 1.5% wt. Au NPs; O₂ 1 atm. Legend: HMF conversion (■), DFF yield (■), HMFCFA yield (■), FFCA yield (■), CO₂ yield (■).

Chapter 5. Glycerol photo-reforming

5.1. Experimental section

Paragraph 5.1 describes the methods utilized to deposit metal nanoparticles on the surface of TiO₂-m_A and commercial titania, DT-51 and P25. The synthesis of TiO₂-m_A was previously described in Chapter 3, section 3.1.1.2.1. Synthesis of Au, Au-Cu (core-shell and alloy nanoparticles) prepared by glucose reduction method and deposited over TiO₂ by incipient-wetness impregnation, and the procedure of Au deposition on TiO₂ by deposition-precipitation method were described in Chapter 4, section 4.1.1.2 and 4.1.1.3.

5.1.1. Synthesis and deposition of nanoparticles

5.1.1.1. Chemicals.

Commercial catalysts: P25 (TiO₂ P25 Degussa), DT-51 (TiO₂ DT-51 Millennium CrystalACTIV).

Metal precursors: Tetraammineplatinum(II) nitrate (99.99%, Alfa Aesar, Premion®) [Pt(NH₃)₄](NO₃)₂, Chloroplatinic acid hydrate (Sigma Aldrich) H₂PtCl₆·xH₂O, Ni(NO₃)₂ x6H₂O (99.9%, Alfa Aesar).

Commercial standards for HPLC calibration and NMR identification: glycerol (99.5% Alfa Aesar), formic acid (98%, Fluka), glyceraldehyde (90%, Sigma-Aldrich), glycolaldehyde dimer (Sigma-Aldrich), glycolic acid (98%, Alfa Aesar), dihydroxyacetone dimer (97%, Sigma-Aldrich).

5.1.1.2. Synthesis of Pt/TiO₂ by deposition-precipitation method.

This material was prepared using 0.001M solution of [Pt(NH₃)₄](NO₃)₂, adjusting pH 8 by adding dropwise a 0.1 M NaOH solution. Then solution of [Pt(NH₃)₄](NO₃)₂ was added dropwise to the titania suspension under vigorous stirring at room temperature, maintaining pH 8. Once the entire platinum solution was transferred to TiO₂ suspension, temperature was increased to 65°C. When the temperature reached the desired value, the stirring was kept for 2 h. The solid was then separated from the solution by centrifugation, washed several times with water, dried at 110°C overnight and calcined at 350°C for 3 h with a rate of 10°C/min in static air and sieved with 60-80 mesh. The Pt NPs were obtained by reduction with H₂/N₂ flow (100 ml/min, 10%) at 350°C for 3h (ramp 10°C/min). According to the type of support used, the resulted catalysts were denoted as Pt/TiO₂-m_A_DP, Pt/DT-51_DP and Pt/P25_DP.

5.1.1.3. Preparation of Pt/TiO₂ by incipient wetness impregnation.

The solution of H₂PtCl₆·xH₂O was loaded on the sample avoiding the complete wetting of the solid, following cycles of loading and drying in oven at 100°C. Finally, the powder was dried at 120°C overnight, calcined at 350°C for 3h (ramp 10°C/min) in static air and meshed 60-80. The Pt NPs were obtained by reduction with H₂/N₂ flow (100 ml/min, 10%) at 350°C for 3h (ramp 10°C/min).

According to the type of support used, the resulted catalysts were denoted as Pt/TiO₂-m_A, Pt/DT-51, and Pt/P25.

For the comparison, the oxides were loaded with metal NPs 1.5% by weight in both methods.

5.1.1.4. Preparation of NiO_x/TiO₂ by incipient wetness impregnation.

The aqueous solution of Ni(NO₃)₂ was impregnated on the powdered TiO₂ in the same way described in section 5.1.1.3. Powder was dried at 100°C overnight, calcined at 350°C for 12h (ramp 10°C/min) in static air. According to the type of support used, the resulted catalysts were denoted as NiO_x/TiO₂-m_A or NiO_x/DT-51. The oxide loading was 10% by weight for comparison with reported data.^[174]

5.1.2. Material characterization

The instruments used for XRD, DRS, N₂ physisorption, TEM are described in Chapter 3 and 4, sections 3.1.2.1, 3.1.2.2, 3.1.2.3, and 4.1.2.1, respectively.

5.1.2.1. Thermogravimetric analysis (TGA).

Thermogravimetric analysis (TGA) were carried out on a TA Instruments SDT Q600, in air atmosphere (flow rate: 100 ml/min) heating from 20°C to 600°C at 10°C/min. For this analysis, post-run catalysts were washed with 10-20 ml of water 1 time and dried at 50°C overnight. Fresh catalysts were analyzed without any pre-treatment. Around 5 mg of powder was taken for each measurement, a half of that was taken for used Pt/TiO₂-m_A_DP.

5.1.2.2. Temperature programmed desorption (TPD).

Temperature programmed desorption (TPD) analysis was carried out and described elsewhere.^[107] In brief, the analysis was performed on a Micromeritics Autochem II instrument equipped with TCD detector and mass analyzer (Cirrus II, MKS). In temperature programmed NH₃ desorption analysis, the sample was first pre-treated at 700°C for 45 min (ramp 10°C/min), then

cooled to 40°C in He atmosphere. The sample was flushed for 1 h at 100°C with a mixture of 10% NH₃ in He (30 cm³/min), then it was purged for 1 h with helium. Finally, desorption measurements were carried out up to 700°C with a ramp of 10°C/min with isotherm of 30 min.

5.1.2.3. Scanning Electron Microscopy (SEM).

SEM technique (Zeiss EP EVO 50; Carl Zeiss, Oberkochen, Germany) with different secondary electron detector (High Vacuum, ~10⁻⁴ Pa; Variable Pressure, 10-1000Pa; Environmental Pressure, <3000Pa) and back scattered electron detector (QBSD).

5.1.3. Test and product identification

5.1.3.1. Photocatalytic test.

Photo-reforming of glycerol was performed in a sealed top-irradiated glass photo-reactor illustrated in Chapter 4, **Figure 4.1**. If not differently indicated, prior the reaction, 7% by volume (1M), aqueous solution of glycerol with 0.5 g/L of catalyst were stirred for 20 min in the dark, while purging continuously N₂. Then, the sealed reactor was irradiated for 6 h using the solar simulator that consists of 300 W Xe-lamp delivering the light in the range of 250-2500 nm (irradiance of ~2 W was measured by radiometer HD2102.2 DELTA OHM equipped with two probes of 315-400 nm and 400-1050 nm). Samples were collected at the end of the reaction.

5.1.3.2. Identification and quantification methods.

After reaction, the samples were qualitatively analyzed by Electrospray Ionization Mass-spectrometry (ESI-MS) and Nuclear Magnetic Resonance (NMR) techniques for identification of the products.

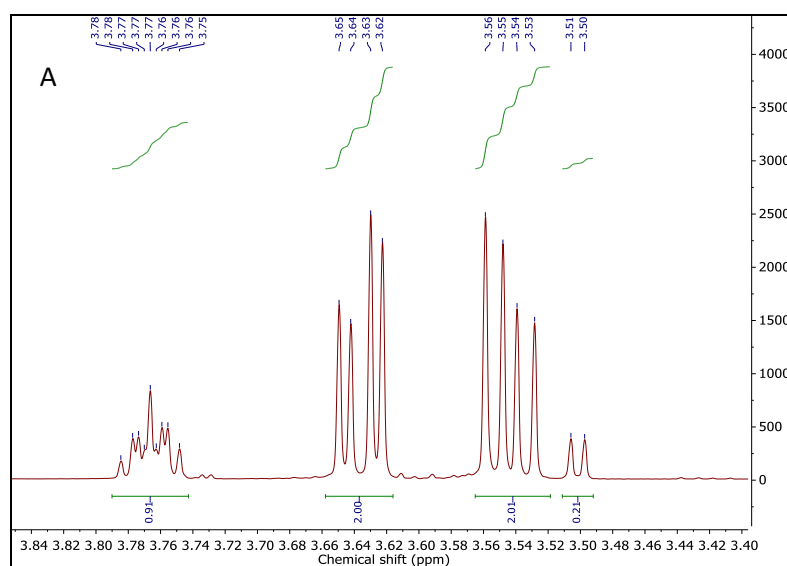
Waters micromass ZQ 4000 instrument with quadrupole mass analyzer was used to perform ESI-MS analysis. Normally, the aqueous product solution was diluted in methanol and injected without further derivatization. Positive ions conditions were 3.53 kV for the probe and 10 V for the cone, while for negative ions the probe voltage was 2.54 kV and 40 V for the cone with a 20 µL/min flux. Among the signals, in positive mode and negative mode were found the ionized species and attributed to the following molecules: glycerol [M+H]: 93, [M+Na]: 115, [M-H]: 91; glyceraldehyde [M-H]: 89; dihydroxyacetone [M-H]: 89; glycolaldehyde [M-H]: 59; acetic acid [M-H]: 59; formic acid [M-H]: 45. These results are presented in the **Table 5.1**.

Table 5.1. Possible products of glycerol photo-reforming found from ESI-MS analysis.

Positive scan ES+				
Name	Formula	MW (g/mol)	m/z	
			[M+H]	[M+Na]
<i>Glycerol</i>	C ₃ H ₈ O ₃	92.02	93	115
Negative scan ES-				
Name	Formula	MW (g/mol)	[M-H]	[M-Cl]
<i>Glycerol</i>	C ₃ H ₈ O ₃	92.02	91	-
<i>Glyceraldehyde</i>	C ₃ H ₆ O ₃	90.08	89	-
<i>Dihydroxyacetone</i>	C ₃ H ₆ O ₃	90.08	89	-
<i>Glycolaldehyde</i>	C ₂ H ₄ O ₂	60.05	59	-
<i>Acetic acid</i>	C ₂ H ₄ O ₂	60.05	59	-
<i>Formic acid</i>	CH ₂ O ₂	46.03	45	-

600 MHz ¹H NMR analysis was performed using Varian Inova (600 MHz for ¹H) equipped with an indirect triple resonance probe. The data treatment was done using a presaturation sequence (PRESAT, with power=4dB and presaturation delay 2s), while analyzing aqueous solutions (the residual H₂O signal δ 4.79 ppm). Since the molecules found by ESI-MS have quite low boiling point, water as a solvent of reaction was not removed. Thus, aqueous solutions of sample was diluted in D₂O in the ratio of sample:D₂O as 90:10 by volume. Obtained NMR spectra were compared to ones of commercial standards. The solutions were prepared taking ~5 mg of standard sample, diluting in ~0.7 ml of D₂O.

NMR resonance spectra are divided in 3 parts for easier understanding and shown in **Figure 5.1**.



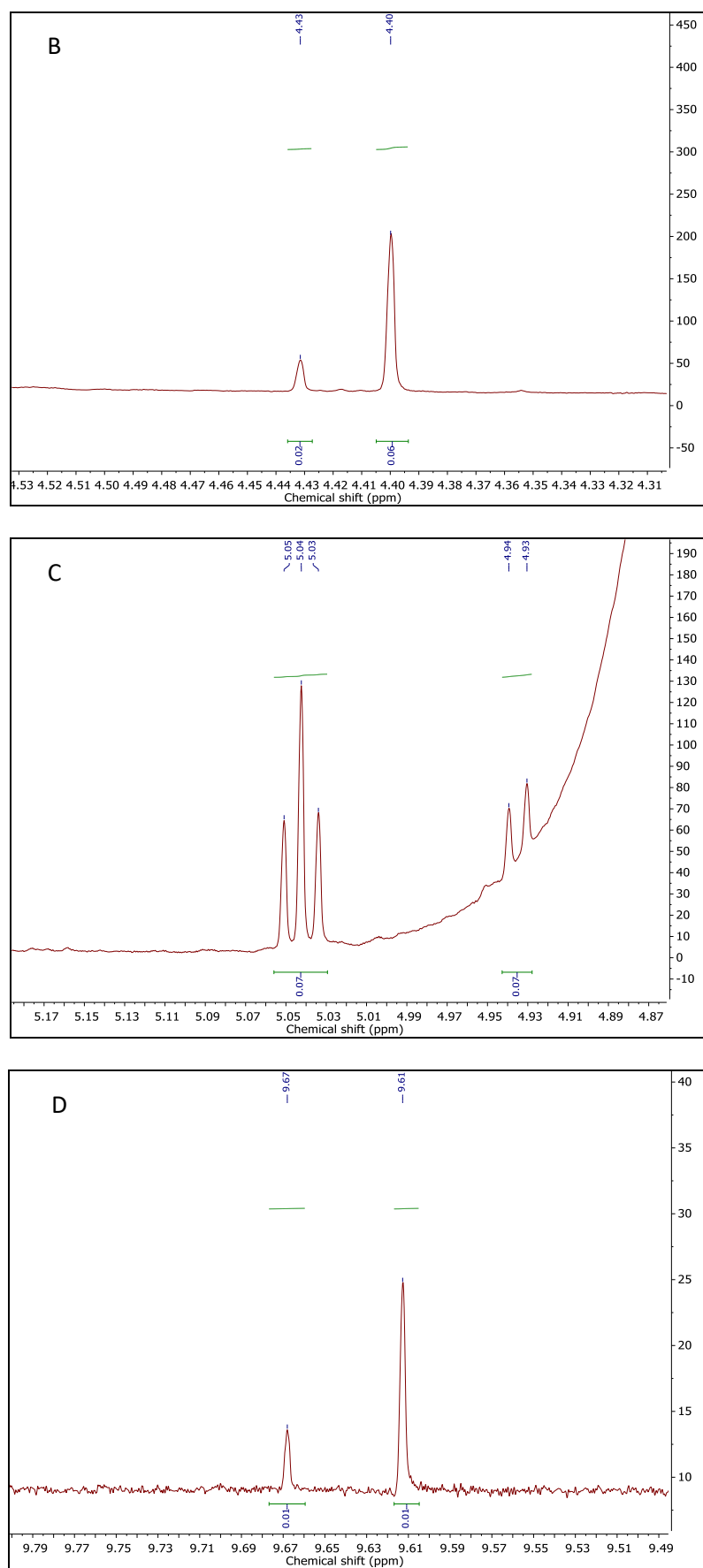


Figure 5.1. ^1H NMR spectrum (divided into 3 parts for easier reading) of reaction mixture in D_2O with a ratio of sample: D_2O as 90:10 by volume. Recorded at 25°C .

The resonance signals were observed at $\delta=3.55$ (dd, 2H), $\delta=3.64$ (dd, 2H), $\delta=3.77$ ppm (m, 1H) attributed to glycerol;^{[175],[176]} at $\delta=3.50$ (d, 2H), $\delta=5.04$ (t, 1H), $\delta=4.43$ (s, 2H), $\delta=9.61$ ppm (s, 1H) was found to be glycolaldehyde;^{[177],[178],[49]} glyceraldehyde in hydrated form showed signal at $\delta=4.94$ ppm (d, 1H), and in formyl form at $\delta=9.67$ ppm (s, 1H);^[49] dihydroxyacetone showed only one signal at $\delta=4.40$ ppm (s, 4H).^[49]

After the reaction, the liquid phase was filtered, diluted 100 times (from 1 M to 0.01 M) or used without dilution (in case of 0.05 M), and analyzed in an Agilent HPLC over Rezex ROA Organic Acid column (0.0025M H₂SO₄ eluent, oven temperature 30°C and 0.6 mL/min flux) with DAD and RID detectors. Aqueous solutions of commercial standards were used to calibrate the products by external method. The main issue associated with quantification of products in some cases was the separation of dihydroxyacetone and glycerol (**Figure 5.2**).

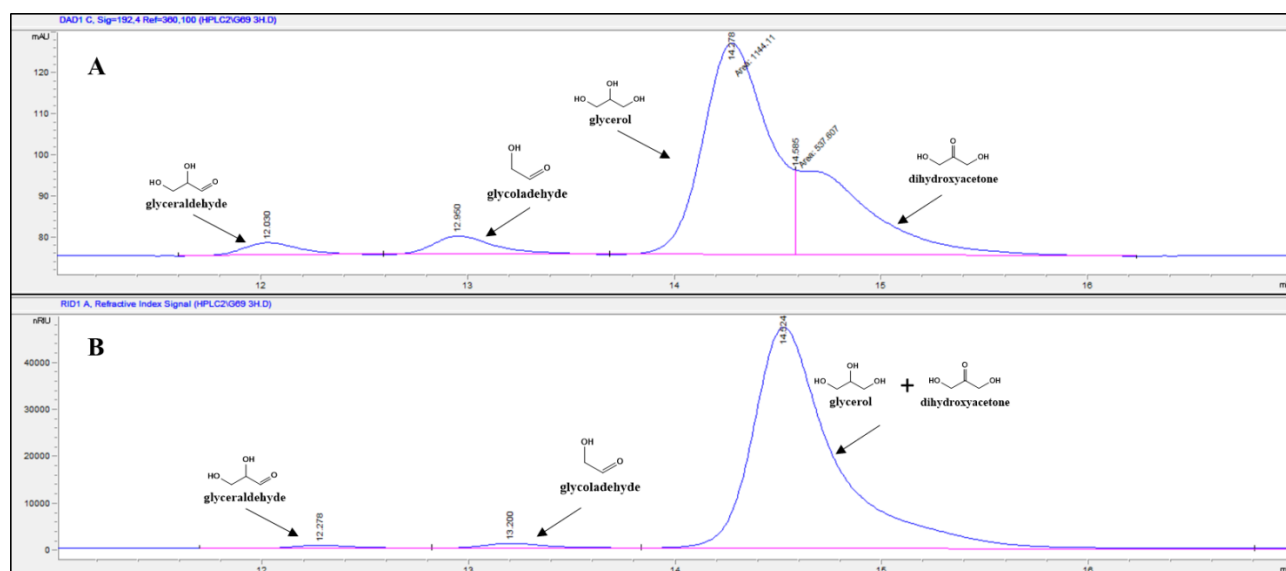


Figure 5.2. Chromatogram of the solution after reaction of glycerol photo-reforming. DAD signal at $\lambda=192$ nm (A) and RID signal (B).

Many different conditions were tried in attempt to separate these compounds, but their peaks were always reported to be overlapped.^{[179],[79]} Therefore, the following analytical solution has been proposed:

- (1). Calibration of DAD (at $\lambda=260$ nm, where glycerol is silent) and RID signals of dihydroxyacetone (DHA) and glycerol (GLY) in separated solutions;
- (2). When the mixture after reaction is being analyzed, the certain moles of DHA found from DAD signal (at 260 nm) can be related to the peak area in RID of this molecule according to the calibration curve recorded in (1);

(3). This peak area in RID found in (2) can be then subtracted from total peak area of glycerol and dihydroxyacetone in RID signal in order to find the moles of glycerol from calibration curve recorded in (1).

This approach delivers relative error less than 7% (**Figure 5.3**, right) for molar ratio of dihydroxyacetone to glycerol from 0.5 to 30%. Recording the total RID signal (total peak area) vs. real total moles of DHA and GLY in the mixture with different DHA/GLY molar ratio showed reasonable value of total peak area in RID (**Figure 5.3**, left), allowing us to use the proposed method in order to calculate final moles of glycerol in the mixture.

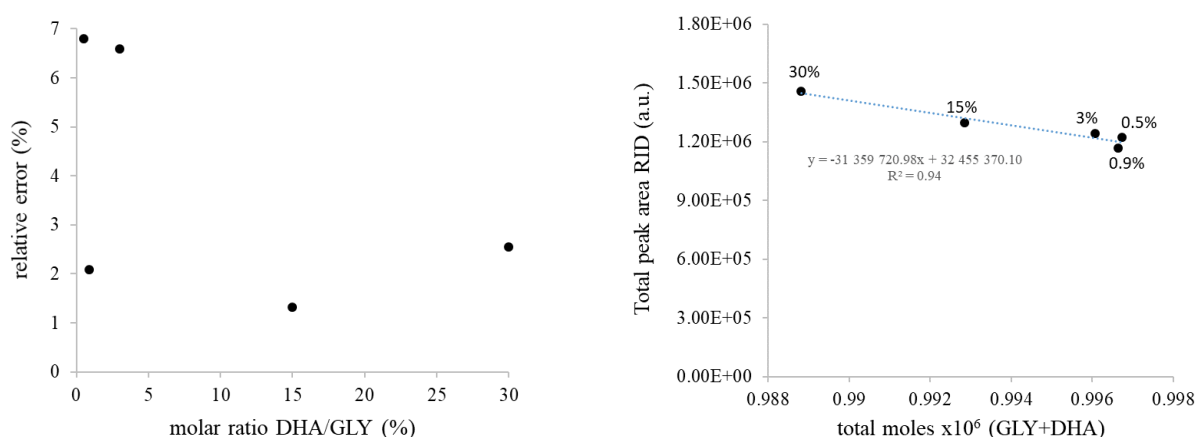


Figure 5.3. Right: Estimation of relative error as a function of molar ratio of dihydroxyacetone (DHA) and glycerol (GLY). Left: Total peak area vs. total moles with the corresponding dihydroxyacetone-to-glycerol molar ratio.

NMR spectra and HPLC chromatograms of products of glycerol photo-reforming reaction such as glycolaldehyde, dihydroxyacetone and formic acid were determined and compared with NMR spectra and HPLC chromatograms of standard solutions of these compounds.

Hydrogen was analyzed in off-line Agilent Technologies GC equipped with CP Molesieve 5A UM 25m x 0.53mm x 50 μ m column and TCD detector. The calibration was done using constant volume (1 ml) of gas-tight syringe with different molar fractions of H₂/N₂. The other gas phase products were analyzed off-line by Autosystem XL GC with CARBOXENE 1000 60-80 mesh column and flame ionization detector. The calibration was done injecting different volumes of the commercial mixture of gases with constant molar fraction.

In the experiments with the more diluted starting concentrations, the conversion of a substrate, e.g. glycerol (X %), yield (Y %) and selectivity (S %) of the products were calculated using the following equations:

$$X \% = \frac{n(\text{glycerol})_{in,mol} - n(\text{glycerol})_{fin,mol}}{n(\text{glycerol})_{in,mol}} \times 100\% \quad (\text{Eq. 5.1})$$

$$Y\% = \frac{n(\text{product}),\text{mol}\cdot\text{SF}}{n(\text{glycerol})_{\text{in},\text{mol}}} \times 100\% \quad (\text{Eq. 5.2})$$

$$S\% = \frac{n(\text{product}),\text{mol}\cdot\text{SF}}{n(\text{glycerol})_{\text{in},\text{mol}} - n(\text{glycerol})_{\text{fin},\text{mol}}} \times 100\% \quad (\text{Eq. 5.3})$$

While in the experiments with 7% by volume (1M) aqueous solution of glycerol the selectivity of products was calculated as:

$$S\%_0' = \frac{n(\text{product}),\text{mol}\cdot\text{SF}}{\sum n(\text{product}),\text{mol}\cdot\text{SF}} \times 100\% \quad (\text{Eq. 5.4})$$

where SF is the stoichiometry factor, which is equal to 1 for glyceraldehyde and dihydroxyacetone, 2/3 for glycolaldehyde, 1/3 for formic acid, CO, CO₂ and CH₄, and 1/4 for H₂.

5.2. Results and discussions

In paragraph 5.2. the main results obtained regarding the characterization of synthesized materials and their photo-catalytic activity in glycerol photo-reforming are presented and discussed.

5.2.1. Summary on material characterization

The XRD patterns of bare supports (P25, DT-51, TiO₂-m_A), presented already in **Figure 3.1**, have been previously studied and discussed in detail in Chapter 3, section 3.2.1.

XRD patterns of Pt containing materials prepared by the incipient wetness impregnation and deposition-precipitation methods with the reduction in hydrogen are shown in **Figure 5.4**. The XRD patterns of Pt-containing materials resemble the data obtained for pristine supports (**Figure 3.1**).

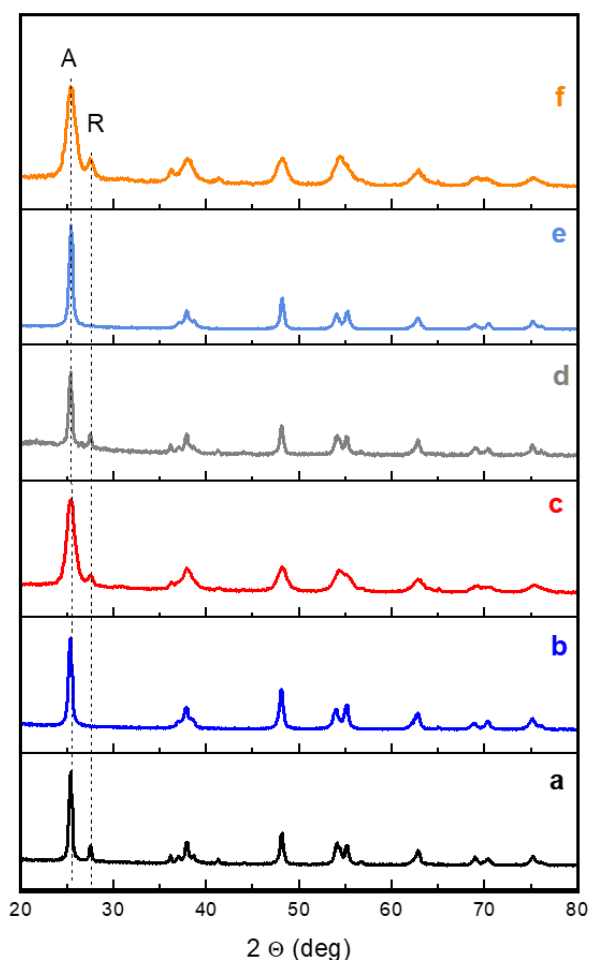


Figure 5.4. XRD patterns of Pt containing materials prepared by the incipient wetness impregnation and deposition-precipitation methods (DP). A: anatase (101), R: rutile (110). a) Pt/P25; b) Pt/DT-51; c) Pt/TiO₂-m_A; d) Pt/P25_DP; e) Pt/DT-51_DP; f) Pt/TiO₂-m_A_DP.

Thus, the deposition of Pt NPs and treatment of Pt-decorated materials do not affect the crystalline size of TiO₂ as well as the phase composition, keeping anatase as major phase with

reflections (101), (004), (200), (105) and (211) at 25.33, 37.82, 48.08, 53.93 and 55.12 2θ , respectively. The crystalline size was calculated by Sherrer formula (**Eq. 3.1**, see section 3.1.2.1) using the anatase (101) reflection. The value of crystalline size of prepared materials are shown in **Table 5.2**.

The XRD of NiO_x containing samples (**Figure 5.5**) showed the appearance of brookite metastable phase in $\text{NiO}_x/\text{TiO}_2\text{-m_A}$ sample with a diffraction peak at 30.7° .^[180] Another peak can be observed at 43.3° attributed to NiO .^[72] Crystalline size of NiO was determined by Scherrer equation (**Eq. 3.1**) and resulted in 4.7 nm for $\text{NiO}_x/\text{TiO}_2\text{-m_A}$ and 6.2 nm for $\text{NiO}_x/\text{DT-51}$ using NiO (200) reflection.

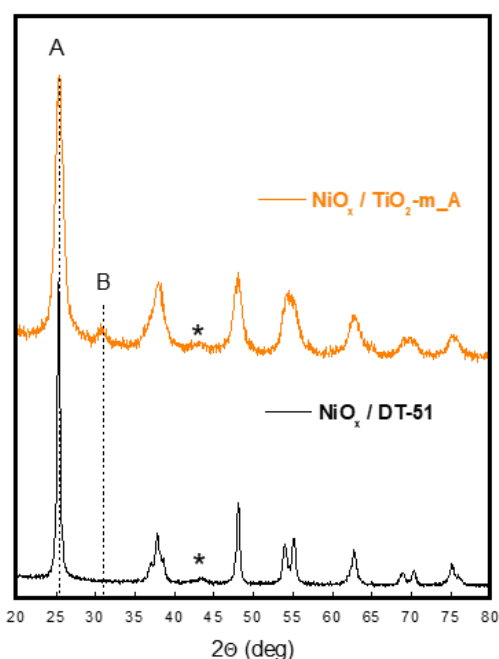


Figure 5.5. XRD patterns of $\text{NiO}_x/\text{TiO}_2\text{-m_A}$ and $\text{NiO}_x/\text{DT-51}$ prepared by incipient wetness impregnation (10% wt.). A: anatase, B: brookite, *: NiO .

Diffuse reflectance spectroscopy was used to calculate Kubelka-Munk (KM) function by equation described in Chapter 3 (**Eq. 3.3**). Considering the KM spectra of Pt-decorated samples demonstrated on **Figure 5.6**, a more pronounced increase of absorption intensity throughout visible and NIR region for $\text{Pt}/\text{TiO}_2\text{-m_A_DP}$ could be ascribed to the presence of PtO_x on the surface of $\text{TiO}_2\text{-m_A}$.^{[65],[181],[182]} However, an evidence from XPS measurements would be needed. On the other hand, such increase was explained by a large absorption cross sections of noble metal nanoparticles (Au, Pt, Ag) that generate intra- and interband transitions via 6sp and 5d band, producing hot electrons, which are then injected into conduction band of semiconductor occurring at the metal-

semiconductor interface. As a result, noble metal nanoparticles facilitate absorption and transfer of visible part of solar energy to semiconductor.^{[65],[156],[67]}

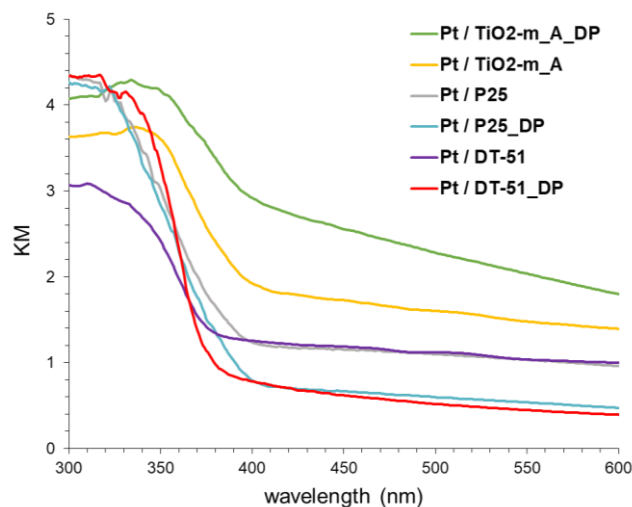


Figure 5.6. KM spectra of Pt containing P25, DT-51 and TiO₂-m_A prepared by incipient wetness impregnation and deposition-precipitation, followed by reduction in flow of H₂.

Regarding DRS results of NiO_x/TiO₂-m_A sample (**Figure 5.7**, left), a remarkable enhancement of visible light absorption could be noticed. This behavior has been explained previously by the d-d transition phenomenon of Ni²⁺ ions, which are responsible for a green color.^{[183],[184]} Whereas NiO_x/DT-51 sample was noted to be rather of a grayish color, therefore KM spectra showed no substantial change of light absorption edge by this photo-catalyst compared to bare support.

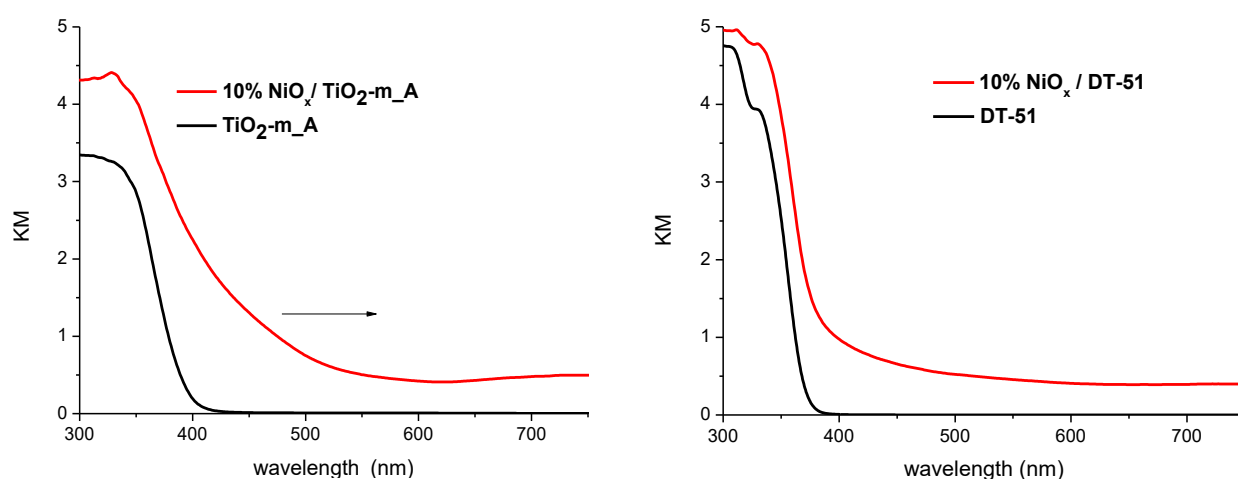
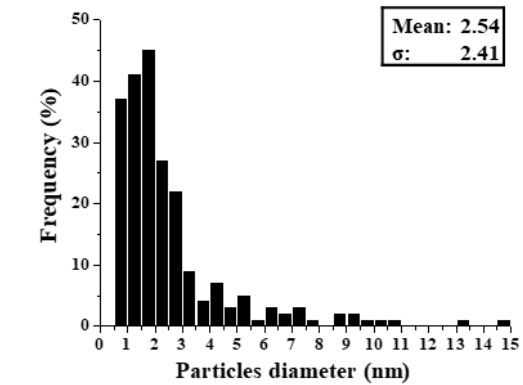
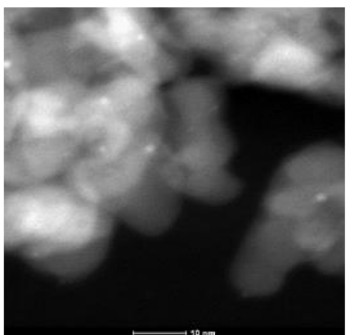
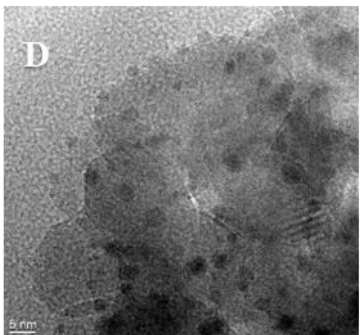
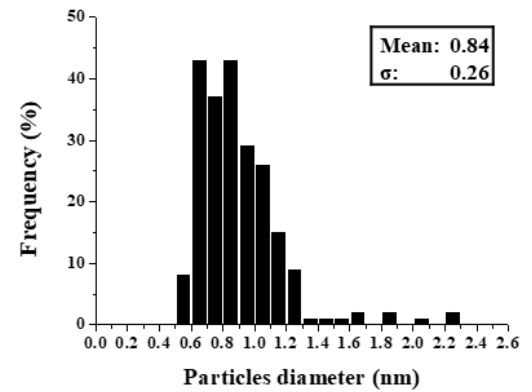
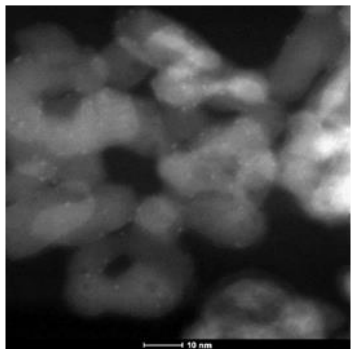
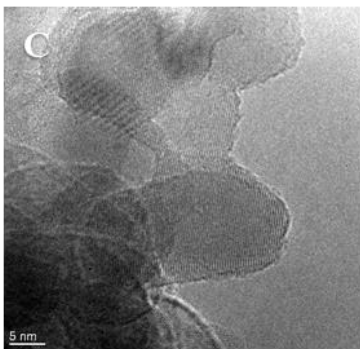
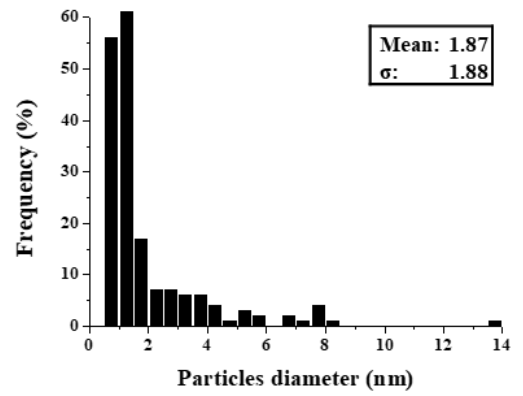
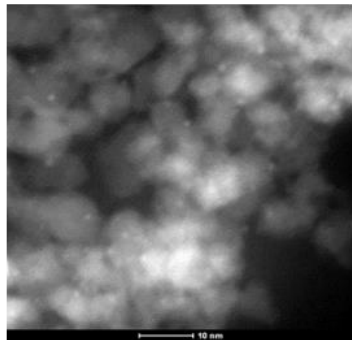
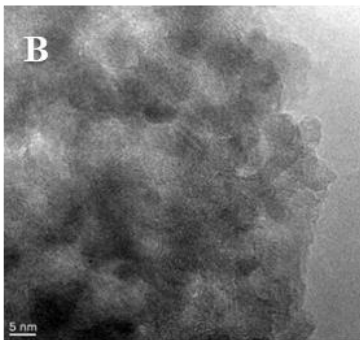
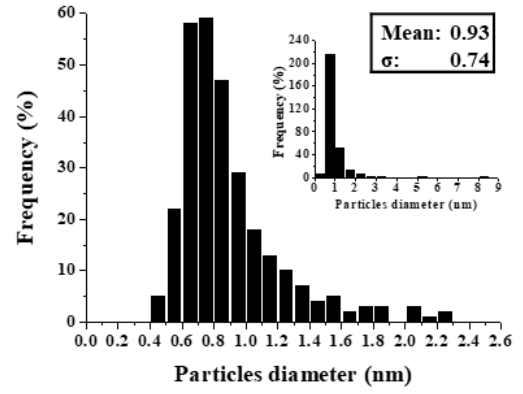
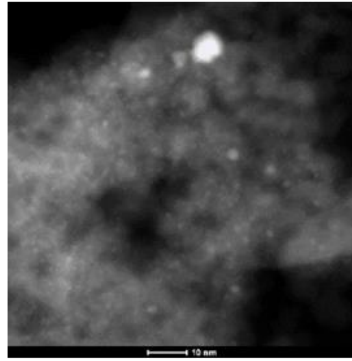
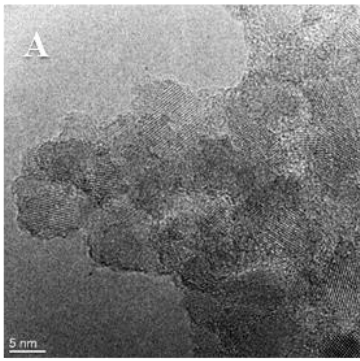


Figure 5.7. KM spectra of NiO_x containing TiO₂-m_A (left) and DT-51 (right) prepared by incipient wetness impregnation.

From KM spectra one can determine the value of energy bandgap (E_g) using **Eq. 3.2**. The values of E_g for NiO_x and Pt-containing materials are reported in **Table 5.2**.



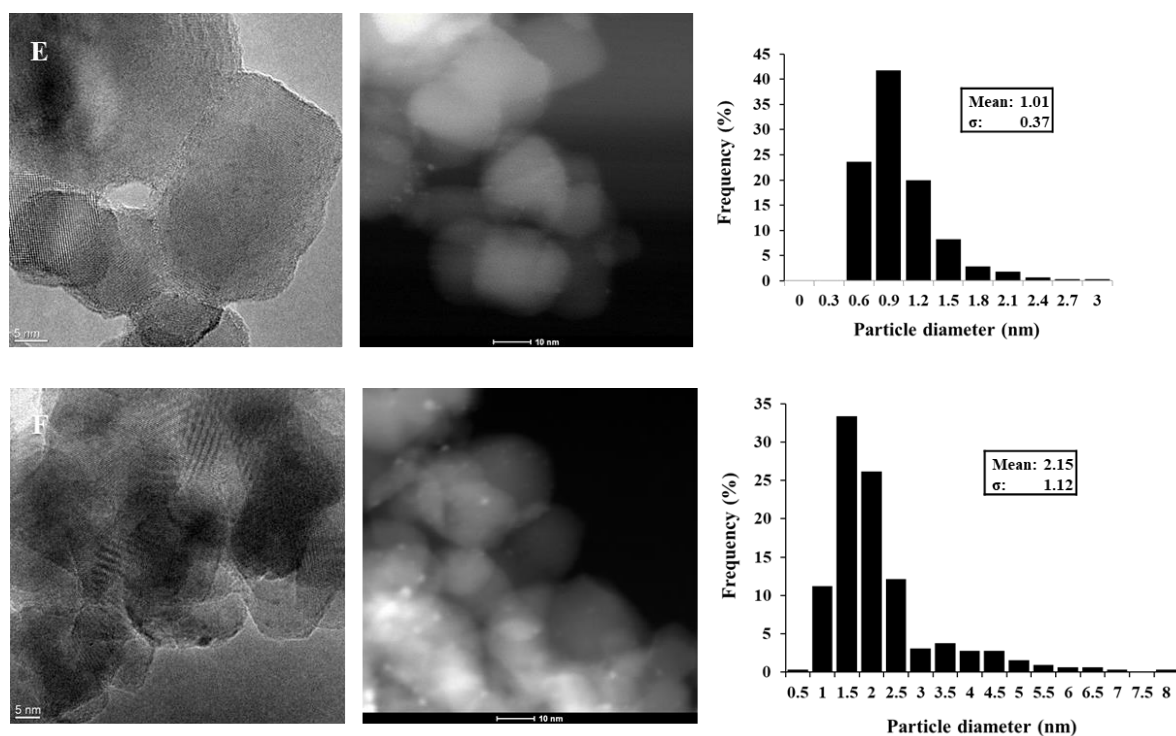


Figure 5.8. TEM images and particle size distribution: A) Pt/TiO₂-m_A_DP, B) Pt/TiO₂-m_A, C) Pt/DT-51_DP, D) Pt/DT-51, E). Pt/P25_DP, F). Pt/P25.

TEM images of Au NPs are presented in Chapter 4, **Figure 4.3**. The mean size of Au NPs is 2.4 and 2.1 nm for TiO₂-m_A and DT-51 supports, respectively. TEM micrographs and size distribution of Pt-decorated samples are shown in **Figure 5.8**. Between two methods, the deposition-precipitation gives access to smaller and homogeneously distributed Pt NPs than classical impregnation, although for both methods big platinum clusters (> 2 nm) could be observed. The mean particle size of Pt is shown in **Table 5.2**.

Table 5.2. Data obtained from DRS, XRD, N₂ physisorption and TEM measurements.

sample	E _g ^a (eV)	S _{BET} (m ² /g)	d ^b (nm)	d _{XRD} ^d (nm)
Pt/TiO ₂ -m_A_DP	3.11	128	0.9	7
Pt/TiO ₂ -m_A	3.11	121	1.9	8
Pt/DT-51_DP	3.28	62	0.8	21
Pt/DT-51	3.27	57	2.5	21
Pt/P25_DP	3.12	40	1.0	24
Pt/P25	3.10	50	2.2	23
NiO _x /TiO ₂ -m_A	2.31	106	5 ^c	8
NiO _x /DT-51	3.25	80	6 ^c	20

^a Energy bandgap estimated from KM spectra.

^b Mean size of Pt NPs determined from TEM.

^c Crystalline size of NiO determined from (200) reflection.

^d Crystalline size of TiO₂ determined from anatase (101) reflection.

5.2.2. Comparative study of different metal and metal oxide nanoparticles over TiO₂ supports

Preliminary tests were carried out to estimate the optimal amount of catalyst loading for maximum rate of hydrogen production per gram of catalyst loaded, which resulted in 0.5 g/L. Additionally, the light transmitted through the suspension of titania in water was measured in order to evaluate the degree of agglomeration/sedimentation of microemulsion-synthesized and commercial TiO₂ used for the reactions. It is worth to mention that in aqueous suspension under simulated solar light such phenomena as absorption, reflectance and scattering can occur. In this case by transmittance it is meant to be the detected light that passes through the suspension perpendicular to the probe. The measurement was performed by radiometer HD2102.2 DELTA OHM equipped with probe of 315-400 nm and using suspended catalyst in water in a beaker of a geometry similar to the used photo-reactor. **Figure 5.9** shows that the chosen concentration was 0.5 g/L. It means this concentration is the lowest one, at which all the particles are supposed to be irradiated while stirring. However, one can notice that three different types of titanium dioxide were responding differently. P25 showed dramatic decrease in transmittance already at 0.1 g/L loading, while at the same concentration, TiO₂-m_A demonstrated 87% of light detected by the probe, suggesting a higher degree of agglomeration/sedimentation by the synthesized powder.

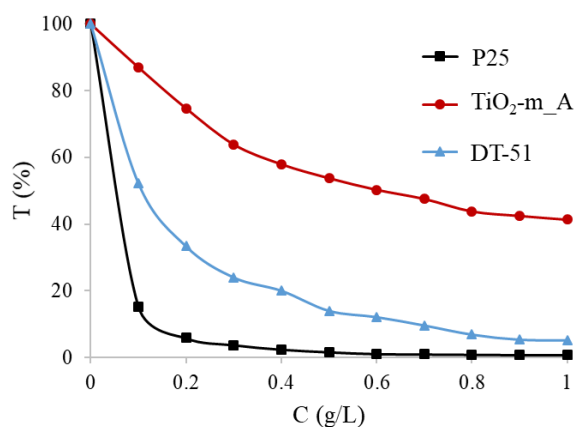


Figure 5.9. Transmittance recorded at different concentration of different types of TiO₂.

On the **Figure 5.10** (Insight), the screening test with only bare supports have revealed just a slight improvement of rate for commercial P25 under the same conditions applied. In the work of Waterhouse^[76] P25 exhibited superior activity compared to synthesized TiO₂ as well. The authors attributed the low rates observed for the synthesized TiO₂ supports to rapid electron-hole annihilation, and the lack of centers for H:H recombination or H⁺ reduction.

Introduction of a metal nanoparticle such as Pt, Au and AuCu on the surface of TiO₂ significantly enhances the rate of hydrogen production for all the types of TiO₂ as could be seen from **Figure 5.10**. This enhancement has been previously explained by experiments based on photoluminescence spectroscopy and was associated to the migration of photo-excited electrons from the conduction band of TiO₂ onto the supported metal nanoparticles, and therefore the decrease the rate in electron-hole recombination phenomena.^{[185],[76],[186],[64]}

The use of Pt, Au and AuCu metals permitted formation of detectable amount of liquid phase products such as glyceraldehyde and glycolaldehyde, which were the main compounds observed in these conditions. No activity was observed, when the reactions have undergone in the dark or when only the visible light (>420 nm) was used. Except hydrogen, among the gas phase products, CO₂, CO and CH₄ were detected.

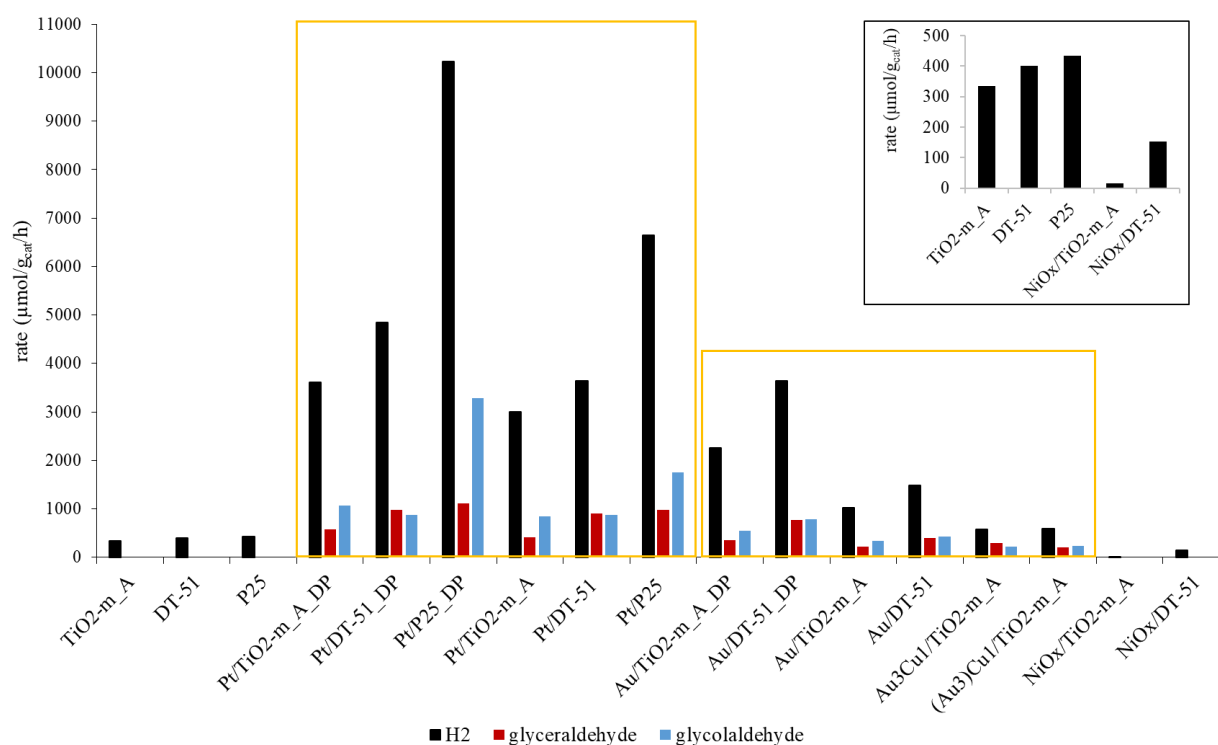


Figure 5.10. The rate of hydrogen production and liquid phase products for Pt, Au, (Au₃)Cu₁, Au₃Cu₁, NiO_x NPs supported on TiO₂-m_A, DT-51 and P25. 1M aqueous solution of glycerol (7% by volume); 30°C; 6 h. Reactions with NiO-supported catalysts were carried out for 3 h.

Comparing the two methods of Au NPs preparation, one can see that the catalysts synthesized by DP exhibit higher rates of hydrogen production, but also higher rates of liquid phase products compared to the impregnation of pre-formed Au NPs. In fact, Au NPs prepared by DP are smaller than that of impregnated samples (see Chapter 4, **Table 4.1** and **4.3**). The advantage of synthesized by DP small Au NPs with narrow particle size distribution, regardless the metal loading, was also pointed out previously.^[187] Furthermore, the highest rate of photo-catalytic hydrogen production from

ethanol in case of the lowest mean particle size of Au supported on titanate nanotubes was observed by the group of Waterhouse.^[186] Superior activity of smaller Au NPs can have two-fold explanation. Firstly, smaller particles owing its high surface area could effectively participate as cathode, reducing H^+ to H_2 . Secondly, the role of co-catalyst in photo-catalysis has been widely investigated,^{[64],[186],[188],[189]} elucidating the reason of suppressed electron-hole recombination by the fact that Au NPs create a rectifying Schottky contact on the surface of TiO_2 , thus trapping the electrons photo-excited into the conduction band of TiO_2 . Meanwhile the remained in the valence band hole efficiently participates in oxidation of organic substrates. Nevertheless, Au NPs supported on the homemade TiO_2 -m_A showed lower activity as compared to commercial DT-51, both for the rate of hydrogen as well as glyceraldehyde and glycolaldehyde formation, which can be assigned to the absorption of lower energy visible light by TiO_2 -m_A compared to DT-51, and faster electron-pair recombination due to the shorter energy band gap.

In attempt to improve the cost efficiency of the Au-containing catalyst, copper was considered in the Au_3Cu_1 alloy and $(Au)_3Cu_1$ core-shell imbedded into TiO_2 -m_A. The results for bimetallic NPs, shown in **Figure 5.10**, as well as the presence of SPR band in **Figure 4.13** confirm that copper in combination with gold can be used as plasmonic catalyst. However, the introduction of bimetallic NPs may lower the efficiency in electron-hole generation and separation^[83] and decreases surface area of catalyst (**Table 4.3**), inhibiting the overall glycerol photo-reforming. The charge recombination phenomena depend on metal oxidation state and loading, and metal-titania surface ratio, which could be found from XPS measurements. On the other hand, insignificant difference in activity between bimetallic Au_3Cu_1/TiO_2 -m_A and $(Au_3)Cu_1/TiO_2$ -m_A can be explained by their quite close values of specific surface area (**Table 4.3**).

Figure 5.10 also shows H_2 production rate for Pt catalysts supported on various types of titanium dioxide. The use of Pt NPs enhances hydrogen production significantly with respect to the data observed for Au NPs. This difference is due to the several of reasons. First of all, in the photo-reforming of 2-propanol, López-Tenllado et al.^[65] associated the higher activity of Pt NPs with its greater work function (Pt 5.7 eV > Au 5.3 eV)^[190] compared to Au NPs. Secondly, the presence of small Pt NPs suppresses the electron-hole recombination more effectively as compared to other metals.^[61]

As in the case of Au NPs, the Pt-containing catalysts prepared by deposition-precipitation method showed the best results of hydrogen production thanks to the well-dispersed small Pt NPs with a high surface area as could be seen in TEM images (**Figure 5.8**).

Similar trend as for the bare supports can be seen in case of addition of Pt NPs, where the highest H_2 generation is observed for commercial samples. Comparing literature reports on lab-synthesized TiO_2 , Pt/ TiO_2 -m_A_DP have a lower activity compared to those reported by the group

of $\text{Fu}^{[191]}$, where $6000 \mu\text{mol}$ of $\text{H}_2/\text{g}_{\text{cat}}/\text{h}$ was observed using 125 W high pressure Hg lamp for 1% wt. loading of Pt NPs over TiO_2 synthesized by sol-gel method (0.25 g/L). Edwards and co-workers^[192] reported lower value ($850 \mu\text{mol}/\text{g}_{\text{cat}}/\text{h}$) under irradiation by 300W Xe lamp over platinized (B, N)-codoped TiO_2 (1 g/L), where the authors prepared (B, N)-codoped TiO_2 by hydrothermal synthesis. There are many other reports regarding the results obtained for Pt supported on lab-synthesized TiO_2 , however even a slight difference in the reaction condition can lead to a different effect.

It has been reported that NiO on TiO_2 improves the hydrogen production from oxygenates photo-reforming process^{[193],[194],[195],[196],[184],[72],[174]} thanks to the presence of p-n junction between NiO (p-type semiconductor) and TiO_2 (n-type semiconductor), which reduces the energy of optical excitation and delay the undesired electron-hole recombination. For example, by Fujita et al.^[72] it has been shown that the photocatalytic H_2 production from aqueous solution of glycerol at 50°C is feasible with transition metal oxide as NiO impregnated over TiO_2 . Therefore, NiO was prepared by impregnation method on $\text{TiO}_2\text{-m_A}$ and DT-51. The results on **Figure 5.10** shows that type of support influences significantly the production of hydrogen when NiO is deposited, although it is anyway lower than of bare supports for both, DT-51 and $\text{TiO}_2\text{-m_A}$. Fujita et al.^[72] reported that higher loading than 2wt.% resulted in a drop of activity due to the decrease in the exposed surface area of TiO_2 that can be illuminated by light. Udine and co-workers^[195] examined the reason of decrease in activity with high loading of NiO, and suggested the importance of spatial arrangement of particles on each other during the preparation of nanocomposites. Excess of NiO tend to form spherical coverage, decreasing asymmetry around the particles and reducing vectorial charge carrier separation. Nevertheless, the loss of activity is more pronounced in case of $\text{NiO}_x/\text{TiO}_2\text{-m_A}$. The drop of activity may originate from the fact that NiO_x blocks the surface of small 8 nm crystallites of $\text{TiO}_2\text{-m_A}$. This can be further confirmed by the drop of specific surface area of this material compared to $\text{TiO}_2\text{-m_A}$ alone (**Table 5.2**), indicating that this method of nickel oxide nanoparticles deposition is not suitable. Regardless the green color owned by $\text{NiO}_x/\text{TiO}_2\text{-m_A}$, the reaction under visible light only ($> 420 \text{ nm}$) did not show any detectable trace of any gas. Therefore, the search for a more accurate method of deposition would require as well as optimization of NiO loading. Another promising approach towards enhancement of hydrogen production rates is Ni-species reduction to form metallic Ni^0 that plays role of a cathode for proton reduction to evolve hydrogen as was reported recently by several research groups.^{[183],[184],[196]}

Figure 5.11 (left and right) shows higher rate of CO_2 for Pt/P25, since it is known to be one of the most active photo-catalysts in reaction of organics decomposition, where CO_2 is the final product of oxidation. Glycerol is rapidly oxidized by the hole over Pt/P25 to glyceraldehyde and glycolaldehyde, which is then oxidized to CO_2 via aliphatic intermediates. High rates of CO_2 were observed also for Pt NPs supported on DT-51, whereas Pt/ $\text{TiO}_2\text{-m_A}$ exhibited milder oxidation of

glycerol, indicating a more selective behavior towards valuable products. Indeed, selectivity of carbon-based products in liquid and gas phases (**Figure 5.11**, left) confirm the fact that both commercial TiO₂ supports (P25 and DT-51) demonstrate greater photocatalytic performance compared to the synthesized TiO₂-m_A support in terms of hydrogen production rate, but lower selectivity toward liquid-phase products. Lower hydrogen selectivity for the commercial samples (**Figure 5.11**, right) may be attributed to its participation in some side reactions. This is also seen in the difference between theoretical and experimental hydrogen yield (**Figure 5.12**). Theoretical yield of hydrogen was calculated by **Eq. 5.5**:

$$n(H_2), mol = \frac{7 \times n(CO_2), mol}{3} + n(\text{glyceraldehyde}), mol + n(\text{glycolaldehyde}), mol \quad (\text{Eq. 5.5})$$

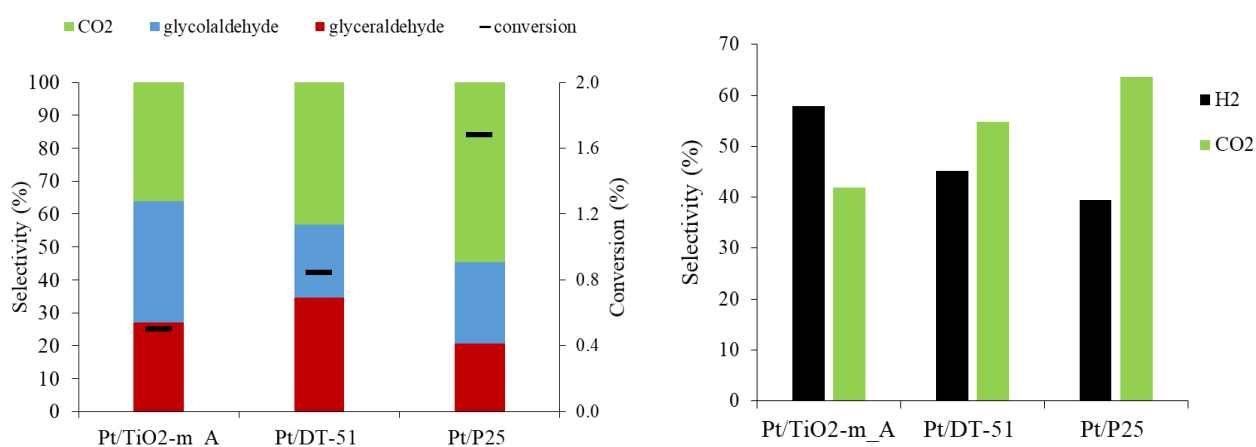


Figure 5.11. Left: Selectivity of carbon-based products: glyceraldehyde, glycolaldehyde and CO₂, and glycerol conversion. Right: gas phase product selectivity. Pt NPs supported on TiO₂-m_A, DT-51 and P25. 1M aqueous solution of glycerol (7% by volume); 30°C; 6 h.

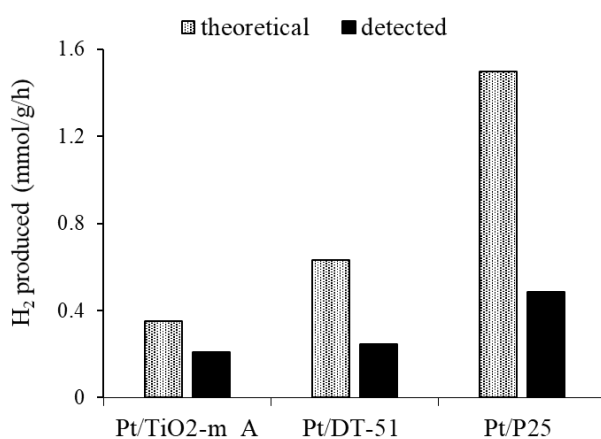


Figure 5.12. Theoretical and experimental yield of hydrogen.

5.2.3. Photo-reforming of glycerol over Pt-based catalysts

5.2.3.1. Glycerol conversion as a function of time.

The study of the effect of the reaction time proceeded with a more diluted starting concentration of glycerol 0.05 M, keeping the amount of catalyst loading 0.5 g/L. The dependency of selectivity of the products from glycerol conversion using Pt/TiO₂-m_A_DP and Pt/DT-51_DP are presented in **Figure 5.13**. The primary products of the reaction for DT-51 support are glyceraldehyde, dihydroxyacetone in liquid phase and CO₂ in gas phase. Then, glycolaldehyde appears as a secondary product with the consumption of both, glyceraldehyde and dihydroxyacetone. Regarding TiO₂-m_A support, glycolaldehyde can be seen already as a primary product together with glyceraldehyde and dihydroxyacetone in liquid phase and CO₂ in gas phase. From this study, the following conclusion can be drawn: both Pt/TiO₂-m_A_DP and Pt/DT-51_DP have the same kinetic profile, yielding glyceraldehyde, glycolaldehyde, dihydroxyacetone and CO₂ as products of glycerol photo-reforming, but the induction period for synthesized TiO₂-m support can be noticed, for which the conversion of glycerol is slower than for DT-51 one, suggesting that catalyst based on commercial DT-51 is a more photo-active material.

Regarding the hydrogen production (**Figure 5.14**), the rates observed for a more diluted glycerol solution over Pt/DT-51_DP are twice higher than that over Pt/TiO₂-m_A_DP, which confirms higher activity of DT-51 support in overall photo-reforming of glycerol.

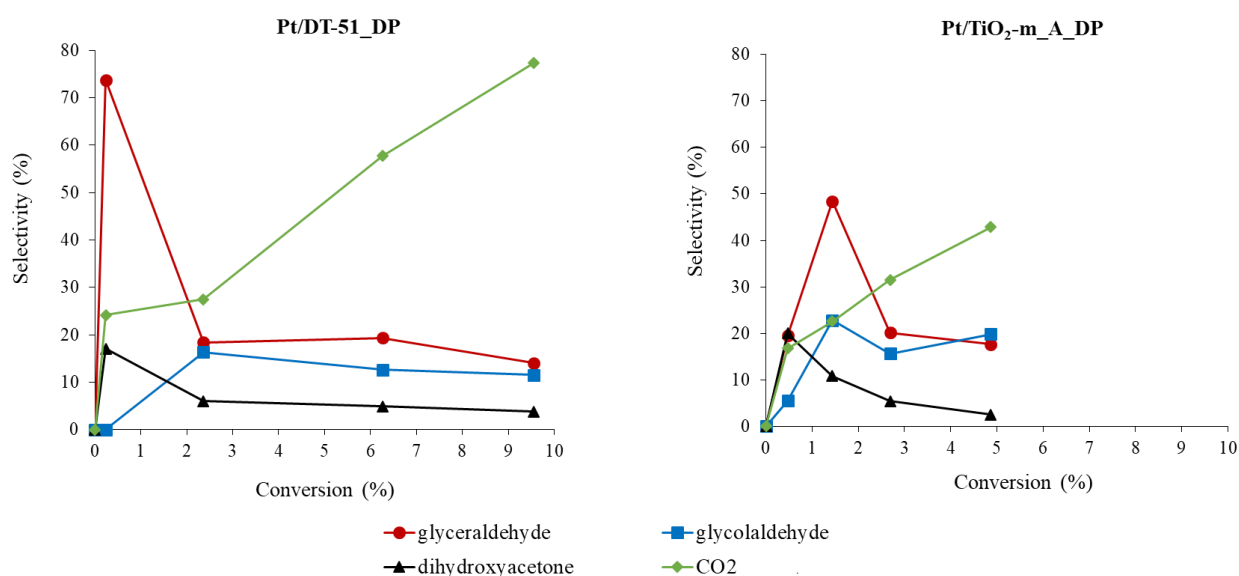


Figure 5.13. Left: Overall selectivity in the products of interest as a function of the conversion of glycerol for Pt/DT-51_DP (left) and Pt/TiO₂-m_A_DP (right) prepared by deposition-precipitation method. 0.05 M aqueous solution of glycerol; 30°C.

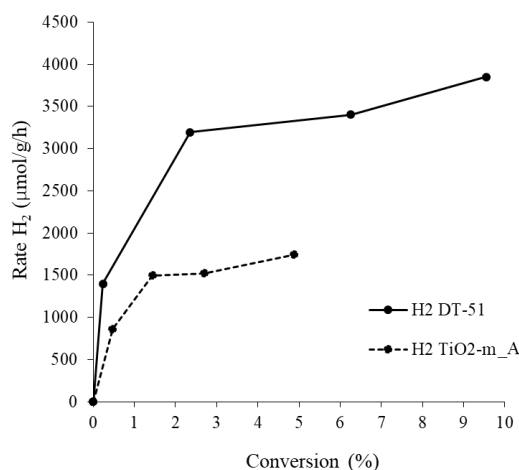


Figure 5.14. Rate of H₂ production with Pt/DT-51_DP and Pt/TiO₂-m_A_DP. 0.05 M aqueous solution of glycerol; 30°C.

With the aim to better understand the difference in activity and possible poisoning/deactivation phenomena, thermal analysis (TGA) has been done (**Figure 5.15**). For fresh samples the first weight loss associated with an endothermic peak around 100°C is due to the water adsorbed on the catalyst. The loss of water is slightly greater for TiO₂-m-based catalyst probably due to the higher specific surface area. The absence of any other peaks indicate that the surface of fresh catalysts is free from organic residues after the synthesis. Regarding the used catalysts, first exothermic peak is appeared around 190-237°C, attributed to organics oxidation, which are the adsorbed glycerol and/or the intermediates of reaction. Comparing these two TGA profiles, the first notice is the temperature of oxidation for Pt/TiO₂-m_A_DP, which is lower than that of Pt/DT-51_DP. Secondly, the weight loss for the second peak is slightly greater for Pt/TiO₂-m_A_DP than for Pt/DT-51_DP materials. Such behavior could originate from the different strength of acid sites of TiO₂-m_A and DT-51 resulting in a different strength of glycerol adsorption and/or intermediates, or the presence of different reaction pathways on the surface of two catalysts, even though HPLC provided the same nature of liquid phase products. As a matter of fact, ammonia temperature programmed desorption (TPD) analysis showed that microemulsion-made TiO₂ is characterized by higher acid site density than the values of commercially available DT-51 (denoted as TiO₂-comm): 0.59 and 0.40 mmol/g, correspondingly. Such behavior can be explained by the relatively high surface area.^[97] The desorption curves, reported in **Figure 5.16** are centered in the range 150-650°C showing for both the supports a convolution of Lewis acid sites (exposed Tiⁿ⁺ cation) of different strength. Copeland et al.^[197] investigated acid sites by differential IR absorption of pyridine on TiO₂ after 200°C desorption, demonstrating absence of Brønsted acid sites (surface-bound hydroxyl group, Ti-OH) of TiO₂. Similar observation has been reported also by Nakajima and co-workers^[104] in their FTIR study on pyridine-adsorbed TiO₂. At temperatures above 450°C, the water and CO₂ release was

detected for both the sample by mass analysis, confirming higher NH_3 adsorption per unit of sample for the microemulsion support.

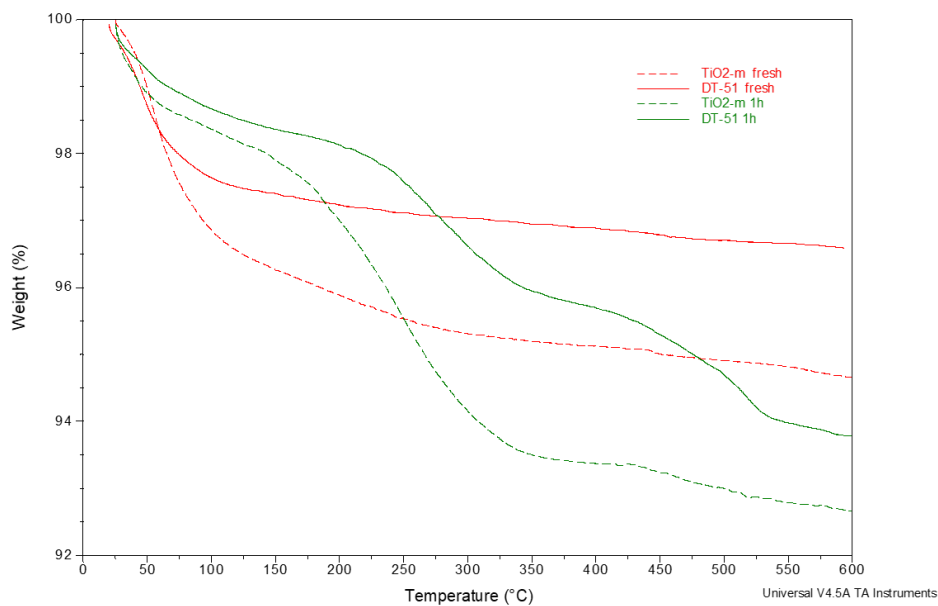


Figure 5.15. TGA results of fresh (red) and post-run (green) catalysts after 1 h reaction on Pt/TiO₂-m_A_DP (dashed line) and Pt/DT-51_DP (solid line).

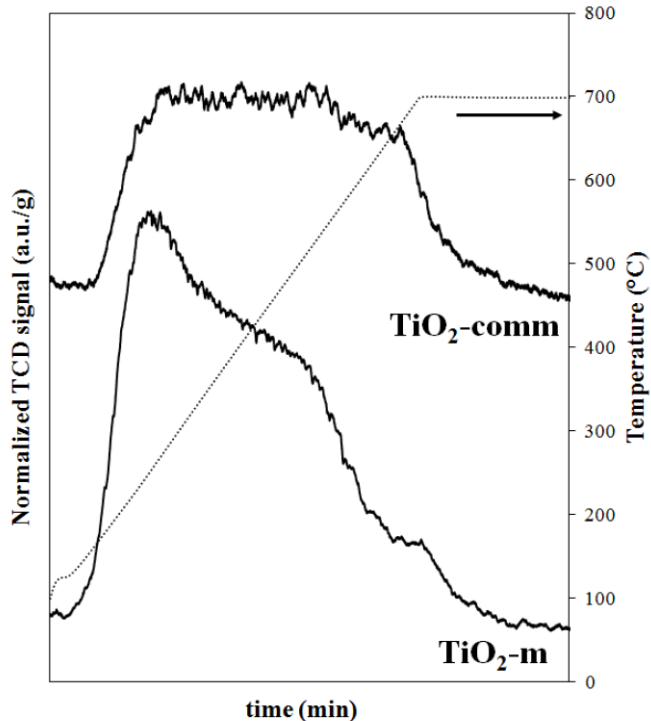


Figure 5.16. NH_3 temperature programmed desorption analysis. Reprinted from PhD thesis of E. Lombardi^[107].

5.2.3.2. Effect of phase composition.

The influence of crystalline phase was considered as an affecting parameter in many studies of photocatalytic hydrogen production from polyols.^[190] For instance, L. Chiarello et al.^[198] reported anatase and brookite polymorphs to be more active under UV irradiation and produced higher amount of hydrogen from methanol-water vapours than rutile. Under irradiation > 400 nm rutile was still active, producing hydrogen, whereas anatase and brookite were inactive at this wavelength of light. In the work of W. Chen and co-workers^[64] Au/P25 demonstrated superior activity followed by pure anatase \approx brookite and finally, rutile, towards H₂ in different alcohol-water mixtures due to the anatase-rutile heterojunction, which decrease the rate of charge recombination.

In this frame, microemulsion method allows preparing samples with different phase composition such as anatase (> 90%) and rutile (> 90%). The XRD patterns and RAMAN spectra of the synthesized catalysts are shown in **Figure 3.1** and **Figure 3.2**. The optical properties are shown in **Figures 3.4, 3.5, 3.6**. The advantage of this method is that rutile phase can be obtained with small crystallite size of 11 nm, hereinafter noted as TiO₂-m_R.

When only supports were tested, **Figure 5.17** demonstrate slightly improved hydrogen rate for TiO₂-m_R, although no liquid phase products were observed at a detectable extent. The enhancement of hydrogen production over Pt/TiO₂-m_R_DP catalyst is even more evident compared to support alone, reaching the value comparable to Pt/DT-51_DP, which is 4667 and 4847 $\mu\text{mol}/\text{g}_{\text{cat}}/\text{h}$, respectively. Analysis of liquid phase showed remarkably higher rates of glycolaldehyde formation for rutile-enriched samples.

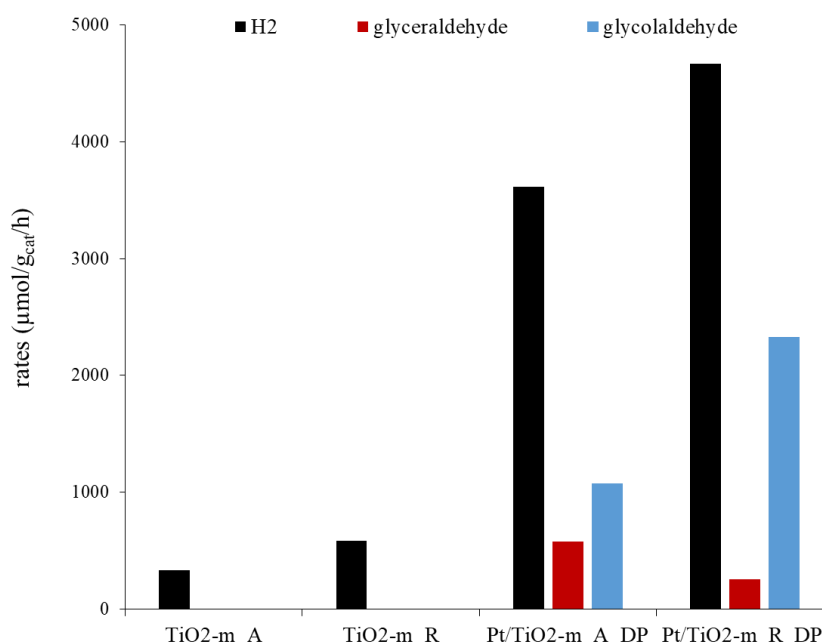


Figure 5.17. The rate of hydrogen production and the products for bare TiO₂-m_A and TiO₂-m_R and corresponding platinumized samples prepared. 1M aqueous solution of glycerol (7% by volume); 0.5 g/L catalyst loading; 30°C; 6 h.

Comparing these results shown in **Figure 5.17** to screening tests shown in **Figure 5.10**, one can notice that P25 and TiO₂-m_R based catalysts demonstrated higher production rates of glycolaldehyde, while DT-51 based ones showed higher productivity to glyceraldehyde. This is in agreement with the calculated values of selectivity using these supports, shown in **Table 5.3**. This difference might be due to the different phase composition of used supports.

Table 5.3. Selectivity of glyceraldehyde and glycolaldehyde with Pt-supported catalysts on different types of titania using deposition-precipitation (DP) method.

Catalyst	DT-51_DP	P25_DP	TiO ₂ -m_A_DP	TiO ₂ -m_R_DP
S (glyceraldehyde), %	63	34	45	14
S (glycolaldehyde), %	37	66	55	86

Similar results were reported by Chong et al., where catalyst composed by rutile phase with {110} facet showed the best selectivity (up to 96%) towards glycolaldehyde. The formation of peroxo species Ti-O-O-Ti that was formed preferentially on rutile {110} and responsible for oxidation of glycerol and glucose was confirmed by EPR and theoretical calculations.^{[199],[200]} Similar behavior of selective C-C cleavage was observed by the group of M. Bellardita and co-workers^[201] on lab synthesized rutile with and without Pt NPs during the glucose photo-reforming. Authors suggested the presence of peroxo species on rutile being beneficial for milder glucose oxidation than anatase that is known to produce in water highly reactive and surface mobile ·OH radicals leading to over-oxidation of organic molecules.

5.2.3.3. Reaction with glyceraldehyde and dihydroxyacetone as intermediate products of glycerol photo-reforming.

In order to elucidate deeper the reason of difference in terms of activity of Pt/TiO₂-m_A_DP and Pt/DT-51_DP and the mechanistic insights behind, the reactions of photo-reforming of glyceraldehyde as intermediate of glycerol photo-reforming was undertaken. In **Figure 5.18** the conversion of glyceraldehyde and products selectivity and yield over Pt/TiO₂-m_DP and Pt/DT-51_DP are presented. Comparison of supports (microemulsion and commercial) gives similar results on photo-reforming of glyceraldehyde in terms of conversion. However, the yield and selectivity to glycolaldehyde are greater for microemulsion support than for commercial one. This further confirms the idea that the presence of rutile has a substantial effect on glycolaldehyde selectivity. In addition, more than 70% of some other by-products, including CO₂, were noticed for commercial support. Interestingly, dihydroxyacetone was observed among the products of glyceraldehyde photo-reforming using Pt/DT-51_DP. This could be explained by the fact that in aqueous medium these

trioses are in fast isomerization equilibrium,^{[202],[203],[204],[205],[206]} that in fact take place via an acid-catalyzed hydride shift, via a base-catalyzed mechanism with a proton shift (and intermediate enol), or via a concerted proton-coupled hydride shift in neutral media.^{[207],[208]}

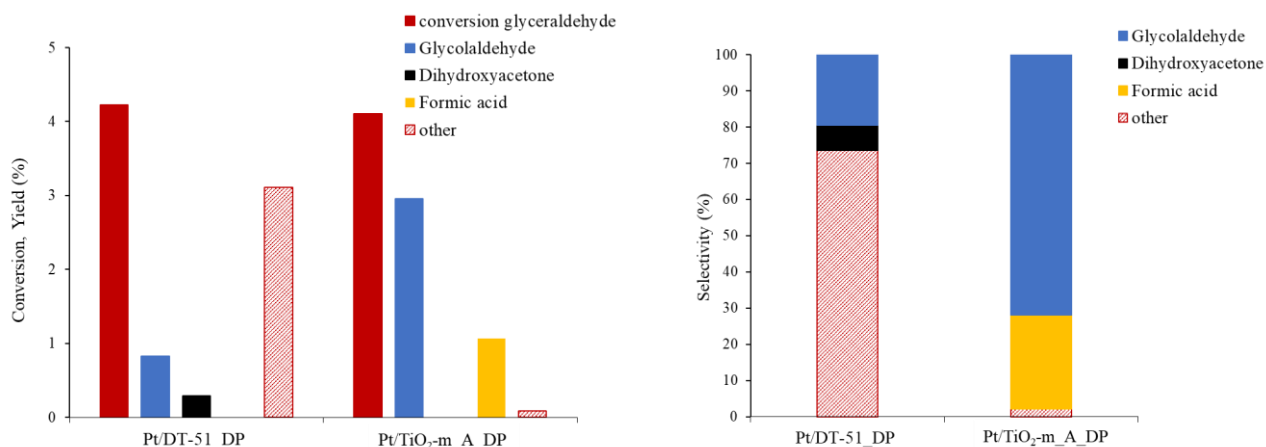


Figure 5.18. Left: Conversion of glycerol and yield of products of interest on different types of Pt-supported titania. Right: Selectivity of products of glycerol photo-reforming. 0.05 M aqueous solution of glycerol; 0.5 g/L catalyst, 30°C, 3 h.

In case of 0.05 M dihydroxyacetone aqueous photo-reforming, within 3 hours of reaction both catalysts demonstrated a very low activity. NMR spectra of products were not possible to analyze due to a high degree of dilution, so that except starting material no other resonance signals were detected. On the other hand, HPLC results showed signal that possibly could be attributed to glycolic acid, comparing the retention time of sample with the ones of commercial standard solutions. Additionally, ESI-MS analysis demonstrated signals with 45, 59, 75 and 89 m/z in negative mode that supports the presence of glycolic acid (76 g/mole) and dihydroxyacetone (90 g/mole), but also some other lower molecular mass aliphatic intermediates.

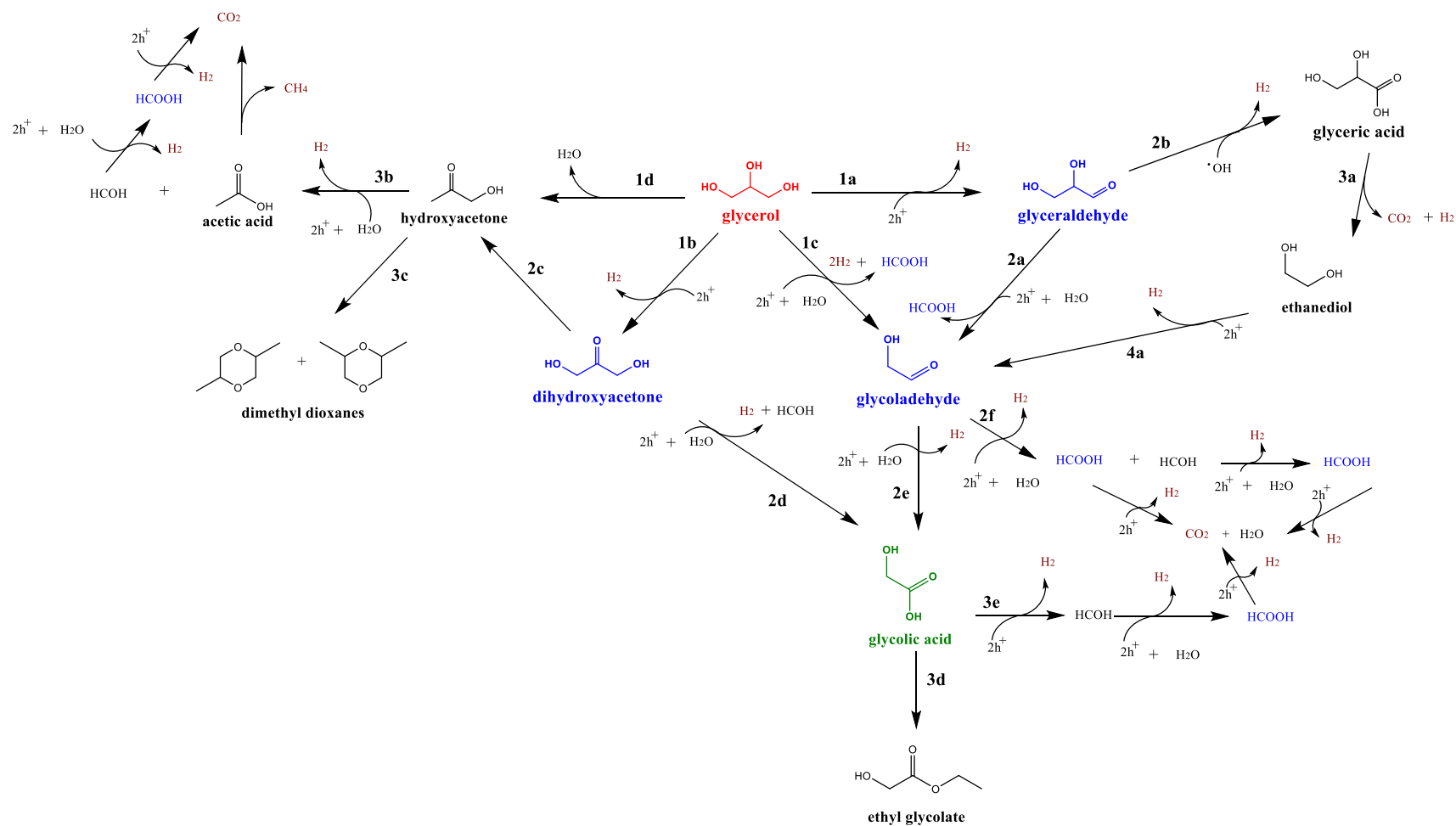
Taking into account experimental data and literature reported mechanisms over glycerol aqueous phase reforming^{[209],[51]} and photo-reforming,^{[49],[210],[5],[211]} it is possible to suggest the scheme of glycerol photo-reforming under study, which is depicted in **Figure 5.19**.

Firstly, in the step **1a** the formation of glycerol as one of the primary products take place via indirect mechanism described by K. Sanwald and co-workers.^[49] In principle, the photo-generated holes are trapped by lattice oxygen sites in TiO₂, abstracting the H-atom from C-H bond with subsequent formation of carbonyl group. One molecule of hydrogen is produced concurrently at a cathodic site. Further oxidation of glycerol can yield glycolaldehyde and formic acid as indicated in **2a**. On the other hand, the group of T. Montini^[211] suggested oxidation of glycerol to glyceric acid (**2b**) by hydroxyl radical. The latter undergo decarboxylation (**3a**) to form ethandiol

with a further oxidation to form glycolaldehyde (**4a**). In the step **1b** another C₃ species, dihydroxyacetone, is generated via two electron oxidation of secondary carbon atom of glycerol. Among the other primary products, glycolaldehyde and formic acid are formed following step **1c**, suggesting the presence of a direct mechanism of C-C cleavage. The group of C. Minero^[80] in the work of glycerol photo-oxidation over commercial titania-based catalysts have described a mechanism that consists of a hole transfer to a chemisorbed glycerol on coordinatively unsaturated Ti(IV)-OH site to generate an alkoxide radical followed by β-C-C-scission. On the other hand, dehydration of glycerol to form hydroxyacetone (**1d**) was reported by K. Sanwald and co-workers.^[49] However, T. Montini et al.^[211] suggested the formation of hydroxyacetone from dihydroxyacetone (**2c**) with subsequent formation of dimethyl dioxanes (**3c**). Alternatively, in the step **3b** hydroxyacetone undergo C-C cleavage to form acetic acid and formaldehyde with subsequent degradation of these molecules to CO₂ as proposed by the group of K. Sanwald.^[49]

Further transformation of dihydroxyacetone or/and glycolaldehyde can yield glycolic acid (detected in HPLC and MS) via step **2d** or/and **2e**, respectively. R. Chong et al.^[199] and Sanwald et al.^[49] observed oxidation of glycolaldehyde (**2f**), yielding formic acid, formaldehyde, H₂ and CO₂. Degradation of glycolic acid (**3e**) up to CO₂ and H₂O was observed by Sanwald et al.^[49] Nonetheless, T. Montini et al.^[211] suggested further transformation of glycolic acid to ethyl glycolate as demonstrated in step **3d**. However, in this study such intermediates as formaldehyde, hydroxyacetone, acetaldehyde, acetic acid or other products shown in **Figure 5.19** indicated in black color have not been observed, suggesting their fast transformation to formic acid or decomposition to CO₂ in such conditions.

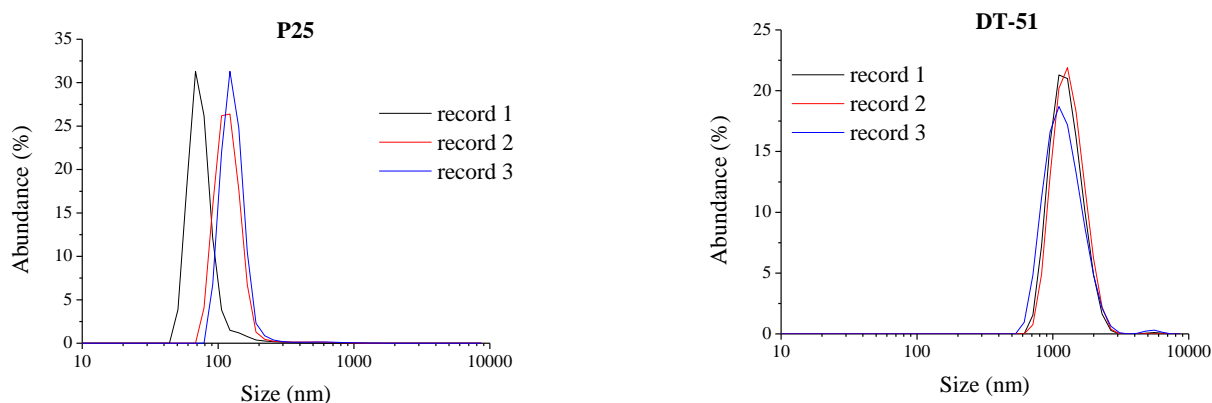
As a matter of fact, T. Montini and co-workers^[211] have shown a complexity of glycerol photo-reforming on Cu/TiO₂ under simulated solar light, meaning the production of multiple intermediates and different rates of their formation. A rapid formation and consumption of intermediates often prevents their identification. For instance, carboxylic moieties tend to bound to the catalyst surfaces, whereas aldehydes and alcohols more likely to desorb into the liquid phase.



5.2.4. Effect of catalyst morphology

The term *hydrodynamic diameter* considers the apparent size of the dynamic hydrated/solvated particle. The effect of hydrodynamic diameter has revealed the great importance on quantum efficiency once the powder is suspended in the water medium.^{[212],[97]} Hydrodynamic diameter could be an indicative of TiO₂ aggregation degree. As reported, smaller aggregates promote higher number of exposed crystals that favour light absorption and reactant access in suspension.^[213] With the aim to evaluate the influence of hydrodynamic particle size on the activity of the different supports, DLS analysis has been done.

Preliminary results of DLS analysis, shown in **Figure 5.20**, have presented significant smaller mean particle size for P25 than for TiO₂-m_A and DT-51, although it is not constant from record to record for P25 and TiO₂-m_A, indicating inhomogeneous particle size. From this comparison one can conclude that not only physico-chemical properties of semiconductors are responsible for their activity as widely accepted, such as the energy bandgap, specific surface area and crystalline size, but also hydrodynamic diameter has to be considered to govern effectively photo-catalytic reactions. Additionally, SEM images of P25, DT-51 and TiO₂-m_A on **Figure 5.21** showed differences in microstructure. The commercial DT-51 has homogeneously distributed small, round-shape particles, while the particles of P25 has a very porous, sponge-like form. The synthesized TiO₂-m_A consists of small, but highly aggregated particles. Comparison of apparent density (the mass of catalyst per unit of volume) of these three types of materials presented in **Table 5.4** indicates also smaller apparent density for P25 owing the most porous morphology, while TiO₂-m_A has the greatest apparent density that is confirming an importance of porosity of catalyst.



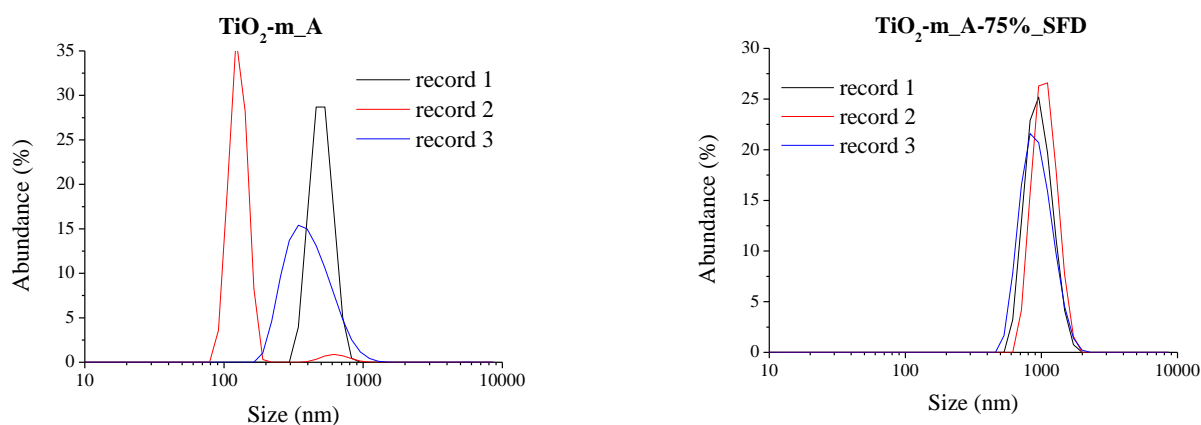


Figure 5.20. Hydrodynamic particle size distribution for P25, DT-51, TiO₂-m_A and TiO₂-m_A-75%_SFD measured at 25°C. Catalyst concentration is 0.25 g/L.

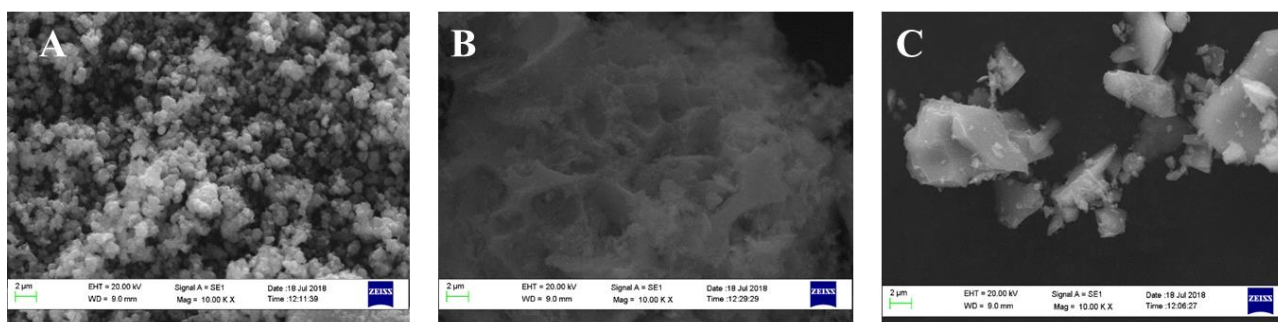


Figure 5.21. SEM micrographs of A) DT-51, B) P25 and C) TiO₂-m_A.

Therefore, in order to reduce the detrimental effect of synthesized TiO₂ aggregation phenomenon on photocatalytic activity in aqueous environment, TiO₂-m_A paste after the synthesis was subjected to Spray-Freeze Drying (SFD) process. This process is described in Chapter 3, Section 3.1.1.4.

The final calcined powder without post-treatment resulted in mixed phases of 75% anatase and 25% rutile as shown in XRD presented in **Figure 3.1**. This sample was denoted as TiO₂-m_A-75%. The same composition was kept for the post-treated material by Spray-Freeze Drying technique even after calcination step. This sample was designated as TiO₂-m_A-75%_SFD.

The resulted powder after SFD technique was having a very porous microstructure without any detectable agglomerates regardless the calcination treatment at 400°C as could be seen in SEM images (**Figure 5.22**).

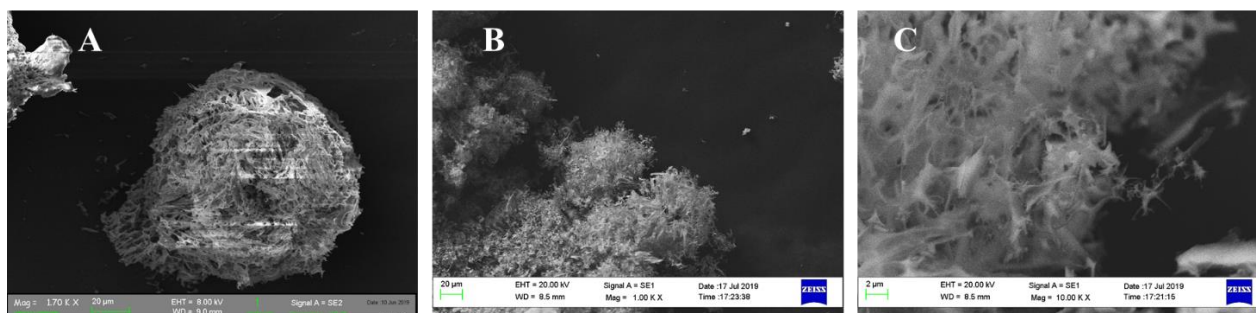


Figure 5.22. SEM micrographs of A) TiO₂-m_A-75%_SFD non calcined, B) and C) TiO₂-m_A-75%_SFD calcined.

Results of DLS analysis presented on **Figure 5.20** shows substantial change in particles size distribution for TiO₂-m_A-75%_SFD sample. The post-treatment resulted in mono-modal distribution of about 1 μm size of particles in aqueous suspension. The analysis of apparent density (**Table 5.4**) points out that porous microstructure makes catalyst less dense, even if hydrodynamic diameter of a catalyst is large.

Table 5.4. Data collected from transmittance measurements (T%) and estimation of apparent density (d). Catalyst concentration used for transmittance is 0.25 g/L.

catalyst	T%	S _{BET} (m ² /g)	d (g/cm ³)
P25	4	49	0.10
DT-51	25	80	0.28
TiO ₂ -m_R	46	50	0.57
TiO ₂ -m_A	70	130	0.86
TiO ₂ -m_A-75%	67	140	0.91
TiO ₂ -m_A-75%_SFD	25	124	0.09

Measurements of light transmittance at a concentration of powder 0.25 g/L are presented in **Table 5.4** and compared to apparent density of catalysts. First thing to note is an evident trend of an increase of light transmittance with an increase of apparent density. A substantial decrease of light transmittance could be noticed for post-treated catalyst, TiO₂-m_A-75%_SFD, compared to untreated ones, TiO₂-m_A and TiO₂-m_A-75%, emphasizing the importance of porous morphology of material for efficient light absorption process inside the pores. The macro-mesoporous structure of photocatalysts has been recently attained a great interest in the field of heterogeneous photo-catalysis.

As it was highlighted by R. Fiorenza and co-workers,^[214] highly exposed surface provided by the pores with intrinsic connectivity allows efficacious charge transfer and reactants mass flow.

Comparing the activity of these materials on hydrogen production from glycerol photo-reforming (**Figure 5.23**), the highest rate of hydrogen production was observed over TiO₂-m_A-75%_SFD, having a low apparent density and well-developed porous structure. Taking into account the fact that TiO₂-m_A-75%_SFD has a mixture of polymorphs, a test has been carried out with TiO₂-m_A-75%, which is the material without SFD process applied and which has the same ratio of anatase and rutile phases, to exclude the contribution of heterojunction effect.

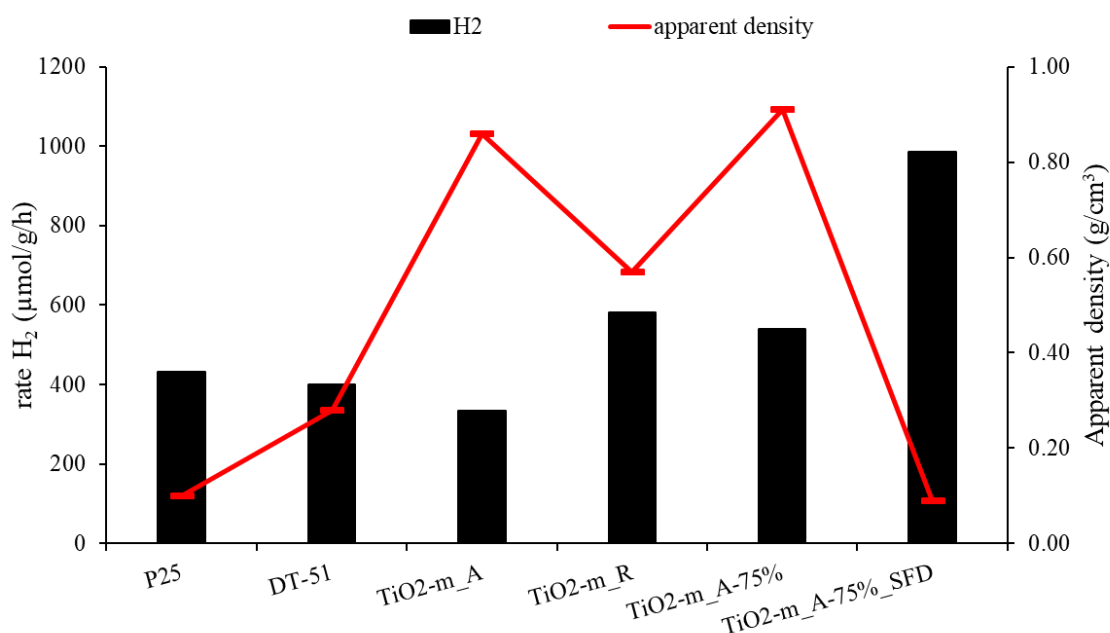


Figure 5.23. The rate of H₂ production and apparent density of different types of TiO₂.

Indeed, the rate of hydrogen production was lower for the material without SFD post-treatment, but higher than the rates of anatase-rich material, TiO₂-m_A, pointing out the importance of both, porosity of semiconductor and the presence of anatase-rutile heterojunction. The improved results of hydrogen productivity using TiO₂-m_A-75%_SFD catalyst was twice as high than commercial benchmark P25 that could be attributed to greater specific surface area of TiO₂-m_A-75%_SFD compared to P25.

Therefore, the comparison of intrinsic activity was done normalizing the results by the specific surface area of the catalysts. On the **Figure 5.24** one can notice that both TiO₂-m_A-75%_SFD and P25 have comparable results since these catalysts have similar macroporous structure and the phase composition. Whereas the greatest result was demonstrated by TiO₂-m_R. Elevated rates of hydrogen production from glucose photo-reforming on rutile-based photo-catalysts were also reported by the groups of M. Bellardita^[201] and R. Chong.^[200]

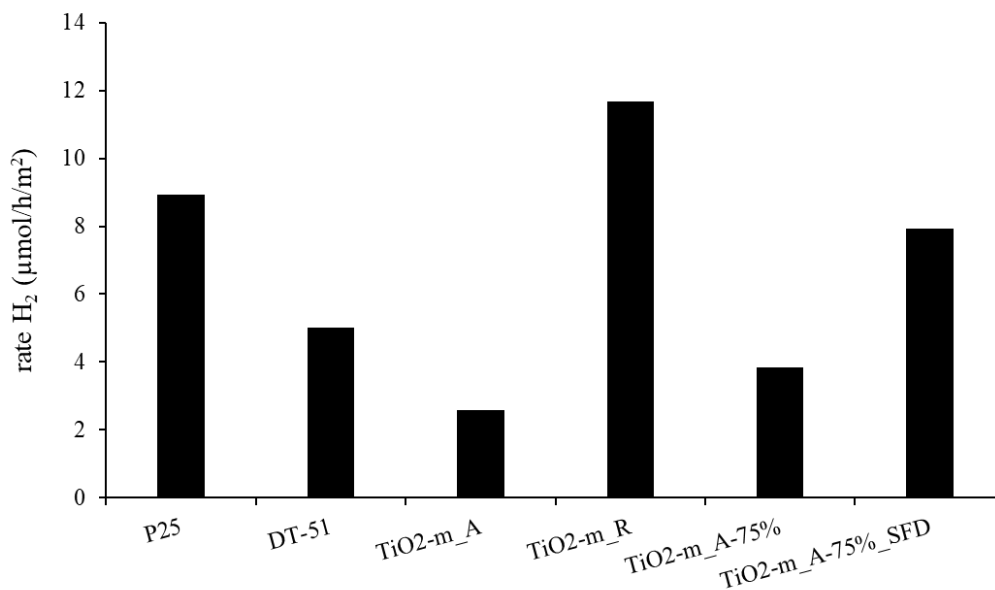


Figure 5.24. The rate of H₂ production normalized by specific surface area for different types of TiO₂.

Summarizing, from the observed results the conclusion that can be drawn is that low apparent density, low hydrodynamic diameter of particles, high porosity, specific surface area, and the presence of rutile crystalline phase are beneficial for the effective absorption of light and high rates of H₂ production for TiO₂ powdered photo-catalysts.

Chapter 6. Surface chemistry on lab-synthesized titanium dioxide

6.1. Experimental section

Paragraph 6.1 describes the methods and chemicals utilized to study surface chemistry of TiO₂ prepared by microemulsion, hereinafter denoted as TiO₂-m_A. The synthetic procedure of TiO₂-m_A and main characterization are discussed in Chapter 3.

6.1.1. Material preparation

6.1.1.1. Chemicals.

Reagents and solvents: n-Butyllithium solution (n-BuLi 2.5 M in hexane, Merck), n-Pentane (99%, Carlo Erba), H₂ was deoxygenated and dried over molecular sieves prior to use.

Metal precursor: (1,5-Cyclooctadiene) dimethylplatinum(II) (Pt(COD)Me₂, Pt 58.5%, Alfa Aesar).

6.1.1.2. Dehydroxylation of TiO₂-m_A surface.

Prior the surface characterization, physisorbed layers of water were removed by dynamic vacuum and surface dihydroxylation was performed as follows: 1 g of catalyst TiO₂-m_A (which is initial material calcined at 400°C with 2°C/min for 3 h) was placed either in a 30 cm glass reactor and heated up to certain temperature (200, 500°C) or in a quartz reactor to reach 700°C with the rate of 3°C/min for 12 h under dynamic vacuum (10⁻⁵ mbar). Samples were transferred in a glovebox, where stored under argon for the further characterization. This dehydroxylated samples are called TiO₂-m_A-T (T= 200, 500 and 700, respectively).

6.1.1.3. Chemical titration.

Chemical titration of TiO₂-m_A-T was performed for the determination of hydroxyls group concentration (including coordinated water molecules, if any) on the surface of dehydroxylated titania. In a typical experiment ~500 mg of TiO₂-m_A-T powder was placed in one part of a double Schlenk flask, while 2 eq. of 2.5 M n-BuLi solution in hexane was added in the other one. These two additions were done inside the glovebox. Degassed dried pentane was used as solvent. After the reaction of n-BuLi with titanium dioxide took place (40 min), released n-butane was analyzed by GC FID with KCl/Al₂O₃ on fused silica column.^[134]

6.1.1.4. Grafting of Pt(COD)Me₂ over dehydroxylated TiO₂-m_A-T surface.

The powder TiO₂-m_A-500 (758.7 mg, 1.1 mmol of OH) was placed in double Schlenk flask in glovebox. Dimethyl(cyclooctadiene)platinum (Pt(COD)Me₂) (0.0195 g, 0.058 mmol) was placed in the second reactor of the double Schlenk flask inside the glovebox. Degassed and dried pentane (5 ml) was added under argon atmosphere to the platinum complex to dissolve it under stirring at room temperature. The solution was then transferred to powder. The reaction was kept for 2 h under stirring at room temperature. The gaseous products of reaction as well as solvent were transferred into 6 L glass balloon for GC and GC-MS analysis. The resulting solid Pt-OM@TiO₂-m_A-500 was dried under dynamic vacuum at room temperature overnight and stored in a glovebox.

6.1.1.5. Reduction of Pt(COD)Me₂ to form Pt nanoparticles (NPs).

The previous platinum-containing solid Pt-OM@TiO₂-m_A-500 (400.4 mg) was transferred to 500 ml glass reactor and exposed to H₂ (450 mbar) at 300°C (5°C/min) for 3 h. The final material is denoted as Pt/TiO₂-m_A_SOMC.

6.1.2. Material characterization

6.1.2.1. XRD analysis.

Powder X-ray diffraction analyses (XRD, Bruker D8 Advance, Cu, K α radiation, $\lambda = 1.5406 \text{ \AA}$, 40 kV, 4 MA) of TiO₂-m_A, TiO₂-m_A-200, TiO₂-m_A-500, TiO₂-m_A-700 samples were performed at CDHL, University of Lyon (Villeurbanne). The samples were prepared in the form of fine homogeneous powder. A thin smooth layer of the samples, deposited by evaporation from a suspension in ethanol on a non-crystalline substrate such as PMMA (Poly (methylmethacrylate)), was held in the path of X-rays. The XRD patterns were recorded from 5° to 70° at a step of 0.02° 2 θ . The final reduced sample Pt/TiO₂-m_A_SOMC was analyzed at University of Bologna in the Chemistry Department "G. Ciamician". XRD measurements were carried out at room temperature with a Bragg/Brentano diffractometer (X'pertPro PANalytical) equipped with a fast X'Celerator detector, using a Cu anode as the X-ray source (K α , $\lambda = 1.5418 \text{ \AA}$). Diffractograms were recorded in the range of 10-80°2 θ with a step of 0.05°2 θ .

6.1.2.2. Diffuse reflectance infrared Fourier transform spectroscopy (DRIFTS).

Diffuse Reflectance Infrared Fourier Transform Spectroscopy (DRIFTS) is an infrared spectroscopy technique used on powder samples. DRIFT spectra were recorded on a Nicolet 6700-FT spectrometer using a cell equipped with CaF₂ window. Typically, 64 scans were accumulated for

each spectrum (resolution 4 cm⁻¹). DRIFT spectra were treated through Kubelka-Munk function (KM).

6.1.2.3. Nitrogen physisorption analysis.

Belsorp-Max from BEL-JAPAN was used to measure nitrogen adsorption desorption isotherms at 77 K after degassing the sample. Typically, ~100-200 mg of powder was filled in the cell. For dehydroxylated titania the sample holders were filled inside glove box. No heat-pretreatment was done for dehydroxylated samples, while the fresh one was pre-treated at 125°C for 2 h prior nitrogen adsorption. The specific surface area of the sample powder was then calculated according to the BET model which takes into account the amount of gas adsorbed on the surface of the powder sample as a function of gas pressure. BJH method was used to calculate the pore size.

6.1.2.4. Elemental analysis.

Elemental analysis of C and Pt was analyzed at the Mikroanalytisches Labor Pascher in Remagen-Bandorf, Germany. For C-analysis the sample was combusted at 1050°C in an oxygen stream. Carbon dioxide was absorbed in 0,1 N NaOH and detected conductometrically. The elements were detected using CH-analyzer (by Heraeus / Mannertz / Mikroanalytisches Labor Pascher) instrument. For analysis of Pt, samples were firstly dissolved in acids. Subsequent detection of Pt was made by ICP-AES (Inductively Coupled Plasma Atomic Emission Spectroscopy). Used instrument for detection: Inductively coupled plasma atomic emission spectrometer; iCap 6500 (by Thermo Fisher Scientific).

6.1.2.5. Nuclear magnetic resonance (NMR).

Solution NMR spectra were recorded on BRUKER AVANCE 300 spectrometer (1H:300.1 MHz). Chemical shifts are given in ppm (h) relative to TMS (tetramethylsilane). Solid state NMR spectra were collected on BRUKER AVANCE III 500 spectrometer operating at 125 MHz for ¹³C. The zirconia rotor of 4 mm is filled with the desired product inside glove box under argon and sealed with a kel-f stopper. It was then transferred into the probe Bruker CP 4 mm spectrometer allowing rotation of the rotor at a speed of 10 kHz. The time between two acquisitions was always optimized to allow complete relaxation of the protons.

6.1.2.6. Transmission Electron Microscopy (TEM).

Transmission electron micrographs of **Pt/TiO₂-m_A_SOMC** were performed at the “Centre Technologique des Microstructures”, UCBL, Villeurbanne, France, using a JEOL 2100F electron

microscope. The acceleration voltage was 200 kV. The samples were prepared by dispersing a drop of the ethanol suspension of a ground sample on a Cu grid covered by a carbon film.

6.1.3. Photocatalytic test on glycerol

The photo-catalytic test with prepared **Pt/TiO₂-m_A_SOMC** was carried out following the procedure described in Chapter 5, section 5.1.3.1. at University of Bologna, Department of Industrial Chemistry “Toso Montanari”. All analytical analyses have been carried out similarly to the ones described in Chapter 5, section 5.1.3.2. The results were then compared to activity of Pt-containing catalysts based on TiO₂-m_A support prepared by deposition-precipitation (DP) and wetness incipient impregnation, the synthetic procedure of which were described in Chapter 5, section 5.1.1.2. and 5.1.1.3.

6.2. Results and Discussions

Paragraph 6.2 includes the results regarding characterization of dehydroxylated **TiO₂-m_A-T**. The main modes observed in spectra recorded by DRIFT were assigned to numerous surface OH_x species, which are evolving on the surface of TiO₂-m_A with an increase of dehydroxylation temperature. The quantity of hydroxyl groups on the surface of TiO₂-m_A has been titrated and found to be depended on the method of TiO₂-m_A synthesis and dihydroxylation temperature. Well-dispersed 1 nm platinum nanoparticles were deposited on the surface of TiO₂-m_A by means of Surface Organometallic Chemistry approach. The resulted material demonstrated improved activity towards hydrogen production by photo-reforming of glycerol.

6.2.1. Characterization of materials

6.2.1.1. Dehydroxylation of TiO₂-m_A surface.

After dehydroxylation process, samples were characterized by XRD, DRIFT and N₂ physisorption analysis. Sample preparation for XRD was done under air at room temperature for all samples since adsorption of molecular H₂O will not affect the crystallinity of TiO₂ Anatase. **Table 6.1** contains the data obtained from XRD patterns. The results show that after dehydroxylation at 200°C, **TiO₂-m_A-200** maintained similar phase composition and crystalline size of particles comparable to starting material. Therefore, the sample remained mostly anatase and no substantial transition of anatase to rutile was observed. At 500°C the phase composition also was kept unchanged, although a slight growth of particles can be observed in **TiO₂-m_A-500**. Moreover, after refinement of diffractograms using Diffrac.Suite Eva software, it was deduced that synthesized **TiO₂-m_A-500** do not possess amorphous phase, instead the XRD peaks are broad due to the nanometric size of particles. Following the 700°C dehydroxylation temperature, the particles size and rutile content increased drastically in **TiO₂-m_A-700**, resulting in shrinking of surface area, while the pore size increases (**Table 6.1**). This is in agreement with Joseph et al.^[215] where agglomeration of small particles occurs to form big crystals, changing the porosity from inter-crystallite pores to inter-agglomerate ones.^[137]

Table 6.1. Phase composition (%), crystalline size (d, nm), specific surface area (S_{BET}), size and volume of pores (d_p , V_p) of different $\text{TiO}_2\text{-m_A}$ pre-treated at a certain dehydroxylation temperature and time of stating material.

catalyst	$\text{TiO}_2\text{-m_A}$ <i>fresh</i> ^a	$\text{TiO}_2\text{-m_A}$ - 200	$\text{TiO}_2\text{-m_A}$ - 500	$\text{TiO}_2\text{-m_A}$ - 700
% (A:R:B) ^b	91:8:1	93:7:0.1	96:4:0	70:30:0
d ^c , nm	8	8	10	36
S_{BET} (m ² /g)	164	152	140	12
V_p (cm ³ /g)	0.29	0.23	0.24	0.06
d_p (nm)	5.41	4.76	7.01	13.62

^a $\text{TiO}_2\text{-m_A}$ *fresh* means starting material calcined at 400°C for 3 h.

^b A – anatase, R – rutile, B – brookite, determined from deconvolution of XRD patterns.

^c crystalline size was estimated from the widths of Anatase (101) reflection obtained by the Scherrer formula.

KM spectra recorded by DRIFT spectroscopy technique and reported on **Figure 6.1** show various types of hydroxyl groups on the surface of titania listed in **Table 6.2**.

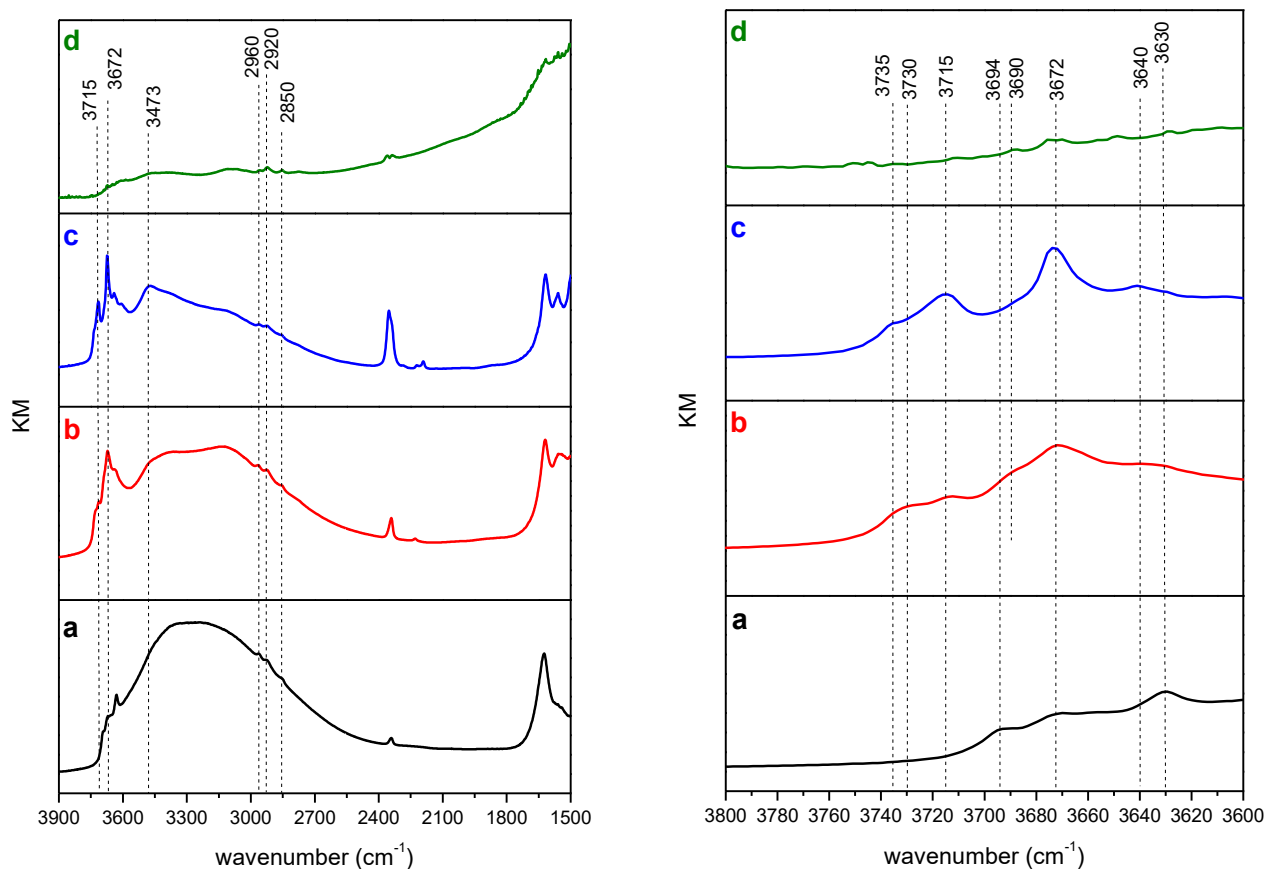


Figure 6.1. KM spectra between 3900 and 1500 cm^{-1} (left) and zoom between 3800 and 3600 cm^{-1} of a). fresh $\text{TiO}_2\text{-m_A}$ (calcined at 400°C for 3 h) and dehydroxylated samples at b). 200°C, c). 500°C and d). 700°C.

Figure 6.1 shows that with increase of dehydroxylation temperature starting from 200°C the broad band around 3000-3400 cm^{-1} assigned to physisorbed water diminishes, while the intensity of different bands corresponding to hydroxyl groups increase namely the ones assigned to bridging (3672 cm^{-1}), isolated (3640, 3715 cm^{-1}) and terminal (3730 cm^{-1}) ones.^[137] **TiO₂-m_A** strongly coordinates water so that even at 500°C some traces could be still observed at 3473 cm^{-1} and around 1620 cm^{-1} , assigned to physisorbed water. The agglomeration observed at 700°C can in art be linked to the dihydroxylation of such surface hydroxyls and coordinated water.

Strongly physisorbed CO₂ (**Figure 6.2**) indicates the presence of basic sites on **TiO₂-m_A**. Interestingly, K. Yamakawa and co-workers^[216] reported different frequencies attributed to CO₂ adsorbed at different sites of TiO₂. Thus, the peak at 2340 cm^{-1} was assigned to defective sites related to oxygen vacancies (V_{os}) that play an important role in photocatalysis, affecting the energy bandgap of the semiconductor. To note, after dehydroxylation process, samples changed color to grayish-blue depending on the temperature, indicating the formation of oxygen deficient sites. On the other hand, the peak at 2350 cm^{-1} was associated with CO₂ adsorbed at the fivefold Ti⁴⁺ sites of anatase. After dehydroxylation at 700°C, the peak at 2361 cm^{-1} is appeared corresponding to stretching of CO₂ adsorbed at Ti_{5c} on rutile (110),^[217] the presence of which is in agreement with the results given by XRD analysis.

The peaks of a weak intensity appeared around 2220 cm^{-1} especially after dehydroxylation at 500°C (**Figure 6.1**) could be assigned to N-containing species^{[218],[219],[220]} such as isocyanate groups (-NCO) or cyanate (-CN), taking into account that in the microemulsion-mediated synthesis of **TiO₂-m_A** nitric acid was used as hydrolyzing agent.

Dehydroxylation process removes most physisorbed water from **TiO₂-m_A**, giving access to non-mobile grafting sites on the surface of titania by SOMC technique.^[134]

Table 6.2. Infrared frequencies of different hydroxyls/H₂O and other groups on TiO₂-m_A observed experimentally.

Frequency, cm^{-1}	Assignment	Ref.
3735	free surface (OH)	[221]
3730	terminal (OH) on (101) Anatase (A)	[222]
3715	isolated (OH) on (100)/(010) or (001) A	[223]
3694	chemisorbed water on (100) coordinated to Ti ⁶⁺ _{6c} (A)	[223]
3690	Ti _{6c} -OH on (100) A	[224]
3672	bridging $\nu(\text{OH})$ on (101) Ti ⁴⁺ -O(H)-Ti ⁴⁺	[225]
3650-3655	bridging $\nu(\text{OH})$ on Ti ⁴⁺ -O(H)-Ti ⁴⁺ of Rutile (R)	[226]
3640	isolated OH	[225]

3630	physisorbed water on (101) (A)	[224]
3000-3400	adsorbed water molecules	[223]
2960, 2920, 2850	$\nu(\text{CH})$ may originate from organics remained after the synthesis	[227]
2361	$\nu(\text{CO}_2)$ adsorbed at the Ti_{5c} on (110) R	[217]
2350	asymmetric $\nu_3(\text{CO}_2)$ at the fivefold Ti^{4+} sites (A)	[216]
2340	$\nu(\text{CO}_2)$ physisorbed at the defective site (V_{OS}) of A	[216]
1620	$\delta(\text{H-O-H})$ coordinated to Ti^{4+} (A)	[228]

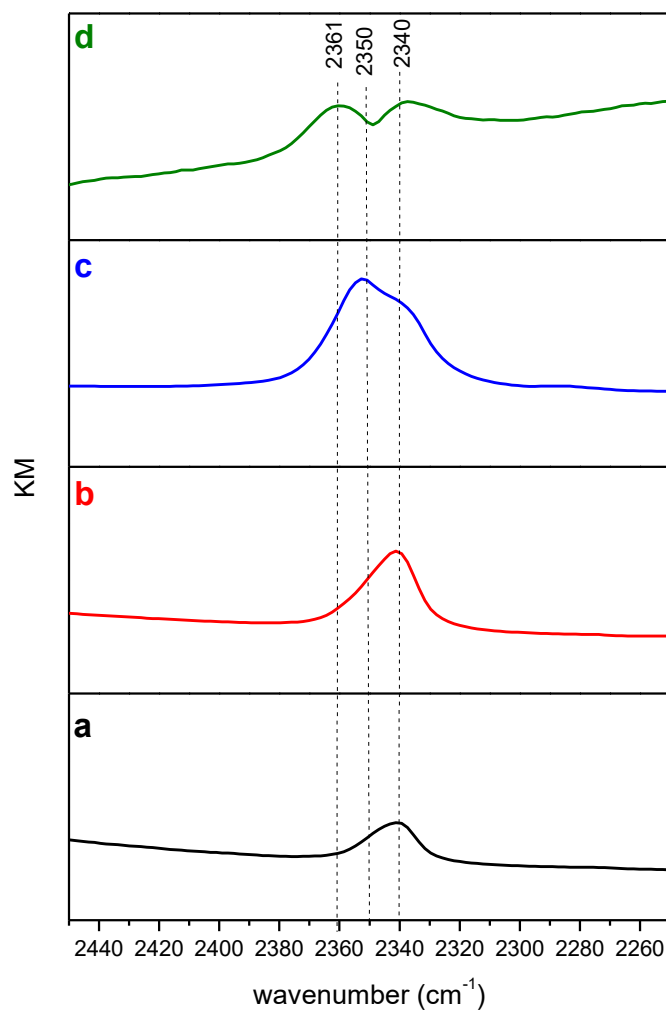
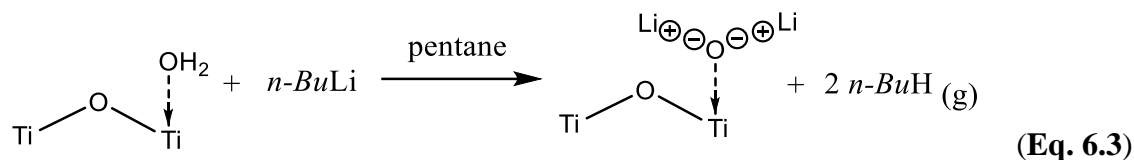
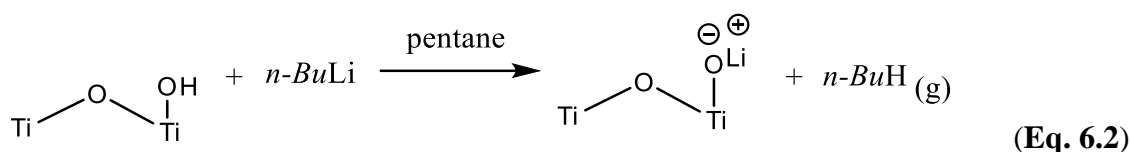
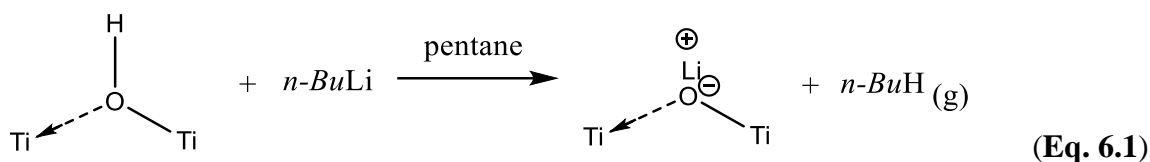


Figure 6.2. KM spectra between 2460 cm^{-1} and 2250 cm^{-1} on a). fresh $\text{TiO}_2\text{-m_A}$ (calcined at 400°C for 3 h) and dehydroxylated samples at b). 200°C , c). 500°C and d). 700°C .

6.2.1.2. Chemical titration of dehydroxylated $\text{TiO}_2\text{-m}_A$.

The method involves quantitative reaction of $n\text{-BuLi}$ with surface hydroxyls/chemisorbed water on $\text{TiO}_2\text{-m}_A\text{-T}$ to yield $n\text{-butane}$ following the reactions below, as already shown for non-microemulsion titania elsewhere^[137]:



The released $n\text{-BuH}$ was quantified by GC and corresponds to moles of hydroxyl groups equivalents (including water molecules). Along with $n\text{-BuH}$, isomers of butene were detected by GC and GC-MS analysis, indicating the reduction capability of dehydroxylated titania, becoming then of a black color.^{[229],[230]} However, various methods of black TiO_2 synthesis other than hydrogenation have been developed up to date.^{[231],[232]}

DRIFT spectra on **Figure 6.3** demonstrate that all the OH_x reacted with $n\text{-BuLi}$.

Hydroxyl groups of the two types of $\text{TiO}_2\text{-m}_A\text{-T}$ with different water-to-surfactant ratio (R_w) used during the synthesis, leading to different properties (**Table 6.3**), were titrated. The titration was performed on $\text{TiO}_2\text{-m}_A\text{-500}$ and $\text{TiO}_2\text{-m}_A\text{-700}$. The batch of material with R_w 21 dehydroxylated at 500°C resulted in 1.5 mmol OH/g or $6.3 \text{ OH}_{\text{eq}}/\text{nm}^2$, while the one with R_w 10 dehydroxylated at 500°C resulted in 0.67 mmol OH/g or $2.6 \text{ OH}_{\text{eq}}/\text{nm}^2$. These results suggest that synthetic method, on top of the dihydroxylation temperature, could have an impact on hydroxylation degree of TiO_2 surface. The value found for $\text{TiO}_2\text{-m}_A\text{-500}$ (R_w 21), viz. $6.3 \text{ OH}_{\text{eq}}/\text{nm}^2$, is large with respect to available titania's surface atoms in the solid lattice: as a comparison value, surface (101) of titania exposes ca. 5 titanium atoms/ nm^2 .^[137] The large apparent number of OH equivalents is in agreement with residual water physisorbed on the titania surface still present after dehydroxylation treatment at 500°C , in agreement with the Infrared spectroscopy results discussed above (see fig 6.1c.)

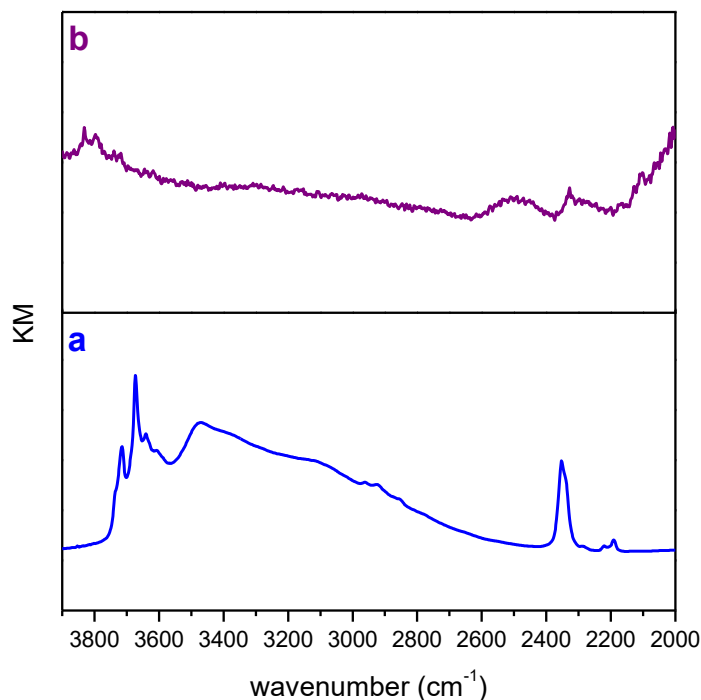


Figure 6.3. KM spectra between 3900 and 2000 cm^{-1} of $\text{TiO}_2\text{-m_A-500}$ a). before and b). after chemical titration with BuLi.

Table 6.3. The properties of $\text{TiO}_2\text{-m_A}$ (specific surface area, S_{BET} , crystalline size of particles, d , pore volume, V_p , pore diameter, d_p) with different R_w and titrated moles of titanols.

R_w	T ($^{\circ}\text{C}$) ^a	S_{BET} , m^2/g	d , nm	V_p , cm^3/g	d_p , nm	OH, mmol/g	$\text{OH}_{\text{eq}}/\text{nm}^2$
21	r.t. ^a	164	8	0.29	5.41	-	-
21	500	140	10	0.24	7.01	1.5	6.3
10	r.t. ^a	164	6	0.09	2.43	-	-
10	500	154	-	0.10	2.43	0.67	2.63

^a The samples were pre-heated in vacuum over 2 h at 125 $^{\circ}\text{C}$ prior the N_2 physisorption analysis.

6.2.1.3. Grafting of $\text{Pt}(\text{COD})\text{Me}_2$ over dehydroxylated titania and reduction to form Pt nanoparticles (NPs).

The deposition of Pt precursor on solid $\text{Pt-OM@TiO}_2\text{-m_A-500}$ was monitored by DRIFT and solid NMR techniques as well as elemental analysis.

Elemental analysis (**Table 6.4**) showed that the platinum content (1.22% wt) corresponds to 0.3 Pt/ nm^2 showing that substantial grafting has occurred, with respect to the estimated starting titanols (6.3 OH/ nm^2 , see above). The ratio of C to Pt was found from elemental analysis to be 13:1, which is higher than the calculated one (9:1) for η^1 -coordinated species [$-\text{O-Pt}(\text{COD})\text{Me}$], suggesting that as some spurious pentane solvent is present in the solid. DRIFT spectra on **Figure 6.4** clearly

show disappearance of titanols and appearance of peaks around 3018 cm^{-1} and $2950\text{-}2850\text{ cm}^{-1}$ that correspond to alkenyl and alkyl C-H stretching of cyclooctadiene and/or methyl of the precursor (and possibly leftover solvent). The disappearance of all the titanols indicates the reaction with all the surface titanols.^[233] Solid-state $^{13}\text{C}\{^1\text{H}\}$ CP-MAS NMR spectrum of **Pt-OM@TiO₂-m_A-500** is shown on **Figure 6.5**. The most distinct resonance signal was observed at δ 25 ppm that could be assigned to CH_2 of cyclooctadiene moiety and/or pentane. Weaker signals around 70 ppm and 110 ppm are also observed. Resonances at δ 115 (C=C), δ 76 (C=C), δ 30 (CH_2) and δ 0 ppm (CH_3) were reported by M. Bonati et al.^[234] In their work the same Pt complex was grafted on dehydroxylated at 500°C surface of SiO_2 . Authors suggested that $\text{Pt}(\text{COD})\text{Me}_2$ complex could be grafted as η^1 -coordinated species, $[(\text{SiO})\text{-Pt}(\text{COD})\text{Me}]$, taking into account the two alkene signals that indicate the presence of a nonsymmetric environment around platinum, and the presence of methyl signal at 0 ppm. Similarly, P. Laurent and co-workers^[233] reported the results on grafting of $(\text{COD})\text{PtMe}_2$ over SiO_2 dehydroxylated at 200°C and 700°C , having resonance signals (ppm) at: 118, 78, 32, 29 and 6 ppm, and 118, 78, 33, 30 and 6 ppm, respectively.

The GC and GC-MS analyses of the gaseous products after the grafting of $\text{Pt}(\text{COD})\text{Me}_2$ over **TiO₂-m_A-500** showed mostly pentane and some traces of CH_4 . The release of only methane was also reported by M. Bonati et al.^[234] In their case, the molar ratio between Pt and amount of evolved gas was found to be 0.83, further suggesting that complex was grafted as $\text{Pt}(\text{COD})\text{Me}$ fragments, η^1 -coordinated to the silica surface.

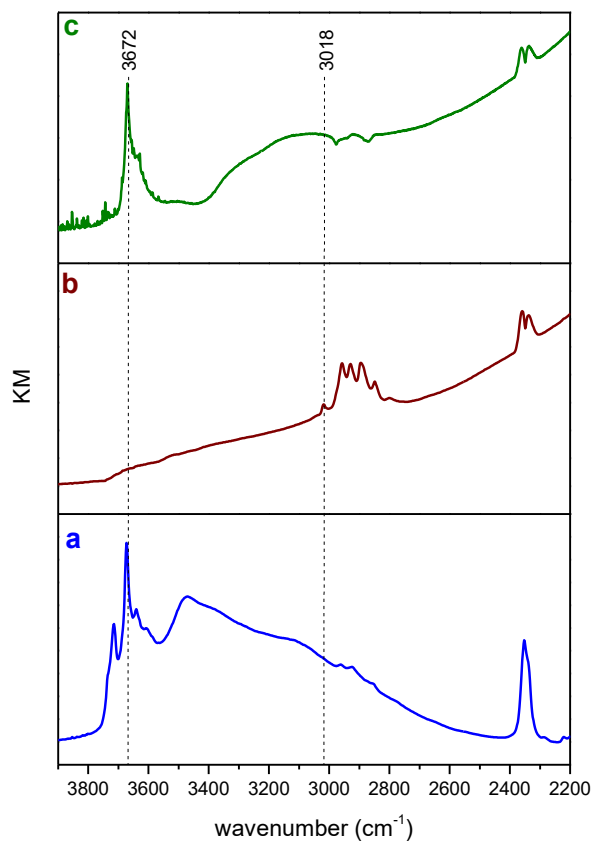


Figure 6.4. KM spectra of a). dehydroxylated TiO₂ at 500°C, b). the sample after grafting of Pt(COD)Me₂ and c). after reduction in static hydrogen to form Pt nanoparticles.

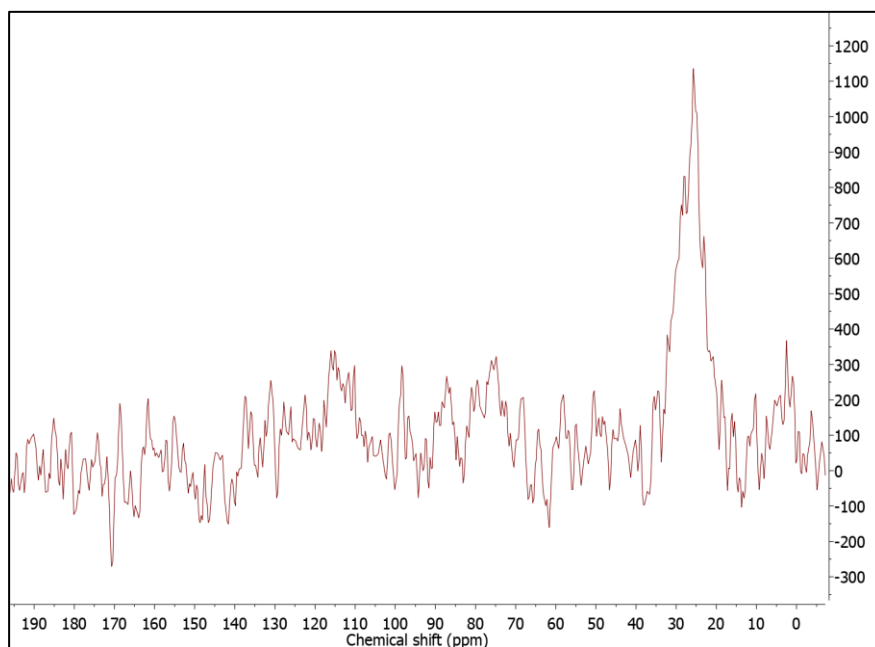


Figure 6.5. Solid-state CP-MAS ¹³C{¹H} NMR (125 MHz, 2 s relaxation time) spectrum of dehydroxylated at 500°C and grafted TiO₂-m_A.

Hydrogenation of material to generate Pt nanoparticles lead to a rapid change of color to dark gray. The gas products of hydrogenation process were analyzed by GC. Methane, ethane and propane were detected, while DRIFT spectra showed disappearance of C-H stretching of alkenyl and alkyl groups (**Figure 6.4**), indicating that COD and CH₃ are at least partially eliminated as hydrogenated volatile byproducts. Meanwhile, the regeneration of bridging hydroxyls on (101) Ti⁴⁺-O(H)-Ti⁴⁺ at 3672 cm⁻¹ is in line with the cleavage of Pt-O bond and formation of Pt nanoparticles.

Elemental analysis for non-reduced sample and TEM analysis for reduced one were carried out, and the results were compared with the samples synthesized at University of Bologna, prepared by deposition-precipitation (DP) and incipient wetness impregnation methods for the photo-catalytic activity tests. The results are presented in **Table 6.4** and **Figure 6.6**.

Table 6.4. Water-to-surfactant ratio (R_w) used for synthesis of titania, specific surface area (S_{BET}) crystalline size of TiO₂-m_A (d), elemental analysis represented in units of mass percent and nominal loading of Pt over titania (Pt % wt.).

Sample name	Element	%wt.	S _{BET} (m ² /g)	Pt %wt.	R _w	d _{Pt} (nm)	d (nm)	E _g ^b (eV)
Pt-OM@TiO₂- m_A-500	C	0.97	121	1.5	21	1.01	-	3.12
	Pt	1.22					9 ^c	
Pt/TiO₂-m_A_DP ^a	Pt	1.22	128	1.5	21	0.93	7	3.11
Pt/TiO₂-m_A ^a	Pt	0.66	121	1.5	21	1.87	8	3.11

^a samples were prepared at University of Bologna by deposition-precipitation (DP) and wetness incipient impregnation methods. XRD and N₂ physisorption of these samples were performed at University of Bologna.

^b Energy bandgap of reduced samples estimated from Kubelka-Munk spectra.

^c Crystalline size of anatase in reduced **Pt/TiO₂-m_A_SOMC**, using anatase (101) reflection.

Elemental analysis demonstrates that grafting method and deposition-precipitation resulted in similar amount of Pt, while the incipient wetness impregnation surprisingly showed two times lower amount of platinum most probably associated with a poor dispersion and formation of large clusters on the surface of titania as shown in TEM images (**Figure 5.8**). Secondly, TEM analysis revealed Pt nanoparticles obtained by grafting technique of around 1 nm with a notably narrower size distribution compared to samples prepared by deposition-precipitation and wetness incipient impregnation methods. XRD and N₂ porosimetry data both made at University of Bologna are collected for comparison in **Table 6.4**.

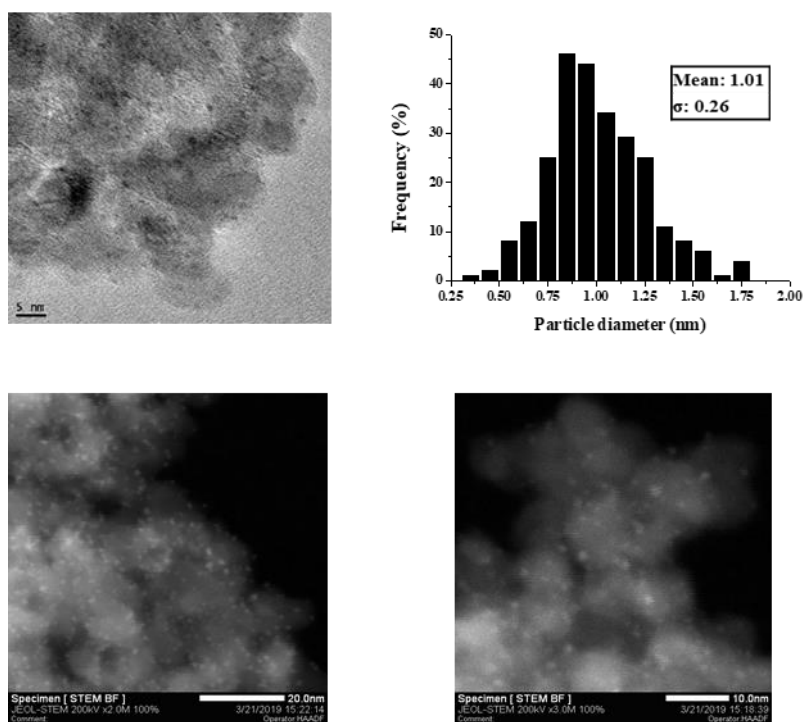


Figure 6.6. TEM images and particle size distribution of Pt/TiO₂-m_A_SOMC catalyst.

Crystalline structure of prepared catalyst was analysed by XRD presented in **Figure 6.7**. After reduction, XRD of Pt/TiO₂-m_A_SOMC showed mainly anatase phase as was observed for starting support (**Figure 3.1**). The average crystallite size of particles was estimated from the widths of anatase (101) reflection obtained from the XRD by the Scherrer formula (**Eq. 3.1**) and the results are shown in **Table 6.4**. As we can see, the reduction step caused a size increase of TiO₂ crystallites.

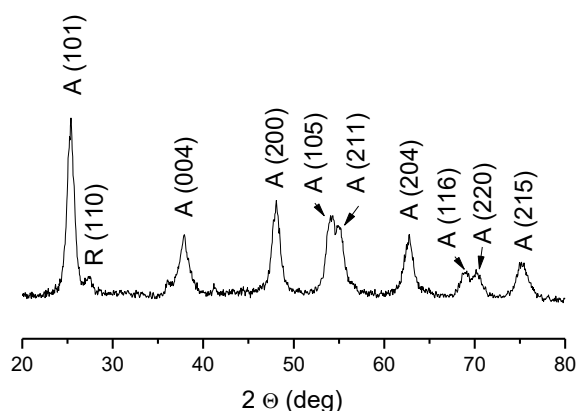


Figure 6.7. XRD pattern of Pt/TiO₂-m_A_SOMC. A: Anatase, R: Rutile.

DRS measurements of Pt/TiO₂-m_A_SOMC sample were carried out in order to find Kubelka-Munk function (KM), described more in detail previously in Chapter 3, (**Eq. 3.3**). From KM spectrum it is possible to determine the energy bandgap (E_g) using **Eq. 3.2** presented in Chapter 3.

KM spectra of **Pt/TiO₂-m_A_SOMC** (Figure 6.8), **Pt/TiO₂-m_A** and **Pt/TiO₂-m_A_DP** (Figure 5.6) demonstrate the absorption edge in UV range of solar spectrum (< 420 nm), having comparable E_g (Table 6.4).

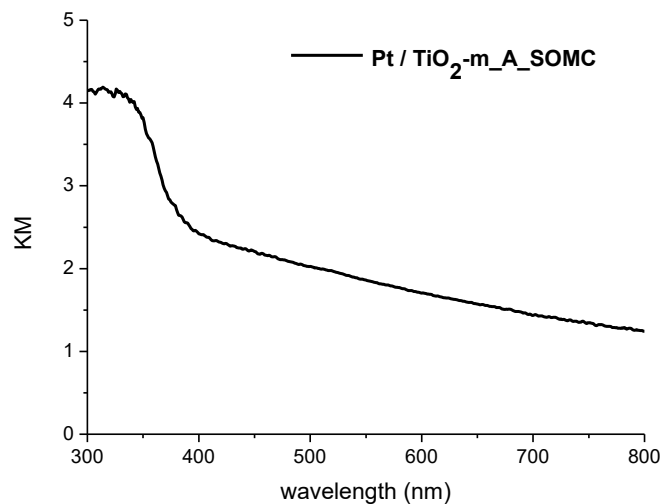


Figure 6.8. KM spectrum of **Pt/TiO₂-m_A_SOMC** catalyst.

6.2.2. Effect of deposition method on glycerol photo-reforming

The advantageous effect of introduction of Pt NPs on the rates of hydrogen production from glycerol photo-reforming compared to other metals and support alone was discussed already in Chapter 5. Figure 6.9 shows hydrogen and liquid phase molecules production rates for Pt NPs supported on **TiO₂-m_A** by incipient wetness impregnation, **Pt/TiO₂-m_A**, deposition-precipitation (DP), **Pt/TiO₂-m_A_DP**, and surface organometallic chemistry (SOMC), **Pt/TiO₂-m_A_SOMC**. Higher H₂ production rates were observed for sample prepared by grafting and subsequent reduction of organometallic complex. Comparing the data from XRD, N₂ physisorption, TEM and DRS one can suggest that the reason of improved hydrogen production rate could be attributed to homogeneously distributed Pt NPs.

The dispersion can be calculated from TEM images. It can be also estimated according to the formula reported by A. Borodziński et al.^[235] that considers the relationship between the crystalline size and dispersion of supported metal catalysts:

$$FE = \frac{2.64}{(d_{rel}(VS))^{0.81}} \quad (\text{Eq. 6.4})$$

Where FE is the dispersion of metal and $d_{rel(VS)}$ is the relative size of metallic particles and can be found as:

$$d_{rel(VS)} = \frac{d_{VS}}{d_{at}} \quad (\text{Eq. 6.5})$$

Where d_{VS} is the mean diameter of particles and d_{at} is the atomic diameter of metal, which was found to be around 0.28 nm for Pt.^[236] The mean diameter d_{VS} was suggested to be calculated as next:

$$d_{VS} = \left(\frac{\sum_i n_i d_i^3}{\sum_i n_i d_i^{2.19}} \right)^{1.23} \quad (\text{Eq. 6.6})$$

Where n_i is the number of particles with the diameter d_i .

According to A. Borodziński et al.^[235] if metal particles have small size ($d \leq 24d_{at}$) then the dispersion can be calculated following the formula in **Eq. 6.4**. The results, summarized in **Table 6.5** indicate that dispersion improves from wetness incipient impregnation to DP, followed by SOMC.

Table 6.5. Relation between crystallite size (d, nm) and dispersion (FE) of Pt supported nanoparticles.

Catalyst	d_{VS} (nm)	FE
Pt/TiO ₂ -m_A_SOMC	1.1	0.87
Pt/TiO ₂ -m_A_DP	3.9	0.31
Pt/TiO ₂ -m_A	13.6	0.11

Hydrogen rate production increases by the type of preparation method from wetness impregnation < DP < SOMC as the dispersion of Pt NPs over **TiO₂-m_A** improves. Secondly, the liquid phase analysis shows higher productivity of glycolaldehyde in all cases confirming the role of rutile in selective C-C cleavage towards glycolaldehyde (see Chapter 5, section 5.2.3.2), while the overall reactivity is better in case of Pt/TiO₂-m_A_SOMC than of other samples.

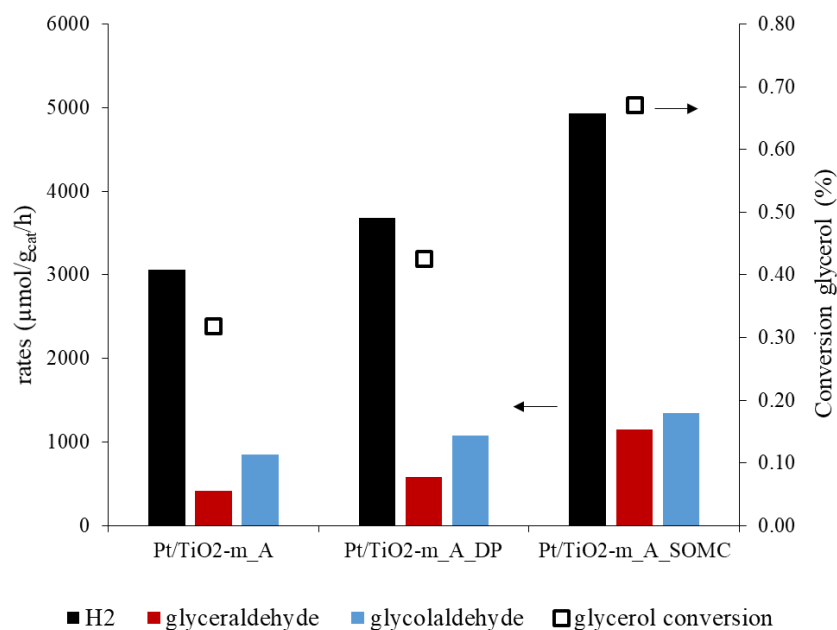


Figure 6.9. The rate of hydrogen production and liquid phase products for Pt NPs supported on TiO₂-m_A by incipient wetness impregnation, deposition-precipitation (DP) methods and Surface Organometallic Chemistry approach (SOMC). 1M aqueous solution of glycerol, 30°C; 6 h, 0.5 g/L catalyst loading.

All in all, Pt(COD)Me₂ complex is a convenient precursor to prepare well-defined Pt(II) surface species and titania-supported Pt nanoparticles with a small 1 nm size, and a narrow distribution. This study opens a possibility to investigate grafting of TiO₂ using the other organometallic precursors with different the ancillary ligands of a similar or different nature than the ones studied here.

Chapter 7. Titanium dioxide thick film preparation and characterization

7.1. Experimental section

Paragraph 7.1 deals with the methods and chemicals utilized to fabricate the thick films based on titanium dioxide materials. All the preparation and characterization have been done in collaboration with Institute of Science and Technology of Ceramics of Faenza (ISTEC-CNR). Four different types of titanium dioxide were deposited as thick films on FTO glass substrates: two commercial samples (P25, DT-51) and two lab-synthesized by microemulsion method (denoted as TiO₂-m_A, TiO₂-m_A-R). The syntheses of the last couple are described previously in Chapter 3. The resulted electrodes were characterized by profilometry, SEM, XRD, optical, electrical, photo-electrochemical methods.

7.1.1. Material preparation

7.1.1.1. Chemicals.

Reference powders: P25 (TiO₂ P25 Degussa), DT-51 (TiO₂ DT-51 Millennium CrystalACTIV).

Support: FTO (Fluorine doped tin oxide coated glass slide, 50x50x2.2 mm, surface resistivity 7 Ω/sq, Sigma Aldrich).

Electrolytes (salts): H₂SO₄ (Sulphuric acid 96-98%, Sigma Aldrich), Na₂SO₄ (Sodium Sulphate, ≥99.0%).

7.1.1.2. TiO₂ ink fabrication.

The ink preparation methods for the application in screen-printing technique has been previously developed at ISTEC-CNR. The procedure consists of the steps illustrated in **Figure 7.1**. Firstly, the dispersant and the solvent (terpineol) were ball-milled for 2h using ZrO₂ grinding media. Then, a certain amount of powder was added to this mixture. Some carboxylic acid as co-solvent used to ensure a good dispersion of particles was added subsequently, and the obtained mixture was ball-milled for 20h. Next, the binder agent was added to the resulted mixture, and the system was ball-milled for 16h. After ambient evaporation of the co-solvent over 24-48h, the system was subjected to the three-roll mill step, employing the suitable instrument equipped with ZrO₂ rollers (Exakt 80E, Exakt, Nordstedt, Germany) in order to homogenize the ink and achieve a proper rheological behaviour.

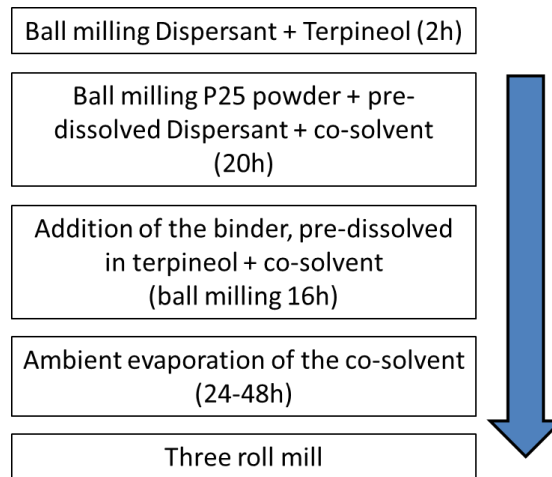


Figure 7.1. Scheme of TiO₂ ink fabrication steps.

The three-roll mill can operate in “gap mode” that fixes a gap between rollers, and “force mode” that by changing automatically the gap between the rollers adjusts the imposed force.

In the “gap mode”, keeping the velocity of 90 mm/s, the distance between rollers was fixed firstly as 30-15 μm , and then 15-5 μm . In the “force mode”, the force initially was applied between rollers as 3-1 N/mm with the velocity of 130 mm/s, and then 0-0 N/mm with the velocity of 150 mm/s.

For DT-51, TiO₂-m_A and TiO₂-m_A-R the parameters described above were performed twice (2 cycles) for each mode. Whereas, for P25, each parameter was applied only once, both in “gap mode” and “force mode”, considering a much more viscous structure (due to the physical properties of the P25 powders) if compared to other samples after the first step of ink preparation.

7.1.1.3. TiO₂ ink deposition by screen-printing technique.

The resulted inks were deposited on FTO electrodes, which were cleaned in isopropanol, sonicated and dried prior the deposition. The screen-printing technique has been applied using Aurel 900E machine. This technique is in principle based on the squeezing of the titania ink through the mesh of a nylon mask onto FTO support. FTO glass was cut into 4 equal squares, on which the ink was deposited with a 0.25 cm² active area, 2 or 3 mm far from the upper edge.

The following parameters, snap-off distance of 900 μm , blades pressure of 4.5 Kg force, blades velocity of 90 mm/s, were used in order to get the optimal thickness and structure of deposited film. The printing mode delivered 2 layers of deposit in 1 cycle. If not indicated otherwise, 2 cycles were performed, followed by a drying step (80°C, 20°C/min, 20 min) between each, using a IR furnace (Nannetti).

The depositions were finalized by sintering them at 450°C in air following this ramp:

1. T=0-325°C, rate 2°C/min, dwell 5 min.

2. T=325-375°C, rate 2°C/min, dwell 5 min.
3. T=375-450°C, rate 2°C/min, dwell 30 min.

7.1.2. Material characterization

7.1.2.1. XRD.

The crystallographic information of TiO₂ electrodes was investigated by X-ray diffraction (XRD, Bruker D8 Diffractometer Germany, Cu, K α radiation). The samples were analyzed on FTO support without any preparation. The XRD patterns were recorded from 10° to 80° at a step of 0.02° 2 θ . The well-known Bragg's equation can be used to determine the interlayer space of the crystals $d = \lambda / (2 \sin \theta)$, where θ is the diffraction angle. All the resulted files were processed in Diffrac. Suite Eva software. XRD of powders were analyzed at University of Bologna in the Chemistry Department "G. Ciamician". The XRD parameters used and obtained patterns of powders were presented previously in Chapter 3.

7.1.2.2. Profilometry.

Profilometry is a technique used to extract topographical data from a surface. The instrument is a 3D Optical Microscopy system (Contour GT-K 3D non-contact profilometer, Bruker, Germany), which operates based on the principle of interferometry.

7.1.2.3. SEM

Morphological properties of TiO₂ electrodes were assessed by scanning electronic microscopy analysis using a Carl Zeiss Sigma NTS (GmbH Oberkochen, Germany) Field Emission Scanning Electron Microscope (FE-SEM). Electrodes were cut and fixed to conductive adhesive tapes and sputter-metallized with gold.

7.1.2.4. Optical characterization.

For each type of electrode, the value of energy bandgap was determined by UV-vis spectrometer (PVE300, Bentham Ltd., UK) equipped with a diffuse reflectance accessory.

Transmittance analysis was recorded in the range from 350 to 800 nm with a step of 2 nm. Prior the use of spectrometer, the detector was calibrated with Germanium and Silicon reference cells.

Reflectance measurements were performed using integrating sphere. Behind the non-conductive surface of the FTO electrode, BaSO₄ window was mounted to insure that no light was transmitted, which was also used as a blank sample.

The optical characterizations of powders were assessed at University of Bologna, Department of Industrial Chemistry “Toso Montanari” by Diffuse reflectance spectroscopy (DRS) using Perkin Elmer Lambda 19 instrument equipped with integrating sphere, in the range 280-800nm. The spectra are presented in Chapter 3, **Figure 3.4**.

7.1.2.5. Electrochemical characterization.

All the electrochemical and photo-electrochemical characterizations were conducted using an AUTOLAB PGSTAT302+FRA32M (Metrohm, the Netherlands) with NOVA 1.2.4 software. Cyclic voltammetry (CV) and electrochemical impedance spectroscopy (EIS) were performed in a standard three-electrode assembly, where TiO₂ electrode was the working one with the active surface area of 0.25 cm², Platinum foil was the counter-electrode and Saturated Calomel Electrode (SCE, KCl 3.5M) was the reference one.

CV analysis was carried out in H₂SO₄ 0.01 M electrolyte in the voltage range between +1.0 and -1.0 vs. SCE, at different scan rates: 10-20-50-100 mV/s. The solution was purged with N₂ for 15 min prior to each analysis.

EIS was performed in the frequency range between 100 kHz and 0.5 Hz with 10 mV amplitude of the AC signal. The potential applied was the Open Circuit Potential (OCP). 0.01 M H₂SO₄ was used as an electrolyte solution, and N₂ was purged for 15 minutes before analysis.

Mott-Schottky (MS) analysis (in the dark) was performed also by means of EIS. Typically, the measurements were conducted in 0.1 M Na₂SO₄ electrolyte solution (pH=5.8) in the potential range between +0.6 and -0.5 V vs. SCE (starting from the anodic potential) by step of 50 mV and waiting time of 300 s before the next spectra recorded. EIS were done in the range of frequency between 10 kHz and 0.5 Hz with 10 mV amplitude of AC signal. The solution was purged with N₂ for 15 minutes prior to start the analysis.

7.1.2.6. Photo-electrochemical characterization.

Linear Sweep Voltammetry (LSV) measurements were conducted under both dark and illumination conditions in order to determine the photocurrent generated by different TiO₂ electrodes. A standard solar simulator (Lot Quantum Design, 300W) was used at 100 mW/cm² AM 1.5G (calibrated with Silicon reference cell). These analyses were performed in a standard three-electrode assembly under stirring, where TiO₂ electrode is the working one with the active surface area of 0.25 cm², Platinum thin film was the counter-electrode and Ag/AgCl electrode was the reference one. The analyses were conducted in 0.1 M Na₂SO₄ electrolyte solution (with known pH) in the potential range between +1.0 V and -0.3 V at a scan rate of 10 mV/s.

7.2. Results and Discussions

This paragraph describes results obtained during the fabrication of TiO₂ films and their characterization. The formulation of inks appeared to be strongly depended on the morphology and surface area of used powders. It was found that microemulsion-based TiO₂ sample resulted in a more fluidic ink compared to P25 and DT-51 due to the presence of chunky agglomerates of particles that weakly interact with additives. Optical characterization of films was in agreement with the results observed for powders. Determined energy bandgap value increases in the order: TiO₂-m_A-R < TiO₂-m_A < P25 < DT-51, both for powders and films. Electrochemical characterization allowed evaluating electronic properties of fabricated electrodes such as charge accumulation, conductivity, number of donors, and the presence of trap states, which are the energy levels that hamper the electronic flow. It was observed that conductivity of the material is governed by the number of donors and the presence of trap states. The lowest charge accumulation at trap states was found for P25, what is in agreement with the highest value of conductivity for this sample. Whereas, photoelectrochemical characterization showed the highest photocurrent for DT-51 that is due to the phase composition. It is known that anatase has greater carrier mobility than that of mixed phase or pure rutile. All in all, in evaluating the activity of these materials in photo-electrochemical reaction it is reasonable to consider all of these parameters.

7.2.1. Formulation and deposition of TiO₂ ink

During the inks formulation, microemulsion-based materials demonstrated the tendency to sediment. Nevertheless, after the treatment on the three-roll mill, it gained a more homogeneous, fluidic consistence and uniformity that remained stable for a long period of time. On the other hand, P25 demonstrated a very high degree of density. Both, a more liquid-like behaviour and a tendency to sediment for microemulsion-based samples might originate from the fact that the exposed surface area of particles is smaller, regardless their high specific surface area, due to the formation of bigger aggregates with large pores, which could be observed by means of SEM analysis (**Figure 7.2**).

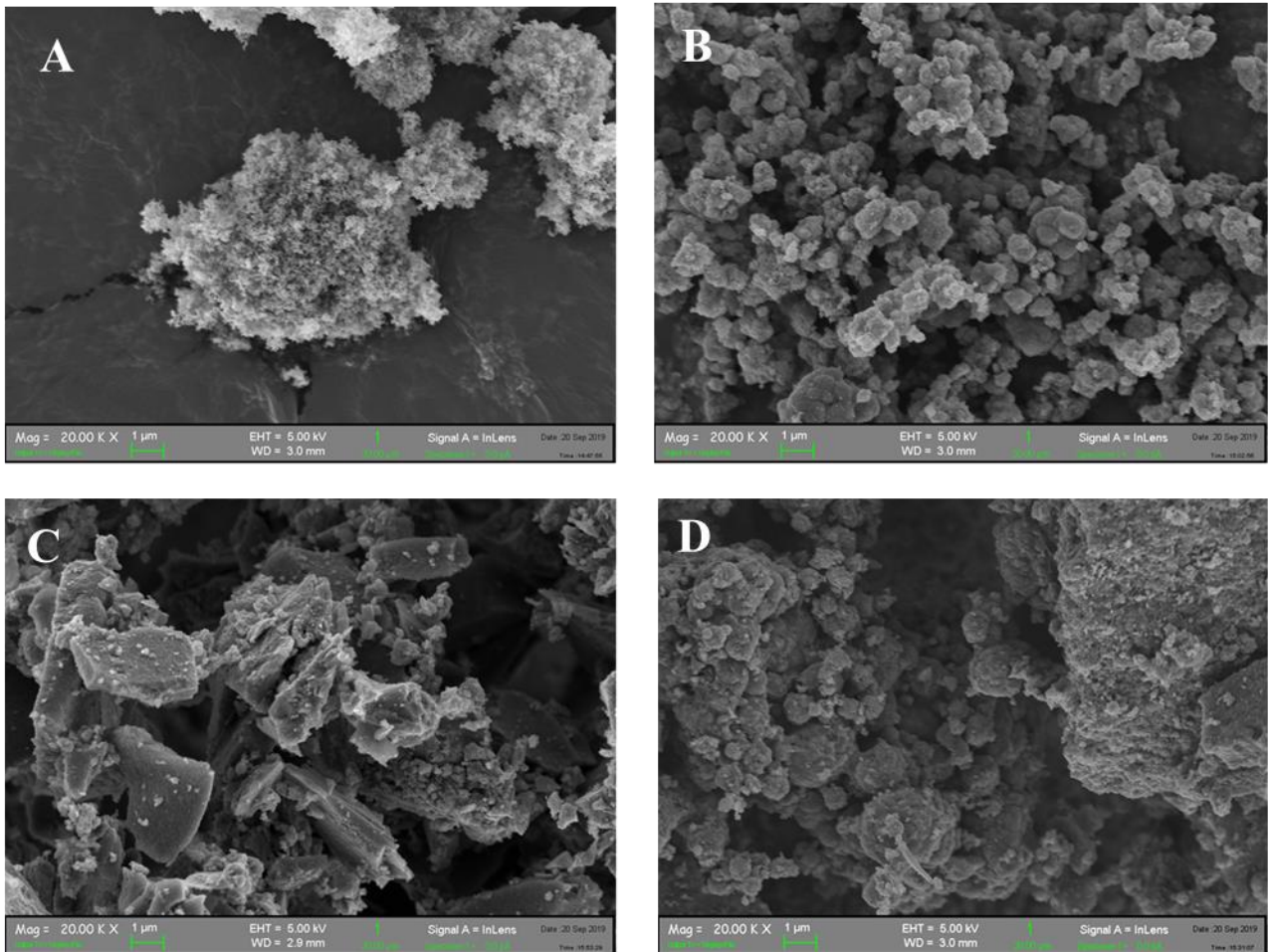


Figure 7.2. SEM images of TiO₂ powders. A). P25, B). DT-51, C). TiO₂-m_A, D). TiO₂-m_A-R.

Thus, the interaction between the binding agent and other additives with the exposed surface was weaker for microemulsion titania than in case of commercial materials, as the morphology of P25 and DT-51 powders is strongly porous.

7.2.2. Characterization of TiO₂ films

7.2.2.1. Profilometry.

Using profilometry technique, the thickness of the films was estimated. All films were of a comparable thickness, which is shown in **Table 7.1**.

7.2.2.2. XRD.

Comparing particle size of TiO₂-m_A and TiO₂-m_A-R for powders and after preparation of films did not show a substantial change. While, XRD results of samples DT-51 and P25 showed different values, indicating that the method of ink preparation influences the crystalline size. Phase composition found from deconvolution of diffractograms and comparing the area under the peak,

showed that in P25 and DT-51 the content of anatase in films is similar of that in powders. While determination of anatase/rutile content in TiO₂-m_A sample was not possible since the peak area of rutile was insufficient to be determined by the software.

Table 7.1. XRD results of powders and films, thickness of TiO₂ films determined from profilometry.

Sample	Anatase ^a , %	Particle size (nm)	Thickness (μm)
Films			
P25	83	26	12.05
DT-51	100	13	11.94
TiO ₂ -m_A	nd	7	11.35
TiO ₂ -m_A-R	50	11 ^b	11.21
Powders			
P25	80	23	-
DT-51	100	20	-
TiO ₂ -m_A	95	8	-
TiO ₂ -m_A-R	49	11 ^b	-

^a Estimated from deconvolution of diffractograms.

^b Particle size determined for Rutile (110) reflection by the Scherrer formula.

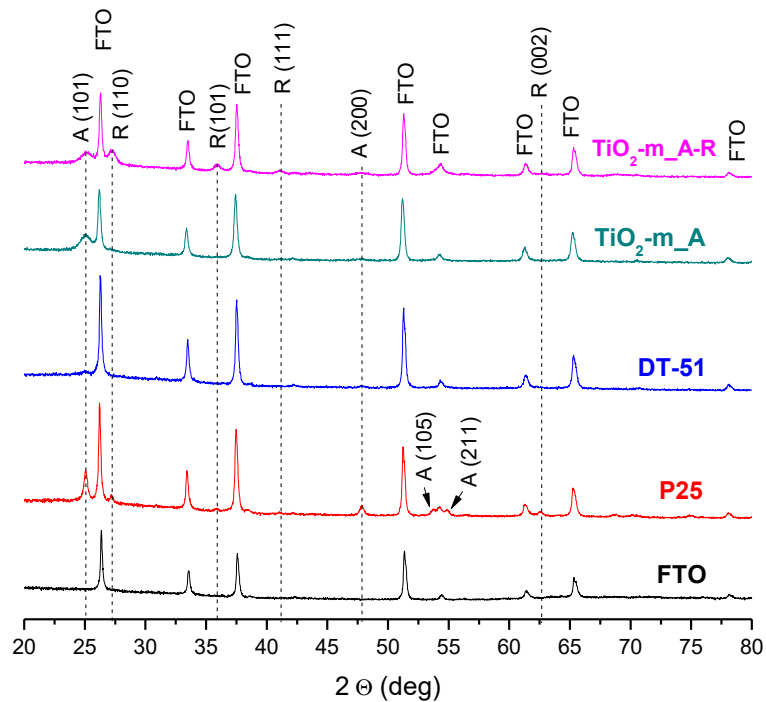
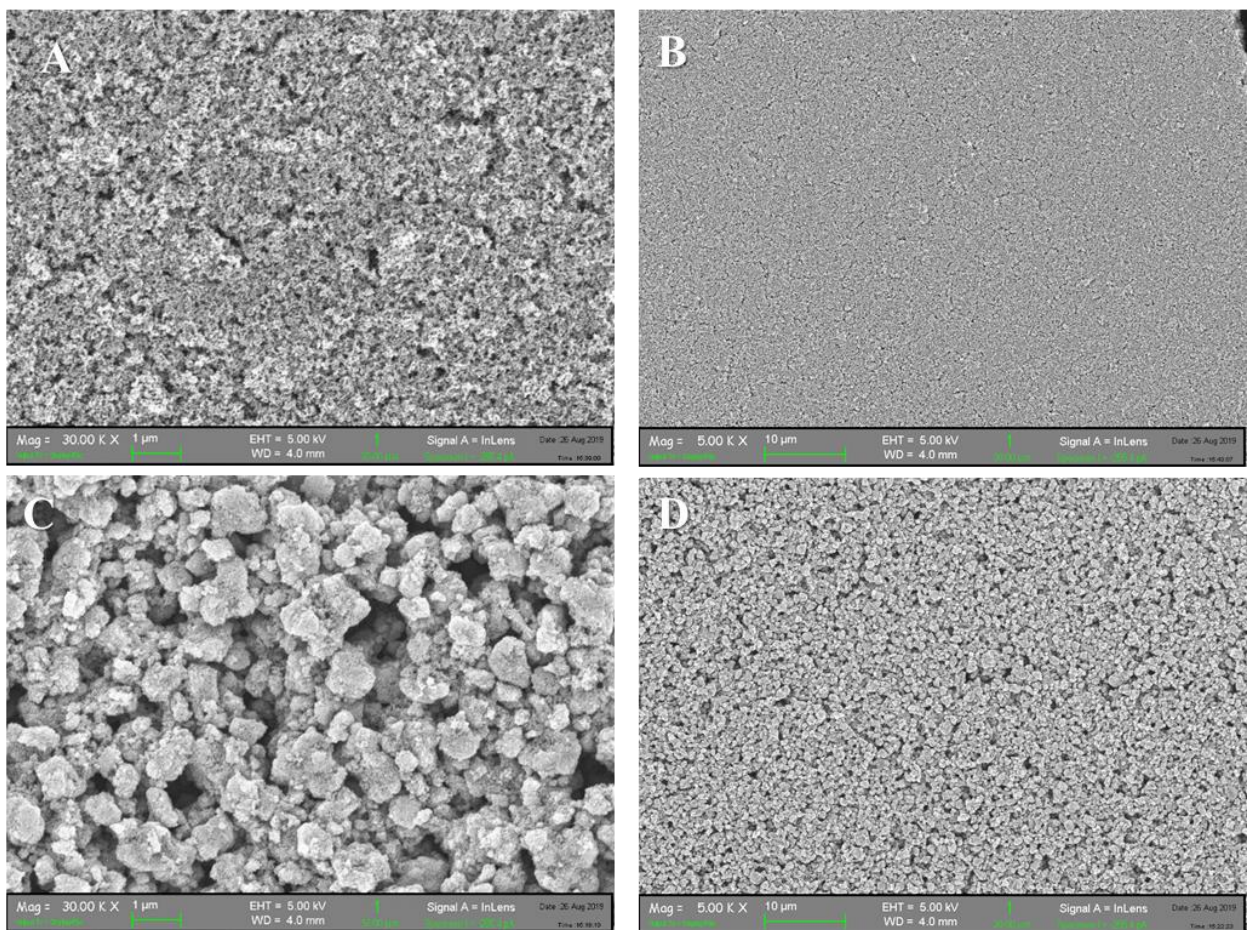


Figure 7.3. XRD of TiO₂ films.

7.2.2.3. SEM.

SEM images of TiO₂ films shown in **Figure 7.4** demonstrate quite homogeneous distribution of TiO₂ particles over FTO substrate on the large area, although with a different morphology and degree of agglomeration. Even though the best formulation was done for microemulsion-based inks, achieving a smooth and uniform films, SEM images show that big agglomerates could be still observed as for powders. SEM analysis of P25 electrode revealed the smallest pores and no aggregates compared to other materials. Therefore, deposition of TiO₂ does not change the porosity of titania, bearing in mind the SEM results, although this approach can avoid the sedimentation phenomenon observed for suspended powder in aqueous media, therefore it enables to better understand the difference in photo-catalytic activity of studied TiO₂ materials.



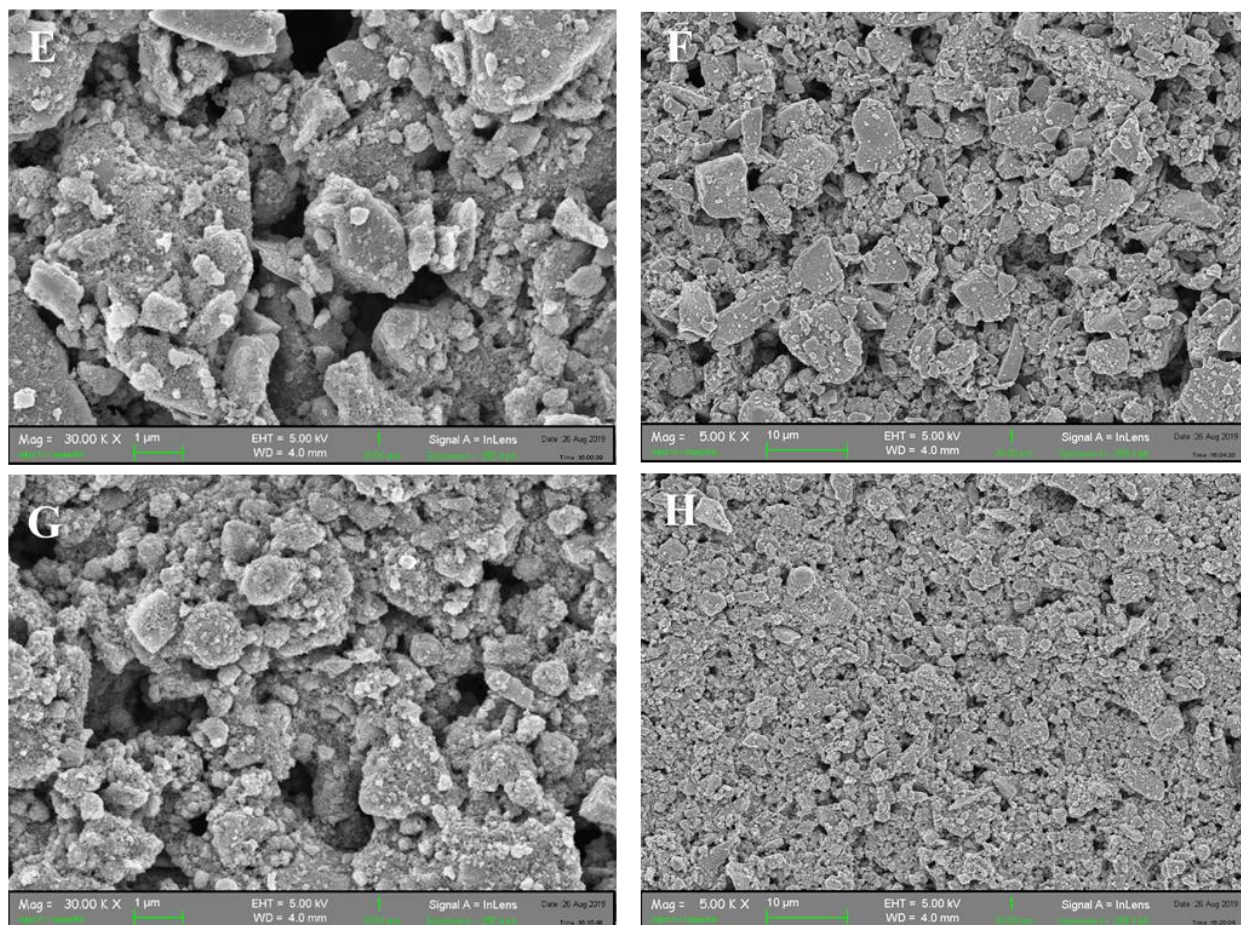


Figure 7.4. SEM images of TiO₂ films at low and high magnifications. A, B: P25; C, D: DT-51; E, F: TiO₂-m_A; G, H: TiO₂-m_A-R.

7.2.2.4. Optical characterization.

The most important optical properties for films for light-driven reaction is the band gap energy. For this purpose, three different methods are used in this Thesis: i) E_g determination from Transmittance spectra, ii) determination from Reflectance spectra, iii) determination by Tauc equation. **Figure 7.5** shows Transmittance spectra recorded for screen-printed films. The feasibility to record the signal of transmitted light indicates that obtained opaque white TiO₂ films are in fact semi-transparent and translucent. The fraction of incident light is drastically decreases at absorption edge of TiO₂, which is around 400 nm. Secondly, a comparison of Transmittance spectra indicates that TiO₂-m_A-R sample has an absorption within the limits of the visible spectrum.

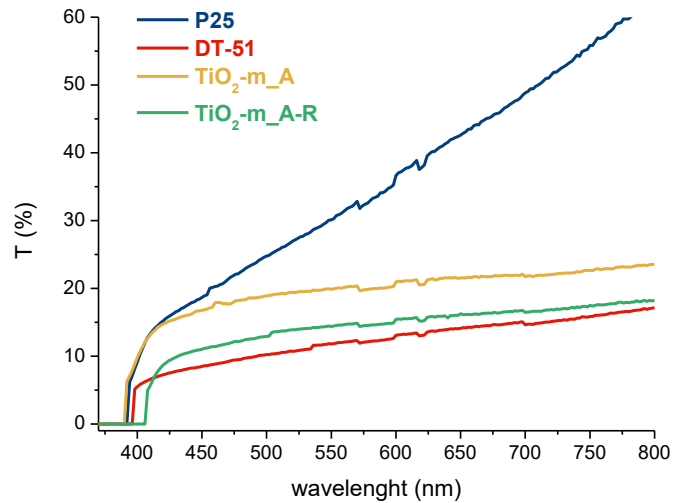


Figure 7.5. Transmittance spectra of TiO₂ screen-printed films.

Reflectance spectra of the films shown in **Figure 7.6** are in agreement with Transmittance spectra, indicating that all TiO₂ absorb in UV range of solar spectrum. Similarly, to Transmittance measurements, TiO₂-m_A-R sample demonstrate slightly greater red shift compared to other samples.

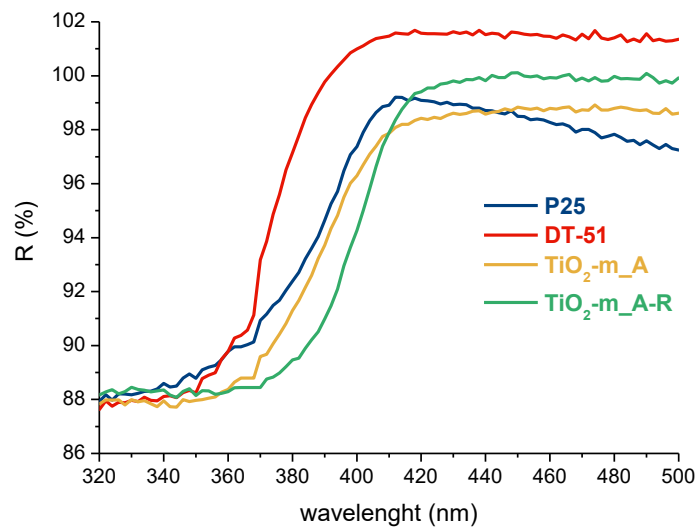


Figure 7.6. Reflectance spectra of TiO₂ screen-printed films.

Using **Eq. 3.2** described in Chapter 3, the Energy bandgap (E_g) of TiO₂ films can be determined using the reflectance spectra. Converting Reflectance data using **Eq. 3.3** from Chapter 3, Kubelka-Munk (KM) spectra can be built as shown in **Figure 7.7**.

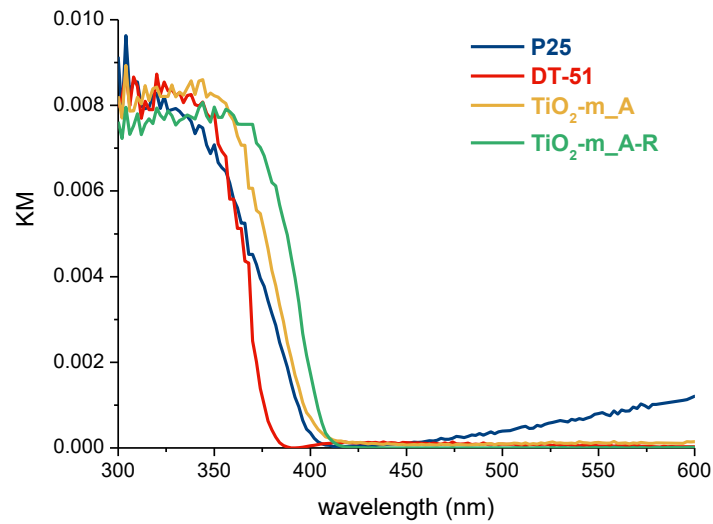


Figure 7.7. Kubelka-Munk (KM) spectra of TiO₂ screen-printed films.

The E_g of TiO₂ films were found in the same way used for Reflectance. All E_g values obtained with Reflectance and KM data are shown in **Table 7.2**.

The bandgap of semiconductors could be calculated also using Tauc equation (**Eq. 3.4**) described in Chapter 3. The value of E_g of different TiO₂ films were found from Tauc plot (**Figure 7.8**), and the results were presented in **Table 7.2**.

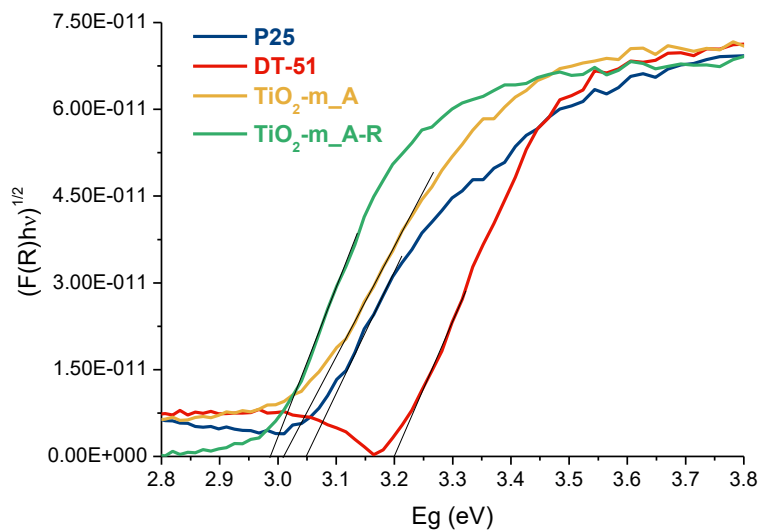


Figure 7.8. Tauc plot of TiO₂ screen-printed films.

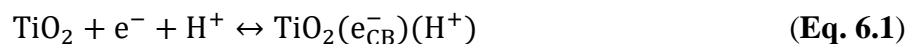
Table 7.2. Comparison of energy bandgap (E_g , eV) for TiO_2 films and powders by different methods of estimation.

sample	Reflectance	KM	Tauc plot
Films			
<i>P25</i>	3.05	3.04	3.05
<i>DT-51</i>	3.16	3.19	3.20
<i>TiO₂-m_A</i>	3.05	3.02	3.02
<i>TiO₂-m_A-R</i>	2.98	2.99	2.98
Powders			
<i>P25</i>	3.02	3.10	3.05
<i>DT-51</i>	3.19	3.26	3.20
<i>TiO₂-m_A</i>	2.98	3.08	2.98
<i>TiO₂-m_A-R</i>	2.96	3.02	2.96

The results of **Table 7.2** show that the values of energy bandgap of the titanium dioxide films are slightly differ from that of powders. These differences are mainly due to the different surface morphologies between the powders and films. The method of calculation is altering the value of energy bandgap. Thus, the results estimated using KM spectra are slightly greater compared to the results obtained from Reflectance spectra and Tauc plot. These observations are in agreement with the work reported by R. Lopez and co-workers.^[148] Nevertheless, energy bandgap increases in the order: TiO_2 -m_A-R < TiO_2 -m_A < P25 < DT-51, both for powders and films.

7.2.2.5. Electrochemical characterization.

Cyclic voltammetry (CV) results presented in **Figure 7.9** showed the general trend of current density increase with the increase of scan rate. On the surface of the TiO_2 electrode upon the potential applied the following reaction is taking place.^{[237],[238],[239],[240]}



or



The current is limited by the diffusion of H^+ to the electrode surface. The concentration gradient of H^+ is controlled by its concentration at the electrode and its diffusion in solution. According to Nernst equation, once the cell voltage was changed, the concentration of H^+ at the

electrode surface is also changed. Therefore, a faster voltage sweep causes a larger concentration gradient near the electrode, resulting in a higher current.

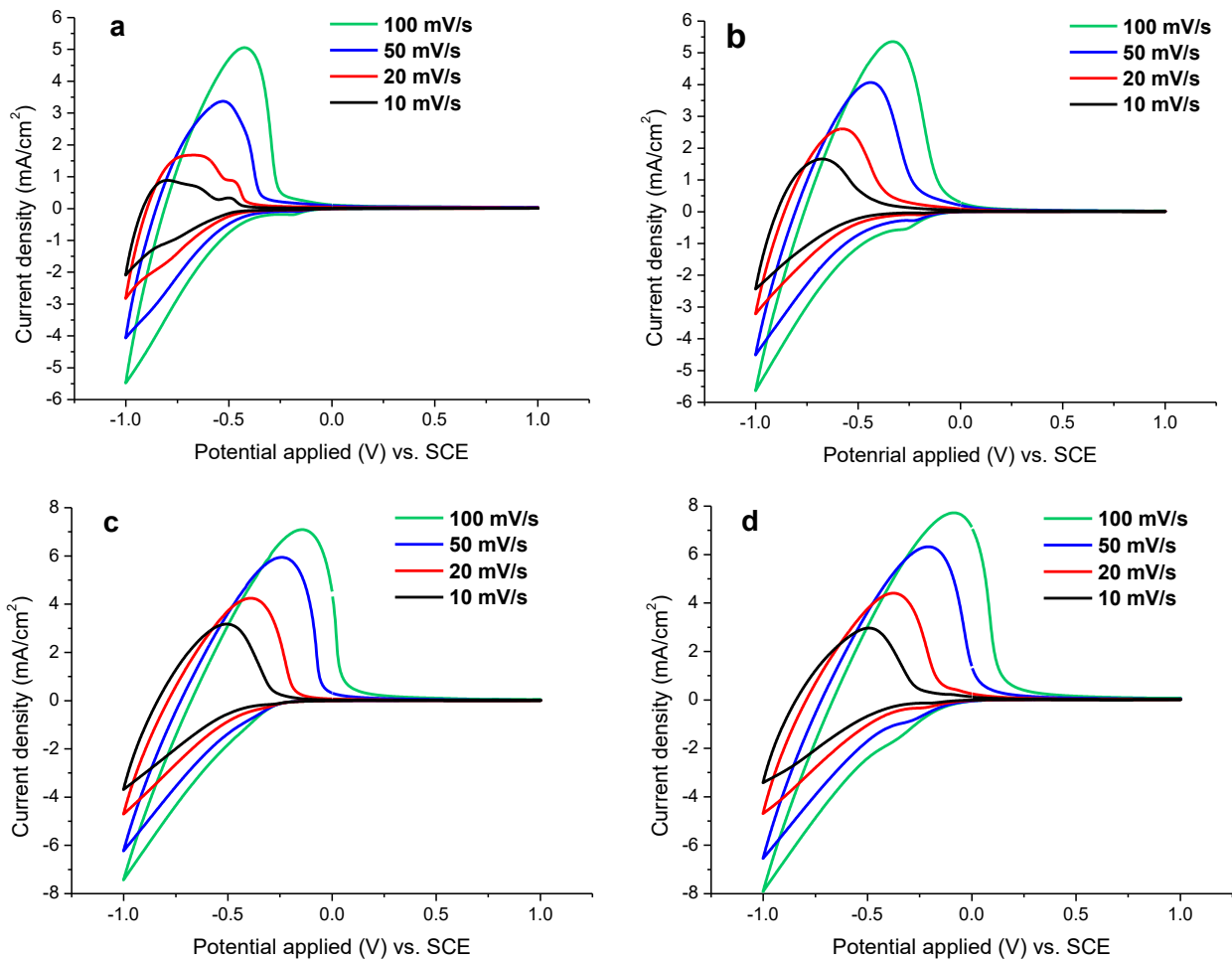


Figure 7.9. Cyclic voltammograms of TiO₂ films: a). P25, b). DT-51, c). TiO₂-m_A, d). TiO₂-m_A-R.

Secondly, the positive and negative current densities for all the electrodes indicate that the reaction of proton uptake is reversible, which is in accordance with the literature and **Eq. 6.1-6.2**. Thus, at negative (reductive) current, TiO₂ was reduced with subsequent H⁺ uptake.

The current density of electrodes was compared at 10 mV/s (**Figure 7.10**). An additional peak for P25 electrode at a positive current (around -0.5 V vs SCE) was observed corresponding to oxidation of some species. Since this is not observed for other electrodes, this behavior was attributed to the structure or intrinsic properties of P25 electrode.

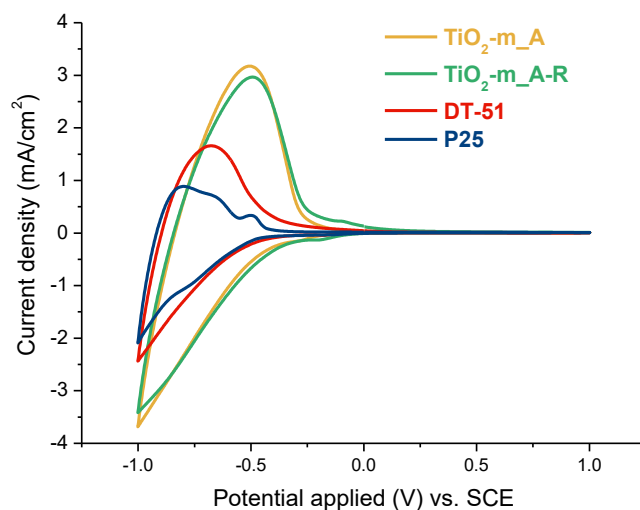


Figure 7.10. Comparison of cyclic voltammograms of different films recorded at 10 mV/s scan rate.

Closer look at SEM images related to P25 film (**Figure 7.11**) revealed some cracks on the surface of the film, resembling the mask of the screen-printing machine. Thus, the additional peak observed on voltammograms in **Figure 7.10** was assigned to the presence of FTO. Indeed, CV measurement using the FTO support only demonstrated the same peak position as could be seen from **Figure 7.12**. Interestingly, this oxidative peak of current was observed at low scan rates (10 and 20 mV/s), but not at high ones (50 and 100 mV/s), which suggests that at high scan rate the scan rate the species did not have time to reach FTO surface to get oxidized. M.Zukalova and co-workers^[237] assigned this anodic current to oxidation of H_2 dissolved in electrolyte solution near the FTO surface.

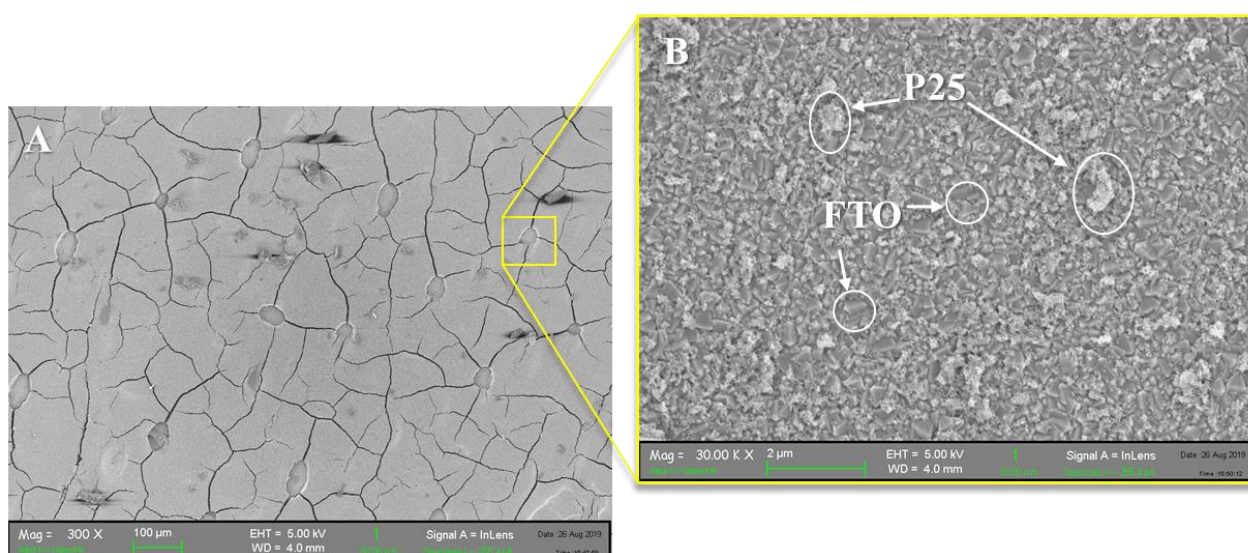


Figure 7.11. SEM images of P25 electrode A) at a wide area, and B) with a magnified zone of a crack.

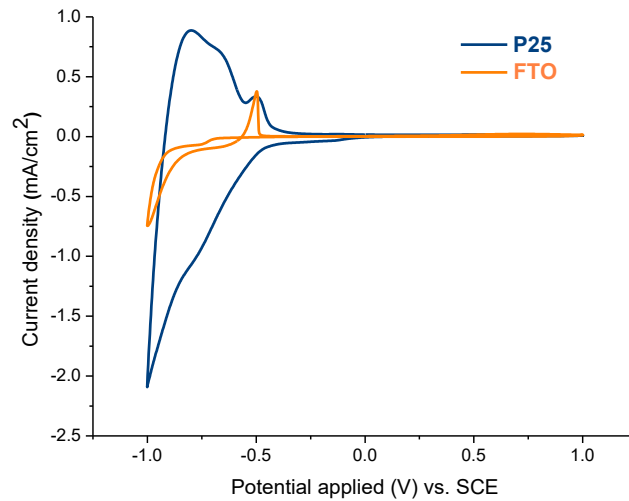


Figure 7.12. Comparison between FTO and P25 electrode in 0.01 M H₂SO₄ electrolyte at 10 mV/s.

The accumulation charges properties of TiO₂ electrodes were determined using the following equation^{[241],[242]}:

$$C = \frac{Q}{\Delta V \cdot m} \quad (\text{Eq. 6.3})$$

Where ΔV is equals to window voltage, Q equals to total charge (integrated area of voltammogram), m is the mass of TiO₂.

Total integral includes two parts of charge accumulations: at Electrical Double Layer (EDL) (accumulation at a surface)^[242], and the bulk one.

Comparing the total charge accumulated in reductive current presented in **Figure 7.13**, the descending trend of total charge accumulation could be observed for all the samples. The protons are accumulated in the structure of TiO₂ to compensate a negative charge that is induced by the potential applied. Therefore, at a high scan rate, the charge does not have enough time to move into pores of TiO₂ and to be accumulated in the structure.

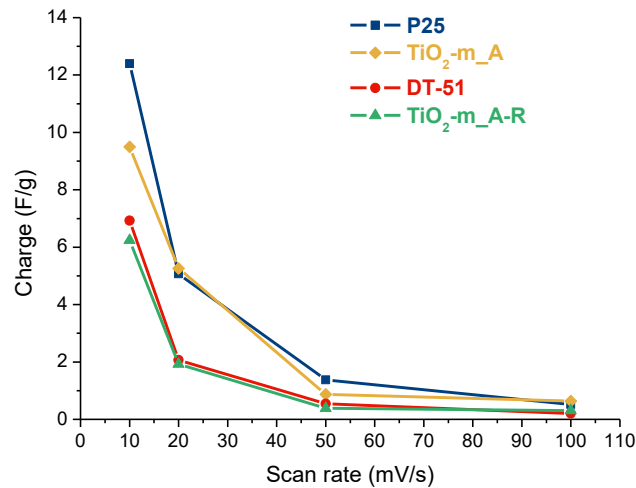


Figure 7.13. Capacitance of the electrodes, normalized by the weight of TiO₂ deposited.

At a low scan rate, P25 electrode has a highest accumulated charge than the other samples. This is probably due to a more porous morphology of the film compare to the other samples. On the other hand, DT-51 has a lower charge accumulation than TiO₂-m_A that somehow contradicts to the fact that it has a more porous structure than microemulsion-based titania. However, it is known that the surface of DT-51 used in this thesis has approximately 1.25 wt.% of SO₃ groups that might adversely affect the interaction of the TiO₂ electrode with H₂SO₄ electrolyte. Therefore, a set of experiments has been conducted using other electrolyte such as 0.01 M HClO₄.

Figure 7.14 shows cyclic voltammetry results and the obtained specific capacities for DT-51 electrode using 0.01 M HClO₄ electrolyte. Indeed, the specific capacities are higher than the other previously reported with H₂SO₄ electrolyte due to better interaction between DT-51 surface (with SO₃ groups) with the HClO₄ solution.

Moreover, using HClO₄ electrolyte, DT-51 electrodes show the presence of oxidation peak around -0.5 V vs SCE as was observed on P25 electrodes, because the influence of FTO substrate is more evident in this acidic condition. Comparison of cyclic voltammetry results of FTO glass only using different electrolytes (**Figure 7.15**) demonstrate a similar anodic peak position in both solutions.

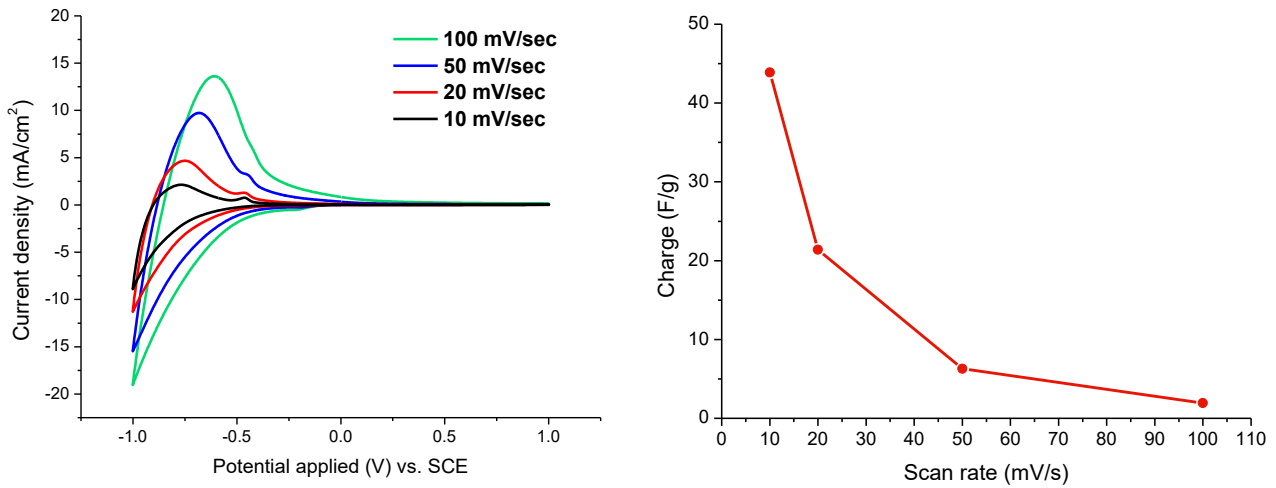


Figure 7.14. Interaction of DT-51 electrode with 0.01 M HClO₄ electrolyte. Right: Cyclic voltammograms at different scan rate. Left: Specific capacity.

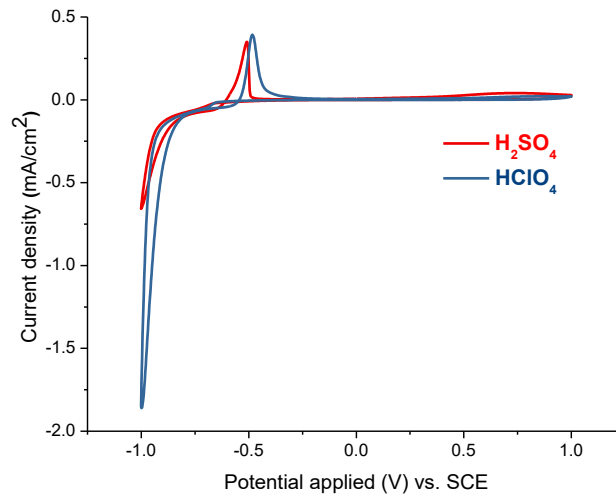


Figure 7.15. Cyclic voltammograms of FTO glass substrate alone in contact with 0.01 M H₂SO₄ and 0.01 M HClO₄ electrolytes.

Particular attention has been devoted to a cathodic signal observed for the electrodes at applied potential above -0.5 V vs SCE (**Figure 7.16**), which was assigned to a charge accumulation at trap states.^{[240],[243],[239]} Trap states are the energy levels lying below the conduction band of TiO₂ semiconductor and can be generated due to the heating, calcination or cooling of titania. Thus, these trap states can be attributed to various types of defects.^{[240],[244],[245]} For instance, oxygen vacancies and the hydroxyl groups are the most common point defects, the trapping nature of which has been confirmed by DFT calculations. Recently, the new types of defects have been considered such as uncoordinated metal ions and particle-particle interactions (grain boundaries).^{[246],[162]} There is a different opinion in the literature regarding the effect of trap states on the photocatalytic performance. Some works reported that the presence of trap states delay recombination and may act as active sites

for catalysts, which explains increase in overall photocatalytic performance.^[244] On the other hand, it has been reported that slow charge transport is attributed to a high concentration of localized states, which act as electron-trapping sites.^[247] Additionally, it has been shown that the diffusion coefficient was strongly affected by both the number and the energy distribution of trap states.^[239]

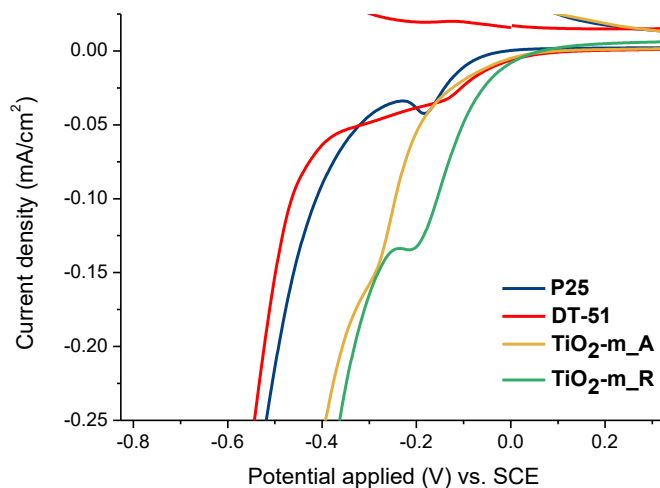


Figure 7.16. Trap states presented at 10 mV/s (magnification of the voltammograms).

In this case, the trap states were found in the region of reductive current. In order to “quantified” the trap states, the capacitance of the trap state peak was calculated using the area under the peak. The obtained results reported in **Table 7.3** suggest that the increase of capacitance is might be due to the increased number of trap states at the grain boundaries. Charge accumulation at 10 mV/s in trap state decreases in the order: $TiO_2\text{-}m_A\text{-}R > DT\text{-}51 > TiO_2\text{-}m_A > P25$, which is in accordance with the results of specific capacity using total charge accumulated (**Figure 7.13**).

Table 7.3. Charge accumulation at trap states region of TiO_2 electrodes at 10 mV/s.

sample	C (mF)
P25	0.15
$TiO_2\text{-}m_A$	0.27
DT-51	0.47
$TiO_2\text{-}m_A\text{-}R$	0.75

Electrochemical Impedance Spectroscopy (EIS) was used to determine the charge-transfer resistance and series resistance (R_s) of the TiO_2 electrodes and used to calculate the electronic conductivity (σ) using the following equation:

$$\sigma = \frac{h}{A \times R_S} \text{ (S/cm)} \quad \text{(Eq. 6.4)}$$

Where A is the electrode area (cm^2) and h is the film thickness (cm).

The equivalent circuits used to determine resistance and conductivity are illustrated in **Figure 7.17**. The circuit A was used to fit the EIS data for DT-51, $\text{TiO}_2\text{-m_A}$ and $\text{TiO}_2\text{-m_A-R}$, while circuit B was used to fit the data for P25. For both circuits, R_1 describe the series resistance related to the substrate and TiO_2 film. The charge-transfer resistance (R_2) and Constant Phase Element (CPE_1) are related to electron transfer and charge accumulation properties of TiO_2 film in contact with the electrolyte. Finally, in the circuit A, the W_o describe the diffusion of the ions inside the electrolyte solution, while in the circuit B, another R_3/CPE_2 system was used due to the different surface properties of the P25 electrode. The R_1 values were used to calculate the electronic conductivity of titania films.

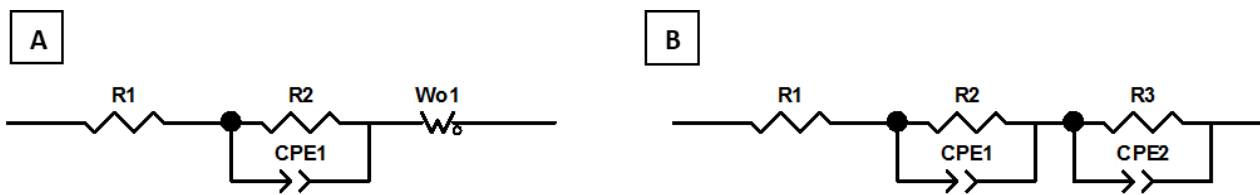


Figure 7.17. Equivalent circuits used to fit the experimental EIS data for A: DT-51, $\text{TiO}_2\text{-m_A}$ and $\text{TiO}_2\text{-m_A-R}$; B: P25 electrodes.

The impedance spectra in form of Nyquist plot and the fitting curve obtained with the equivalent circuits are shown in **Figure 7.18**.

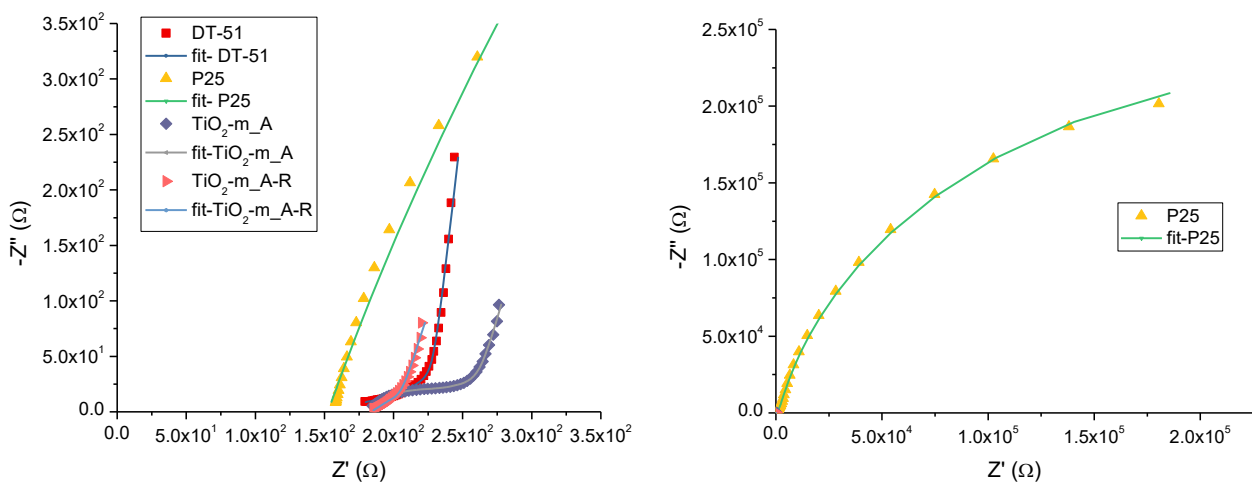


Figure 7.18. Nyquist plots with data fitting obtained for titania electrodes.

Table 7.4. Data used for calculating and conductivity (σ) of TiO₂ films.

sample	Thickness (h, cm)	Area (A, cm ²)	R ₁ (Ω)	σ (S cm ⁻¹)
DT-51	12	0.25	167	$2.87 \cdot 10^{-5}$
P25	12		153	$3.14 \cdot 10^{-5}$
TiO ₂ - m_A	11		180	$2.44 \cdot 10^{-5}$
TiO ₂ - m_A-R	11		183	$2.40 \cdot 10^{-5}$

The results obtained from EIS measurements indicate that P25 has the highest conductivity, followed by DT-51, TiO₂-m_A and, finally, TiO₂-m_A-R. The presence of higher number of trap states (**Table 7.3**) may indeed decrease the flow of electrons, thus the conductivity.

The electronic properties of the titania-based electrodes were determined by Mott-Schottky (MS) equation as followed:

$$\frac{1}{C^2} = \frac{2}{\epsilon\epsilon_0 e A^2 N_D} \left(V - V_{fb} - \frac{kT}{e} \right) \quad (\text{Eq.6.5})$$

The number of donors (N_D), or doping density, and the Flat band potential (V_{fb}) could be found from linear dependence of $1/C^2$ vs. applied potential (V) (**Figure 7.19**), according to the equations below:

$$\frac{1}{C^2} = \frac{2}{\epsilon\epsilon_0 A^2 e N_D} V - \frac{2}{\epsilon\epsilon_0 e N_D} \left(V_{fb} + \frac{kT}{e} \right) \quad (\text{Eq. 6.6})$$

$$N_D = \frac{2}{\text{slope} \times \epsilon\epsilon_0 e} \quad (\text{Eq.6.7})$$

$$V_{fb} = \frac{\text{intercept}}{\text{slope}} - \frac{kT}{e} \quad (\text{Eq. 6.8})$$

Where dielectric vacuum permittivity $\epsilon = 8.85 \cdot 10^{-12}$ C²/J/m; $\epsilon_0 = 31$ (anatase), 114 (rutile), 55 (mixture); electrical charge $e = 1.60 \cdot 10^{-19}$ C; surface area of material $A^2 = 6.25 \cdot 10^{-10}$ m⁴, k is the Boltzman constant and T is absolute temperature. The MS plots are reported in Figure 7.19.

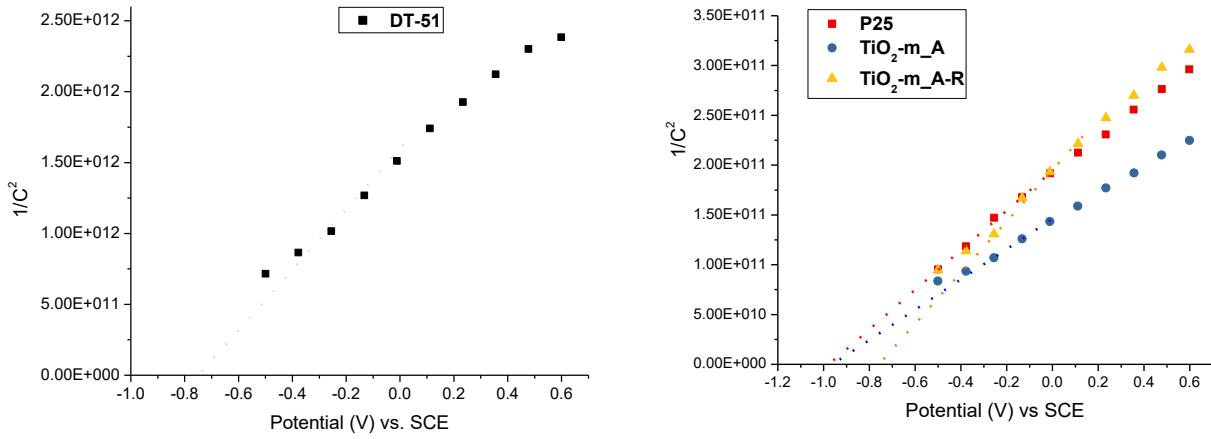


Figure 7.19. Mott-Schottky plot for DT-51 (right) and P25, TiO₂-m_A, TiO₂-m_A-R (left) recorded at 10 kHz frequency.

Number of donors and Flat band potential were calculated and the results are presented in **Table 7.5**. The highest conductivity of P25 is in agreement with high number of donors for this sample. A high value of number of donors was found also for TiO₂-m_A, however the conductivity for this sample is lower than that of P25 probably due to presence of the trap states.

Since in the n-type semiconductor the Flat Band potential is close to the Conduction Band, it allows establishing the semiconductor conduction band level with respect to the reference potential:

$$V_{NHE} = V_{SCE} + V_{SCE}^0 + 0.059 \times pH \quad (\text{Eq.6.9})$$

Where $V_{SCE}^0 = +0.241$ V and pH=5.8 (0.1M Na₂SO₄).

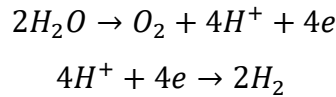
Table 7.5. Dielectric permittivity (ϵ_0), Number of donors (N_D) and Flat band potential (V_{fb}) of TiO₂ electrodes.

sample	ϵ_0	N_D (m ⁻³)	V_{fb} (V) vs. SHE	V_{fb} (V) vs. NHE
DT-51	31	$3.58 \cdot 10^{25}$	-0.755	-0.1718
P25	55	$2.04 \cdot 10^{26}$	-0.973	-0.3898
TiO ₂ -m_A	55	$2.74 \cdot 10^{26}$	-0.972	-0.3888
TiO ₂ -m_A-R	55	$1.60 \cdot 10^{26}$	-0.773	-0.1898

Therefore, having the value of energy bandgap (E_g) determined from Tauc plot, the value of the Valence band (E_{VB}) can be determined as follow:

$$E_{VB} = E_g + E_{CB} \quad (\text{Eq.6.10})$$

Based on the results obtained, the energy diagram for each corresponding materials could be built, which is shown in **Figure 7.20**. The diagram demonstrates that P25 and TiO₂-m_A have comparable energy levels of conduction and valence bands, capable of water splitting, followed by the half-reactions in acidic pH^[248]:



Whereas, reduction potential of DT-51 and TiO₂-m_A-R lie just below the limit of proton reduction half-reaction. In this case, the application of an external bias is required to produce hydrogen. Nevertheless, valence band potential value for all the types of electrodes is making the process of glycerol oxidation thermodynamically feasible, $E^0(CO_2/C_3H_8O_3) = -0.004$ V vs. NHE at pH=0.^[61]

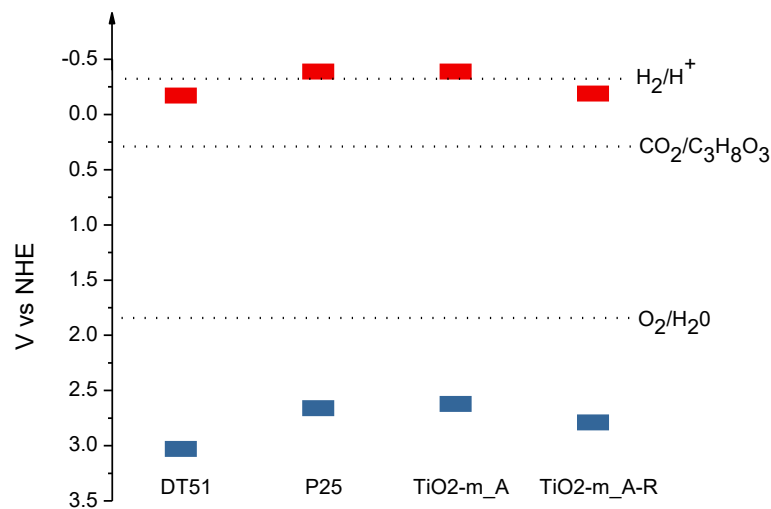


Figure 7.20. Energy diagram for TiO₂ electrodes drawn up based on the results of MS analysis and Tauc plot.

7.2.2.6. Photoelectrochemical characterization

Linear sweep voltammograms of TiO₂ electrodes under dark and illumination conditions are illustrated in **Figure 7.21**. The dark curves show the presence of small “dark-current” due to the corrosion phenomena related to metallic electrodes. The photocurrent trend increase is following the order: TiO₂-m_A-R < TiO₂-m_A < P25 and confirms the previously electrochemical results. In fact, P25 electrode shows highest capability to accumulate charge, possess the highest electrical conductivity and number of donors with small amount of traps state (with reduced recombination

electrons-holes). Whereas microemulsion TiO_2 based electrodes, the best electronic and photoelectrochemical properties are found for the electrodes based on anatase instead of the one with mixed phase. Different result was found for the DT-51 electrode able to produce the highest photocurrent in oxidative conditions. This is probably due to the high carriers' mobility for pure anatase based electrode compared to the other mixed phases electrodes.^{[109], [110]}

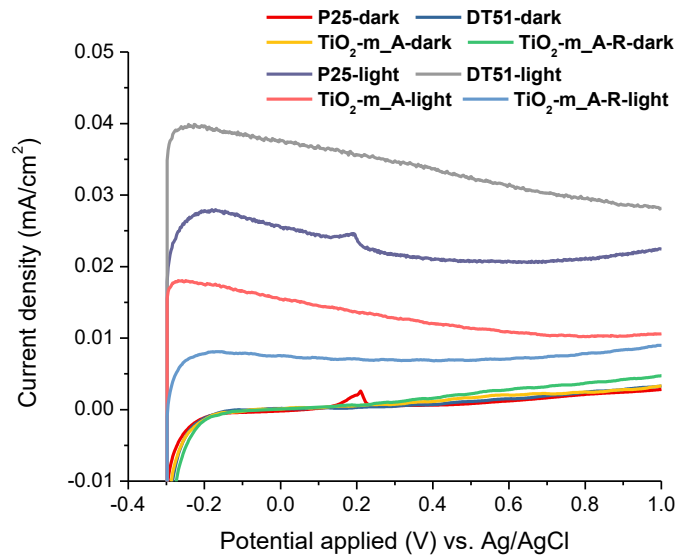


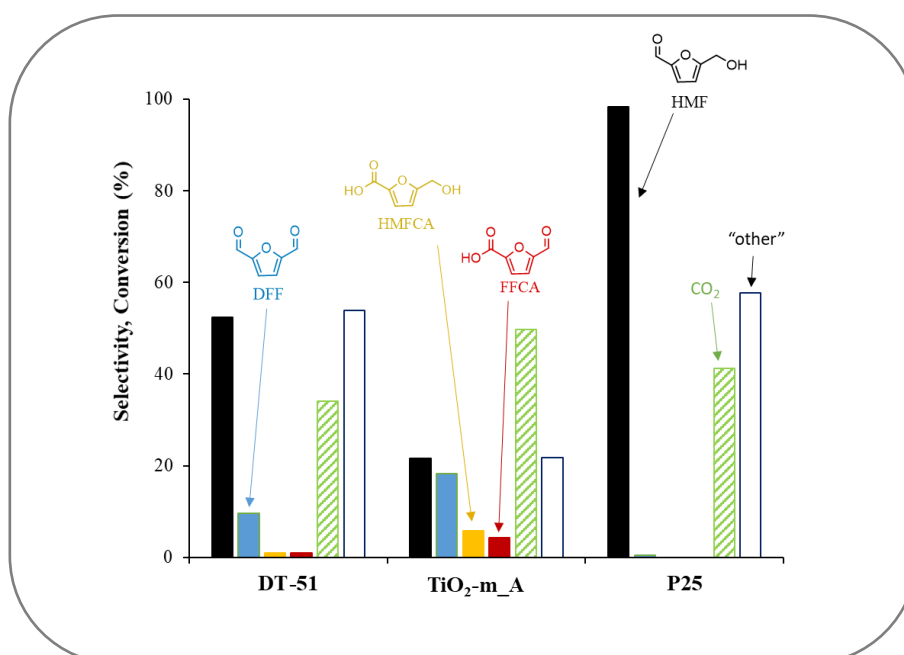
Figure 7.21. Linear sweep voltammograms of prepared electrodes in the dark and under illumination.

Conclusions

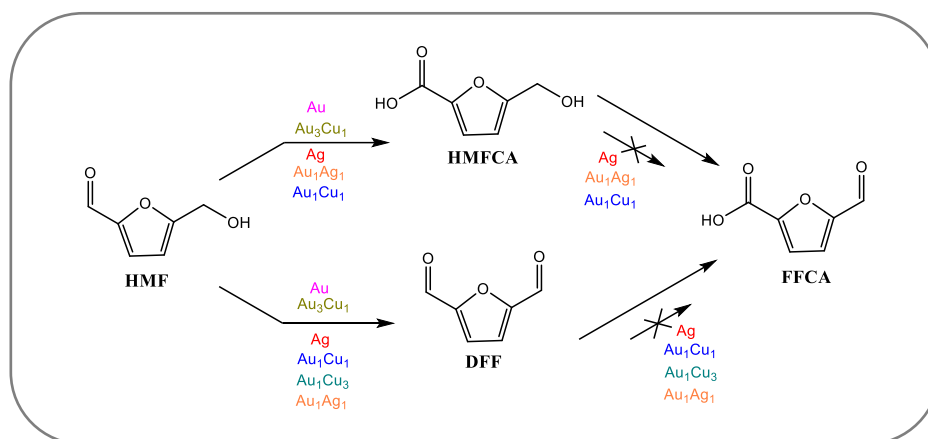
The presented work is the part of ongoing progressive shift from the use of fossil fuels to renewable feedstock as biomass and its sustainable upgrading. In this view, lignocellulosic biomass and triglycerides are considered as primary sources due to its availability, abundance and virtual carbon neutral nature. Therefore, in this work we targeted two molecules such as 5-hydroxymethylfurfural (HMF), a sugar-derived platform, and glycerol, a waste from biodiesel plants, with the aim to produce chemicals and fuels through the processes such as selective photo-oxidation and photo-reforming, respectively.

The work started from the synthesis of titanium oxide using water-in-oil microemulsion method. The method was also used to prepare different crystalline phases of titania, which are rutile and anatase. The resulted nano-oxides were found to have smaller average crystalline size, higher surface area and narrower band gap than commercial TiO₂ samples, P25 and DT-51. With the aim to improve absorbing capabilities of TiO₂ various metal and metal oxide nanoparticles were deposited by incipient wetness impregnation of metal salt and pre-formed sols; and deposition-precipitation of metal precursor salt.

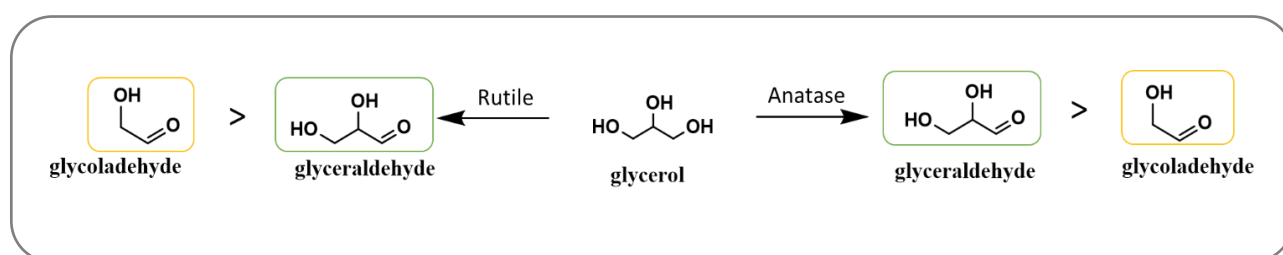
Chapter 4 reveals the results on heterogeneous photo-oxidation of HMF. As general observation, in the base-free conditions for all the samples CO₂ was detected, suggesting an overall decomposition tendency. Despite, the synthesized titania (TiO₂-m_A) demonstrated a better selectivity towards liquid phase products such as 2,5-hydroxymethyl furfural (HMFCFA), 2,5-diformyl furan (DFF) and also 2,5-formylfuran carboxylic acid (FFCA) compared to commercial analogues (DT-51 and P25).



The monometallic gold nanoparticles deposited on microemulsion-derived titania demonstrated to be the most selective material towards liquid phase products such as HMFCFA, DFF and FFCA. In contrast to catalytic reaction, in photo-catalytic one, the combination of Au-Cu in alloy or core-shell did not show a beneficial effect. The presence of Ag nanoparticles did not allow the formation of other liquid products than HMFCFA and DFF.



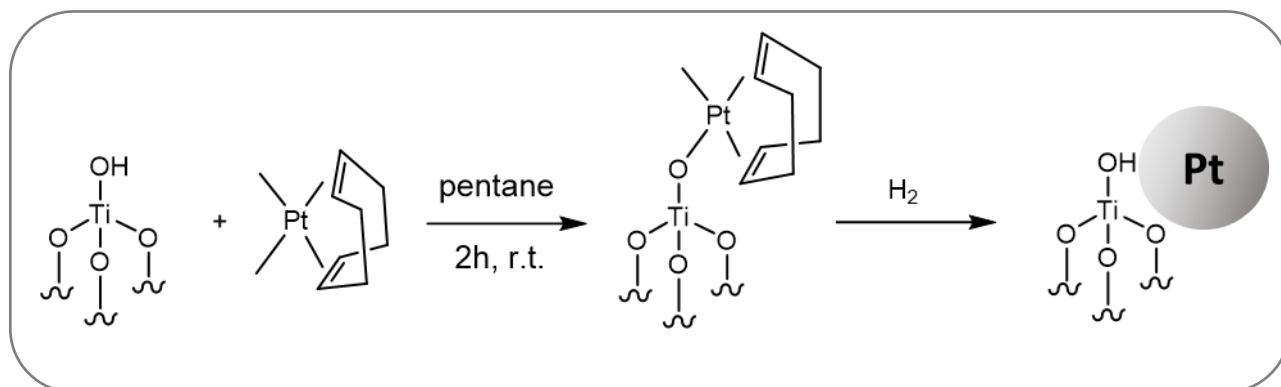
Chapter 5 discusses on the results of glycerol photo-reforming. Within the supports used, commercial TiO₂ P25 demonstrated greater rates of hydrogen production compared to DT-51 and microemulsion-synthesized titania, regardless the type of noble metal co-catalyst. Among all the metal-decorated catalysts tested, Pt nanoparticles prepared by deposition-precipitation showed the most promising results towards hydrogen production, because of the small and homogeneously distributed nanoparticles. The phase composition was found to be effecting the selectivity of liquid phase products. Rutile was more selective to direct C-C cleavage to form glycolaldehyde, while anatase was more selective towards glyceraldehyde.



The spray-freeze drying technique allowed preparing lab-synthesized titania with a well-developed porous microstructure, decreasing its apparent density comparable to P25. This post-treatment led to a remarkable enhancement of hydrogen production by home-made material, exceeding the rates of commercial benchmark P25 due to a greater specific surface area.

The favorable parameters for effective hydrogen and liquid phase intermediates production from glycerol photo-reforming were assigned to the catalyst porosity, the type of polymorph, the specific surface area, the type and size of metal co-catalyst.

Surface organometallic chemistry (SOMC) is bridging the gap between homogeneous and heterogeneous catalysts by designing well-defined complexes. From the SOMC perspective, the concentration of hydroxyl groups of the lab-synthesized titania was chemically titrated with *n-BuLi*. Isolated hydroxyl groups were clearly observed at 500°C; however adsorbed molecules of water were still present as well. At 700°C the hydroxyls and coordinated water undergo dehydration, forming agglomerates, followed by the phase transition from anatase to rutile. Using SOMC approach Pt complex was grafted on lab-synthesized TiO₂ surface with the subsequent reduction to form Pt nanoparticles. The prepared sample outperformed in the reaction of glycerol photo-reforming the samples with Pt deposited by incipient wetness impregnation and deposition-precipitation owing to a better dispersion of Pt nanoparticles.



Widely used in industry screen-printing technique has been used for thick TiO₂ films fabrication on FTO support with the aim to avoid the agglomeration and sedimentation phenomena of suspended powders in water and differences in apparent density of TiO₂ powders. The electrochemical characterization gave deep insights into the electronic structure of the titania powders. The results showed that the presence of trap states may decrease the flow of electrons, thus the conductivity. The found value of capacitance at a trap state region was associated to a number of the trap states. Thus, commercial P25 showed a high value of conductivity and number of donors, which is in agreement with the lowest charge accumulation at a trap state.

Summarizing all, this work show that even though the yield of liquid products is still low, it is possible to oxidize selectively biomass-derived molecules such as glycerol and HMF by means of solar energy over TiO₂-based catalysts. However, the catalyst optimization still has to be done with the aim to improve the selectivity of HMF conversion. A process of electro-photo-reforming can be proposed as an alternative and efficient way of glycerol upgrade by means of film preparation. The results of glycerol photo-reforming suggests that the process can be also transferred to more complex molecules (e.g. glucose).

Bibliography

- [1] F. Cherubini, *Energy Convers. Manag.* **2010**, *51*, 1412–1421.
- [2] ‘IEA. IEA bioenergy Task 42 on biorefineries: co-production of fuels, chemicals, power and materials from biomass. In: Minutes of the third Task meeting, Copenhagen, Denmark, 25–26 March 2007’, can be found under <https://www.iea-bioenergy.task42-biorefineries.com/en/ieabiorefinery.htm>, **2008**.
- [3] R. Muktham, S. K. Bhargava, S. Bankupalli, A. S. Ball, *J. Sustain. Bioenergy Syst.* **2016**, *6*, 72–92.
- [4] R. A. Sheldon, *Green Chem.* **2014**, *16*, 950–963.
- [5] A. V. Puga, *Coord. Chem. Rev.* **2016**, *315*, 1–66.
- [6] F. Basile, S. Albonetti, F. Cavani, E. Lombardi, R. Mafessanti, in *Chem. Fuels from Bio-Based Build. Blocks*, **2016**, pp. 79–110.
- [7] F. H. Isikgor, C. R. Becer, *Polym. Chem.* **2015**, 4497–4559.
- [8] Z. Sun, A. De Santi, S. Elangovan, K. Barta, *Chem. Rev.* **2018**, *118*, 614–678.
- [9] J. J. Bozell, G. R. Petersen, *Green Chem.* **2010**, *12*, 539–554.
- [10] R. Van Putten, J. C. Van Der Waal, E. De Jong, C. B. Rasrendra, H. J. Heeres, J. G. De Vries, *Chem. Rev.* **2013**, *113*, 1499–1597.
- [11] L. T. Mika, E. Csefalvay, A. Nemeth, *Chem. Rev.* **2018**, *118*, 505–613.
- [12] F. N. D. C. Gomes, L. R. Pereira, N. F. P. Ribeiro, M. M. V. M. Souza, *Brazilian J. Chem. Eng.* **2015**, *32*, 119–126.
- [13] S. Albonetti, T. Pasini, A. Lolli, M. Blosi, M. Piccinini, N. Dimitratos, J. A. Lopez-sanchez, D. J. Morgan, A. F. Carley, G. J. Hutchings, et al., *Catal. Today* **2012**, *195*, 120–126.
- [14] J. G. de Vries, in *Heterocycl. Chem. 21st Century* (Eds.: E.F. V Scriven, C.A.B.T.-A. in H.C. Ramsden), Academic Press, **2017**, pp. 247–293.
- [15] L. Hu, G. Zhao, W. Hao, X. Tang, Y. Sun, S. Liu, *RSC Adv.* **2012**, *2*, 11184–11206.
- [16] R. He, X. Huang, P. Zhao, B. Han, T. Wu, Y. Wu, *Waste and Biomass Valorization* **2018**, *9*, 657–668.
- [17] M. J. Antal, W. S. L. Mok, G. N. Richards, *Carbohydr. Res.* **1990**, *199*, 91–109.
- [18] C. Moreau, R. Durand, S. Razigade, J. Duhamet, P. Faugeras, P. Rivalier, P. Ros, G. Avignon, *Appl. Catal. A Gen.* **1996**, *145*, 211–224.
- [19] M. Bicker, D. Kaiser, L. Ott, H. Vogel, *J. Supercrit. Fluids* **2005**, *36*, 118–126.
- [20] A. Harlin, in *Handb. Bioplastics Biocomposites Eng. Appl.*, John Wiley & Sons, Inc., **2011**, pp. 511–553.

- [21] S. Albonetti, A. Lolli, V. Morandi, A. Migliori, C. Lucarelli, F. Cavani, *Appl. Catal. B Environ.* **2015**, *163*, 520–530.
- [22] J. Artz, S. Mallmann, R. Palkovits, *ChemSusChem* **2015**, *8*, 672–679.
- [23] T. Pasini, M. Piccinini, M. Blosi, R. Bonelli, S. Albonetti, N. Dimitratos, J. A. J. Lopez-Sanchez, M. Sankar, Q. He, C. C. J. Kiely, et al., *Green Chem.* **2011**, *13*, 2091–2099.
- [24] J. Tuteja, H. Choudhary, S. Nishimura, K. Ebitani, *ChemSusChem* **2014**, *7*, 96–100.
- [25] A. Hussain Motagamwala, W. Won, C. Sener, D. M. Alonso, C. T. Maravelias, J. A. Dumesic, *Sci. Adv.* **2018**, *4*, 1–8.
- [26] R. Wojcieszak, C. P. Ferraz, J. Sha, S. Houda, L. M. Rossi, S. Paul, *Catalysts* **2017**, *7*, 1–23.
- [27] A. Lolli, S. Albonetti, L. Utili, R. Amadori, F. Ospitali, C. Lucarelli, F. Cavani, *Appl. Catal. A Gen.* **2015**, *504*, 408–419.
- [28] A. Lolli, R. Amadori, C. Lucarelli, M. G. Cutrufello, E. Rombi, F. Cavani, S. Albonetti, *Microporous Mesoporous Mater.* **2016**, *226*, 466–475.
- [29] D. Bonincontro, A. Lolli, A. Villa, L. Prati, N. Dimitratos, G. M. Veith, G. Botton, L. E. Chinchilla, F. Cavani, S. Albonetti, *Green Chem.* **2019**, DOI 10.1039/c9gc01283d.
- [30] S. E. Davis, B. N. Zope, R. J. Davis, *Green Chem.* **2012**, *14*, 143–147.
- [31] G. Yi, S. P. Teong, Y. Zhang, *Green Chem.* **2016**, *18*, 979–983.
- [32] V. Augugliaro, V. Loddo, G. Palmisano, L. Palmisano, *ACS Sustain. Chem. Eng* **2013**, *1*, 456–461.
- [33] I. Krivtsov, M. Ilkaeva, E. Salas-colera, Z. Amghouz, J. R. Garc, D. Eva, S. Ordo, S. Villarrodil, *J. Phys. Chem. C* **2017**, *121*, 6770–6780.
- [34] B. Zhou, J. Song, Z. Zhang, Z. Jiang, P. Zhang, B. Han, *Green Chem.* **2017**, *19*, 1075–1081.
- [35] H. Zhang, Q. Wu, C. Guo, Y. Wu, T. Wu, *ACS Sustain. Chem. Eng.* **2017**, *5*, 3517–3523.
- [36] G. Han, Y. H. Jin, R. A. Burgess, N. E. Dickenson, X. M. Cao, Y. Sun, *J. Am. Chem. Soc.* **2017**, *139*, 15584–15587.
- [37] I. Krivtsov, E. I. García-lópez, G. Marci, L. Palmisano, E. Díaz, Z. Amghouz, J. R. García, S. Ordó, *Appl. Catal. B Environ. Environ.* **2017**, *204*, 430–439.
- [38] S. Xu, P. Zhou, Z. Zhang, C. Yang, B. Zhang, K. Deng, S. Bottle, H. Zhu, *J. Am. Chem. Soc.* **2017**, *139*, 14775–14782.
- [39] M. Ilkaeva, I. Krivtsov, J. R. García, E. Díaz, S. Ordóñez, E. I. García-lópez, G. Marci, L. Palmisano, M. I. Maldonado, S. Malato, *Catal. Today* **2018**, *315*, 138–148.
- [40] M. Ilkaeva, I. Krivtsov, E. I. García-lópez, G. Marci, O. Khainakova, J. R. García, L. Palmisano, *J. Catal.* **2018**, *359*, 212–222.
- [41] V. R. Battula, A. Jaryal, K. Kailasam, *J. Mater. Chem. A* **2019**, *7*, 5643–5649.

- [42] H. Zhang, Z. Feng, Y. Zhu, Y. Wu, T. Wu, *J. Photochem. Photobiol. A Chem.* **2019**, *371*, 1–9.
- [43] V. Augugliaro, M. Bellardita, V. Loddo, G. Palmisano, L. Palmisano, S. Yurdakal, *J. Photochem. Photobiol. C Photochem. Rev.* **2012**, *13*, 224–245.
- [44] U. Ibrahim, A. Halim, *J. Photochem. Photobiol. C Photochem. Rev.* **2008**, *9*, 1–12.
- [45] Q. Wu, Y. He, H. Zhang, Z. Feng, Y. Wu, T. Wu, *Mol. Catal.* **2017**, *436*, 10–18.
- [46] J. A. Melero, J. Iglesias, A. Garcia, *Energy Environ. Sci.* **2012**, *5*, 7393–7420.
- [47] I. Kubičková, D. Kubička, *Waste and Biomass Valorization* **2010**, *1*, 293–308.
- [48] G. Bagnato, A. Iulianelli, A. Sanna, A. Basile, *Membranes* **2017**, *7*, 1–31.
- [49] K. E. Sanwald, T. F. Berto, W. Eisenreich, O. Y. Gutiérrez, J. A. Lercher, *J. Catal.* **2016**, *344*, 806–816.
- [50] G. Dodekatos, S. Schünemann, H. Tüysüz, *ACS Catal.* **2018**, *8*, 6301–6333.
- [51] Y. C. Lin, *Int. J. Hydrogen Energy* **2013**, *38*, 2678–2700.
- [52] J. Gao, Y. Wang, Y. Ping, D. Hu, G. Xu, F. Gu, F. Su, *RSC Adv.* **2012**, *2*, 2358–2368.
- [53] J. L. G. Fierro, R. M. Navarro, M. A. Pena, *Chem. Rev.* **2007**, 3952–3991.
- [54] M. Markiewicz, Y. Q. Zhang, A. Bösmann, N. Brückner, J. Thöming, P. Wasserscheid, S. Stolte, *Energy Environ. Sci.* **2015**, *8*, 1035–1045.
- [55] H. Barthelemy, M. Weber, F. Barbier, *Int. J. Hydrogen Energy* **2016**, *42*, 7254–7262.
- [56] P. Preuster, Q. Fang, R. Peters, R. Deja, *Int. J. Hydrogen Energy* **2017**, *43*, 1758–1768.
- [57] E. Gianotti, M. Taillades-jacquín, J. Rozie, D. J. Jones, *ACS Catal.* **2018**, *8*, 4660–4680.
- [58] C. A. Schwengber, H. J. Alves, R. A. Schaffner, F. Alves da Silva, R. Sequinel, V. R. Bach, R. J. Ferracin, *Renew. Sustain. Energy Rev.* **2016**, *58*, 259–266.
- [59] D. I. Kondarides, V. M. Daskalaki, A. Patsoura, X. E. Verykios, *Catal. Letters* **2008**, *122*, 26–32.
- [60] M. Yasuda, T. Matsumoto, T. Yamashita, *Renew. Sustain. Energy Rev.* **2018**, *81*, 1627–1635.
- [61] Z. H. N. Al-azri, W. Chen, A. Chan, V. Jovic, T. Ina, H. Idriss, G. I. N. Waterhouse, *J. Catal.* **2015**, *329*, 355–367.
- [62] X. Jiang, X. Fu, L. Zhang, S. Meng, S. Chen, *J. Mater. Chem. A* **2015**, *3*, 2271–2282.
- [63] V. M. Daskalaki, D. I. Kondarides, *Catal. Today* **2009**, *144*, 75–80.
- [64] W. Chen, A. Chan, Z. H. N. Al-azri, A. G. Dosado, M. A. Nadeem, D. Sun-Waterhouse, H. Idriss, G. I. N. Waterhouse, *J. Catal.* **2015**, *329*, 499–513.
- [65] F. J. López-Tenllado, J. Hidalgo-Carrillo, V. Montes, A. Marinas, F. J. Urbano, J. M. Marinas, L. Ilieva, T. Tabakova, F. Reid, *Catal. Today* **2017**, *280*, 58–64.
- [66] H. Bahruji, M. Bowker, P. R. Davies, L. S. Al-Mazroai, A. Dickinson, J. Greaves, D. James,

- L. Millard, F. Pedrono, *J. Photochem. Photobiol. A Chem.* **2010**, *216*, 115–118.
- [67] Z. H. N. Al-Azri, W. T. Chen, A. Chan, V. Jovic, T. Ina, H. Idriss, G. I. N. Waterhouse, *J. Catal.* **2015**, *329*, 355–367.
- [68] J. Yu, Y. Hai, M. Jaroniec, *J. Colloid Interface Sci.* **2011**, *357*, 223–228.
- [69] A. Petala, E. Ioannidou, A. Georgaka, K. Bourikas, D. I. Kondarides, *Appl. Catal. B Environ.* **2015**, *178*, 201–209.
- [70] Y. Li, B. Wang, S. Liu, X. Duan, Z. Hu, *Appl. Surf. Sci.* **2015**, *324*, 736–744.
- [71] D. Praveen Kumar, N. Lakshmana Reddy, M. Mamatha Kumari, B. Srinivas, V. Durga Kumari, B. Sreedhar, V. Roddatis, O. Bondarchuk, M. Karthik, B. Neppolian, et al., *Sol. Energy Mater. Sol. Cells* **2015**, *136*, 157–166.
- [72] S. Ichiro Fujita, H. Kawamori, D. Honda, H. Yoshida, M. Arai, *Appl. Catal. B Environ.* **2016**, *181*, 818–824.
- [73] H. X. Sang, X. T. Wang, C. C. Fan, F. Wang, *Int. J. Hydrogen Energy* **2012**, *37*, 1348–1355.
- [74] R. P. Panmand, Y. A. Sethi, S. R. Kadam, M. S. Tamboli, L. K. Nikam, J. D. Ambekar, C.-J. Park, B. B. Kale, *CrystEngComm* **2015**, *17*, 107–115.
- [75] G. Carraro, C. MacCato, A. Gasparotto, T. Montini, S. Turner, O. I. Lebedev, V. Gombac, G. Adami, G. Van Tendeloo, D. Barreca, et al., *Adv. Funct. Mater.* **2014**, *24*, 372–378.
- [76] W. T. Chen, A. Chan, Z. H. N. Al-Azri, A. G. Dosado, M. A. Nadeem, D. Sun-Waterhouse, H. Idriss, G. I. N. Waterhouse, *J. Catal.* **2015**, *329*, 499–513.
- [77] D. Praveen Kumar, M. V. Shankar, M. Mamatha Kumari, G. Sadanandam, B. Srinivas, V. Durgakumari, *Chem. Commun.* **2013**, *49*, 9443–9445.
- [78] S. G. Babu, R. Vinoth, D. Praveen Kumar, M. V. Shankar, H. L. Chou, K. Vinodgopal, B. Neppolian, *Nanoscale* **2015**, *7*, 7849–7857.
- [79] V. Maurino, A. Bedini, M. Minella, F. Rubertelli, E. Pelizzetti, C. Minero, *J. Adv. Oxid. Technol.* **2008**, *11*, 184–192.
- [80] C. Minero, A. Bedini, V. Maurino, *Appl. Catal. B Environ.* **2012**, *128*, 135–143.
- [81] P. Panagiotopoulou, E. E. Karamerou, D. I. Kondarides, *Catal. Today* **2013**, *209*, 91–98.
- [82] H. Pan, A. Steiniger, M. D. Heagy, S. Chowdhury, *J. CO₂ Util.* **2017**, *22*, 117–123.
- [83] L. Guo, Q. Sun, K. Marcus, Y. Hao, J. Deng, K. Bi, Y. Yang, *J. Mater. Chem. A* **2018**, *6*, 22005–22012.
- [84] G. Dodekatos, H. Tüysüz, *Catal. Sci. Technol.* **2016**, *6*, 7307–7315.
- [85] V. Augugliaro, H. A. H. El Nazer, V. Loddo, A. Mele, G. Palmisano, L. Palmisano, S. Yurdakal, *Catal. Today* **2010**, *151*, 21–28.
- [86] V. Amendola, R. Pilot, M. Frascioni, O. M. Marago, M. A. Iati, *J. Phys. Condens. Matter* **2017**,

29, p.203002.

- [87] H. Pan, A. Steiniger, M. D. Heagy, S. Chowdhury, *J. CO₂ Util.* **2017**, *22*, 117–123.
- [88] G. Dodekatos, H. Tüysüz, *Catal. Sci. Technol.* **2016**, *6*, 7307–7315.
- [89] I. Ali, *RSC Adv.* **2018**, 30125–30147.
- [90] D. S. Kim, S. Kwak, *Appl. Catal. A Gen.* **2007**, *323*, 110–118.
- [91] C. Ampelli, F. Tavella, S. Perathoner, G. Centi, *Chem. Eng. J.* **2017**, *320*, 352–362.
- [92] M. A. Malik, M. Younus, M. A. Hashim, *Arab. J. Chem.* **2012**, *5*, 397–417.
- [93] C. Tojo, D. Buceta, M. A. Lo, *J. Phys. Chem. C* **2018**, *122*, 20006–20018.
- [94] M. Sanchez-Dominguez, C. Aubery, C. Solans, in *Smart Nanoparticles Technology*, **2012**, pp. 196–220.
- [95] E. Nourafkan, H. Gao, Z. Hu, D. Wen, *Chem. Eng. Res. Des.* **2017**, *125*, 367–384.
- [96] D. Das, A. Shivhare, S. Saha, A. K. Ganguli, *Mater. Res. Bull.* **2012**, *47*, 3780–3785.
- [97] J. Carbajo, A. Bahamonde, M. Faraldos, *Mol. Catal.* **2017**, *434*, 167–174.
- [98] E. Nourafkan, M. Asachi, H. Gao, G. Raza, D. Wen, *J. Ind. Eng. Chem.* **2017**, *50*, 57–71.
- [99] J. Kou, C. Lu, J. Wang, Y. Chen, Z. Xu, *Chem. Rev.* **2017**, *117*, 1445–1514.
- [100] S. Eriksson, U. Nylén, S. Rojas, M. Boutonnet, *Appl. Catal. A Gen.* **2004**, *265*, 207–219.
- [101] M. Boutonnet, S. Lögdberg, E. E. Svensson, *Curr. Opin. Colloid Interface Sci.* **2008**, *13*, 270–286.
- [102] M. Sanchez-Dominguez, L. F. Liotta, G. Di, G. Pantaleo, A. M. Venezia, C. Solans, M. Boutonnet, *Catal. Today* **2010**, *158*, 35–43.
- [103] G. Martra, *Appl. Catal. A Gen.* **2000**, *200*, 275–285.
- [104] K. Nakajima, R. Noma, M. Kitano, M. Hara, *J. Phys. Chem. C* **2013**, *117*, 16028–16033.
- [105] T. Komanoya, K. Nakajima, M. Kitano, M. Hara, *J. Phys. Chem. C* **2015**, *119*, 26540–26546.
- [106] L. Atanda, A. Silahua, S. Mukundan, A. Shrotri, G. Torres-torres, J. Beltramini, *RSC Adv.* **2015**, *5*, 80346–80352.
- [107] E. Lombardi, ‘Catalytic Aqueous Phase Conversion of Polyols to Hydrogen and Chemicals’, Università di Bologna, **2017**.
- [108] Z. Wu, S. Cao, C. Zhang, L. Piao, *Nanotechnology* **2017**, *28*, 1–12.
- [109] T. Luttrell, S. Halpegamage, J. Tao, A. Kramer, E. Sutter, M. Batzill, *Sci. Rep.* **2014**, *4*, 1–8.
- [110] J. Zhang, P. Zhou, J. Liu, J. Yu, *Phys. Chem. Chem. Phys.* **2014**, *16*, 20382–20386.
- [111] T. Zhang, J. Low, K. Koh, J. Yu, T. Asefa, *ACS Sustain. Chem. Eng* **2018**, *6*, 531–540.
- [112] Y. Sohn, W. Huang, F. Taghipour, *Appl. Surf. Sci.* **2017**, *396*, 1696–1711.
- [113] Q. Zhang, L. Gao, J. Guo, *Appl. Catal. B Environ.* **2000**, *26*, 207–215.
- [114] M. Andersson, A. Kiselev, L. Österlund, A. E. C. Palmqvist, *J. Phys. Chem. C* **2007**, *111*,

6789–6797.

- [115] W. Zhou, F. Sun, K. Pan, G. Tian, B. Jiang, Z. Ren, C. Tian, *Adv. Funct. Mater.* **2011**, *21*, 1922–1930.
- [116] S. E. Braslavsky, A. M. Braun, A. E. Cassano, A. V Emeline, M. I. Litter, L. Palmisano, V. N. Parmon, N. Serpone, *Pure Appl. Chem.* **2011**, *83*, 931–1014.
- [117] V. Loddo, M. Bellardita, G. Camera-Roda, F. Parrino, L. Palmisano, in *Curr. Trends Futur. Dev. Membr. Photocatalytic Membr. Photocatalytic Membr. React.*, Elsevier Inc., **2018**, pp. 1–43.
- [118] F. Parrino, M. Bellardita, E. I. García-López, G. Marci, V. Loddo, L. Palmisano, *ACS Catal.* **2018**, *8*, 11191–11225.
- [119] M. Tahir, N. S. Amin, *Energy Convers. Manag.* **2013**, *76*, 194–214.
- [120] F. Parrino, V. Loddo, V. Augugliaro, G. Camera-Roda, G. Palmisano, L. Palmisano, S. Yurdakal, *Catal. Rev.* **2019**, *61*, 163–213.
- [121] M. Heule, S. Vuillemin, L. J. Gauckler, *Adv. Mater.* **2003**, *15*, 1237–1245.
- [122] D. Levy, M. Zayat, in *Sol-Gel Handb.*, **2015**, pp. 277–310.
- [123] J. M. Szeifert, J. M. Szeifert, D. Fattakhova-Rohlfing, D. Fattakhova-Rohlfing, D. Georgiadou, D. Georgiadou, V. Kalousek, V. Kalousek, J. Rathouský, J. Rathouský, et al., *Chem. Mater.* **2009**, *21*, 1260–1265.
- [124] T. Brezesinski, J. Wang, J. Polleux, B. Dunn, S. H. Tolbert, *Mater. Sci.* **2009**, *131*, 1–2.
- [125] P. Innocenzi, L. Malfatti, *J. Nanoparticle Res.* **2018**, *20*, 1–13.
- [126] L. J. Guo, *Adv. Mater.* **2007**, *19*, 495–513.
- [127] A. Biswas, I. S. Bayer, A. S. Biris, T. Wang, E. Dervishi, F. Faupel, *Adv. Colloid Interface Sci.* **2012**, *170*, 2–27.
- [128] Z. S. Rak, J. Walter, *J. Mater. Process. Technol.* **2006**, *175*, 358–363.
- [129] T. Berger, D. Monllor-satoca, M. Jankulovska, T. Lana-villarreal, *ChemPhysChem* **2012**, *13*, 2824–2875.
- [130] R. Peng, C. Xia, D. Peng, G. Meng, *Mater. Lett.* **2004**, *58*, 604–608.
- [131] N. Novaković, Dragoljub Kašiković, G. Vladić, M. Pál, *Print. Polym.* **2016**, 247–261.
- [132] D. Astruc, in *Organomet. Chem. Catal.*, **2007**, pp. 5–20.
- [133] C. Copéret, M. Chabanas, R. Petroff Saint-Arroman, J. M. Basset, *Angew. Chemie - Int. Ed.* **2003**, *42*, 156–181.
- [134] C. Copéret, A. Comas-Vives, M. P. Conley, D. P. Estes, A. Fedorov, V. Mougel, H. Nagaie, F. Núñez-Zarur, P. A. Zhizhko, *Chem. Rev.* **2016**, *116*, 323–421.
- [135] J.-M. Basset, A. Baudouin, F. Bayard, J.-P. Candy, C. Copret, D. A. Mallmann, G. Godard, E.

- Kuntz, F. Lefebvre, C. Lucas, et al., in *Mod. Surf. Organomet. Chem.*, **2009**, pp. 23–73.
- [136] M. K. Samantaray, E. Pump, A. Bendjeriou-Sedjerari, V. D'Elia, J. D. A. Pelletier, M. Guidotti, R. Psaro, J. M. Basset, *Chem. Soc. Rev.* **2018**, *47*, 8403–8437.
- [137] T. Saboo, 'Surface Organometallic Chemistry on Titania', Université Claude Bernard Lyon 1, **2018**.
- [138] L. Li, E. Abou-Hamad, D. H. Anjum, L. Zhou, P. V. Laveille, L. Emsley, J. M. Basset, *Chem. Commun.* **2014**, *50*, 7716–7719.
- [139] A. Choplin, *J. Mol. Catal.* **1994**, *86*, 501–512.
- [140] T. Alphazan, A. Bonduelle-Skrzypczak, C. Legens, A. S. Gay, Z. Boudene, M. Girleanu, O. Ersen, C. Copéret, P. Raybaud, *ACS Catal.* **2014**, *4*, 4320–4331.
- [141] S. Cadot, O. Renault, M. Frégnaux, D. Rouchon, E. Nolot, K. Szeto, C. Thieuleux, L. Veyre, H. Okuno, F. Martin, et al., *Nanoscale* **2017**, *9*, 538–546.
- [142] A. Lolli, M. Blosi, S. Ortelli, A. L. Costa, I. Zanoni, D. Bonincontro, F. Carella, S. Albonetti, *Catal. Today* **2019**, *334*, 193–202.
- [143] Y. Duan, M. Zhang, L. Wang, F. Wang, L. Yang, X. Li, C. Wang, *Appl. Catal. B Environ.* **2017**, *204*, 67–77.
- [144] S. Challagulla, K. Tarafder, R. Ganesan, S. Roy, *Sci. Rep.* **2017**, *7*, 1–11.
- [145] H. L. Ma, J. Y. Yang, Y. Dai, Y. B. Zhang, B. Lu, G. H. Ma, *Appl. Surf. Sci.* **2007**, *253*, 7497–7500.
- [146] V. Swamy, *Phys. Rev. B* **2008**, *77*, 195414(4).
- [147] T. K. Das, P. Ilaiyaraja, P. S. V. Mocherla, G. M. Bhalerao, C. Sudakar, *Sol. Energy Mater. Sol. Cells* **2016**, *144*, 194–209.
- [148] R. López, R. Gómez, *J. Sol-Gel Sci. Technol.* **2012**, *61*, 1–7.
- [149] C. Lucarelli, A. Lolli, A. Giugni, L. Grazia, S. Albonetti, D. Monticelli, A. Vaccari, *Appl. Catal. B Environ.* **2017**, *203*, 314–323.
- [150] F. J. López-tenllado, J. Hidalgo-carrillo, V. Montes, A. Marinas, F. J. Urbano, *Catal. Today* **2017**, *280*, 58–64.
- [151] J. Lan, J. Lin, Z. Chen, G. Yin, *ACS Catal.* **2015**, *5*, 2035–2041.
- [152] Y. Yamauchi, A. Fatehmulla, A. Farooq, T. Yoshikawa, T. Masuda, K. C.-W. Wu, *ChemCatChem* **2017**, *32023*, 361–365.
- [153] S. Yurdakal, B. Sina, *Catal. Today* **2017**, *281*, 53–59.
- [154] S. K. Burgess, O. Karvan, J. R. Johnson, R. M. Kriegel, W. J. Koros, *Polymer (Guildf)*. **2014**, *55*, 4748–4756.
- [155] Z. Yuan, W. Zhao, Z. Liu, B. Xu, *J. Catal.* **2017**, *353*, 37–43.

- [156] Y. Chen, Y. Wang, W. Li, Q. Yang, Q. Hou, L. Wei, L. Liu, F. Huang, M. Ju, *Appl. Catal. B Environ.* **2017**, *210*, 352–367.
- [157] M. L. Brongersma, *Proc. IEEE* **2016**, *104*, 2349–2361.
- [158] Y. K. Lee, C. H. Jung, J. Park, H. Seo, G. A. Somorjai, J. Y. Park, *Nano Lett.* **2011**, *11*, 4251–4255.
- [159] C. Zhou, W. Deng, X. Wan, Q. Zhang, Y. Yang, Y. Wang, *ChemCatChem* **2015**, *7*, 2853–2863.
- [160] I. Krivtsov, E. I. Garcia-Lopez, G. Marci, L. Palmisano, Z. Amghouz, J. R. Garcia, S. Ordonez, E. Diaz, *Appl. Catal. B Environ.* **2017**, *204*, 430–439.
- [161] S. Qourzal, N. Barka, M. Belmouden, A. Abamrane, S. Alahiane, M. Elouardi, A. Assabbane, Y. Ait-Ichou, *Fresenius Environ. Bull.* **2012**, *21*, 1972–1981.
- [162] R. Qian, H. Zong, J. Schneider, G. Zhou, T. Zhao, Y. Li, J. Yang, D. W. Bahnemann, J. H. Pan, *Catal. Today* **2019**, *335*, 78–90.
- [163] A. Kubacka, M. Fernández-García, G. Colón, *Chem. Rev.* **2012**, *112*, 1555–1614.
- [164] R. Castro-Muñoz, *J. Food Eng.* **2019**, *253*, 27–39.
- [165] R. Molinari, C. Lavorato, P. Argurio, K. Szymański, D. Darowna, S. Mozia, *Catalysts* **2019**, *9*, 239(38).
- [166] M. Bellardita, G. Camera-Roda, V. Loddo, F. Parrino, L. Palmisano, *Catal. Today* **2020**, *340*, 128–144.
- [167] V. Augugliaro, G. Camera-rodà, V. Loddo, G. Palmisano, L. Palmisano, J. Soria, S. Yurdakal, *J. Phys. Chem. Lett.* **2015**, *6*, 1968–1981.
- [168] G. Camera-Roda, V. Augugliaro, A. Cardillo, V. Loddo, G. Palmisano, L. Palmisano, *Chem. Eng. J.* **2013**, *224*, 136–143.
- [169] G. Camera-Roda, V. Loddo, L. Palmisano, F. Parrino, *Chem. Eng. Trans.* **2019**, *75*, 1–6.
- [170] M. A. Garcia, *J. Phys. D: Appl. Phys.* **2011**, *44*, 283001(43).
- [171] S. W. Verbruggen, M. Keulemans, B. Goris, N. Blommaerts, S. Bals, J. A. Martens, S. Lenaerts, *Appl. Catal. B Environ.* **2016**, *188*, 147–153.
- [172] O. R. Schade, K. F. Kalz, D. Neukum, W. Kleist, J. Grunwaldt, *Green Chem.* **2018**, *20*, 3530–3541.
- [173] J. An, G. Sun, H. Xia, *ACS Sustain. Chem. Eng.* **2019**, *7*, 6696–6706.
- [174] R. Liu, H. Yoshida, S. ichiro Fujita, M. Arai, *Appl. Catal. B Environ.* **2014**, *144*, 47–45.
- [175] M. A. Govindaraju V, Young K, *NMR Biomed* **2000**, *13*, 129–153.
- [176] M. C. Gutiérrez, M. L. Ferrer, L. Yuste, F. Rojo, F. Del Monte, *Angew. Chemie - Int. Ed.* **2010**, *49*, 2158–2162.

- [177] J. Kua, M. M. Galloway, K. D. Millage, J. E. Avila, D. O. De Haan, *J. Phys. Chem. A* **2013**, *117*, 2997–3008.
- [178] A. K. Eckhardt, M. M. Linden, R. C. Wende, B. Bernhardt, P. R. Schreiner, *Nat. Chem.* **2018**, *10*, 1141–1147.
- [179] H. Chen, B. Fang, Z. Hu, *Chromatographia* **2007**, *65*, 629–632.
- [180] K. J. Jiang, T. Kitamura, H. Yin, S. Ito, S. Yanagida, *Chem. Lett.* **2002**, 872–873.
- [181] H. Khan, N. Usen, D. C. Boffito, *J. Environ. Chem. Eng.* **2019**, *7*, 103267.
- [182] Y. Hu, X. Song, S. Jiang, C. Wei, *Chem. Eng. J.* **2015**, *274*, 102–112.
- [183] G. I. N. Waterhouse, W. Chen, A. Chan, D. Sun-Waterhouse, J. Llorca, H. Idriss, *J. Catal.* **2018**, *367*, 27–42.
- [184] W. T. Chen, A. Chan, D. Sun-Waterhouse, T. Moriga, H. Idriss, G. I. N. Waterhouse, *J. Catal.* **2015**, *326*, 43–53.
- [185] G. R. Bamwenda, S. Tsubota, T. Nakamura, M. Haruta, *J. Photochem. Photobiol. A Chem.* **1995**, *89*, 177–189.
- [186] A. G. Dosado, W. T. Chen, A. Chan, D. Sun-Waterhouse, G. I. N. Waterhouse, *J. Catal.* **2015**, *330*, 238–254.
- [187] R. Zanella, S. Giorgio, C. R. Henry, C. Louis, *J. Phys. Chem. B* **2002**, *106*, 7634–7642.
- [188] M. Bowker, H. Bahruji, J. Kennedy, W. Jones, G. Hartley, C. Morton, *Catal. Letters* **2015**, *145*, 214–219.
- [189] E. Kowalska, O. O. P. Mahaney, R. Abe, B. Ohtani, *Phys. Chem. Chem. Phys.* **2010**, *12*, 2344–2355.
- [190] E. Environ, K. Shimura, H. Yoshida, *Energy Environ. Sci.* **2011**, *4*, 2467–2481.
- [191] X. Fu, X. Wang, D. Y. C. Leung, Q. Gu, S. Chen, H. Huang, *Appl. Catal. B, Environ.* **2011**, *106*, 681–688.
- [192] N. Luo, Z. Jiang, H. Shi, F. Cao, T. Xiao, P. P. Edwards, *Int. J. Hydrogen Energy* **2009**, *34*, 125–129.
- [193] N. Lakshmana Reddy, K. K. Cheralathan, V. Durga Kumari, B. Neppolian, S. Muthukonda Venkatakrishnan, *ACS Sustain. Chem. Eng.* **2018**, *6*, 3754–3764.
- [194] S. Fang, Z. Sun, Y. H. Hu, *ACS Catal.* **2019**, *9*, 5047–5056.
- [195] M. T. Uddin, Y. Nicolas, C. Olivier, W. Jaegermann, N. Rockstroh, H. Junge, T. Toupance, *Phys. Chem. Chem. Phys.* **2017**, *19*, 19279–19288.
- [196] N. T. Catalysts, J. Hidalgo-carrillo, J. Mart, J. Morales, J. C. Espejo, F. Jos, A. Marinas, *Energies* **2019**, 3351.
- [197] J. R. Copeland, I. A. Santillan, S. M. Schimming, J. L. Ewbank, C. Sievers, *J. Phys. Chem. C*

- 2013**, *117*, 21413–21425.
- [198] G. L. Chiarello, D. Paola, E. Selli, *Photochem. Sci.* **2011**, *10*, 335–350.
- [199] R. Chong, J. Li, X. Zhou, Y. Ma, J. Yang, L. Huang, H. Han, F. Zhang, C. Li, *Chem. Commun.* **2014**, *50*, 165–167.
- [200] R. Chong, J. Li, Y. Ma, B. Zhang, H. Han, C. Li, *J. Catal.* **2014**, *314*, 101–108.
- [201] M. Bellardita, E. I. García-López, G. Marci, L. Palmisano, *Int. J. Hydrogen Energy* **2016**, *41*, 5934–5947.
- [202] E. Jolimaitre, D. Delcroix, N. Essayem, C. Pinel, M. Besson, *Catal. Sci. Technol.* **2018**, *8*, 1349–1356.
- [203] A. Takagaki, H. Goto, R. Kikuchi, S. T. Oyama, *Appl. Catal. A Gen.* **2019**, *570*, 200–208.
- [204] M. A. Haider Shipar, *Food Chem.* **2006**, *98*, 395–402.
- [205] K. M. A. Santos, E. M. Albuquerque, G. Innocenti, L. E. P. Borges, C. Sievers, M. A. Fraga, *ChemCatChem* **2019**, 3054–3063.
- [206] S. Lux, M. Siebenhofer, *Chem. Biochem. Eng. Q.* **2015**, *29*, 575–585.
- [207] M. Hara, K. Nakajima, K. Kamata, *Sci. Technol. Adv. Mater.* **2015**, *16*, 034903(22).
- [208] R. S. Assary, L. A. Curtiss, *J. Phys. Chem. A* **2011**, *115*, 8754–8760.
- [209] D. L. King, L. Zhang, G. Xia, A. M. Karim, D. J. Heldebrant, X. Wang, T. Peterson, Y. Wang, *Appl. Catal. B Environ.* **2010**, *99*, 206–213.
- [210] T. Montini, M. Monai, A. Beltram, I. Romero-Ocaña, P. Fornasiero, *Mater. Sci. Semicond. Process.* **2016**, *42*, 122–130.
- [211] T. Montini, V. Gombac, L. Sordelli, J. J. Delgado, X. Chen, G. Adami, P. Fornasiero, *ChemCatChem* **2011**, *3*, 574–577.
- [212] A. Tolosana-Moranchel, J. A. Casas, J. Carbajo, M. Faraldos, A. Bahamonde, *Appl. Catal. B Environ.* **2017**, *200*, 164–173.
- [213] J. Carbajo, A. Tolosana-Moranchel, J. A. Casas, M. Faraldos, A. Bahamonde, *Appl. Catal. B Environ.* **2018**, *221*, 1–8.
- [214] R. Fiorenza, S. Sciré, L. D’Urso, G. Compagnini, M. Bellardita, L. Palmisano, *Int. J. Hydrogen Energy* **2019**, *44*, 14796–14807.
- [215] K. A. R. Joseph, B. Viswanathan, *Indian J. Chem. - Sect. A Inorganic, Phys. Theor. Anal. Chem.* **2009**, *48*, 1378–1382.
- [216] K. Yamakawa, Y. Sato, K. Fukutani, *J. Chem. Phys.* **2016**, *144*, 154703(7).
- [217] Y. Cao, S. Hu, M. Yu, S. Yan, M. Xu, *Phys. Chem. Chem. Phys.* **2015**, *17*, 23994–24000.
- [218] P. Sampedro, G. Colón, M. Fernández-García, *J. Photochem. Photobiol. A Chem.* **2008**, *199*, 136–143.

- [219] W. Jiang, M. Zhang, J. Wang, Y. Liu, Y. Zhu, *Appl. Catal. B Environ.* **2014**, *160–161*, 44–50.
- [220] F. Chen, W. Zou, W. Qu, J. Zhang, *Catal. Commun.* **2009**, *10*, 1510–1513.
- [221] K. Hadjiivanov, D. Klissurski, G. Busca, V. Lorenzelli, *J. Chem. Soc. Faraday Trans.* **1991**, *87*, 175–178.
- [222] K. S. Finnie, D. J. Cassidy, J. R. Bartlett, J. L. Woolfrey, *Langmuir* **2001**, *17*, 816–820.
- [223] K. Tanaka, J. M. White, *J. Phys. Chem.* **1982**, *86*, 4708–4714.
- [224] C. Arrouvel, M. Digne, M. Breysse, H. Toulhoat, P. Raybaud, *J. Catal.* **2004**, *222*, 152–166.
- [225] H. Huang, J. Lin, L. Fan, X. Wang, X. Fu, J. Long, *J. Phys. Chem. C* **2015**, *119*, 10478–10492.
- [226] H. Lin, J. Long, Q. Gu, W. Zhang, R. Ruan, Z. Li, X. Wang, *Phys. Chem. Chem. Phys.* **2012**, *14*, 9468–9474.
- [227] M. Setvín, B. Daniel, V. Mansfeldova, L. Kavan, P. Scheiber, M. Fidler, M. Schmid, U. Diebold, *Surf. Sci.* **2014**, *626*, 61–67.
- [228] V. Augugliaro, S. Coluccia, V. Loddo, L. Marchese, G. Martra, L. Palmisano, M. Schiavello, *Appl. Catal. B Environ.* **1999**, *20*, 15–27.
- [229] X. Chen, L. Liu, P. Y. Yu, S. S. Mao, *Science*. **2011**, *331*, 746–750.
- [230] G. Wang, H. Wang, Y. Ling, Y. Tang, X. Yang, R. C. Fitzmorris, C. Wang, J. Z. Zhang, Y. Li, *Nano Lett.* **2011**, *11*, 3026–3033.
- [231] H. Song, C. Li, Z. Lou, Z. Ye, L. Zhu, *ACS Sustain. Chem. Eng.* **2017**, *5*, 8982–8987.
- [232] C. Kim, S. Kim, J. Lee, J. Kim, J. Yoon, *ACS Appl. Mater. Interfaces* **2015**, *7*, 7486–7491.
- [233] P. Laurent, L. Veyre, C. Thieuleux, S. Donet, C. Copéret, *Dalt. Trans.* **2013**, *42*, 238–248.
- [234] M. L. M. Bonati, T. M. Douglas, S. Gaemers, N. Guo, *Organometallics* **2012**, *31*, 5243–5251.
- [235] A. Borodziński, M. Bonarowska, *Langmuir* **1997**, *13*, 5613–5620.
- [236] M. S. A. Karunaratne, R. C. Reed, *Acta Mater.* **2003**, *51*, 2905–2919.
- [237] M. Zúkalová, M. Bousa, Z. Bastl, I. Jirka, L. Kavan, *J. Phys. Chem. C* **2014**, *118*, 25970–25977.
- [238] T. Berger, D. Monllor-Satoca, M. Jankulovska, T. Lana-Villarreal, R. Gómez, *ChemPhysChem* **2012**, *13*, 2824–2875.
- [239] T. Berger, T. Lana-Villarreal, D. Monllor-Satoca, R. Gómez, *J. Phys. Chem. C* **2007**, *111*, 9936–9942.
- [240] J. Löberg, J. Perez Holmberg, I. Mattisson, A. Arvidsson, E. Ahlberg, *Int. J. Dent.* **2013**, *2013*, 1–14.
- [241] H. Jiang, L. Yang, C. Li, C. Yan, P. S. Lee, J. Ma, *Energy Environ. Sci.* **2011**, *4*, 1813–1819.
- [242] X. Li, S. Pustulka, S. Pedu, T. Close, Y. Xue, C. Richter, P. Taboada-Serrano, *Nanomaterials* **2018**, *8*, DOI 10.3390/nano8060404.

- [243] T. Berger, T. Lana-Villarreal, D. Monllor-Satoca, R. Gómez, *Electrochem. commun.* **2006**, *8*, 1713–1718.
- [244] C. S. Kerr, A. Kryukovskiy, J. I. L. Chen, *J. Phys. Chem. C* **2018**, *122*, 17301–17308.
- [245] Y. Nam, J. H. Lim, K. C. Ko, J. Y. Lee, *J. Mater. Chem. A* **2019**, *7*, 13833–13859.
- [246] N. Q. Le, I. V. Schweigert, *J. Phys. Chem. C* **2017**, *121*, 14254–14260.
- [247] J. M. Jiménez, G. R. Bourret, T. Berger, K. P. McKenna, *J. Am. Chem. Soc.* **2016**, *138*, 15956–15964.
- [248] Y. Cheng, S. P. Jiang, *Prog. Nat. Sci. Mater. Int.* **2015**, *25*, 545–553.